UNIVERSITY OF SOUTHAMPTON

FACULTY OF ENGINEERING AND APPLIED SCIENCE

School of Engineering Sciences

The Aerodynamics of Multi-Element Wings in Ground Effect

by

Stephen Alexander Mahon

Thesis for the degree of Doctor of Philosophy

March 2005

UNIVERSITY OF SOUTHAMPTON

ABSTRACT

FACULTY OF ENGINEERING AND APPLIED SCIENCES

SCHOOL OF ENGINEERING SCIENCES

Doctor of Philosophy

THE AERODYNAMICS OF MULTI-ELEMENT WINGS IN GROUND EFFECT

Stephen Alexander Mahon

A comprehensive investigation into a multi-element wing in ground effect was conducted. A dual strategy was used within the research incorporating both experimental and computational techniques. The primary application of this research is within the field of motorsport. However the results also have applications within the field of aeronautics and offer insights into the flow physics of fundamental aerodynamic features.

The experimental test rig consisted of a generic multi-element wing supported by an automated motion system. Measurements were obtained in the form of forces, surface pressures, oil flow visualisations and off-surface flow field data. The experimental aspect of the research evolved from investigating basic configuration variables to quantifying the effects of passive flow control techniques. An evolutionary strategy was also adopted for the computational aspect of the research developing from an aerofoil in ground effect to a multi-element wing in ground effect. The computational results were obtained by solving the Reynolds Averaged Navier Stokes equations.

The experimental part of the research offered improvements over the current knowledge of ground effect and high-lift aerodynamics. At low ride heights the generated flow field and corresponding forces were found to be dependent on the direction of ride height variation, a novel finding. Variations in flap incidence directly influenced this dependency. An off-surface separation within the wake of the main element was found to be one of the primary lift-limiting mechanisms. The use of passive flow control was found to influence both the surface flow field and characteristics of the vortical flows. The computational aspect of the research also offered improvements over the current knowledge. Accurate predictions of a single element aerofoil, multi-element aerofoil and multi-element wing were obtained quantifying the effects of grid resolution, turbulence model and ride height.

Contents

List of Figures

List of Tables

Acknowledgements

This thesis represents the culmination of work conducted over the last three years. However it has not been a solo effort by any means. The unquestionable support of my family throughout my life has allowed me to follow my dreams, challenge myself and achieve my goals even when people have doubted my abilities. In addition my heart felt thanks must go to Shaz who has put up with the many sleepness nights, my random babbling and given me the confidence to push myself. As some reward she can now hold a comprehensive conversation concerning motorsport and wings in ground effect.

For the opportunity to do this research my thanks must go to Xin. Over the years he has pushed me to my limits mentally and then made me surpass them. His support has been unquestionable and his counsel more than I could have hoped for. I class him now more than a just supervisor and more as a friend. My thanks must go to the whole BAR team, in particular Willem Toet and Jonathan Zerihan. Their support and technical input was invaluable and in Jonathan's case the business meetings in the pub were gratefully received.

My thanks must go to Geoff Baldwin, Geoff Thomas, Mike Thomas, Mike Tudor-Pole and Charlie Williams for their help, guidance and countless cups of tea. I now know far too much about the history of Southampton and have now been fully trained in the art of washing up. Their humor and warmth has set a high standard for all future wind tunnel testing which I shall aspire to.

Although the last few years have been challenging I have also had a lot of fun due to my fellow Phd'ers. Cheers to Irish Dave, Martijn, Simon, Scottie-too-Hottie and Sammie for the daily 4 O'clock tea break, obviously in addition to the 11 O'clock tea break for which I must thank Maureen. For the countless trips to the Hobbit, Orange Rooms, Rhinos and other alcoholic establishments I must thank the afore mentioned and Kate, Kimmy, Gav, Sabrina, the unforgettable Neil, Astro Dave, Andreas, Jim, Raj and Ed.

Nomenclature

A_r	=	Frontal area of wind tunnel test rig
AR	=	Aspect ratio, b/c
A_{wt}	=	Cross sectional area of wind tunnel test section, 3.4m^2
b	=	Wing span, 580mm
b_d	=	Height of wind tunnel test section
c	=	Total chord of wing, 284mm
c_f	=	Flap chord, 145mm
c_m	=	Main element chord, 139mm
c_s	=	Tyrrell 026 single element chord, 223.4mm
c_t	=	Total chord of the Tyrrell 026 double-element aerofoil, 380mm
C_D	=	Coefficient of drag, $D/q_\infty bc$
C_{Di}	=	Coefficient of lift induced drag, $(k_i/(\pi AR))C_L{}^2$
C_{Dmax}	=	Maximum drag coefficient
C_F	=	Force coefficient
C_{Ff}	=	Force coefficient corrected to unconstrained flow conditions
C_l	=	Total sectional downforce, $C_l = (C_{lc} + C_{lt})/2$
C_{lc}	=	Sectional downforce at wing centre span
C_{ld}	=	Double-Element Tyrrell 026 sectional coefficient of downforce, $L/q_\infty c_t$
C_{ls}	=	Single element Tyrrell 026 sectional coefficient of downforce, $L/q_\infty c_s$
C_{lt}	=	Sectional downforce at wing tip
C_L	=	Coefficient of downforce, $L/q_\infty bc$
C_{Lmax}	=	Maximum coefficient of downforce
C_M	=	Coefficient of pitching moment, $M/q_\infty bc^2$
C_{Mmax}	=	Maximum pitching moment coefficient
c_{ph}	=	Specific heat at constant pressure

C_P	=	Coefficient of pressure, $(p - p_\infty)/q_\infty$
C_{Pscale}	=	Scaled pressure coefficient, $1 - ((C_P - 1)/(C_{Psuc} - 1))$
C_{Pstag}	=	Coefficient of pressure at the stagnation point
C_{Psuc}	=	Coefficient of pressure at the point of maximum suction
d_h	=	Hydraulic diameter of vortex
d_i	=	Streamwise distance from the camera lens to the laser plane
d_o	=	Camera lens focal length
D	=	Drag, positive in the positive x-direction
D_{coup}	=	Coupled drag force
D_i	=	Lift induced drag
h	=	Ride height
h_d	=	Dynamic head in freestream
h_{dep}	=	Ride height at which forces become dependent on ride height direction
H_s	=	Boundary layer shape parameter, δ^*/θ
H_w	=	Width of wind tunnel test section
I	=	Turbulence Intensity, u'/U_∞
k	=	Turbulent kinetic energy
k_i	=	Induced drag factor
l_s	=	Turbulence length scale
L	=	Lift, positive indicates downforce i.e. force in a negative y-direction
L_{coup}	=	Coupled lift force
M	=	Pitching moment measured about the main element leading edge
M_{coup}	=	Coupled pitching moment
p	=	Static pressure
q_∞	=	Dynamic head, $\frac{1}{2}\rho {U_\infty}^2$
r^*	=	Radial distance from vortex centre at which maximum rotation rate occurs
R	=	Residual value at a given iteration
R_s	=	Rossby number, $u/(r^*\ \omega)$
R_0	=	Initial residual value
Re	=	Reynolds number based on wing chord, $\rho U_\infty c/\mu$
Re_{mod}	=	Modified Reynolds number, $\rho U_\infty/\mu$
s	=	Distance downstream of maximum suction
$\mathbf{S}$	=	Symmetric part of $\nabla \mathbf{u}$

s_t	=	s at trailing edge of element
t	=	Time
T	=	Temperature
u, v, w	=	Streamwise, transverse and spanwise velocity components
u', v', w'	=	Streamwise, transverse and spanwise perturbations
U_∞	=	Freestream velocity
u_{conf}	=	Streamwise velocity component at the confluence point
u_{min}	=	Minimum streamwise velocity component within a wake profile
V_D	=	Raw drag voltage
V_{Dzero}	=	Zero drag voltage
V_L	=	Raw lift voltage
V_{Lzero}	=	Zero drag voltage
V_M	=	Raw pitching moment voltage
V_{Mzero}	=	Zero pitching moment voltage
x, y, z	=	Cartesian coordinates, x positive downstream, y positive up, z positive to starboard
x_f	=	Streamwise coordinate measured downstream from the flap leading edge
x_{sep}	=	Streamwise location of separation on the suction surface
x_t	=	Streamwise location of transition on the suction surface of wing
y^+	=	Non-dimensional height, yU_τ/υ

Greek Symbols

α_f	=	Flap incidence
α_m	=	Main element incidence
α_s	=	Tyrrell 026 single element incidence
β	=	Wing efficiency, C_L/C_D
δ_g	=	Flap gap
δ_{low}	=	Lower boundary of wake as measured by 99% displacement thickness
δ_o	=	Flap overlap
δ_{top}	=	Upper boundary of wake as measured by 99% displacement thickness
δ_{99}	=	Wake thickness as measured by 99% displacement thickness
δ^*	=	Boundary layer displacement thickness
ε	=	Turbulence dissipation rate

γ_y, γ_z	=	Vertical and spanwise perspective error
μ	=	Viscosity
υ_t	=	Eddy viscosity
θ	=	Boundary layer momentum thickness
ρ	=	Density
ω	=	Maximum rotation rate within vortex
$\mathbf{\Omega}$	=	Asymmetric part of $\nabla \mathbf{u}$
Ω_x	=	Non-dimensional vorticity, $(\partial v/\partial z - \partial w/\partial y)c/U_\infty$
ξ_y	=	Azimuthal angle between a seeding particle and the x-axis
ξ_z	=	Inclination angle between a seeding particle and the x-axis

Subscripts

f	=	Flap
low	=	Main element wake
m	=	Main element
top	=	Flap wake
v	=	Centre of vortex
∞	=	Freestream

Glossary

CBL	:	Confluent Boundary Layer
CFD	:	Computational Fluid Dynamics
FIA	:	Federation Internationale de L'Automobile
LDA	:	Laser Doppler Anemometry
PIV	:	Particle Image Velocimetry
RANS	:	Reynolds Averaged Navier Stokes
SA	:	Spalart-Allmaras (turbulence model)
URANS	:	Unsteady Reynolds Averaged Navier Stokes

Chapter 1

Introduction

1.1 Introduction to Topic

Prior to 1966 the aerodynamic developments of racing cars had been limited to streamlining the overall profile of the car while maintaining adequate engine cooling [1]. The introduction of wings in 1966 heralded a new era in racing car aerodynamics. Currently all modern racing cars utilise aerodynamic devices of one form or another to generated negative lift (downforce). Through the use of downforce the mechanical grip between the tyres and the road surface can be significantly increased. Therefore increased cornering speeds and lateral accelerations may be achieved. One category of motorsport where aerodynamic development has had a significant impact is Formula One. Since 1969 wings in Formula One have been limited in size and placement resulting in a constant drive for optimum wing performance. The true potential of ground effect aerodynamics was realised in 1977 with the introduction of the Lotus type 78 [1]. Through the use of flexible side skirts, wings close to the ground and a shaped underbody the Lotus type 78 represented a milestone in ground effect aerodynamics within Formula One. Increases in the frequency of racing accidents in the 1980's due to sudden losses of downforce, resulted in the banning of shaped undertrays and side skirts. Since then racing car aerodynamics has focused on the front wing, rear wing and rear diffuser.

Modern day open wheeled racing cars racing cars utilise both a front wing and a rear wing. The front wing is located upstream of the main body of the car and suspension and operates in ground effect. Typically ground clearances range between 70 and 100mm [2]. The front wing of a racing car generates approximately 25-30% of the total downforce of the car [3]. However, it is also commonly used as a trimming device balancing the car laterally.

The combination of physical restrictions due to technical regulations and the requirement for maximum downforce has resulted in highly complex front wing designs. Currently all modern racing cars utilise multi-element front wings and passive flow control devices to maximise the downforce generated. Although the design of the front wing is critical consideration must also be taken concerning the location. Front wings are positioned such that the generated wake and edge vortices influence downstream components of the car for example the undertray, diffuser and radiators. Therefore both surface and far field aspects of the flow field are critical during the design of a racing car.

Previous research into wings in ground effect have all focussed on the case of an inverted wing positioned statically above a ground plane. However, voids still exist within the understanding of the flow field generated by a wing in ground effect. An additional topic which is relevant but has not previously been investigated is aerodynamic hysterisis. The influence of ride height on a wing in ground effect has similarities to the influence of incidence on a wing in freestream. Hysterisis within the forces generated by a wing in freestream due to incidence variation and stall is a well documented phenomena [4–6]. It therefore stands to reason that similar force hysterisis phenomena may be observed with a wing in ground effect. Currently there exists a lack of understanding concerning force hysterisis due to ride height variation. Ruhrmann & Zhang [7] offer the only previous relevant research. There exists a lack of understanding concerning the flow field generated by a multi-element wing in ground effect, be it static or in motion.

1.2 Applicability of Research

The main application of this research may be found within the field of motorsport. In particular categories of motorsport which utilise inverted wings in ground effect. There exists a lack of quantitative data concerning the surface and off-surface flow field generated by a multi-element wing in ground effect. In addition the predictive capabilities of computational investigations remain unclear due to the lack of quantitative validation. This research will offer high quality quantitative data. Therefore progressions within the understanding of wings in ground effect and validation of current computational techniques will be achieved.

An additional application of this research may be found in the field of aviation. The topic of high-lift wings is one which currently attracts significant research. An inverted

multi-element wing in ground effect may be considered as a high-lift wing over which an adverse pressure gradient may be imposed. Therefore insights into the lift enhancing and lift limiting mechanisms may be gained from this research.

Another application of this research may be found within the field of aeroacoustics. All modern aircraft utilise multi-element wings which possess semi-span flaps and slats. Due to the finite dimensions of the flap a vortex is generated at the outboard tip of the flap known as a 'flap side edge vortex'. When the flap is set at a high incidence the adverse pressure gradient over the flap can cause the flap side edge vortex to burst. The resulting noise generation is significant enough to warrant research [8]. An inverted wing in ground effect equipped with endplates generates a vortex located beneath the wing [9]. Therefore a wing in ground effect represents a generic situation where an adverse pressure gradient may be imposed on a vortex. Results concerning the behaviour of the vortices generated by a wing in ground effect may therefore be applicable to the acoustics of flap side edge vortices.

The wing profiles used within this research were specifically developed for use within motorsport. However the features of the profiles offer similarities to those used within the aeronautical field. The profiles of the wing were supercritical and cambered, possessing finite trailing edges. These features are typical within high lift devices for use on aeronautical applications. Therefore direct applications of the data obtained within this research may be found within the wider field of aeronautical high lift devices.

1.3 Aims of Research

The aims of this research were as follows.

- To investigate and quantify the flow field generated by a multi-element wing in ground effect.
- To investigate the effects of ride height variation on the performance of a multi-element wing in ground effect.
- To investigate any dependency of the forces generated by a multi-element wing in ground effect on the direction of ride height variation. This will be achieved though the use of an automated motion system.

- To investigate the influence of passive flow control devices on the performance of a multi-element wing in ground effect.
- To quantify the predictive capabilities of numerical techniques with regards to a multi-element wing in ground effect.
- To provide high quality experimental and computational data to act as a foundation for future investigations.
- To further the understanding of the flow fields generated by high-lift wings.

1.4 Structure of Thesis

This thesis is divided into four main sections. Firstly previous investigations and literature relevant to this topic of research will be reviewed (Chapter 2). Secondly the experimental details and results of this research will be discussed within Chapters 3 to 7. The numerical results of this research will then be covered within Chapters 9 to 11. Finally both the experimental and computational results will be summarised and recommendations for future investigations will be offered (Chapter 12).

Chapter 2

Literature Review

This chapter reviews previous investigations pertinent to the topic of multi-element wings in ground effect. A review of fundamental aerodynamic phenomena regarding the aerodynamics of wings and ground effect will be presented first. Secondly previous research concerning multi-element wings in freestream and wings in ground effect will be covered with fundamental aspects of each flow field discussed separately.

2.1 Aerodynamic Flow Phenomena

2.1.1 Wing Tip Vortices

Wing tip vortices are a feature of all three-dimensional wings designed for subsonic use. The wing tip vortices of wings are typically generated as a result of the pressure difference between the pressure and suction surfaces of the wing. The pressure difference induces a spanwise circulation which in turn causes the streamlines to converge on the suction surface and diverge on the pressure surface. At the tips of the wing the combination of the pressure difference and the opposing flow direction causes the flow to swirl and detach from the wing thus forming a vortex. Numerous computational [8, 10–12] and experimental investigations [13–17] into wing tip vortices have been performed covering the initial development [18–20], downstream development and decay of the vortex.

Wing tip vortices are complex in structure containing inherent instabilities and unsteadiness and are prone to wandering [14]. Although early investigations linked vortex wandering to freestream turbulence and unsteadiness [13, 14, 17], recent investigations have proposed that wandering may be linked to shear layer instabilities [21, 22] or the interac-

tion of multiple instabilities [23, 24]. Currently the true cause of vortex wandering remains elusive.

The interaction between trailing vortices and a ground plane is a topic which lends itself to a wing in ground effect. Of the previous investigations into such interactions [10, 25–27] the work of Harvey & Perry [28] is most applicable. The flow of a wing tip vortex generated by a half span wing, and the interaction with a moving ground was experimentally investigated. Separation and subsequent entrainment of the ground boundary layer was observed with a large ground to vortex vertical distance. Reducing the vertical distance resulted in the formation of a secondary vortex with circulation in the opposite sense to the main vortex. The interaction between the two vortices forced the main vortex upwards away from the ground plane.

2.1.2 Lift Induced Drag

Lift induced drag occurs as a direct result of the downwash generated by the tip vortices of a three-dimensional wing. Figure 2.1 presents a section of a three-dimensional wing in freestream. Combining the downwash generated by the wing tip vortices (v_i) with the freestream velocity (U_∞) generates an effective freestream velocity (U_e). The rotation of the freestream velocity results in the lift being resolved into two components. Firstly the effective lift (L_e) normal to the effective freestream velocity and secondly a component of drag (D_i). This drag component due to the rotation of the lift component is known as the *lift induced drag*. Equation 2.1 presents the relationship between the lift induced drag and the lift based on the Lanchester-Prandtl lifting line theory [29].

$$C_{Di} = \left(\frac{k_i}{\pi AR}\right) {C_L}^2 \tag{2.1}$$

where AR is the aspect ratio of the wing and k_i is the induced drag factor. Therefore through the analysis of the relationship between the drag and the square of the lift the lift induced drag factor may be calculated.

2.1.3 Flow Separation

Flow separation in a steady two-dimensional flow is defined as the point along a surface where the wall shear stress is equal to zero. Viscous flow separation is primarily caused by

adverse pressure gradients which act on the flow within a boundary layer in such a way as to decelerate it and cause it to detach from the surface. The process of flow separation is of particular importance to wing design since it is one of the primary lift limiting mechanisms. Due to the importance of flow separation various empirical models predicting the separation location of a turbulent boundary layer over an aerofoil exist which are reviewed by Cebeci *et al* [30]. Such schemes offer limited applicability to a multi-element situation due to the interactive viscous flow features.

Flow separation on aeronautical wings is generally caused by setting the incidence of the wing at too great a value such that the adverse pressure gradient is too high for the boundary layer to remain attached. An inverted wing in ground effect however, can have separation at zero incidence. The shape of the passage that the suction surface and ground create resembles a venturi. The downstream expansion of the passage causes the flow to decelerate and thus creates a streamwise adverse pressure gradient the magnitude of which is dependent on the ride height. Flow separation in this case is highly three-dimensional and dominated by a three-dimensional separation bubble [31] as illustrated by the results of Zerihan [9].

2.1.4 Vortex Breakdown

Vortex breakdown as defined by Leibovich [32], is a change in vortex structure initiated by a variation in the characteristic ratio of tangential to axial velocity components. Dilatation of the vortex core and the presence of a stagnation point on the centre-line of the vortex are also distinctive features [33]. Depending on the application vortex breakdown can be either detrimental in the case of delta wings, or beneficial in the case of following aircraft. Numerous experimental investigations into vortex breakdown exist using various measurement techniques such as dye visualisation [34, 35], schlieren [36] and LDA [37]. Lucca-Negro & O'Doherty [38] offer a comprehensive review of previous experimental, computational and theoretical investigations with respect to vortex breakdown.

Sarpkaya [34,35] investigated vortex breakdown within a divergent channel, varying the swirl of the flow and the mass flow rate within the water tunnel. Three types of breakdown were observed; double helix, spiral and axisymmetric (bubble), using a dye visualisation technique. Leibovich [32] further classified vortex breakdown into seven modes combining distinct features of the three types defined by Sarpkaya. The type and mode of vortex breakdown was found to be primarily dependent on the Reynolds number and swirl intensity

of the vortical flow. In 1965 Chanaud [39] investigated swirling flows within a vortex whistle and a cyclone separator. The results indicated that the location at which vortex breakdown occurred within the flow, was time dependent. The frequency of this oscillatory motion, due to instabilities within the flow, was found to be dependent on the angular velocity characteristics within the steady swirling flow. The implications of the unsteady nature of vortex breakdown on delta wings were discussed by Gursul & Xie [40]. It was shown that at high angles of attack significant contributions to buffeting of the wing were caused by the unsteady nature of vortex breakdown and the corresponding fluctuations in breakdown location.

The breakdown of tip vortices on rectangular wings due to increases in incidence has also been investigated [8, 41]. The situation of an inverted wing in close proximity to the ground generates a vortex at each tip present within the divergent section of the passage created by the ground plane and suction surface of the wing. Within such a situation vortex breakdown can be initiated by reductions in ride height [42]. Vortex breakdown in the context of ground effect devices, and its impact on downforce has been previously noted by Zerihan & Zhang [42], Senior & Zhang [43] and Ruhrmann & Zhang [7]. Since vortex breakdown can produce sudden detrimental variations in the forces generated by a ground effect device it is a topic which requires thorough investigation. The evolution of a vortex in an adverse pressure gradient and any subsequent breakdown has applications to flap side edge aeroacoustics [8], a topic which is currently at the fore-front of aeroacoustics research. An additional application may be found in the validation of computational schemes such as detached eddy simulations [44] and large eddy simulations [45].

2.2 Multi-Element Wing Aerodynamics

2.2.1 Background

The lift generated by a single element wing increases with incidence until a limit is reached, caused by separation of the boundary layer on the suction surface. Altering the profile of the wing can offer improvements in lift through modifying the boundary layer profile in order to prevent separation and maximise the magnitude of the surface pressure distribution. In comparison much greater improvements in lift can be achieved through the use of additional wing elements located upstream and downstream of the main wing element. In 1914 experiments were performed on a wing with a hinged rear section [46] however the true

origins of multi-element wings can be traced back to 1921 and an investigation into wings with slots [47] performed over a period of 10 years. The understanding of the true flow physics of multi-element wings remained incorrect until the historic presentation given by Smith in 1974 [48]. Smith reviewed all the previous work and theoretically investigated the effects of slots on the surface pressure distribution over multi-element wings. The widely accepted notion that the slots present between the slat, main element and flap acted as boundary layer control devices was disproved. Alternatively it was shown that the slots have the effect of manipulating the pressure distribution over each element via five primary effects: Slat effect, Circulation effect, Dumping effect, Off-the-surface pressure recovery and Fresh-boundary-layer effect. Detailed explanations and illustrations of these five effects are presented in Appendix A. More recently [49] and in addition to the work of Smith, a vortex based method was offered modelling the effects of flap incidence on the interaction between the individual elements of a wing.

The combination of improved lift production and the requirement for ever increasingly efficient aircraft wings has resulted in multi-element wings being used on all modern aircraft. Retractable elements ensure that the performance of the aircraft is optimum both during cruise and approach stages. Numerous experimental and numerical investigations into multi-element wings have been conducted over the last 30 years. Aspects such as Reynolds number effects, merging boundary layers and performance during slat and flap extension/retraction have been investigated. The following subsections will review the most relevant and thorough investigations into the main topics pertinent to multi-element wings.

2.2.2 Confluent Boundary Layers

The traditional configuration of a multi-element wing consists of a combination of three types of elements. The element located upstream of the main element leading edge is referred to as a slat, whereas the elements downstream of the main element are known as flaps. Since the elements are physically separated each element generates a separate boundary layer which develops along the element and detaches at the trailing edge. Due to the close proximity of the elements a merging or confluence occurs between the wake of an upstream element and the suction surface boundary layer of a downstream element (Figure 2.2). This feature is referred to as a confluent boundary layer (CBL) and is the dominant viscous feature on all multi-element wings.

Due to the complex flow physics and interactions associated with a CBL, building block

investigations were initially performed to gain an insight into individual aspects of the flow field. The confluence of a wake and a boundary layer was experimentally investigated by Bario *et al* [50] using a tandem symmetric aerofoil configuration in a variable pressure gradient wind tunnel. Off-surface velocity measurements were obtained at a Reynolds number (Re) of 1.2×10^6 based on the total aerofoil chord. It was concluded that the flow field could be separated into three viscous regions; the wall boundary layer, the internal, and the external half wake. Squire [51] further separated the wake and boundary layer interaction into three successive regions; unmerged with the wake and boundary layer separated by a potential zone, initial merging of the viscous layers and fully merged.

The interaction of an aerofoil wake with a flat plate boundary layer was investigated by Zhou & Squire [52]. Streamwise and vertical off-surface velocity measurements were obtained at a Reynolds number of 8×10^5 based on the aerofoil chord. The pressure gradient within the test section was varied using gauze sheets attached to the exit of the test section therefore imposing an adverse pressure gradient. Within the initial merging of the wake and the boundary layer a region was observed where the Reynolds shear stress ($\overline{u'v'}$) was of opposite sign to the mean velocity gradient. In accordance with the Boussinesq assumption (Equation 2.2) the eddy viscosity (υ_t) was negative, as theorised by Olson & Orloff [53].

$$\frac{\partial}{\partial y}(\overline{u'v'}) = \frac{\partial}{\partial y}\left(\upsilon_t \frac{\partial \overline{u}}{\partial y}\right) \tag{2.2}$$

This particular feature of a CBL has been repeatedly reported within multi-element wing flows [54–57] and continues to limit numerical predictive capabilities.

More recently the instabilities present within a CBL have been numerically investigated and validated with experimental data [58]. The numerical model comprised a Blasius boundary layer superimposed over a wake located above the boundary layer. The results indicated that the presence of the wake had a direct influence on the growth and transition characteristics of the boundary layer via amplifying any boundary layer instability present. It was also noted that a reduction in wake height had the effect of stabilising the unstable modes within the wake, an effect also observed by Chin *et al* [59].

In summary, numerous two-dimensional investigations into the flow physics of a CBL have been performed. The complexity of the shear layers and presence of highly curved streamlines has meant that computational simulations have contained discrepancies when

compared to experimental data. To date experimental investigations on finite span wings have been extremely limited and no previous research concerning the effects of ground proximity on a CBL have been performed.

2.2.3 Lift Limiting Mechanisms

The exact flow mechanisms responsible for limiting the maximum lift attainable by a multi-element wing are currently not fully understood. Typically on multi-element wings at low values of incidence the main element produces the majority of the lift followed by the flap and then the slat [60]. The stall of a multi-element wing due to increases in incidence is gradual unlike the leading edge stall phenomena and can occur without the presence of flow separation on the suction surfaces [60].

In 1978 Petrov [61, 62] experimentally investigated a four-element wing at high values of incidence obtaining force measurements, surface pressures and flow field visualisations through the use of tufts. The Reynolds number based on the chord of the wing ranged between 8.6×10^5 and 1.55×10^6. The results indicated the presence of a stable region of reversed flow located within the main element wake at high angles of attack. Petrov [61] theorised that this flow feature unique to multi-element wing flows could be responsible for the gradual stall observed, although it was not proven conclusively. Within all investigations into multi-element wings conducted both before and after Petrov an off-surface flow reversal region has not been observed, with the exception of Drela [63]. The numerical investigation into optimising multi-element aerofoils conducted by Drela, included a scheme designed to optimise the lift generated by a four-element aerofoil through the parameters of incidence and surface geometry. The solution indicated that that lift was limited by a rapid dilation of the main element wake due to the adverse pressure gradient over the flap suction surface.

To date the lift limiting mechanisms of multi-element wings in freestream are unclear. The findings of Petrov and Drela indicate that one mechanism responsible is the rapid dilation of the main element wake generating a gradual stall. All other investigations have failed to capture this stable reversal region within the main element wake. However, Petrov and Drelas investigations were valid and the results may be more applicable to a ground effect situation where the pressure gradients are more adverse than freestream.

2.2.4 Reynolds Number Effects

The effects of variations in Reynolds number on the performance of multi-element wings is one of increasing interest. Increases in Reynolds number typically cause boundary layers to become more resistant to adverse pressure gradients and therefore beneficially affect separation characteristics. On multi-element wings increases in Reynolds number can promote separation via processes collectively known as adverse Reynolds number effects. These phenomena were first recognised in the early 1990's [64, 65] and are due to the interactions between the boundary layers and the slots. With increases in Reynolds number the thickness of the boundary layers decrease which increases the effective slot gap. These changes in slot settings can cause the peak suction on an aft element to increase and promote separation on the trailing edge of the upstream element.

The main implication of this phenomena as highlighted by Ying *et al* [56] and Spaid [66] is that such effects could allow poorly performing full scale wings to enter production. The combination of adverse Reynolds number effects and variations in boundary layer structure with Reynolds number results in force trends which do not allow for reliable extrapolation. Few facilities allow for testing at realistic Reynolds numbers therefore care must be taken when interpreting and comparing data from scaled multi-element wings.

2.2.5 Configuration Effects

The most simple and effective method of manipulating the flow field generated by a multi-element wing is through alterations in the configuration of the main element, flap and slat. Variations in flap setting have been shown to influence not only the aerodynamic forces but also the structure of the wake produced [67]. In the majority of previous multi-element wing investigations the effects of varying rigging configurations have been investigated [59,66,68]. The effects of varying the flap incidence and flap location with respect to the main element, are to alter the transition of the boundary layer on the suction surface of the flap. This in turn effects the separation and stalling of the wing. The effects of rigging settings in ground effect have also been investigated [9] albeit briefly. In all cases with a fixed Reynolds number, a single optimum configuration exists depending on the flow variable being optimised.

Experimental optimisation of multi-element wing configurations was investigated by Valarezo *et al* [69] and more recently by Landman & Britcher [5, 70]. To reduce the wind tunnel time Landman & Britcher utilised an automated system which allowed the flap set-

ting to be optimised in situ. The results showed a single optimum flap and slat setting which provided maximum lift for a fixed Reynolds number. The investigation performed by Landman & Britcher also incorporated hysteresis effects due to flap extension/retraction. Hysteresis effects result when an aerodynamic device is in motion with respect to a fixed frame of reference. The effects are generated by aerodynamic phenomena which are path dependent such as vortex breakdown or boundary layer separation. The tests performed by Landman & Britcher all incorporated free transition to allow for any separation bubble induced hysteresis effects, as explained by Meuller & Batill [71], to occur. Biber & Zumwalt [6] observed that the main hysteresis effects were caused by the separation of the flap boundary layer. They noted that once the flow over the suction surface of the flap had separated it formed a stable bubble shaped region which persisted as the flap incidence was reduced to below the stall angle.

Increasing the incidence of a flap causes the flow over the suction surface of the flap to experience a more adverse pressure gradient. Similarities may be drawn between such a situation and a ground effect case where the ride height was reduced. It could therefore be theorised that hysteresis effects may occur on an inverted multi-element wing in ground effect. To date the only experimental research which has presented hysteresis effects due to ride was conducted by Rurhmann & Zhang [7] in which the effect of ride height on the performance of an diffuser equipped bluff body in ground effect was investigated.

2.2.6 Computational Investigations

Over the last 20 years a major effort has been underway to numerically investigate the flow field of multi-element wings. A detailed review of all previous numerical investigations may be found in Rumsey & Ying [60]. Historically numerical simulations of high-lift flows have failed to predict the maximum lift limits with acceptable accuracy. The main issues are a direct result of the CBL, the corresponding highly curved streamlines and the interactive viscous flow physics. Firstly, the inaccurate modelling of transition in a flow field dominated by shear layers causes the predicted wake creation, development and dissipation to be inaccurate. This common cause of inaccuracy was highlighted in the work of Mason [72] concerning leading edge-trailing edge interactions. The second problem arises due to a thin region close to the suction surface of a downstream element where the Reynolds stress and normal velocity gradient have opposite signs. This region violates the eddy viscosity hypothesis [60] (Boussinesq assumption) thus limiting the predictive capabilities of many

turbulence models.

The previous numerical investigations have all utilised various combinations of turbulence model, numerical solver and grid strategy. A summary of the previous computational investigations and the techniques utilised is presented in Tables 2.1 and 2.2. The differences between each investigation can be attributed to various factors, chief among them are type of grid, grid resolution and turbulence models employed within the Reynolds Averaged Navier-Stokes (RANS) simulation.

In order to grid the complex geometry of a multi-element wing four gridding techniques may be used; fully structured, structured chimera, unstructured and hybrid. A fully structured grid offers minimal dissipation of flow features however the requirement for minimal skewness and aspect ratio results in large grids [41,73] and therefore dramatically increases the computational cost. A method for reducing the number of structured cells used with multi-element wing grids is to employ a chimera structured grid [74–76]. This strategy overlays grids for each element onto a domain grid joining and removing nodes as required. Such a scheme is more flexible than a fully structured scheme however computational costs are increased due to additional processing required. An unstructured strategy [77–80] is the most flexible of the four however flow features are quickly dissipated due to the misalignment of the cell walls to the streamlines. The final strategy is a hybrid one which incorporates both structured and unstructured blocks therefore reducing the computational cost while maintaining adequate accuracy. To date no numerical investigation into wings in ground effect has utilised a hybrid grid strategy.

The method of modelling turbulence within a multi-element flow field is critical to the accuracy of the simulation and is also the main area of under-performance. Previous experimental investigations [56, 57] have indicated that the flow field close to the suction surface of a downstream element violates the Boussinesq assumption. The Boussinesq assumption is used in the majority of current turbulence models and assumes that the turbulent shear stress is directly proportional to the strain. Improvements may be found with the use of non-linear turbulence models, for example the explicit algebraic stress model (EASM) [81] and full Reynolds stress model (RSM). However the robustness of the these models limits their application.

2.3 Wing in Ground Effect Aerodynamics

2.3.1 Background

The influence of ground plane proximity on the performance of aircraft has been reported by pilots since the early days of flight. Every aircraft encounters ground effect when landing, observed as an increase in lift and decrease in drag. Since the 1920's experimental [82,83], computational [84–86] and theoretical [87–93] investigations have been conducted into the influence of ground proximity on aeronautical wings. Applications may be found on aircraft operating in close proximity to the surface of a body of water, known as Ekranoplans.

The flow physics generated by an inverted wing in ground effect i.e. with the suction surface closest to the ground plane, are fundamentally different to the non-inverted case. For this reason the remainder of this section will only refer to investigations concerning inverted wings in ground effect. Zahm & Bear [82] conducted the first investigation into an inverted wing in ground effect in 1921. The study focused primarily on aeronautical wings however for completeness an inverted situation was also considered. The results obtained for the inverted case were labelled as having *little practical importance* and hence were not published. Currently inverted wings in ground effect are used extensively in motorsport to increase the cornering capabilities of the racing car and therefore decrease the lap times. However, there still remains a lack of understanding with respect to inverted wings in ground effect, especially multi-element wings. The following subsections will review the topics pertinent to a ground effect situation in addition to the most relevant and thorough investigations into inverted wings in ground effect.

2.3.2 Representation of Ground Plane

Models tested within a wind tunnel are typically located in freestream in order to reduce any influence of the test section walls on the flow field generated. The flow entering the test section must be of good quality to obtain accurate and realistic results. When investigating a ground effect situation an additional requirement for accurate ground plane simulation is introduced which is of equal importance to the quality of the freestream flow. There exist four methods for representing a ground plane within a wind tunnel; a fixed ground plate, a fixed ground plate with tangential blowing, a reflection plane (image plane) or a moving belt technique.

The most basic representation of a ground plane may be obtained through the use of a

fixed ground plate, a method which in the past was common [80,94–97] due to its simplicity. Although imposing a zero cross-flow condition this method is unrealistic due to the presence of a boundary layer developing downstream from the upstream edge of the ground plate. The ground plate boundary layer may be reduced by shortening the upstream distance of the ground however it cannot be removed. Through the use of tangential suction and blowing at prescribed streamwise locations the boundary layer can be removed [98,99]. The complexity of imposing such a system inhibits the use within a large scale wind tunnel. In addition the ground plane simulation would not be generic with the suction and blowing distributions varying depending on the geometry and configuration of the model.

The reflection or image method for ground plane representation entails the use of two identical models located directly opposite each other with the lower model inverted [100]. In the case of an aerofoil such a method would cause the flow at the equidistant point between the two models to be parallel to freestream therefore generating an imaginary ground plane without a ground boundary layer. This method enforces a zero cross flow condition at the imaginary ground plane. However, the streamwise velocity of the imaginary ground plane is dependent on nature of the flow between the two models therefore generating a variable imaginary ground plane velocity. Therefore the reflection or image method for ground plane representation is physically incorrect and may not be used in situations where flow three-dimensionality is observed.

The use of a moving belt to simulate a moving ground plane was first published in 1934 by Klemin [101], however the origin of the method may be traced back to Eiffel twenty years earlier, albeit with unsuccessful attempts. A moving belt technique used in conjunction with boundary layer suction located upstream, offers a true representation of a ground plane. Although technically challenging to maintain a flat ground plane this method is the most robust, scalable and generic. Accordingly this technique is currently used within all large scale automotive wind tunnels and is the preferred method within research [9, 102–104]

2.3.3 Experimental Investigations

Prior to the 1990's experimental investigations into inverted wings in ground effect had resulted from larger investigations into whole car aerodynamics [105, 106]. The first experimental study dedicated solely to inverted wings in ground effect was conducted by Knowles *et al* [107] in 1994. A finite span wing of GA(W)-1 profile equipped with large endplates was tested at various ride heights and incidences. Tests were performed at a Reynolds num-

ber of 4.3×10^6, with a moving belt technique used to simulate the ground plane. Forces and surface pressures were obtained which indicated that increases in downforce and drag resulted from decreases in ride height. Stalling of the wing was captured at very low ride heights observed as a reduction in downforce and increase in drag. Within the same year and later in 1996 Ranzenbach & Barlow [95, 108] investigated symmetric and cambered wings respectively of infinite span in ground effect ($Re = 1.5 \times 10^6$). In both studies the ground plane was modelled using a fixed ground plate resulting in an unrealistic velocity profile close to the ground and a thick ground boundary layer. The forces possessed similar trends to Knowles *et al* with stall being attributed to the merging of the ground and wing boundary layers.

The first experimental investigation into an inverted multi-element wing in ground effect was conducted by Ranzenbach & Barlow in 1997 [96]. A NACA $62_2 - 215$ Mod B wing of infinite span possessing a flap cove region, with a 30% single slotted flap was investigated. Force results were obtained for various ride heights at a Reynolds number of 1.5×10^6. Similar to previous investigations [95, 108] the ground plane was modelled using a fixed ground plate. For all ride heights greatly increased values of downforce were observed when compared to the single element cases. Based on previous research [95, 108] the force reduction phenomena was again attributed to the merging of the ground and aerofoil boundary layers.

Jasinski & Selig [97] experimentally investigated an inverted double-element wing in ground effect in 1998. The main element and flap were specifically designed for the investigation and were mounted in a single slotted flap configuration. The wing was of finite span equipped with endplates characteristic of those found on Champ Cars and Formula One racing cars. The ground was stationary and impermeable during all investigations producing an unrealistic ground boundary layer. Downforce results were presented for various flap incidences and freestream velocities (Re=7.0×10^5 to 1.3×10^6) for a fixed ride height of 0.3 of the chord. The flow field data covered an area downstream of the wing tip using a seven-hole probe, indicated the presence of two vortical flows; the first located inboard of the endplate below the wing and, the second located outboard of the endplate above the wing. The importance of the vortical flows on the performance of an inverted wing in ground effect remained unclear until recently.

The most comprehensive investigation into inverted wings in ground effect to date was conducted by Zerihan [9]. The study included both a single element (modified GA(W)-

1 profile) and double-element (as before with 74% flap) finite span wing equipped with generic endplates. Tests were performed at chord based Reynolds numbers of 4.5×10^6 and 7.5×10^6 for the single element and double-element wings respectively. The ground plane was modelled using a moving belt technique ensuring a realistic velocity profile towards the ground plane with no ground boundary layer. Zhang & Zerihan [109] investigated the centre span wake flow field for the single element wing using Laser Doppler Anemometry (LDA) and Particle Image Velocimetry (PIV) techniques. The results indicated a thickening and downward shift of the wake as the ride height was reduced. Zerihan & Zhang [42] presented forces, surface pressures and surface flow field data using an oil flow visualisation technique for a single element wing. Increases in downforce with reduced ride height and subsequent stalling were captured. Stalling was attributed to separation on the suction surface revising the theory of Ranzenbach & Barlow [95]. In 2002 Zhang *et al* [110] investigated the wing tip flow field of the single element of Zerihan wing using a PIV technique. Breakdown of the vortex inboard of the endplate beneath the wing was captured at low ride heights in conjunction with a reduction in the rate of downforce increase. Zhang & Zerihan [111,112] investigated the double-element wing of Zerihan in 2002 and 2003 presenting forces, surface pressures, oil flow visualisations and flow field data using PIV and LDA techniques. The force trends were similar to those observed with the single element wing however the impact of the lower vortex bursting on the downforce was more pronounced. Stalling of the wing was observed at low ride heights with separation occurring on the flap suction surface.

In 2002 Lawson *et al* [113] experimentally investigated a finite span single element GA(W)-1 wing in ground effect without endplates. Tests were performed at a Reynolds number of 6.9×10^5. PIV techniques were used to obtain streamwise data in the region between the suction surface and the ground plane, which was simulated using a moving belt technique. Centre span flow field data and surface pressures were presented at various ride heights.

2.3.4 Computational Investigations

Numerous computational investigations into inverted single element wings in ground effect have been previously conducted. However there exists a lack of computational investigations into inverted multi-element wings in ground effect. Computational investigations into inverted wings in ground effect started in the 1980's. The earliest work was done by Katz [114] in which a single element wing in ground effect was modelled using a panel

method. Ground effect was modelled using the image plane method. This method did not taken into account viscous effects and as a result no downforce reduction, at low ride heights, was observed. Knowles *et al* [107] replicated the method of Katz with a single element GA(W)-1 aerofoil comparing the numerical results with experimental measurements previously obtained by Knowles *et al.* Simulations were performed at a Reynolds number of 4.3×10^6. The agreement between the numerical and experimental results was poor due to the direct comparison between inviscid simulations and viscous measurements.

In engineering applications, numerical solutions of Reynolds Averaged Navier-Stokes equations, often in steady state, are generally obtained. The work by Ranzenbach & Barlow [95,108] studied two-dimensional aerofoils in ground effect. In [95], a NACA 0015 airfoil at zero incidence was studied. The Reynolds number was 1.5×10^6. A RANS solution was sought with the effect of turbulence modelled by a variant of the $k - \varepsilon$ model [115]. The multi-block fully structured grids contained a total of 20,000 to 30,000 grid points. In [108], a cambered airfoil (NACA 4412) was employed. Again the incidence was zero and the Reynolds number was 1.5×10^6. In all cases the ground was stationary thus producing a ground boundary layer and an inaccurate ground plane simulation. In both [95] and [108] the downforce compared well with experimental data, obtained by Ranzenbach & Barlow, for a stationary ground case. The results indicated a sharp reduction in downforce at ride heights of the order of 0.05 of the chord. Due to the presence of a thick ground boundary layer this phenomena, referred to as the force reduction phenomena was attributed to the merging of the aerofoil and ground boundary layers.

In 1997 Razenbach *et al* [96] computationally investigated an inverted NACA $62_2 - 215$ Mod B aerofoil possessing a cove, with a 30% single slotted flap. RANS simulations were performed with a moving ground at a Reynolds number of 1.5×10^6 based on the chord. A fully structured chimera grid was used containing 30,734 cells with turbulence modelled by a variant of the standard $k - \varepsilon$ model. The grid used was extremely coarse compared to current computational investigations (Tables 2.1 and 2.2) in which grids typically contain of the order of 200,000 cells. The variation of the sectional forces with ride height was presented in conjunction with vorticity contour plots. The absolute values of the sectional forces showed little agreement with experimental data previously obtained by Ranzenbach *et al* [96]. However the variation in sectional forces with ride height was captured in conjunction with the force reduction phenomena. Based on previous research [95, 114] the force reduction phenomena was attributed to the merging of the ground and aerofoil

boundary layers.

Recently in a series of studies into an inverted wing in ground effect, Zerihan & Zhang performed a study and comparison with experimental measurements in order to establish a numerical model [116]. The method used solutions of the Reynolds Averaged Navier-Stokes equations with turbulence modelled by the Spalart-Allmaras model [117] and the $k-\omega$ SST model [118]. Fully structured grids were used containing up to 30,000 grid points. The results were compared to measured surface pressures and velocities taken at the centre of a wing span in ground effect. Major features of the flow were captured. The results yielded good qualitative trends for the aerodynamic performance, using the one-equation model when the surface pressures were compared at different ride heights. In general, the wake thickness was predicted reasonably well in the region near to the trailing edge. Further downstream, the wake was predicted to be thicker than that found in the experiments, with reduced velocities. The ground boundary layer was predicted well using the one-equation model, however the thickness was overpredicted using the two-equation model. In all cases a moving ground was simulated.

In 2002 Lawson *et al* [113] conducted a numerical study of a GA(W)-1 aerofoil in ground effect, through solutions of the RANS equations on a fully structured grid. The total number of grid points was 48,500. Turbulence was modelled using the Spalart-Allmaras model. The computational results were compared to experimental surface pressures and PIV images obtained with a finite wing. A moving ground was simulated in all computational and experimental cases. The agreement between the experimental and computational data was poor due to different values of freestream velocity employed in the experimental and computational studies, thus assuming zero scaling effects. Although the surface pressures were presented the computational force variations with ride height were not presented.

2.4 Flow Control

A flow control device, as defined by Flatt [119], is any mechanism or process which causes a flow field to behave differently than normal. Flow control can be achieved by either passive or active means depending on the application and level of control required. Active flow control techniques are prohibited within the majority of motorsport due to safety issues concerning possible malfunction. Passive flow control techniques are permitted within motorsport and are currently extensively used. The passive flow control devices which have

been, or are currently being used in conjunction with multi-element wings in ground effect are described in the remainder of this section.

2.4.1 Endplates

Endplates are primarily utilised for automotive applications where downforce must be maximised for given wing dimensions. The design of endplates have evolved from flat plates into highly complex three-dimensional shapes influencing many aspects of the wing tip aerodynamics. Hoerner & Borst [120] compared the use of endplates to increasing the effective span of the wing, and through experimentation linked the alteration in wing performance to aspect ratio. The resulting relationship produced a value for effective aspect ratio depending on the geometry of the endplates. The actual influence of endplates on wing characteristics is complex and the simplicity of Hoerner & Borsts theory is misleading but nevertheless has been used verbatim by many authors, for example Gopalarathnam *et al* [121].

Previous experimentation [9] has shown that endplates influence both the spanwise lift distribution of a wing and the vortical flows associated with the wing tips. Acting similarly to a dam, the endplates separate the pressure and suction surfaces of the wing thus producing a finite value of lift, or downforce, at the wing tip. As the height of the endplates is increased the wing flow gradually changes from being mainly three-dimensional to mainly two-dimensional. In addition two vortices are produced at each wing tip due to the pressure differences between the suction surface, freestream and pressure surface. In summary, a lack of quantitative data and understanding exists concerning the design and associated flow phenomena of endplates especially in ground effect.

2.4.2 Gurney Flaps

The Gurney flap is a simple device consisting of a thin strip of material, between 1–5% of aerofoil chord in height, attached perpendicular to the surface of an aerofoil usually at the trailing edge. Although the device itself is simple the flow field it produces and the effect on wing performance characteristics can be complex. The time averaged flow field generated by a Gurney flap consists of a region of separation located directly upstream and a pair of attached counter-rotating vortices directly downstream. The investigations performed by Jeffrey & Zhang [122] and Jeffery *et al* [3] revealed an instantaneous flow field with a wake of alternately shed vortices. These findings were reinforced by the more recent work of

Zerihan & Zhang [123]. More recently Gai & Palfrey [124] performed an investigation using both solid and serrated Gurney flaps on a symmetric aerofoil. In addition to capturing the influence of the Gurney flap on the wing, Gai & Palfrey offered an expression for the effectiveness of the Gurney flap. The relationship, based on the work performed by Liebeck [125], hypothesised that the effectiveness was dependent primarily on the Gurney flap height and the ratio of pressure surface and suction surface velocities at the trailing edge.

Myose *et al* [126], Ross *et al* [127] and Papadakis *et al* [128] all investigated the use of Gurney flaps primarily for separation control on multi-element wings. Ross *et al* found that the use of a Gurney flap located at the trailing edge of the main element caused the flap gap flow to be turned. This flow manipulation effectively reduced the incidence of the flow with respect to the flap and resulted in increased values of lift and wing efficiency. Myose *et al* [126] also observed the turning effects associated with a Gurney flap located within the cove region however only minimal performance gains were reported. This unexpectedly small influence was attributed to the flap gap settings which were configured without the Gurney flap present. Carrannanto *et al* [129] computationally investigated the use of a Gurney flap located within the flap cove using a RANS solver and Baldwin-Barth turbulence model. The results re-illustrated the predictive problems associated with high-lift flow fields but did manage to accurately capture the impact of the Gurney flap on the flow field and forces.

2.4.3 Vortex Generators

A vortex generator is a device which produces streamwise vortices to prevent flow separation by exchanging the momentum between the upper and lower layers of a boundary layer. Many different types of vortex generators exist however the majority may be classified as either submerged or unsubmerged. Submerged vortex generators are small in height such that they are completely enclosed within the boundary layer. In contrast unsubmerged vortex generators are large in height therefore protruding past the boundary layer. Since they are enclosed within the boundary layer, submerged vortex generators offer reduced values of parasitic drag.

Storms & Jang [130] investigated, in addition to Gurney flaps, the use of Wheeler wishbone type vortex generators on a single element wing in freestream. As predicted, the vortex generators prevented trailing edge separation and therefore increased the maximum

lift and the stall angle. The results also indicated that the combined use of vortex generators and Gurney flaps offered greater lift enhancement than either device could offer individually. Lin *et al* [131] experimented with both trapezoid wing and delta wing vortex generators on a multi-element wing. The vortex generators were configured such that either co-rotating or counter-rotating vortex pairs were produced. The results indicated that both counter-rotating and co-rotating configurations improved flow separation on the flap equally. Reductions in the shear-stress fluctuations, which were observed on the suction surface of the flap, were also noted.

In 2003 Kerho & Kramer [132] conducted an experimental and computational investigation into the use of vortex generators on natural laminar flow wings, with the intent of maximising wing performance. The influence of the vortex generator on the wing boundary layer flow was included in a computational design tool. The result was a series of natural laminar flow wing profiles possessing a pressure recovery more aggressive than normally possible with conventional natural laminar flow wing profiles. The resulting profiles offered net increases in lift with significant decreases in drag, highlighting the effectiveness of vortex generators.

2.4.4 Finite Trailing Edges

Varying the design of trailing edges from the classic sharp trailing edge was first considered during the design of wings for transonic cruise aircraft. Thompson & Whitelaw [133] experimentally investigated the effects of varying the trailing edge design on wake characteristics and surface pressures. Blunt, round and sharp trailing edges were investigated with the results indicating that the design of the trailing edge had an influence on the size and structure of the trailing edge separation region and hence the wake flow field. Thompson & Whitelaw [134] further investigated trailing edge design using both experimental and numerical techniques. The numerical results indicated that at low angles of attack simple turbulence models resolve the trailing edge flow accurately. However once separation is present at high angles of attack simple turbulence models are insufficient due to the importance of the turbulent normal stresses. Thompson & Lotz [135] simulated a single aerofoil equipped with a divergent trailing edge however the simulations were dominated by shocks thus masking the true variations in flow field due to the trailing edge design.

The wing profiles used within motorsport in ground effect applications typically possess blunt trailing edges. The exact reasons for this design feature is unclear however two

plausible reasons are as follows. Firstly motorsport wing elements are of hollow construction manufactured from composite material. A sharp trailing edge would cause manufacturing difficulties and the inherent brittleness of the material would make it fragile. Secondly the chordwise surface pressure distribution of a wing equipped with a finite trailing edge is such that a finite pressure difference occurs at the trailing edge. This feature is attractive in a situation where downforce must be maximised for a fixed wing geometry.

2.5 Chapter Summary

A review of the previous research concerning multi-element wings, ground effect and related topics has been performed. It has been shown that a large gap exists in the current understanding of high-lift flows and the influence of ground proximity. Numerous experimental investigations concerning multi-element wings exist, however the exact lift limiting mechanisms present remain unknown. The dominance and interactions of viscous effects within high-lift flows has also resulted in inaccurate computational investigations. To date hysteresis effects due to ride height on a multi-element wing in ground effect have not been investigated either experimentally or computationally. In addition there exists a lack of computational investigations into multi-element wings/aerofoils in ground effect and the applicability of current turbulence models to a ground effect situation.

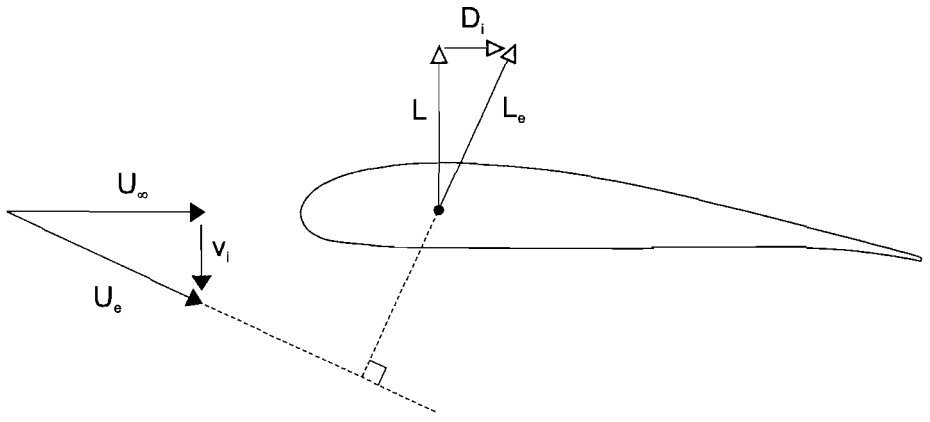

Figure 2.1: Schematic of the generation of lift induced drag.

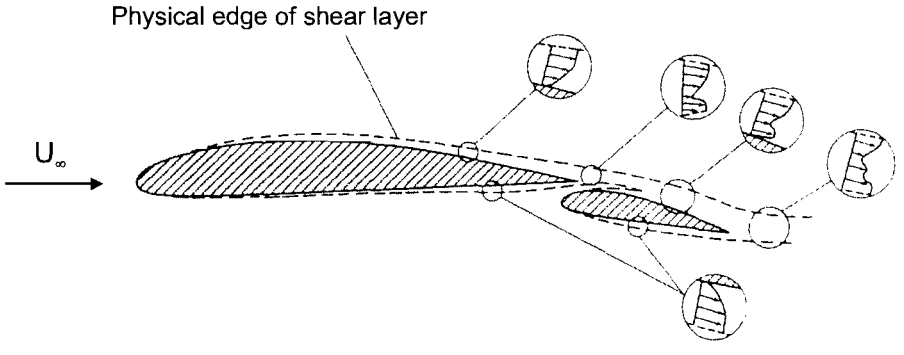

Figure 2.2: Illustration of boundary layer merging on a multi-element wing [136].

Author(s)	Year	2D/3D	Re	Numerical solver	Grid strategy	Cells	Turbulence model(s)
King & Williams [137]	1988	2D	3.5×10^6	Panel method & b.l method	Structured	N/A	N/A
Rogers *et al* [138]	1993	2D	1.52- to 9×10^6	RANS	Structured	55,000	Baldwin-Barth (BB), Baldwin-Lomax (BL)
Anderson *et al* [77]	1993	2D	5- and 9×10^6	RANS	Unstructured	22,491	BB, Spalart-Allmaras (SA)
Nelson *et al* [139]	1994	2D	1.8×10^6	RANS	Structured	70,000	BB
Rogers [74]	1994	2D	9×10^6	RANS	Structured, Chimera		BB, $k-\omega$
Rogers *et al* [140]	1994	2D	5- and 9×10^6	RANS	Structured, Chimera	68,000	BB, SA, $k-\omega$ SST , Durbin-Mansour
Valarezo & Mavriplis [78]	1995	2D	5- and 9×10^6	RANS	Unstructured	48-250,000	BB, SA, $k-\varepsilon$
Anderson *et al* [79]	1995	2D	9×10^6	RANS	Unstructured	49-87,783	SA
Godin *et al* [141]	1997	2D	2.51×10^6	RANS	Structured	182,295	SA, $k-\omega$ SST
Mathias *et al* [75]	1998	3D	3.7×10^6	RANS	Structured, Chimera	900,000	BB
Rumsey *et al* [142]	1998	2D	9×10^6	RANS	Structured	150,000	SA, $k-\omega$ SST
Rogers *et al* [73]	2000	3D	14.7×10^6	RANS	Structured	14,000,000	SA
Kim *et al* [76]	2000	2D	2.51×10^6	RANS	Structured, Chimera	25,294	$k-\varepsilon$, $k-\omega$, $k-\omega$ SST

Table 2.1: Summary of previous numerical investigations concerning multi-element wings, part (a).

Author(s)	Year	2D/3D	Re	Numerical solver	Grid strategy	Cells	Turbulence model(s)
Czerwiec *et al* [143]	2000	2D	9×10^6	RANS	Structured	150,000	$k-\zeta$
Khorrami *et al* [144]	2000	3D	3.6- to 19×10^6	URANS	Structured	271,000	$k-\omega$ SST
Rumsey & Gatski [81]	2000	2D	9×10^6	RANS	Structured	135,428	$k-\varepsilon$, $k-\omega$
Khorrami *et al* [41]	2002	3D	5.65×10^6	RANS	Structured	17,500,000	SA
Moitra [80]	2002	2D	9×10^6	RANS	Unstructured	215,240	SA
Rumsey *et al* [145]	2003	3D	9×10^6	RANS	Structured	4,470,000	SA

Table 2.2: Summary of previous numerical investigations concerning multi-element wings, part (b).

Author(s)	Year	Re	No. of elements	2D/3D	Endplates	Ground plane	Measurements obtained
Knowles *et al* [107]	1994	4.3×10^6	Single	3D	Yes	Moving	Forces, Surface Pressures
Ranzenbach & Barlow [95]	1994	1.5×10^6	Single	2D	N/A	Fixed	Forces
Ranzenbach & Barlow [108]	1996	1.5×10^6	Single	2D	N/A	Fixed	Forces
Ranzenbach & Barlow [96]	1997	1.5×10^6	Double	2D	N/A	Fixed	Forces
Jasinski & Selig [97]	1998	0.7- to 1.3×10^6	Double	3D	Yes	Fixed	Forces, Wing tip flow field u-velocity
Zhang & Zerihan [109]	2000	4.3- to 4.6×10^5	Single	3D	Yes	Moving	Center span wake u, v-velocities via PIV and LDA
Zerihan & Zhang [42]	2000	2×10^6	Single	3D	Yes	Moving	Forces, Oil flow, surface pressures
Zerihan [9]	2001	4.5- and 7.5×10^6	Single & double	3D	Yes	Moving	Forces, surface pressures, oil flow, wing tip v, w-velocities via PIV, center span u, v-velocities via PIV & LDA
Zhang *et al* [110]	2002	4.5×10^6	Single	3D	Yes	Moving	Forces, Wing tip v, w-velocities via PIV & LDA
Lawson *et al* [113]	2002	6.9×10^5	Single	3D	No	Moving	Surface pressures, center span u, v-velocities via PIV
Zhang & Zerihan [111]	2002	7.5×10^5	Double	3D	Yes	Moving	Forces, oil flow, surface pressures, center span u, v-velocities via LDA
Zhang & Zerihan [112]	2003	7.5×10^5	Double	3D	Yes	Moving	Forces, oil flow, surface pressures, center span u, v-velocities via PIV & LDA

Table 2.3: Summary of previous experimental investigations concerning inverted wings in ground effect.

Author(s)	Year	2D/3D	*Re*	Ground plane	No. of elements	Numerical solver	Grid Strategy	Cells	Turbulence model(s)
Katz [114]	1985	3D	Unknown	Image plane	Single	Panel method	N/A	N/A	N/A
Knowles *et al* [107]	1994	2D	4.3×10^6	Image plane	Single	Panel method	N/A	N/A	N/A
Ranzenbach & Barlow [95]	1994	2D	1.5×10^6	Fixed	Single	RANS	Structured	20- to 30,000	$k-\varepsilon$
Ranzenbach & Barlow [108]	1996	2D	1.5×10^6	Fixed	Single	RANS	Structured	29,980	$k-\varepsilon$
Ranzenbach & Barlow [96]	1997	2D	1.5×10^6	Moving	Double	RANS	Structured, Chimera	30,734	$k-\varepsilon$
Zerihan & Zhang [116]	2001	2D	4.6×10^5	Moving	Single	RANS	Structured	30,000	SA, $k-\omega$ SST
Lawson *et al* [113]	2002	2D	6.9×10^5	Moving	Single	RANS	Structured	48,500	SA

Table 2.4: Summary of previous numerical investigations concerning inverted wings in ground effect.

Chapter 3

Description of Experiments

This chapter introduces the experimental section of the research. The strategy used during testing will be set out first followed by the design of the experimental test rig and the wind tunnel facility used. The flow conditions will be stated followed by the measurement techniques.

3.1 Experimental Strategy

The front wings used within motorsport are typically highly complex three-dimensional custom wings incorporating twist, variable profiles and in some cases sweep. Such a wing would be inappropriate within this research since the current knowledge concerning multi-element wings in ground effect is incomplete even for wings of basic design. A compromise between a basic wing design and a realistic wing design was therefore required. A multi-element wing was required possessing the primary features of automotive wings such as cambered, supercritical profiles and endplates. The complexity of the wing was also required to be great enough to be applicable to motorsport.

The forces and flow field generated by a multi-element wing in freestream are dependent on numerous variables. With the additional complexity introduced by a ground effect situation, the testing matrix required to fully investigate a multi-element wing in ground effect is impractically large. A logical testing strategy was therefore required progressing from investigating the low priority variables up to the variables of most importance. Initially the effects of flap gap and overlap were investigated at a ride height typical for motorsport applications. Optimum values of flap gap and overlap were sought with regards to downforce, since this variable is of significant importance within motorsport. With the

location of the flap optimised the next stage was to investigate the influence of ride height on the performance of the wing and the corresponding flow field. The incidences of the main element and flap were fixed during this part of the research.

With the influence of flap gap, flap overlap and ride height investigated the effects of flap incidence could be quantified. Tests were performed with various flap incidences at ride heights of importance, as indicated by the forces obtained with fixed main element and flap incidence. Once all the variables of the wing had been investigated in isolation and quantified it was possible to investigate the effects of flow control devices. The influence of flow control devices located on the endplates was quantified at various ride heights. The baseline tests performed previously allowed for the exact variations in flow field to be mapped.

3.2 Wind Tunnel Model

3.2.1 Wing Design

The wing investigated in this research comprised of two separate elements in a single slotted flap configuration. Since the intention of this research was to investigate a generic, realistic wing, profiles developed by the industrial partner were used. Tables 3.1 to 3.4 present the coordinates of the profiles in non-dimensional format as illustrated in Figure 3.1. The main element and flap profiles were of constant chord across the span of the wing resulting in an unswept rectangular planform wing with zero twist. When mounted within the wind tunnel test section the wing was inverted such that the suction surfaces of the wing were closest to the ground plane.

The dimensions of the wing were set at 50% scale with respect to the 2002 Federation Internationale de L'Automobile (FIA) technical regulations [146]. The span of the wing (b) was set at 580mm. The chords of the main element (c_m) and flap (c_f) were set at 139mm and 145mm respectively. To remove the dependence of the overall chord of the wing on the configuration of the flap, the variable of total chord (c) was defined and set a value of 284mm. This value of total chord was used in the calculation of all non-dimensional values. The corresponding aspect ratio of the wing (AR) was 2.04.

3.2.2 Wing Construction

The two elements of the wing were manufactured from carbon fibre composites. Each element comprised a pressure and suction surface skin bonded together to form the overall profile required. The skins were formed by laying up the carbon fibre to a depth of 1.5mm in aluminium moulds, which were then placed in an autoclave and allowed to cure. This construction produced a hollow main element and flap allowing for the mounting brackets of the wing to be installed internally within the main element. Aluminium inserts containing threaded holes were bonded into each tip of the main element and flap to allow for the attachment of tip flow devices.

3.2.3 Endplate Design

All modern front wings used within motorsport applications are equipped with solid plates located at the tips of the wing, known as endplates. These devices are critical to the operation of the wing as they produce a finite pressure difference at the wing tip therefore increasing the downforce generated by the wing. The endplates currently used within motorsport are highly complex in shape and are designed to modify the flow field generated by the wing. It was therefore decided to use generic endplates at a scale consistent with that of the wing.

The endplates were manufactured from aluminium and measured 5mm in thickness, 275mm in length and 115mm in height. The leading edge, trailing edge and upper edges of each endplate were rounded with a radius of 2.5mm in accordance with the FIA technical regulations. The endplates were attached to the main element and flap by countersunk screws which screwed into the aluminium tip inserts. The endplates were positioned on the main element such that the leading edge of each endplate was 2.5mm upstream of the main element leading edge. In addition the lower edge of each endplate was located 5mm below the lowest point on the suction surface of the main element. The endplates were designed such that with a main element incidence of $+4^{\circ}$ the base of the endplates was parallel with the ground plane.

The endplates provided the only structural connection between the main element and the flap. This design feature allowed the location of the flap relative to the main element to be easily altered. Pitching of the flap was obtained through the use of a single pivot point located close to the flap leading edge and multiple holes located towards the flap trailing

edge. The flap angle holes were located such that the flap incidence could be varied between 0° and +30° in steps of 1°.

A common feature on the majority of endplates used within motorsport are horizontal shelves extending outwards located at the lower edge of each endplate. These structures will be referred to as *endplate feet* in the remainder of this thesis. The exact influence endplate feet on the flow field of the wing is currently unknown. For certain tests endplate feet measuring 5mm in thickness, 275mm in length and 55mm in width, were attached to the endplates using five countersunk screws per endplate. The leading edge, downstream edge and outer edge of each endplate foot were rounded with a radius of 2.5mm. The overall span of the wing equipped with endplates and endplate feet was therefore set at 700mm, corresponding to the maximum span permitted by the FIA technical regulations at a scale of 50%.

3.2.4 2.1m x 1.7m Wind Tunnel Model Support System

The traditional method for supporting a wing in a wind tunnel is to use a tricycle system with two upstream struts recording lift and drag forces and a central downstream strut measuring pitching moment. This configuration is useful in investigating aeronautical wings in freestream since incidence is the primary variable investigated. In a ground effect situation ride height is the primary variable therefore a tricycle support system is inappropriate and inefficient. Current industrial ground effect wind tunnel tests use automated motion systems supporting the model through a dual strut system. This configuration allows the ride height of the model to be varied with the model in situ. It was decided to use a similar mounting system within the 2.1m×1.7m tunnel in order to increase the efficiency of testing.

The support system for the wind tunnel model was designed to connect the wing to the automated motion system through a single strut, located centrally within the span of the test section. The main strut was manufactured out of steel and supported both the basic weight of the test rig and any additional downforce produced by the wing. In order to minimise any flow disturbances the entire support system was enclosed within a two piece fiber glass shroud. This shroud allowed cables and tubing to be routed from the wing to outside the test section. Force data was obtained using a three component steady state load cell capable of measuring downforce, drag and pitching moment simultaneously. The three component load cell attached to the lower surface of the main strut using an aluminium right angle bracket. An additional right angle bracket attached to the live face

of the load cell to a horizontal steel bar. The horizontal bar was designed such that the expected maximum downforce generated by the wing would cause a deflection of less than 0.05mm at the tips of the bar.

To increase the stability of the model during testing the wing was supported by two aluminium pillars which connected the main element to the horizontal bar. The cross section of the pillars were symmetric aerofoils to minimise the wake which could impinge onto the pressure surface of the flap. Pitching of the entire wing was achieved through the use of interchangeable attachments located between the pillars and the main element. These pillar feet were designed to produce a specific angle of incidence on the main element and were fixed to the pillars and wing using dowels. Through the use of the pillar feet the main element incidence could be varied between 0° and $+10^\circ$ in steps of 2°. This design feature allowed the wing to be pitched while maintaining the angle of each force components relative to the load cell. This design therefore avoided any complex coupling between the individual components of the load cell due to the wing being angled. The pillar feet were attached to the main element of the wing using specially machined mounting points. These were bolted and bonded to the inside of the main element suction surface. An exploded view of the entire experimental rig including the wing is shown in Figure 3.2. Figure 3.3 shows the installation of the wind tunnel model, support system and automated motion system within the test section of the 2.1m$\times$1.7m wind tunnel.

3.2.5 Pressure Tapped Wing Design

Within the research two wind tunnel models were used identical in dimension and configuration; firstly a clean model used for forces, oil flow visualisation and PIV and secondly, a pressure tapped model used to obtain surface pressures. The pressure tapped model contained 180 surface pressure tappings catagorised into eight groups according to location on the wing. The main element contained 86 pressure tappings arranged in two chordwise groups; the first at the centre span of the wing and the second towards the port tip of the wing (Table 3.5). In addition a spanwise group of tappings was present extending from the port tip to the centre span of the main element at the quarter chord of the main element (Table 3.6). The flap contained 86 pressure tappings again at the centre span and port tip of the flap (Table 3.7) and a spanwise group located at the quarter chord of the flap (Table 3.8). The chordwise taps were concentrated on the suction surfaces of the wing and at the leading edge of each element. The spanwise taps were concentrated towards the port

tip of the wing. Four tappings were located on the inboard surface of the port endplate beneath the flap suction surface at the flap quarter chord (Table 3.9). In addition four tappings were located on the port endplate foot again at the flap quarter chord location (Table 3.10).

Each pressure tapping was constructed from hypodermic stainless steel tubing with an internal diameter of 0.85mm, mounted flush and perpendicular to the surface. Flexible plastic tubing was attached to the end of each pressure tapping to allow for easy routing through the wing. The tubing from the flap pressure tappings was required to exit the flap at either tip and enter the main element through the corresponding tip. In order to minimise any disturbances to the flow field the flexible tubes were routed through hollow endplates constructed from aluminium and carbon fibre composites.

The surface pressures were measured using a 64 channel pressure transducer capable of simultaneously measuring two groups of 32 pressures. Due to the small size of the wing it was decided to locate the pressure transducer in the shroud located directly above the wing. In order to connect the surface pressure tappings to the pressure transducer, rebates were designed into the aluminium pillars supporting the main element. Hypodermic tubing was layed into the rebates and connected to the flexible tubing contained within the wing. This design feature provided minimal flow disturbances while allowing the maximum number of pressure tappings to be fitted within the wing. Figure 3.4 shows the pressure tapped wing installed within the 2.1m×1.7m wind tunnel test section. It may be noted that when the pillars were used in conjunction with the clean wing aluminium fillers were fixed into the rebates within the pillars.

3.3 Wing Configuration Variables

In order for accurate reproduction of the setup of the wing, the configuration of the wing was defined using five variables (Figure 3.5). The ride height of the wing (h) was defined as the vertical distance between the ground plane and the lowest point on the main element suction surface. The ride height of the wing was set using shims which were slid in between the main element suction surface and the ground plane. The automated motion system allowed the ride height of the wing to be set with an accuracy of ±0.05mm. Combining the automated motion system and model support structure, it was possible to continuously vary the ride height of the wing between 6mm ($0.021c$) and 180mm ($0.634c$) with the model

in situ.

The incidence of the main element (α_m) and flap (α_f) were defined as the angle between the horizontal and the chord of the individual element. Positive incidence was defined as a nose down rotation. The location of the flap with respect to the main element was defined using values of flap gap (δ_g) and flap overlap (δ_o). The flap gap was defined as the vertical distance between the lowest point on the suction surface of the flap and the pressure side of the main element trailing edge. The flap overlap was similarly defined as the horizontal distance between the leading edge of the flap and the pressure side of the main element trailing edge.

The origin of the model and wind tunnel was defined as the port tip of the main element leading edge. The axes were defined such that x, y and z corresponded to the streamwise, vertical and spanwise axis respectively. The positive sign convention of each axis was set as x positive downstream, y positive upwards and z positive from starboard to port, in accordance with a right-handed coordinate system (Figure 3.6).

3.4 2.1m x 1.7m Wind Tunnel Facility

The 2.1m×1.7m wind tunnel facility at the University of Southampton is of a conventional closed loop, closed jet design with fixed solid walls. The test section is rectangular in cross-section with a 45° fillet in each corner. The wind tunnel propeller is located within the return section of the wind tunnel generating a maximum freestream velocity (U_∞) of 45m/s.

When experimentally investigating a ground effect situation it is critical to correctly model the ground plane, in particular the velocity profile close to the ground. The 2.1m×1.7m wind tunnel employs a moving belt technique in conjunction with a boundary layer suction device located upstream of the belt (Figure 3.7). The belt is manufactured from two ply teraline with an overall thickness of 1.5mm. The belt is driven by a steel roller powered by an electric motor located at the downstream end of the assembly. The tension within the belt is maintained using a tension roller which is loaded with static weights. Tracking of the belt is constantly monitored and altered by a tracking roller, which is vertically actuated with a hydraulic ram. Although tension is applied to the belt situations can arise where the belt is lifted off the steel platen over which the belt slides. For example the suction forces generated by a body located directly above the ground plane can be sufficient

to induce belt lift. To prevent belt lift and therefore maintain accurate modelling of the ground plane, suction is applied between the belt and the steel platen through small holes drilled through the platen. The suction is applied to the belt using six side chambers and three centre chambers as shown in Figure 3.8. The distribution of the belt suction can therefore be varied to supply sufficient suction over the entire geometry of the ground effect device. Within this research belt suction was applied through suction chambers C2 and S2. A direct result of the belt suction is heating of the platern via friction between the belt and the platern. In order for the temperature of the platen and the belt to remain constant cooling water is continuously pumped through the platen and cooled external to the test section.

The boundary layer removal system uses a two stage process where the majority of the boundary layer is scooped away using a vertical slot and the remainder of the boundary layer is removed using a horizontal, perforated plate across which suction is applied. The combination of the moving ground and boundary layer suction produces a velocity profile, perpendicular to the moving ground, which is within $\pm 0.2\%$ of U_∞ at a height of 2mm.

3.5 Flow Conditions

The moving ground facility within the 2.1m×1.7m wind tunnel is limited to a maximum velocity of 40m/s due to limitations within cooling of the moving belt. However it was found that sufficient belt suction could not be maintained above 35m/s therefore not guaranteeing accurate ground plane simulation. All force, oil flow visualisation, surface pressure and PIV results were obtained with the freestream velocity set at a constant dynamic head of 56.19mm of water, corresponding to U_∞=30m/s at sea level under standard atmospheric conditions. For all cases boundary layer transition on the wing was not fixed, i.e. free transition.

Due to variations within atmospheric pressure and air temperature the density of the air within the tunnel test section continuously changed during testing. Taking these variations into account the Reynolds number based on the total chord of the wing ranged between $Re = 5.65 \times 10^5$ and 5.91×10^5. As previously stated multi-element wings can suffer from adverse Reynolds number effects resulting in unpredictable scaling effects (Section 2.2.4). The freestream velocity experienced by a racing car can typically reach 90m/s (201mph). The corresponding full scale Reynolds number for the wing investigated in this research

was approximately 3.4×10^6. This represented a Reynolds number ratio of approximately 6 between the wing investigated in this research and a realistic situation. However it may be noted that the Reynolds number of a racing car front wing constantly varies due to the dependency of freestream velocity on the location of the racing car on the track.

The turbulence intensity level within the 2.1m×1.7m wind tunnel facility has been experimentally measured previously using a hot-wire technique. The freestream turbulence intensity (I) and length scale (l_s) were quantified at 0.3% and 0.039m respectively at a freestream velocity of 30m/s.

3.6 Measurement Techniques

3.6.1 Forces

Force measurements were achieved through the use of a three component solid state load cell capable of simultaneously measuring downforce, drag and pitching moment. Each bridge within the load cell was individually temperature compensated from 0 to 60°C during the strain gauging process. The incompatibility of the data acquisition system within the 2.1m×1.7m wind tunnel and the load cell resulted in an unorthodox system configuration. The output signal from the load cell was unamplified therefore requiring external amplification which was achieved through the use of amplifiers originally intended for measuring wheel drag values. Due to the novel setup of the load cell re-calibration was required prior to use (Appendix B). This was achieved by replacing the wing with a generic bar and adding a known load either directly downwards for downforce, directly downstream for drag or as a nose up rotation for pitching moment. Using the resulting calibration curves a custom Fortran 90 code was written capable of decoupling the forces external to the data acquisition system.

In order to obtain a single downforce, drag and pitching moment measurement samples were taken over a period of 30 seconds then averaged using a moving-average scheme. The forces were sampled at a frequency of 100Hz. The uncertainty and repeatability within the force measurements are discussed in Appendix C. The forces were defined such that positive downforce and drag referred to forces in the negative y-axis and positive x-axis direction respectively. Pitching moment was defined as being positive for a nose down rotation and was resolved about the center span of the wing at $x = 53$mm.

3.6.2 Particle Image Velocimetry

Particle Image Velocimetry is a non-intrusive measurement technique capable of recording velocity at multiple points simultaneously within a flow field. The behaviour of the flow field is visualised through the use of seeding particles generated by a smoke generator. Within all the tests obtaining PIV data the smoke generator was located downstream of the test section. The water based smoke generates particles approximately 1 micron in diameter. The quality of the results was found to be critically dependent on the level of seeding, too little resulting in displacement of the measured velocities towards zero and too much resulting in a high signal-to-noise ratio. The seeding density within the test section was continuously monitored and varied to obtain consistent results of the highest possible quality.

The seeding within the plane of interest was illuminated using a Gemeni PIV 15 laser, containing two Tempest Ng:YAG lasers. Each laser produced a beam 120mJ/pulse in power at a wavelength of 532nm (green wavelength) since CCD cameras are most sensitive to a blue/green spectrum. The beam from each laser was fired through a semi-circular prism generating a laser sheet approximately 1mm in thickness. The overlap of the two laser sheets was variable and typically set such that the combined laser beam sheet was approximately 3mm in thickness within the region of interest. In order to obtain two images within close succession, required to track the displacements of each seeding particle, a fixed time interval was introduced between the firing of each laser. Typically the timing between laser sheets was set between $10\mu s$ and $40\mu s$. For cross-flow measurements (v,w) the laser was mounted external to the wind tunnel test section with the laser sheet vertical and perpendicular to freestream. To obtain cross-flow data beneath the suction surfaces of the wing optical access was required. A transparent port endplate and port endplate foot were manufactured from polycarbonate measuring 5mm in thickness (Figure 3.9). The dimensions of the transparent endplate and foot were identical to the aluminium counterparts they replaced.

The images generated by the illuminated seeding particles were recorded using a Dantec HiSense digital camera (type 13 gain 4) mounted perpendicular to the laser sheet. The camera had a resolution of 1280×1024 pixels producing an image of approximately 220mm×170mm when fitted with a 105mm Nikkor lens. The type of flow field measured within the research using PIV techniques was a cross-flow which possessed a large out-of-plane velocity component (u) especially beneath the wing. Errors will therefore occur within the image due to the out-of-plane motion of the seeding particles within the laser

sheet. Such errors are common within two-dimensional PIV and are referred to as perspective errors. The perspective errors within a time averaged PIV image, typical of the measurements obtained within this research, are quantified in Appendix C.6.

To obtain instantaneous velocity data within the flow field two images were recorded, corresponding to the two laser sheets generated at a fixed time interval. Within the first stage of processing the two raw images were divided into regular arrays known as interrogation areas. Within an interrogation area the location of each seeding particle was detected and then correlated to the corresponding seeding particle in the equivalent interrogation area in the second image. Dividing the resulting displacement of each seeding particle with the user defined time interval it was possible to calculate the velocity magnitude, direction and therefore velocity components of each seeding particle within the flow field. Since the seeding particles are displaced within the second image an overlap between the interrogation areas was introduced. In this research an interrogation area of 32×32 pixels was used with a horizontal and vertical overlap of 75% generating a vector map of 157×125 vectors. The physical resolution of the generated vector map was 1.25mm×1.25mm.

Due to the finite size of the interrogation areas erroneous vectors were introduced by seeding particles entering and exiting the interrogation area. In order to eliminate these erroneous vectors a second stage of processing was conducted in the form of a velocity-range validation scheme. The limits of the velocity-range validation were varied according to the characteristics of the flow field. The resulting vector map then underwent an third processing stage in the form of a moving-average validation scheme. Within this third stage vectors were rejected based on a comparison between neighboring vectors i.e. unrealistic vectors.

To obtain a time averaged velocity flow field multiple instantaneous images, typically 500 double images, were recorded at a frequency of 4Hz. Once processed with the three stage method stated previously the resulting instantaneous vector maps were averaged producing a time averaged velocity field.

3.6.3 Oil Flow Visualisation

Oil flow visualisation is a flow mapping technique capable of providing surface flow data. The data is presented in the form of streamlines near to the surface, which in a steady flow are identical to streaklines. The streaklines can be interpreted to yield data concerning the surface flow field. Numerous techniques for obtaining oil flow visualisations exist each

designed to capture certain flow features within specific flow conditions. The technique used within this research was to apply a solvent based suspension to all the surfaces of the wing and the endplates. The wind tunnel was then run at the required flow conditions, until the solvent had evaporated. A liquid suspension of titanium dioxide (TiO_2) in paraffin was used since it provided a reasonable drying time and good contrast with the surfaces of the model. Once obtained, the surface streaklines upon each surface of the wing were captured using a six megapixel digital camera.

3.6.4 Surface Pressures

The surface pressures over the wing and port endplate were measured using a 32 channel zero, operate and calibrate (ZOC22B) pressure transducer manufactured by Scanivalve. The ZOC22B pressure transducer is capable of simultaneously measuring 32 channels. However through the use of a dual switching system present on each channel a total of 64 channels may be measured in two groups of 32. Switching between the two banks of channels is achieved pneumatically using compressed nitrogen gas. Each sensor is capable of a scanning rate of 20kHz with a pressure range of 0 to 50psi.

In order for a single channel within the pressure transducer to measure a surface pressure three stages were required. Initially the zero reading for the sensor was recorded with the tunnel in a wind-off condition. Secondly the sensor was calibrated against an input pressure of known magnitude (4psi) thereby obtaining a gain and offset value for the sensor. Finally the pressure was measured with the wind tunnel in a wind-on condition and output as a voltage. This process was executed simultaneously for the first 32 channels then repeated for the second 32 channels thereby obtaining 64 pressure measurements. The zero reading and calibration process was repeated at the start of each run compensating for variations in atmospheric conditions and sensor drift.

The wing contained a total of 180 surface pressure tappings arranged in a chordwise and spanwise sense. Three complete runs were therefore required to obtain surface pressure measurements from every pressure tapping. The uncertainties and repeatability within the surface pressure measurements are discussed and quantified in Appendix C.

3.6.5 Wake Profiles

Traditionally wake flow field data has been obtained through the use of non-intrusive measurement techniques such as PIV or LDA. At the time of this research it was not possible

to obtain wake flow field data with either of these systems. It was therefore decided to use a pressure rake technique in conjunction with the pressure transducer described in section 3.6.4. The pressure rake consisted of six pitot tubes spaced 20mm apart each with an internal diameter of 1.0mm. The rake was mounted onto the redundant downstream traverse within the automated motion system using an aluminium strut. This configuration allowed the wing and pressure rake to be moved either independently or in tandem with identical accuracies. Figure 3.10 shows the wing mounted within the 2.1m$\times$1.7m wind tunnel test section with the pressure rake located directly downstream. During all tests the pressure rake was mounted vertically with the upstream ends of the each pitot tube coincidental at the specified streamwise location.

To obtain a single pressure measurements from each pitot tube 60 samples were obtained at a frequency of 100Hz which were then averaged using a moving-average scheme. Similar to the surface pressure measurements the pressure transducer was zeroed and calibrated at the start of each run. The pressure measurements were taken at vertical locations ranging between 8mm ($0.028c$) and 282mm ($0.993c$) above the ground plane at a resolution of 2mm. During certain tests extension tubes were attached to the two lowest pitot tubes extending upstream underneath the suction surface of the flap. The pressure measurements were subsequently converted into streamwise velocities.

3.7 Chapter Summary

An experimental test rig of a multi-element wing in ground effect has been designed and manufactured. The rig is capable of continuous ride height variations in situ allowing for hysterisis effects due to ride height to be investigated. Additional configuration variables such as flap gap, flap overlap, flap incidence and wing incidence may also be investigated. It is possible to obtain data in the form of forces, surface pressures, surface streaklines, wing tip flow field (v, w) and wake flow (u) using a combination of experimental techniques. The uncertainty and repeatability within the measurements has been quantified.

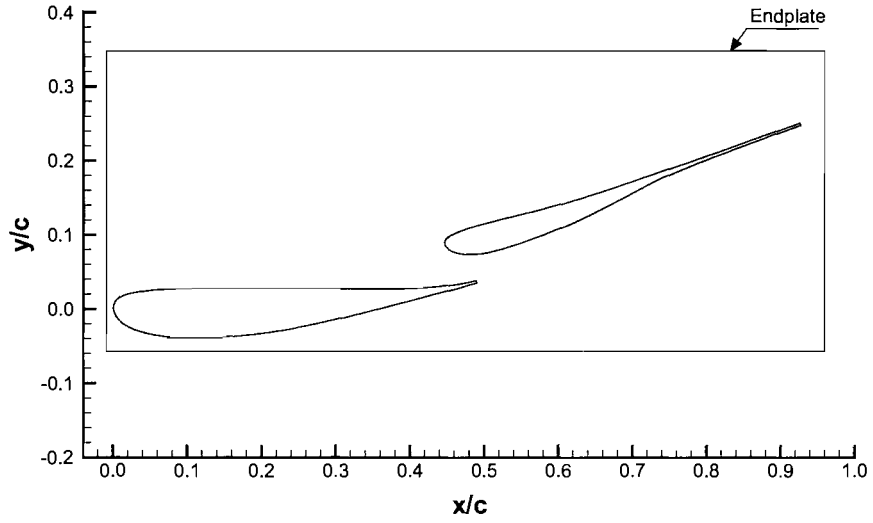

Figure 3.1: Non-dimensional profiles of the wing.

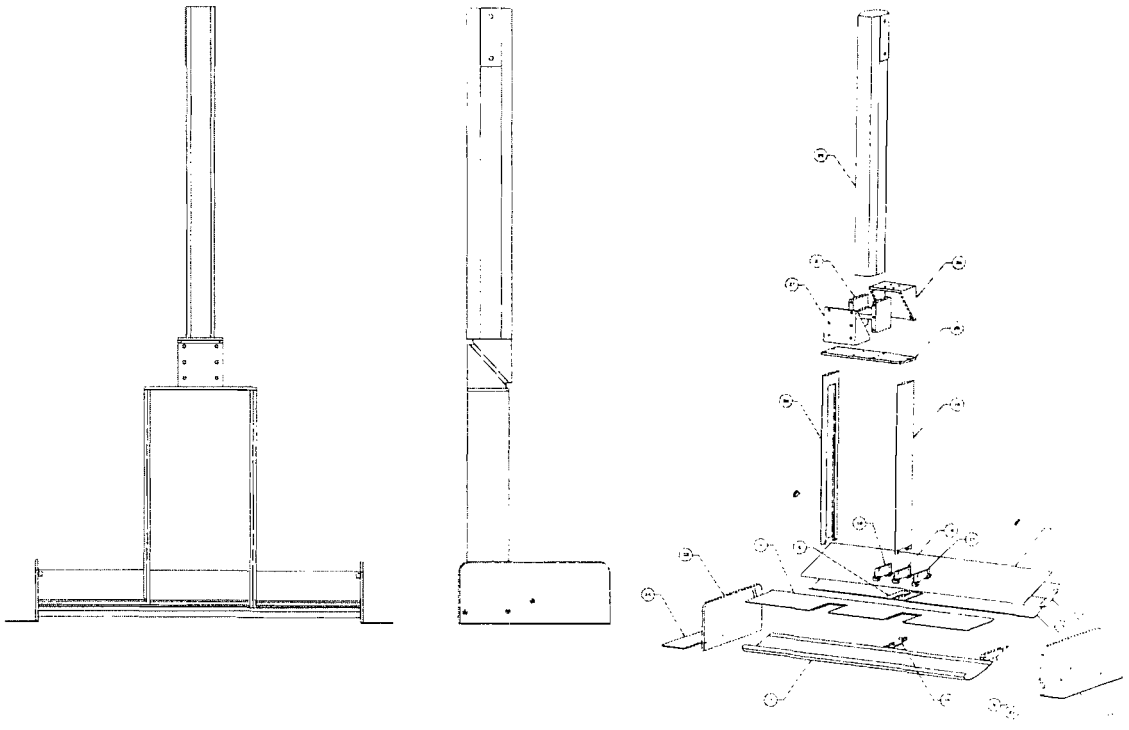

Figure 3.2: Exploded view of the complete experimental test rig.

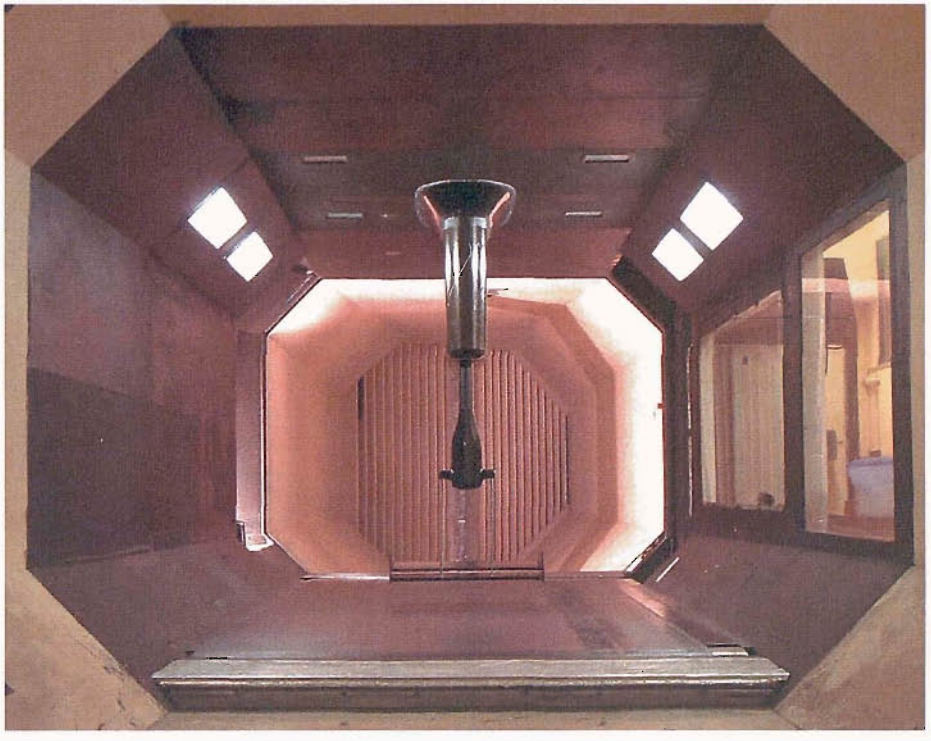

Figure 3.3: Installation of the complete test rig and automated motion system within the 2.1m×1.7m wind tunnel test section.

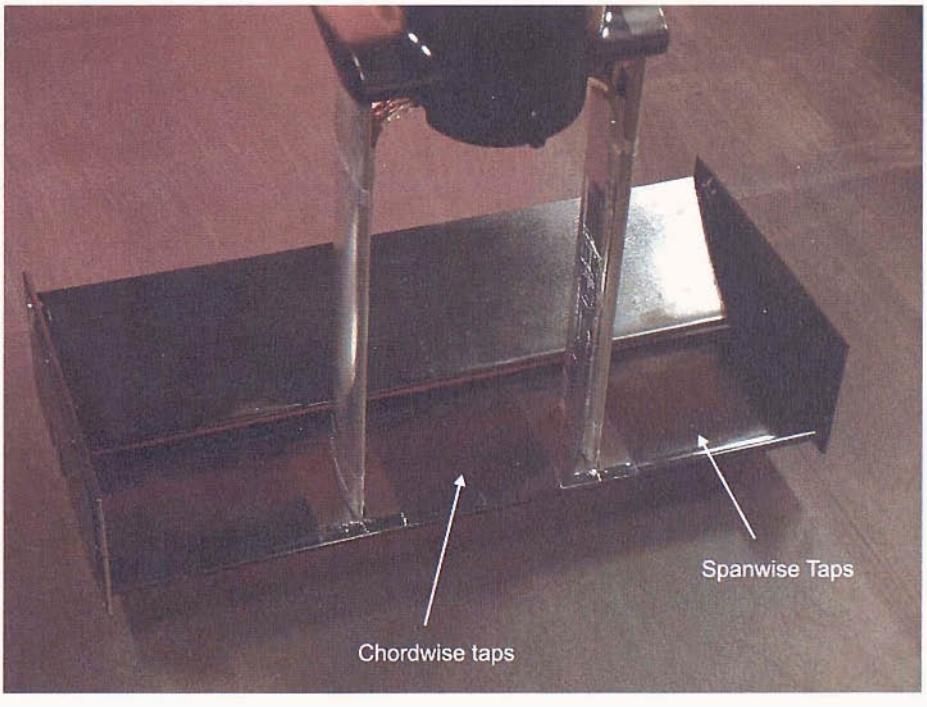

Figure 3.4: Installation of the pressure tapped wing within the 2.1m×1.7m wind tunnel test section.

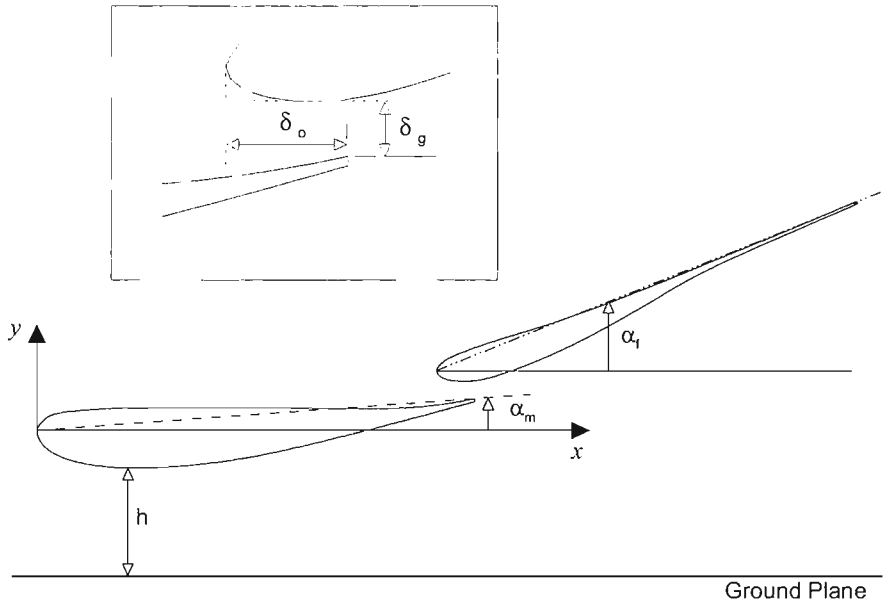

Figure 3.5: Definition of the configuration variables of the wing.

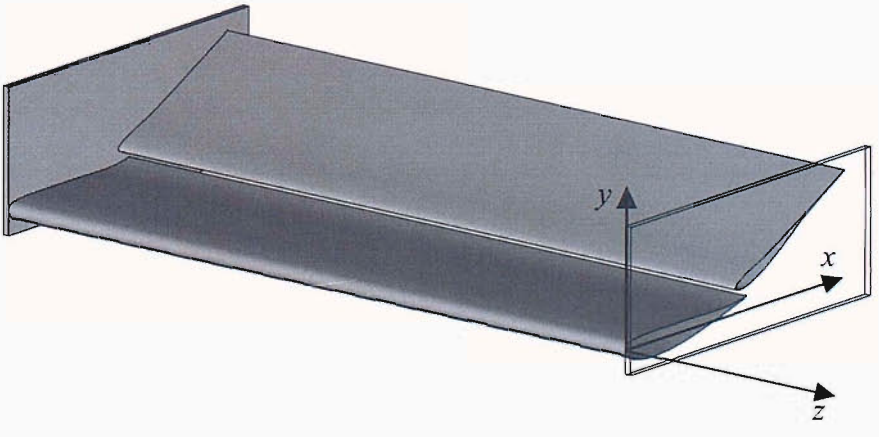

Figure 3.6: Definition of the origin of the wing and positive axis sign convention.

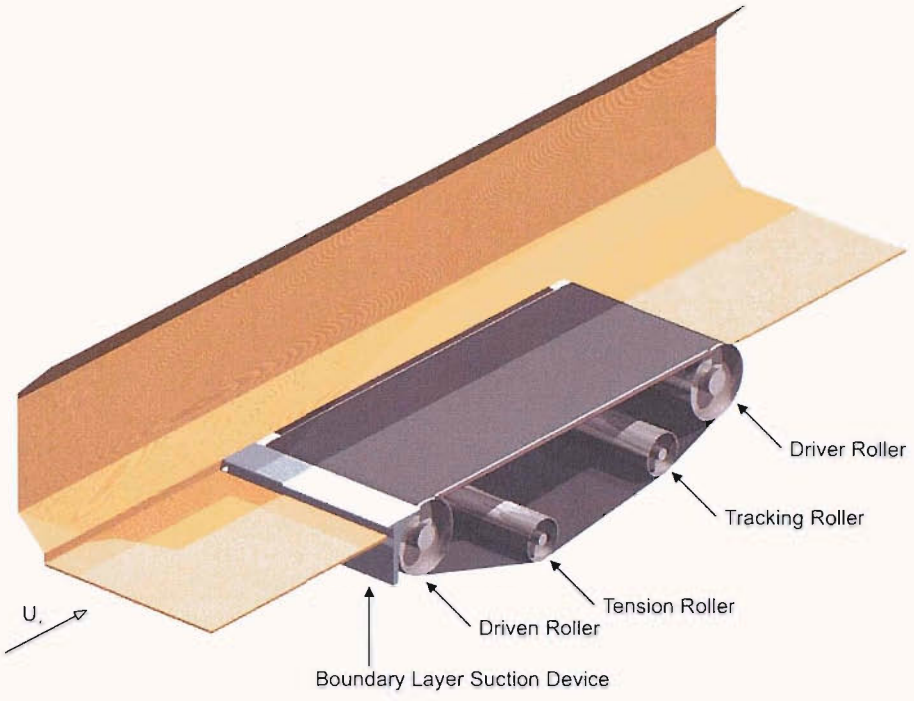

Figure 3.7: Three-dimensional representation of the moving ground facility within the 2.1m×1.7m wind tunnel.

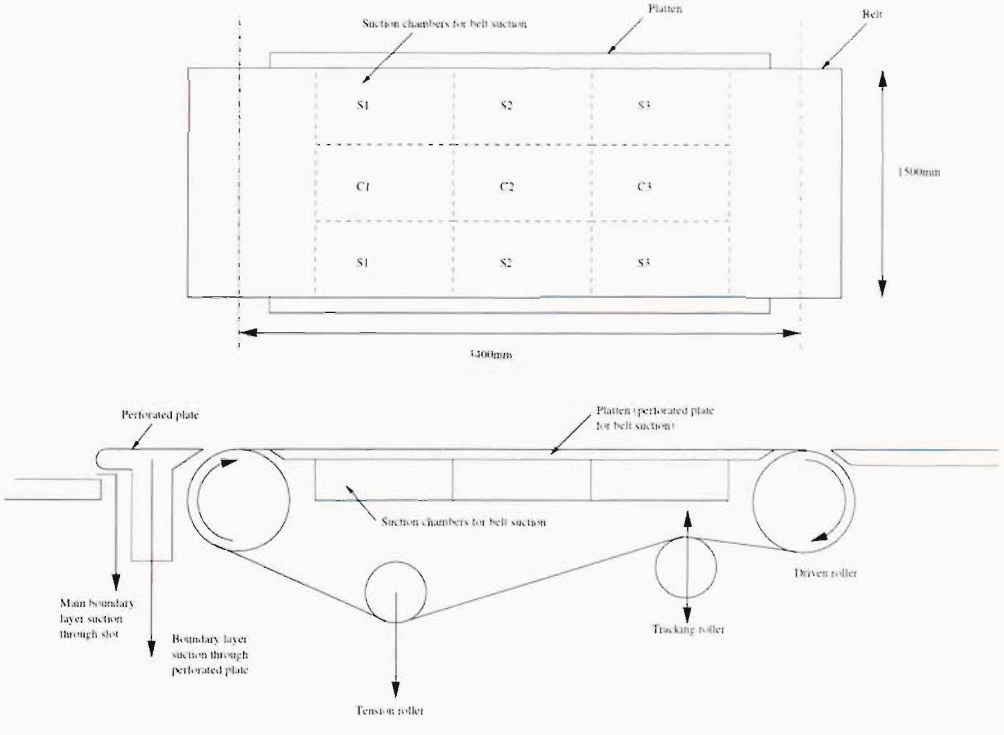

Figure 3.8: Schematic of the moving ground facility within the 2.1m×1.7m wind tunnel illustrating the belt suction distribution.

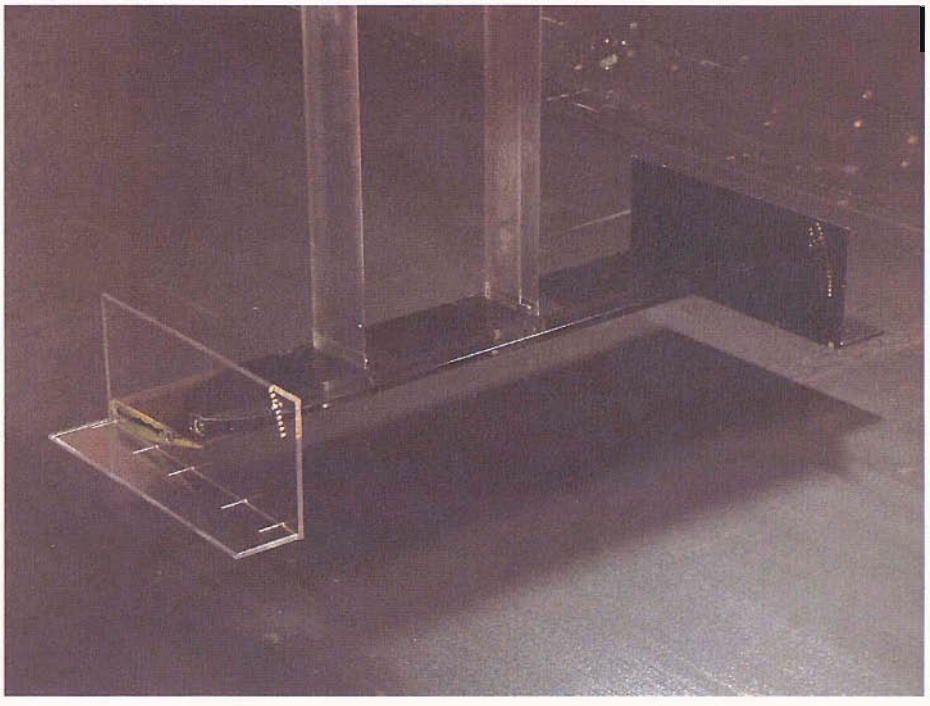

Figure 3.9: Installation of the wing equipped with the transparent port endplate and port endplate foot.

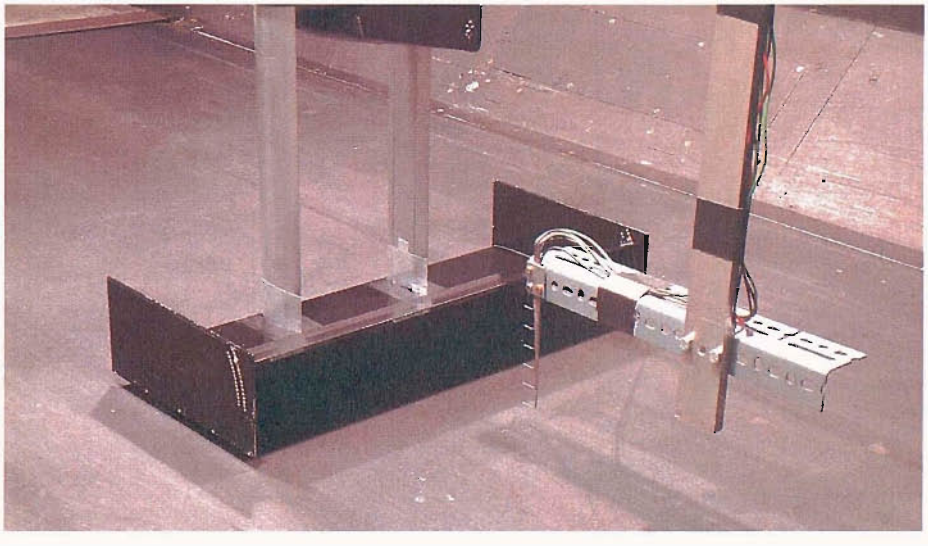

Figure 3.10: Installation of the wing with the pitot rake assembly located downstream.

node	x/c	y/c	node	x/c	y/c	node	x/c	y/c
1	0.0000	0.0000	41	0.1886	-0.0339	81	0.3867	0.0081
2	0.0012	-0.0049	42	0.1936	-0.0333	82	0.3916	0.0093
3	0.0036	-0.0094	43	0.1986	-0.0326	83	0.3965	0.0106
4	0.0067	-0.0134	44	0.2037	-0.0320	84	0.4014	0.0119
5	0.0104	-0.0169	45	0.2087	-0.0313	85	0.4063	0.0132
6	0.0144	-0.0199	46	0.2137	-0.0306	86	0.4112	0.0145
7	0.0187	-0.0226	47	0.2187	-0.0298	87	0.4161	0.0158
8	0.0233	-0.0248	48	0.2237	-0.0290	88	0.4210	0.0170
9	0.0279	-0.0268	49	0.2287	-0.0282	89	0.4259	0.0184
10	0.0327	-0.0285	50	0.2337	-0.0274	90	0.4308	0.0196
11	0.0375	-0.0301	51	0.2387	-0.0265	91	0.4357	0.0209
12	0.0424	-0.0314	52	0.2437	-0.0255	92	0.4406	0.0223
13	0.0473	-0.0326	53	0.2486	-0.0246	93	0.4455	0.0235
14	0.0523	-0.0337	54	0.2536	-0.0236	94	0.4504	0.0249
15	0.0573	-0.0347	55	0.2586	-0.0226	95	0.4553	0.0262
16	0.0623	-0.0355	56	0.2636	-0.0216	96	0.4602	0.0276
17	0.0673	-0.0363	57	0.2685	-0.0206	97	0.4651	0.0289
18	0.0723	-0.0369	58	0.2734	-0.0195	98	0.4699	0.0302
19	0.0773	-0.0375	59	0.2784	-0.0184	99	0.4748	0.0316
20	0.0824	-0.0379	60	0.2833	-0.0173	100	0.4797	0.0330
21	0.0875	-0.0383	61	0.2883	-0.0162	101	0.4845	0.0344
22	0.0925	-0.0386	62	0.2932	-0.0150	102	0.4894	0.0358
23	0.0975	-0.0388	63	0.2982	-0.0139			
24	0.1026	-0.0389	64	0.3031	-0.0127			
25	0.1077	-0.0389	65	0.3081	-0.0116			
26	0.1128	-0.0389	66	0.3129	-0.0104			
27	0.1178	-0.0388	67	0.3179	-0.0092			
28	0.1229	-0.0387	68	0.3228	-0.0080			
29	0.1279	-0.0385	69	0.3277	-0.0068			
30	0.1330	-0.0383	70	0.3327	-0.0056			
31	0.1381	-0.0381	71	0.3376	-0.0044			
32	0.1432	-0.0378	72	0.3425	-0.0031			
33	0.1482	-0.0375	73	0.3474	-0.0019			
34	0.1532	-0.0371	74	0.3523	-0.0006			
35	0.1583	-0.0368	75	0.3572	0.0006			
36	0.1634	-0.0364	76	0.3621	0.0018			
37	0.1684	-0.0359	77	0.3671	0.0031			
38	0.1735	-0.0355	78	0.3720	0.0043			
39	0.1785	-0.0349	79	0.3769	0.0056			
40	0.1835	-0.0345	80	0.3818	0.0069			

Table 3.1: Non-dimensional coordinates of the main element suction surface; $\alpha_m = +4°$.

node	x/c	y/c
1	0.0000	0.0000
2	0.0004	0.0050
3	0.0024	0.0096
4	0.0055	0.0137
5	0.0094	0.0169
6	0.0138	0.0194
7	0.0185	0.0211
8	0.0234	0.0224
9	0.0284	0.0233
10	0.0335	0.0239
11	0.0385	0.0245
12	0.0436	0.0250
13	0.0486	0.0255
14	0.0536	0.0260
15	0.0587	0.0264
16	0.0638	0.0267
17	0.0688	0.0270
18	0.0739	0.0273
19	0.0789	0.0276
20	0.0840	0.0277
21	0.0891	0.0278
22	0.0941	0.0280
23	0.0992	0.0281
24	0.1043	0.0281
25	0.1093	0.0282
26	0.1144	0.0283
27	0.1195	0.0283
28	0.1245	0.0283
29	0.1296	0.0284
30	0.1346	0.0284
31	0.1397	0.0284
32	0.1448	0.0284
33	0.1499	0.0284
34	0.1550	0.0284
35	0.1600	0.0285
36	0.1651	0.0285
37	0.1701	0.0285
38	0.1752	0.0285
39	0.1803	0.0285
40	0.1853	0.0286

node	x/c	y/c
41	0.1904	0.0286
42	0.1955	0.0286
43	0.2005	0.0286
44	0.2056	0.0287
45	0.2107	0.0287
46	0.2157	0.0287
47	0.2208	0.0287
48	0.2259	0.0287
49	0.2310	0.0287
50	0.2360	0.0287
51	0.2411	0.0287
52	0.2461	0.0287
53	0.2512	0.0287
54	0.2563	0.0286
55	0.2614	0.0286
56	0.2664	0.0285
57	0.2715	0.0285
58	0.2765	0.0284
59	0.2816	0.0283
60	0.2867	0.0283
61	0.2918	0.0282
62	0.2968	0.0281
63	0.3019	0.0280
64	0.3069	0.0280
65	0.3120	0.0279
66	0.3171	0.0278
67	0.3221	0.0278
68	0.3272	0.0277
69	0.3323	0.0276
70	0.3373	0.0275
71	0.3424	0.0275
72	0.3475	0.0274
73	0.3525	0.0274
74	0.3576	0.0273
75	0.3627	0.0273
76	0.3678	0.0273
77	0.3728	0.0274
78	0.3779	0.0274
79	0.3829	0.0275
80	0.3880	0.0276

node	x/c	y/c
81	0.3931	0.0277
82	0.3982	0.0279
83	0.4032	0.0281
84	0.4083	0.0283
85	0.4133	0.0286
86	0.4184	0.0289
87	0.4235	0.0293
88	0.4285	0.0297
89	0.4335	0.0301
90	0.4386	0.0307
91	0.4436	0.0313
92	0.4486	0.0319
93	0.4537	0.0326
94	0.4587	0.0333
95	0.4637	0.0341
96	0.4687	0.0349
97	0.4737	0.0359
98	0.4786	0.0368
99	0.4836	0.0378
100	0.4886	0.0388

Table 3.2: Non-dimensional coordinates of the main element pressure surface; $\alpha_m = +4°$.

node	x/c	y/c
1	0.4533	0.0931
2	0.4547	0.0891
3	0.4584	0.0861
4	0.4628	0.0840
5	0.4677	0.0826
6	0.4728	0.0817
7	0.4780	0.0812
8	0.4832	0.0811
9	0.4884	0.0812
10	0.4937	0.0817
11	0.4989	0.0824
12	0.5040	0.0833
13	0.5091	0.0845
14	0.5142	0.0858
15	0.5192	0.0873
16	0.5242	0.0888
17	0.5291	0.0905
18	0.5340	0.0922
19	0.5389	0.0939
20	0.5437	0.0957
21	0.5486	0.0975
22	0.5534	0.0994
23	0.5582	0.1013
24	0.5630	0.1033
25	0.5678	0.1052
26	0.5725	0.1072
27	0.5772	0.1093
28	0.5819	0.1114
29	0.5866	0.1135
30	0.5913	0.1156
31	0.5959	0.1178
32	0.6006	0.1200
33	0.6052	0.1222
34	0.6098	0.1245
35	0.6143	0.1268
36	0.6189	0.1291
37	0.6234	0.1314
38	0.6280	0.1338
39	0.6325	0.1362
40	0.6370	0.1386

node	x/c	y/c
41	0.6415	0.1410
42	0.6459	0.1434
43	0.6504	0.1459
44	0.6548	0.1483
45	0.6592	0.1508
46	0.6637	0.1533
47	0.6681	0.1558
48	0.6725	0.1584
49	0.6769	0.1609
50	0.6812	0.1634
51	0.6856	0.1660
52	0.6900	0.1686
53	0.6943	0.1711
54	0.6987	0.1737
55	0.7030	0.1763
56	0.7074	0.1789
57	0.7117	0.1815
58	0.7161	0.1841
59	0.7204	0.1867
60	0.7248	0.1892
61	0.7292	0.1917
62	0.7337	0.1941
63	0.7382	0.1966
64	0.7427	0.1989
65	0.7472	0.2012
66	0.7518	0.2035
67	0.7564	0.2058
68	0.7610	0.2080
69	0.7656	0.2102
70	0.7703	0.2124
71	0.7749	0.2146
72	0.7796	0.2167
73	0.7843	0.2189
74	0.7889	0.2210
75	0.7936	0.2231
76	0.7983	0.2252
77	0.8030	0.2273
78	0.8077	0.2294
79	0.8124	0.2315
80	0.8172	0.2335

node	x/c	y/c
81	0.8219	0.2356
82	0.8266	0.2376
83	0.8313	0.2397
84	0.8360	0.2417
85	0.8408	0.2438
86	0.8455	0.2458
87	0.8502	0.2479
88	0.8550	0.2499
89	0.8597	0.2519
90	0.8644	0.2540
91	0.8692	0.2560
92	0.8739	0.2580
93	0.8786	0.2601
94	0.8834	0.2621
95	0.8881	0.2641
96	0.8928	0.2662
97	0.8976	0.2682
98	0.9023	0.2702
99	0.9070	0.2723
100	0.9118	0.2743
101	0.9165	0.2764
102	0.9212	0.2784

Table 3.3: Non-dimensional coordinates of the flap suction surface; $\alpha_f = +24°$, $\delta_g = 12$mm, $\delta_o = 10$mm.

node	x/c	y/c
1	0.4533	0.0931
2	0.4549	0.0973
3	0.4580	0.1009
4	0.4619	0.1040
5	0.4662	0.1066
6	0.4708	0.1088
7	0.4756	0.1109
8	0.4804	0.1128
9	0.4852	0.1147
10	0.4900	0.1165
11	0.4949	0.1183
12	0.4998	0.1200
13	0.5047	0.1217
14	0.5096	0.1233
15	0.5146	0.1250
16	0.5195	0.1265
17	0.5245	0.1281
18	0.5295	0.1296
19	0.5344	0.1311
20	0.5394	0.1327
21	0.5444	0.1342
22	0.5494	0.1357
23	0.5544	0.1372
24	0.5594	0.1387
25	0.5643	0.1403
26	0.5693	0.1419
27	0.5742	0.1435
28	0.5792	0.1451
29	0.5841	0.1467
30	0.5890	0.1484
31	0.5940	0.1500
32	0.5989	0.1517
33	0.6038	0.1534
34	0.6087	0.1551
35	0.6136	0.1569
36	0.6184	0.1586
37	0.6233	0.1604
38	0.6282	0.1622
39	0.6330	0.1640
40	0.6379	0.1658

node	x/c	y/c
41	0.6428	0.1676
42	0.6476	0.1694
43	0.6524	0.1713
44	0.6573	0.1731
45	0.6621	0.1750
46	0.6669	0.1769
47	0.6717	0.1788
48	0.6765	0.1806
49	0.6813	0.1825
50	0.6861	0.1845
51	0.6909	0.1864
52	0.6957	0.1883
53	0.7005	0.1902
54	0.7053	0.1922
55	0.7101	0.1941
56	0.7149	0.1961
57	0.7197	0.1980
58	0.7244	0.2000
59	0.7292	0.2019
60	0.7340	0.2039
61	0.7388	0.2058
62	0.7435	0.2078
63	0.7483	0.2098
64	0.7531	0.2117
65	0.7579	0.2137
66	0.7626	0.2156
67	0.7674	0.2176
68	0.7722	0.2196
69	0.7770	0.2215
70	0.7817	0.2235
71	0.7865	0.2254
72	0.7913	0.2274
73	0.7961	0.2293
74	0.8009	0.2313
75	0.8057	0.2332
76	0.8104	0.2351
77	0.8152	0.2371
78	0.8200	0.2390
79	0.8248	0.2410
80	0.8296	0.2430

node	x/c	y/c
81	0.8343	0.2449
82	0.8391	0.2469
83	0.8439	0.2489
84	0.8486	0.2509
85	0.8534	0.2529
86	0.8581	0.2549
87	0.8629	0.2568
88	0.8676	0.2589
89	0.8724	0.2609
90	0.8771	0.2629
91	0.8819	0.2649
92	0.8866	0.2669
93	0.8914	0.2689
94	0.8961	0.2709
95	0.9008	0.2730
96	0.9056	0.2750
97	0.9103	0.2770
98	0.9151	0.2790
99	0.9198	0.2811

Table 3.4: Non-dimensional coordinates of the flap pressure surface; $\alpha_f = +24°$, $\delta_g =$ 12mm, $\delta_o = 10$mm.

Suction Surface	
x (mm)	x/c
0	0.000
2	0.007
4	0.014
6	0.021
8	0.028
10	0.035
15	0.053
20	0.070
25	0.088
30	0.106
35	0.123

Suction Surface	
x (mm)	x/c
45	0.159
55	0.194
65	0.229
75	0.264
85	0.299
95	0.335
100	0.370
115	0.405
125	0.440
130	0.458
135	0.475

Pressure Surface	
x (mm)	x/c
0	0.000
2	0.007
4	0.014
6	0.021
8	0.028
10	0.035
15	0.053
35	0.123
55	0.194
75	0.264
95	0.335

Pressure Surface	
x (mm)	x/c
115	0.405
130	0.458
135	0.475

Table 3.5: Locations of chordwise pressure taps on the main element; $z/c = -0.088$ and $z/c = -1.021$.

Suction Surface	
z (mm)	z/c
-10	-0.035
-15	-0.053
-25	-0.088
-50	-0.176
-75	-0.264
-100	-0.352
-125	-0.440
-150	-0.528
-200	-0.704
-250	-0.880
-290	-1.021

Pressure Surface	
z (mm)	z/c
-10	-0.035
-15	-0.053
-25	-0.088
-50	-0.176
-75	-0.264
-100	-0.352
-125	-0.440
-150	-0.528
-250	-0.880
-290	-1.021

Table 3.6: Locations of the spanwise pressure taps on the main element; $x/c = 0.123$.

Suction Surface	
x_f (mm)	x_f/c
0	0.000
2	0.007
4	0.014
6	0.021
8	0.028
10	0.035
12	0.042
14	0.049
16	0.056
18	0.063
20	0.070
25	0.088

Suction Surface	
x_f (mm)	x_f/c
30	0.106
36	0.127
45	0.158
55	0.194
65	0.229
75	0.264
85	0.299
95	0.335
105	0.370
115	0.405
125	0.440

Pressure Surface	
x_f (mm)	x_f/c
0	0.000
2	0.007
4	0.014
6	0.021
8	0.028
10	0.035
20	0.070
36	0.127
55	0.194
75	0.264
95	0.335
115	0.405

Table 3.7: Locations of chordwise pressure taps on the flap; $z/c = -0.088$ and $z/c = -1.021$.

Suction Surface		Pressure Surface	
z (mm)	z/c	z (mm)	z/c
-10	-0.035	-10	-0.035
-15	-0.053	-15	-0.053
-25	-0.088	-25	-0.088
-50	-0.176	-50	-0.176
-75	-0.264	-75	-0.264
-100	-0.352	-100	-0.352
-125	-0.440	-125	-0.440
-150	-0.528	-150	-0.528
-200	-0.704	-200	-0.704
-250	-0.880	-250	-0.880
-290	-1.021	-290	-1.021

Table 3.8: Locations of the spanwise tappings on the flap, $x_f/c = 0.127$.

y (mm)	y/c
-6.05	-0.021
3.95	0.014
13.95	0.049
20.95	0.074

Table 3.9: Locations of the vertical tappings on the inboard face of the port endplate; $x/c = 0.614$, $z/c = 0.000$.

z (mm)	z/c
15.00	0.053
26.67	0.094
38.34	0.135
50.00	0.176

Table 3.10: Locations of the spanwise tappings on the lower face of the port endplate foot; $x/c = 0.614$, $y/c = -0.057$.

Chapter 4

Flap Location Optimisation

This chapter discusses measurements for various flap gaps and flap overlaps. The experimental setup will be stated followed by discussions of the force and surface flow field data. The aim of this investigation was two fold; first to quantify the effect of varying flap position on the forces generated by the wing and secondly, to find optimum values of flap gap and overlap with respect to downforce. In the remainder of this thesis a single combination of flap gap and overlap will be referred to as an individual flap location.

4.1 Experimental Details

The flap optimisation investigation was performed at a ride height of 55mm (0.194c). The incidences of the main element and flap were $+4^\circ$ and $+24^\circ$ respectively. To produce a maximum number of flap gap and overlap combinations, seven separate sets of endplates were used. Instead of using individual holes to secure the flap to the endplates, horizontal slots were used. This design allowed for a range of overlaps to be achieved for a constant value of flap gap, using a single set of endplates. Each set of endplates positioned the flap relative to the main element with a prescribed flap gap. During testing the overlap was varied between zero and 20mm (0.07c) in increments of 2mm (0.007c). In addition the flap gap was varied between 2mm (0.007c) and 16mm (0.056c) in increments of 2mm. In total 70 separate flap locations were achieved and tested. Force data was obtained for each flap location. The surface flow field was also mapped using oil flow visualisation techniques at three specific flap locations; the optimum flap location, an optimum flap gap with minimum overlap, and a minimum flap gap with optimum overlap.

4.2 Forces

Figure 4.1 presents the variation of downforce coefficient (C_L) with flap location. Upon first inspection it may be noted that the majority of flap locations produced similar values of downforce ($C_L \approx 2.45$). In contrast, flap locations towards the extrema of those tested generated significantly reduced values of downforce ($C_L \approx 1.85$). The transition between the regions of high downforce and reduced downforce was abrupt. The flow mechanisms responsible for this abrupt force variation will be discussed later in this chapter. Increasing the flap overlap within the region of high downforce caused the downforce to linearly decrease. Increasing the flap gap caused the downforce to increase to a local maximum value at $\delta_g = 0.042c$, then decrease. Figure 4.2 presents the coefficient of drag (C_D) for various flap locations. Similar to the downforce, regions of significantly reduced drag were noted at the extrema of flap locations tested. It was noted that the drag was dependent on the downforce with high values of drag corresponding to high values of downforce and visa versa. The variation in pitching moment coefficient (C_M) with flap location is presented in Figure 4.3. Increasing the flap gap caused the pitching moment coefficient to increase (i.e. becoming more negative). Increases in flap overlap also resulted in increased values of pitching moment. Similar to the downforce and drag, regions of reduced pitching moment were observed with minimum values of flap gap and overlap. For completeness Figure 4.4 presents the variation in wing efficiency (β) with flap location.

4.3 Oil Flow Visualisation

Oil flow visualisations were performed to gain an insight into the variations in surface flow field. The resulting surface steaklines on the pressure surfaces and suction surfaces of the wing are shown in Figures 4.5 and 4.6 respectively. Figures 4.5(a) and 4.6(a) present the pressure surface and suction surface streaklines obtained with a flap gap and overlap of $0.042c$ and $0.035c$ respectively. The flow over both the pressure surface and suction surface of the wing was fully attached. Boundary layer transition was observed on both the main element and flap (Appendix D). The streamwise location of transition on the flap was constant at $x/c = 0.06$. Two minor disturbances due to the presence of the wing pillars, were visible within the flap transition line. The main element transition line moved upstream towards the wing tips decreasing from $x/c = 0.07$ at the centre span location. At the centre span the streaklines indicated a quasi two-dimensional surface flow field. In

contrast the flow field towards the wing tips became highly three-dimensional. Upon close inspection it was noted that at the wing tips, boundary layer transition was replaced by a vortical flow.

Figures 4.5(b) and 4.6(b) present the pressure surface and suction surface streaklines obtained with a flap gap of $0.042c$. The overlap was set to zero in order to obtain surface streaklines at the lower extreme of the overlaps tested. The most predominant feature of both the pressure and suction surface streaklines were regions of separated flow. A region of separation across the entire span of the main element pressure surface was observed originating at $x/c = 0.35$. The separation region was located at a streamwise position corresponding to the start of the concave region of the main element pressure surface. The streaklines on the main element suction surface were largely unaffected by the reduction in flap overlap. The flap suction surface streaklines indicated a region of separation over the central third of the wing span. Unfortunately the structure of the separation region was not fully captured by the streaklines. While observing the flow visualisation two regions of strong counter-rotation were observed on the flap suction surface. These recirculation regions seemingly burst mid-way through the test resulting in the super-imposed streakline structure presented.

Figures 4.5(c) and 4.6(c) present the pressure surface and suction surface streaklines obtained with an overlap of $0.035c$. The flap gap was set at $0.007c$. Regions of separation were clearly visible on both the pressure and suction surfaces. Transition occurred on the main element suction surface at a centre span location of $x/c = 0.07$. However, no transition was visible on the suction surface of the flap. A separation bubble and area of recirculation was identified on the main element pressure surface at $x/c = 0.30$. A large area of separation was also present on the flap suction surface across the entire span of the wing. The flap separation region was curved and included two nodes and two regions of counter-rotating flow. The structure of the separation region resembled the model proposed by Winklemann & Barlow [31].

4.4 Discussion

Drawing conclusions concerning the exact variations in flow field due to flap location was inappropriate due to the amount of data obtained. Instead theories are offered. The variations in downforce, drag and pitching moment with flap gap were consistent with variations

in the magnitude of the circulation effect [48]. It could be theorised that decreasing the flap gap caused the circulation effect to increase in magnitude. Accordingly the circulation over the flap would have increased, observed as increased pitching moment and downforce. The dependency of the drag on the downforce indicated that the drag variations were primarily due to variations in lift induced drag. Increasing the flap overlap caused the downforce and pitching moment to decrease. These force variations may be attributed to a combination of flow field variations and the mechanics of the wing. The forces generated by both the main element and flap may be resolved to produce a single force acting through each element at a single streamwise location. Increasing the flap overlap translated the resolved flap downforce component upstream, mechanically decreasing the pitching moment.

Minimum values of flap gap generated significantly reduced values of downforce, drag and pitching moment. The corresponding oil flow visualisations (Figures 4.5(c) and 4.6(c)) revealed separation on the suction surface of the flap consistent with that of a single element wing of similar aspect ratio [31]. In addition transition was not present on the flap suction surface. It could be theorised that at such low values of flap gap the slot became essentially choked by the main element and flap boundary layers. As a result the two elements of the wing acted as one thus eliminating transition on the suction surface of the flap, removing the five beneficial effects stated by Smith [48] and promoting separation.

Flap locations which possessed minimal overlap and maximum gap values generated significantly reduced values of downforce, pitching moment and drag. The oil flow visualisation (Figure 4.6(b)) revealed separated flow over the suction surface of the flap. The size of this region of separation was less than that obtained with a minimum value of flap gap. Accordingly the detrimental effect on the forces was less. For such flap locations the circulation effect would be minimal, promoting separation on the flap.

4.5 Chapter Summary

The influence of flap location on the performance of the wing was quantified. The majority of flap locations produced forces of similar magnitude. However, flap locations towards the extrema of those tested produced significantly reduced forces, caused by separation on the flap suction surface. The optimum values of flap gap and overlap which generated a global maximum value of downforce were 12mm ($\delta_g = 0.042c$) and 10mm ($\delta_o = 0.035c$) respectively.

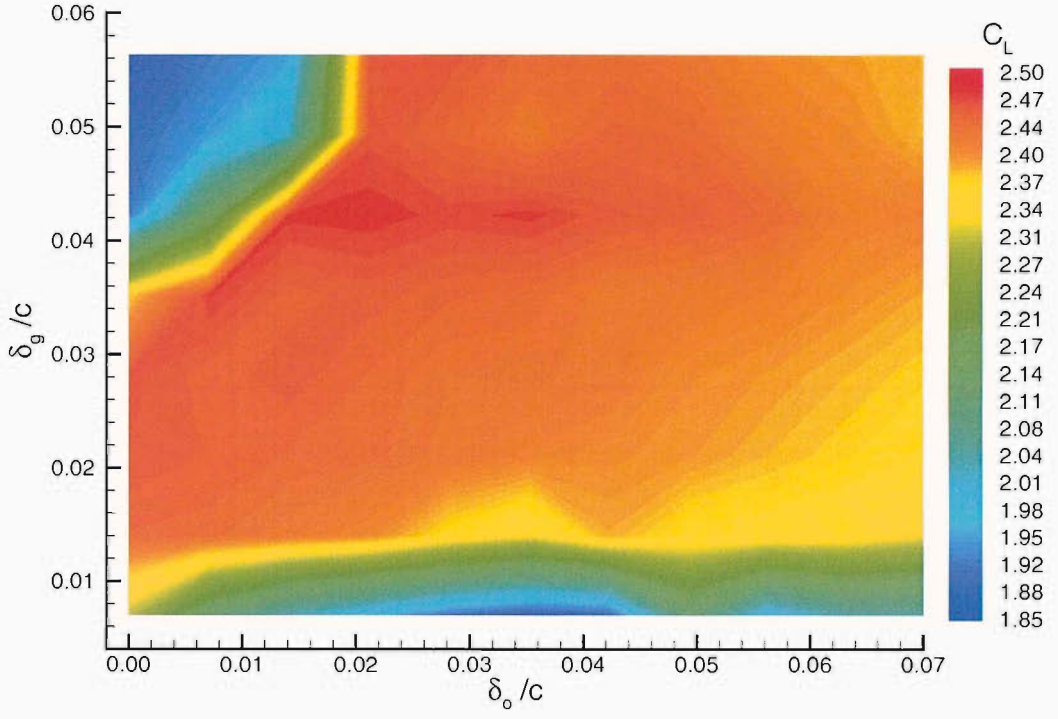

Figure 4.1: Variation of downforce coefficient with flap gap and overlap.

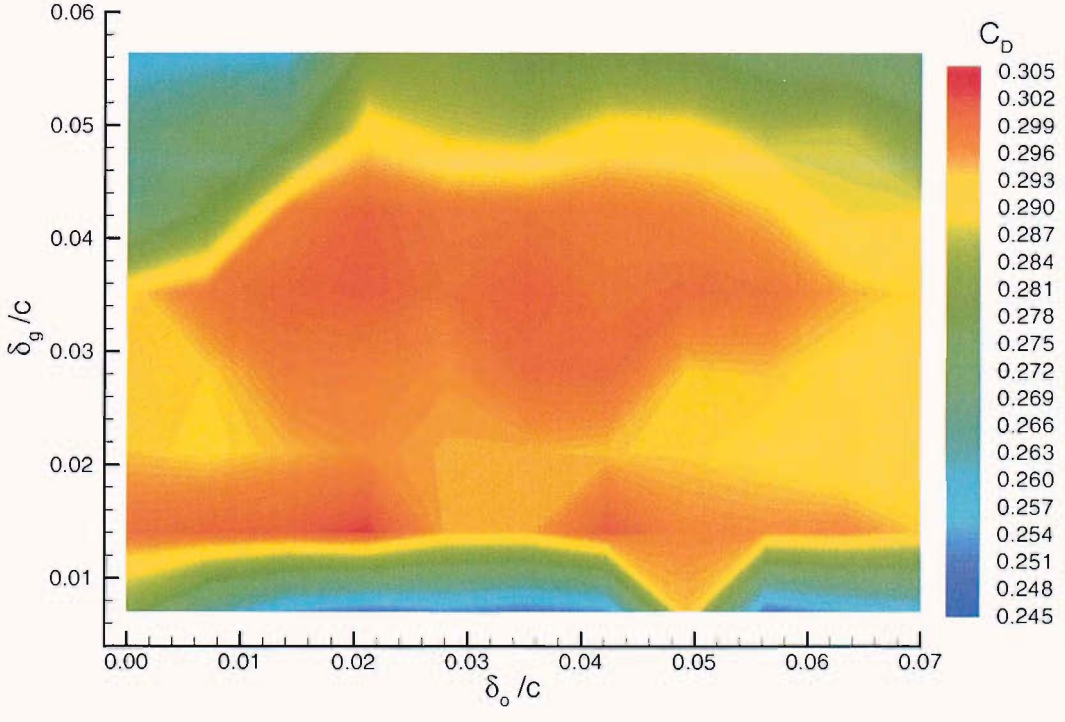

Figure 4.2: Variation of drag coefficient with flap gap and overlap.

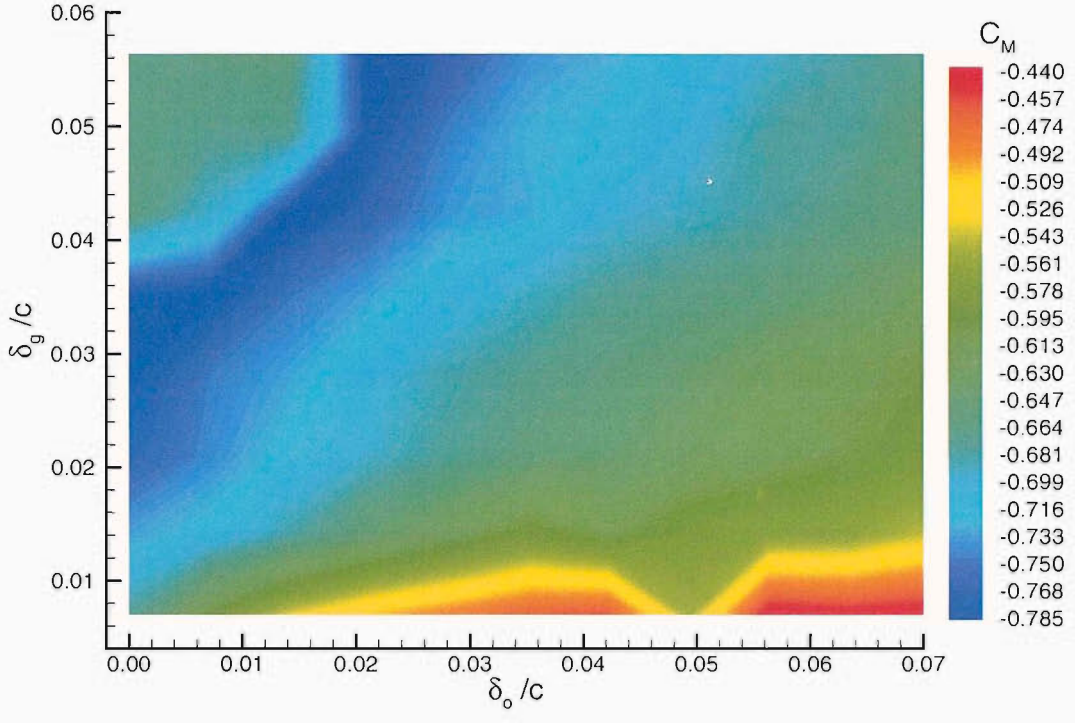

Figure 4.3: Variation of pitching moment coefficient with flap gap and overlap.

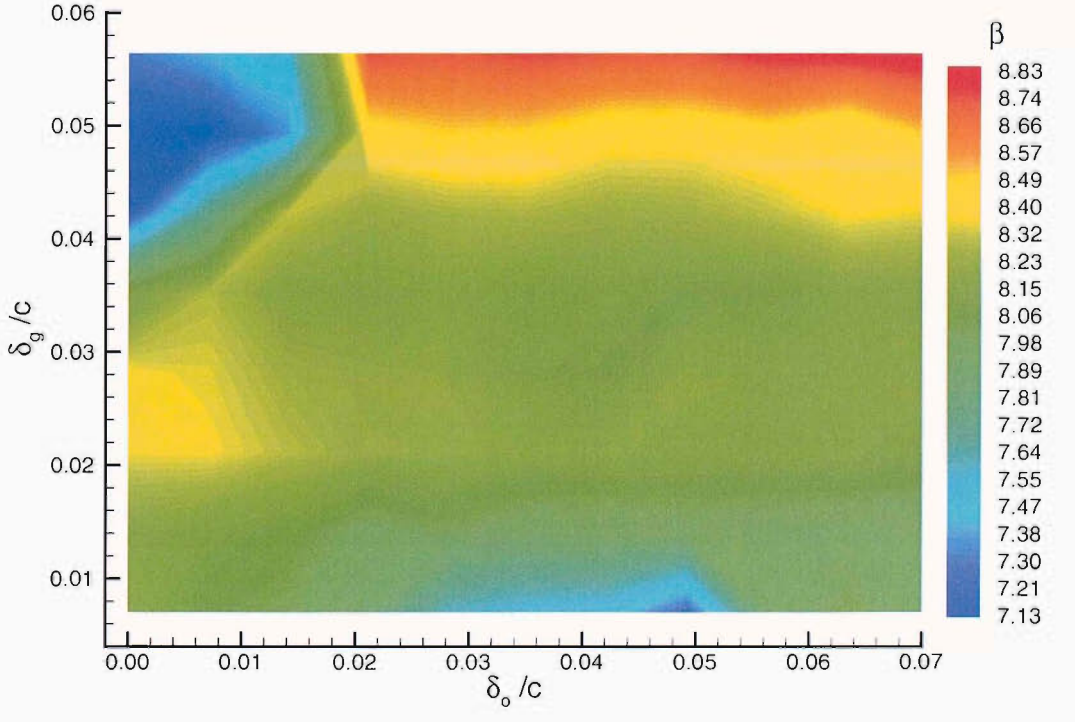

Figure 4.4: Variation of wing efficiency with flap gap and overlap.

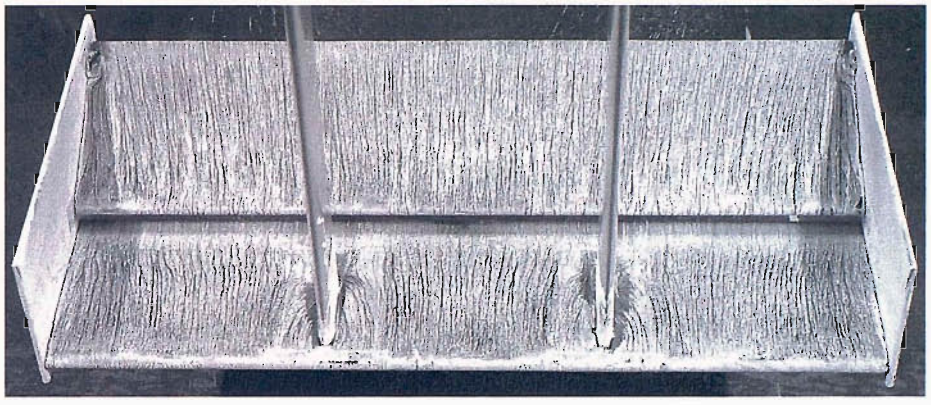

(a) $\delta_g/c = 0.042$, $\delta_o/c = 0.035$ (optimum flap location).

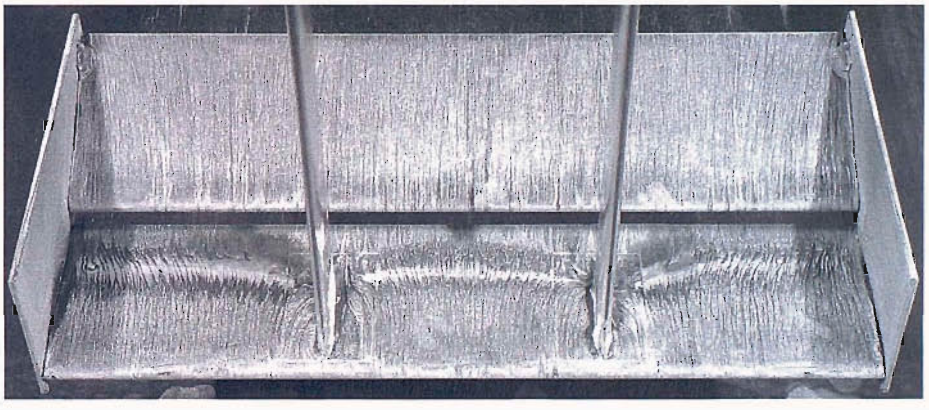

(b) $\delta_g/c = 0.042$, $\delta_o/c = 0.000$.

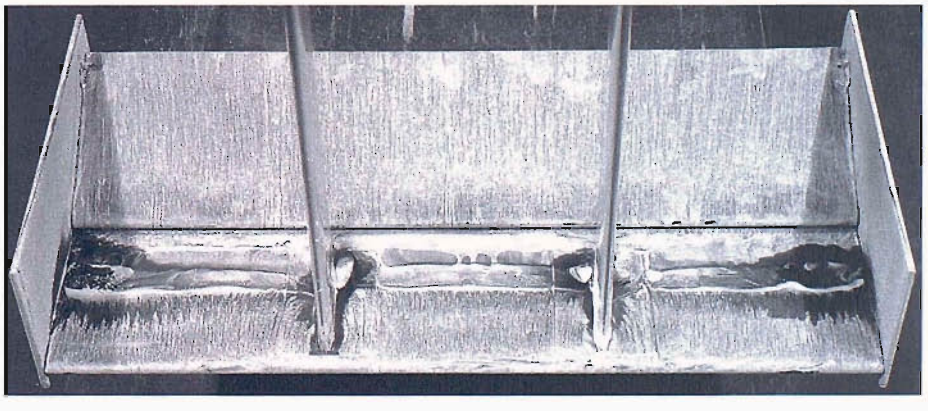

(c) $\delta_g/c = 0.007$, $\delta_o/c = 0.035$.

Figure 4.5: Pressure surface streaklines for various flap gap and overlap (leading edge lowest most).

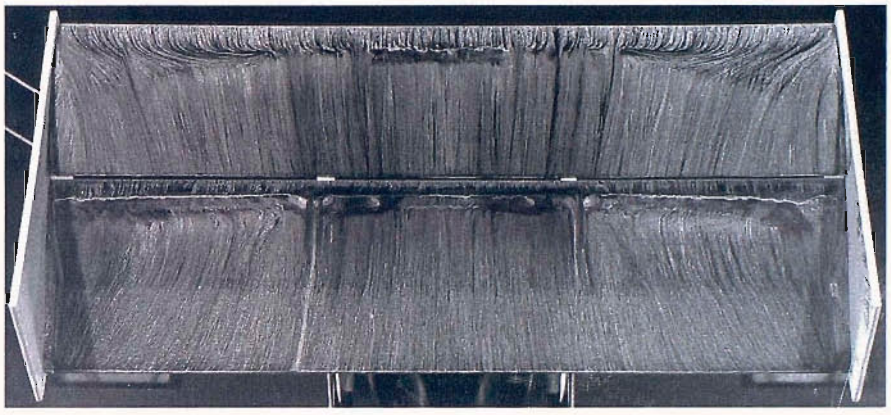

(a) $\delta_g/c = 0.042$, $\delta_o/c = 0.035$ (optimum flap location).

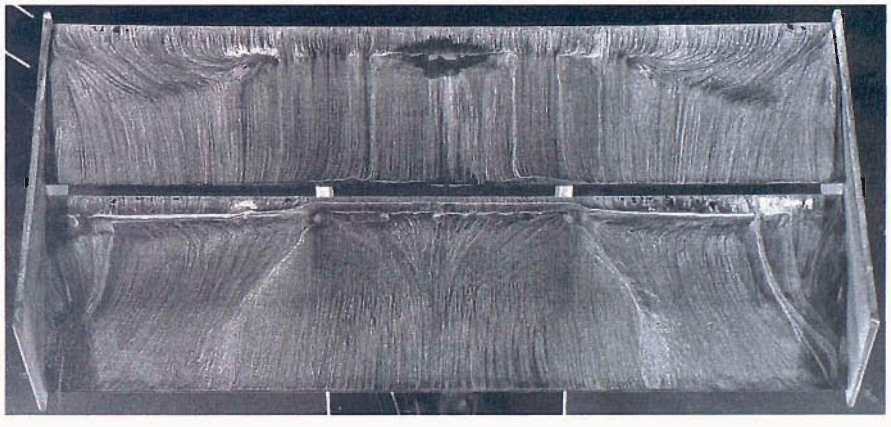

(b) $\delta_g/c = 0.042$, $\delta_o/c = 0.000$.

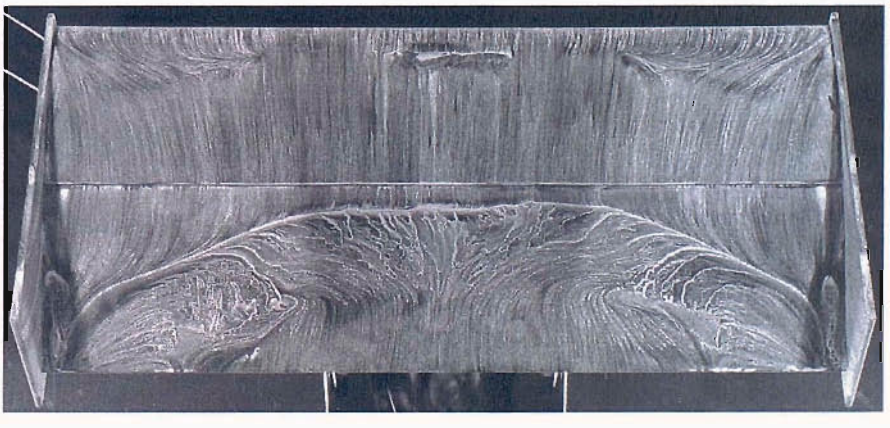

(c) $\delta_g/c = 0.007$, $\delta_o/c = 0.035$.

Figure 4.6: Suction surface streaklines for various flap gap and overlap (leading edge upper most).

Chapter 5

Influence of Ride Height on Wing Performance

This chapter discusses experimental results obtained at various ride heights. The experimental setup is stated followed by discussions of the data. The results are then discussed in combination. In addition the flow field variations responsible for the alterations in wing performance are identified.

5.1 Experimental Details

During this investigation the incidences of the main element and flap were $+4^{\circ}$ and $+24^{\circ}$ respectively. The flap gap and overlap were assigned optimum values of $0.042c$ and $0.035c$ respectively. Within a single test run the ride height of the wing was varied in two stages; first an upstroke stage (increasing h) followed by a downstroke stage (decreasing h). During the upstroke stage the ride height was increased from 10mm ($0.035c$) to 180mm ($0.634c$) with the wing in situ in a continuous wind-on state. During the downstroke stage the ride height was decreased from 180mm to 10mm again with the wing in situ in a continuous wind-on state. The incremental variation in ride height was set according to the variations in the force measurements and refined in areas of importance. Downforce, drag and pitching moment data was obtained at all ride heights. On-surface and off-surface data was then obtained at ride heights of importance as identified by the forces.

5.2 Forces

The downforce, drag, pitching moment and wing efficiency at various ride heights are presented in Figures 5.1, 5.3, 5.4 and 5.5 respectively. The force measurements were catagorised into three types; increasing ride height, decreasing ride height and independent of direction. The latter category referred to force data which was independent of the direction of ride height variation. Figure 5.2 presents the variation in downforce slope ($dC_L/d(h/c)$) with ride height. Upon inspection six regions were identified and labelled force regions a to f.

In Zerihan [9], the downforce variation for the 'high flap angle' (as referred to by Zerihan) possessed features similar to Figure 5.1. The force regions defined within this research directly corresponded to force regions observed by Zerihan. Force region a in this work corresponded to force region a within the work of Zerihan. Force region b within the work of Zerihan incorporated force regions b, c and d of this work. Force region f within this work corresponded to force region c in the work of Zerihan [112]. Force region e was not captured by Zerihan due to the static nature of the experimental rig with regards to ride height. It was noted that additional force regions were observed within this research when compared to Zerihan. The finer ride height resolution within this research allowed for more subtle force regions to be captured.

The variation in downforce coefficient with ride height is presented in Figure 5.1. Decreasing the ride height from a maximum value to $0.236c$ caused the downforce to increase asymptotically from $C_L = 1.62$ to 2.29 (region a). Further ride height reductions resulted in the downforce decreasing gradually initially until $h/c = 0.225$. The downforce then abruptly decreased from $C_L = 2.30$ to 2.26 at a ride height of $0.218c$. This range of ride heights was labelled region b. A linear increase in downforce was observed between $h/c = 0.218$ and 0.134 (region c), within which the downforce increased from $C_L = 2.26$ to 2.44. Between $h/c = 0.134$ and 0.081 the downforce remained relatively constant at $C_L = 2.45$ (region d). Below a ride height of $0.081c$ the downforce was found to be dependent on the direction of ride height variation. Decreasing the ride height from $0.081c$ (region e) resulted in the downforce gradually increasing, reaching a maximum value (C_{Lmax}) of 2.46 at $h/c = 0.067$. Further reductions in ride height resulted in the downforce sharply decreasing until a minimal value of ride height was achieved. Increasing the ride height from a minimal value (region f) caused the downforce to increase sharply then round off at $C_L = 2.23$ for $h/c = 0.063$. Increasing the ride height further resulted in the downforce

decreasing initially then abruptly increasing. Between ride heights of $0.077c$ and $0.081c$ the downforce significantly increased from $C_L = 2.21$ to 2.45. The downforce variations in regions e and f were largely similar albeit offset. Values of downforce in region f were reduced by approximately 10% when compared to region e.

The variation in drag coefficient with ride height is presented in Figure 5.3. Decreasing the ride height from a maximum value to $0.236c$ caused the drag to increase asymptotically to $C_D = 0.264$ (region a). Between $h/c = 0.236$ and 0.218 the rate of drag increase was significantly reduced (region b). The drag varied linearly between $h/c = 0.218$ and 0.176 increasing from $C_D = 0.265$ to 0.280 (region c). A maximum value of drag (C_{Dmax}) of 0.284 was achieved at a ride height of $0.141c$. Reducing the ride height from $0.284c$ to $0.081c$ resulted in the drag decreasing, gradually at first then rapidly (region d). Below a ride height of $0.081c$ the drag was found to be dependent on the direction of ride height variation. Increasing the ride height from a minimal value to $0.077c$ (region f) resulted in the drag increasing linearly then decreasing abruptly between $h/c = 0.077$ and 0.081. Decreasing the ride height from $0.081c$ (region e) resulted in the drag decreasing linearly until $h/c = 0.049$, after which the drag increased abruptly then rounded off.

The influence of ride height on pitching moment coefficient is presented in Figure 5.4. Reducing the ride height from a maximum value to $0.236c$ caused the pitching moment to increase from $C_M = -0.493$ to -0.673 (region a). Decreasing the ride height further from $0.236c$ to $0.218c$ (region b) caused the pitching moment to increase gradually then decrease abruptly. Further reductions in ride height resulted in the pitching moment increasing, reaching a maximum value (C_{Mmax}) of -0.674 at $h/c = 0.169$ (region c). Below a ride height of $0.169c$ the pitching moment decreased until a minimum value of ride height was achieved. Unlike the downforce and drag the pitching moment was relatively independent of ride height direction below $0.081c$.

The variation in wing efficiency with ride height is presented in Figure 5.5. Since dependent on both the downforce and drag, the wing efficiency exhibited similar trends to the downforce and drag. A maximum wing efficiency of 9.29 was achieved at a ride height of $0.063c$, corresponding to force region e.

5.3 Wing Tip Flow Field

The flow field of the port wing tip was visualised using PIV (Section 3.6.2). Ride heights of $0.317c$, $0.247c$, $0.211c$, $0.141c$, $0.099c$, $0.063c$ and $0.039c$ were investigated. Figures 5.6 to 5.9 present contours of time-averaged non-dimensional vorticity (Ω_x) at $x/c = 0.995$ for various ride heights. Positive and negative vorticity was defined as clockwise and anti-clockwise rotations respectively. The geometry of the wing, port endplate and ground plane have also been included.

In order to identify a vortex present within the wing tip flow field the identification method of Jeong & Hussain [147] was used. This method is based on the eigenvalues of the symmetric tensor $\mathbf{S}^2 + \mathbf{\Omega}^2$. $\mathbf{S}$ and $\mathbf{\Omega}$ represent respectively the symmetric and asymmetric parts of the velocity gradient tensor $\nabla\mathbf{u}$. This criterion defined a vortex as the coincidental existence of locally spiralling or curved streamlines and a local pressure minimum. The hydraulic diameter (d_h) of any resulting vortex was defined as the diameter of the outer boundary of the vortex as defined by the method of Jeong & Hussain.

Figure 5.6(a) presents the vorticity contours at a ride height of $0.317c$. This ride height was typical for force region *a*. The most prominent feature of the flow field was a concentrated vortex inboard of the endplate, beneath the wing. This vortex will be referred to as the 'lower edge vortex'. The lower edge vortex was a direct result of the finite pressure difference between the freestream flow and the flow beneath the wing, due to the endplates. The lower edge vortex was centred at $z/c = -0.08$, $y/c = -0.03$ with a hydraulic diameter of $0.04c$. A shear layer, originating from the lower edge of the endplate, was entrained into the vortex. The vorticity within the centre of the vortex core was seemingly less than the surrounding area ($\Omega_x = -116$). The centrifugal forces within the core of the vortex forced the seeding particles outwards. The lack of seeding within the vortex core consequently resulted in an artificially low value of vorticity. A boundary layer along the ground plane was observed as a region of positive vorticity. Since the ground plane was provided with a freestream velocity this feature may appear to be incorrect. However it must be remembered that the wing generated an adverse streamwise pressure gradient due to the recovery of the flow beneath the suction surface. This in turn generated the boundary layer along the ground plane.

The wing tip flow field at a ride height of $0.247c$ (near region a/b boundary) is presented in Figure 5.6(b). As before the flow field was dominated by the lower edge vortex, associated

shear layer and ground plane boundary layer. Reducing the ride height resulted in the lower edge vortex dilating and moving inward. The lower edge vortex was centred at $z/c = -0.11$, $y/c = -0.03$ with a hydraulic diameter of $0.07c$. The vorticity within the centre of the vortex was significantly reduced ($\Omega_x = -54$). Figure 5.7(a) presents the wing tip flow field at a ride height of $0.211c$ (region b). The vorticity contours indicated the presence of the ground plane boundary layer and lower edge vortex shear layer. However, the lower edge vortex was replaced by a region of anti-clockwise recirculation. The centre of the recirculation region was located at $z/c = -0.13$, $y/c = -0.01$.

Reducing the ride height to $0.141c$ (Figure 5.7(b)) resulted in the lower region of recirculation elongating in a spanwise sense. This ride height was typical for force region c. The centre of the lower recirculation region translated inward and downward to $z/c = -0.16$, $y/c = -0.05$. A concentrated vortex was identified outboard of the endplate above the wing. This vortex will be referred to as the 'upper edge vortex'. For ride heights above this value the upper edge vortex was present. However, the dimensions of the data field was such that it was not visible. The upper edge vortex was centred at $z/c = 0.06$, $y/c = 0.32$ with a hydraulic diameter of $0.02c$. Reducing the ride height further to $0.099c$ (Figure 5.8(a)) resulted in the flow field remaining largely unchanged. This ride height was typical for force region d. The location and hydraulic diameter of the upper edge vortex were unaffected. The lower recirculation region became more elongated in a spanwise sense. The centre of the lower region of recirculation moved inward to $z/c = -0.15$, $y/c = -0.05$.

Figures 5.8(b) and 5.9(a) present the wing tip flow field for $0.063c$ and $0.039c$ respectively with decreasing ride heights (region e). The upper edge vortex moved upward however, the size was unaffected by the variation in ride height. Reducing the ride height caused the lower recirculation region to move outward and upward translating from $z/c = -0.23$, $y/c = -0.03$ to $z/c = -0.21$, $y/c = -0.02$. The vorticity within the ground plane boundary layer decreased accompanied by a significant reduction in span. Figures 5.9(b) presents the wing tip flow field for $h/c = 0.063$ with increasing ride height (region f). When compared to Figure 5.8(b) minimal variations in flow field were observed. The upper edge vortex and lower recirculation region were similar in dimension and location with both increasing and decreasing ride heights. Table 5.1 presents quantitative data concerning the upper and lower edge vortices for various ride heights.

5.4 Surface Flow Field

Figures 5.10 to 5.16 present surface streaklines obtained at various ride heights obtained using an oil flow visualisation technique (Section 3.6.3). Ride heights of $0.317c$, $0.247c$, $0.211c$, $0.099c$, $0.063c$ and $0.039c$ were investigated. Within each figure the subfigures (a), (b) and (c) present the streaklines on the pressure surface, suction surface and inboard surface of the starboard endplate respectively.

The streaklines obtained at a ride height of $0.317c$ are presented in Figure 5.10 (region *a*). The suction surface and pressure surface streaklines indicated a fully attached flow. The line of transition on the suction surfaces of both the main element and flap was slightly curved, moving downstream towards the wing tips. At the centre span transition was observed at $x/c = 0.07$ and 0.54 on the main element and flap respectively. The streaklines on the inboard face of the endplate (Figure 5.10(c)) indicated the presence of a vortical flow, the lower edge vortex. The vortex extended along the full length of the endplate. For this ride height the lower edge vortex was present directly beneath the flap. The upwash generated by the lower edge vortex altered the flow field near the wing tips such that the wing incidence was effectively decreased. Accordingly transition near the wing tips occurred at a more downstream location. Since the upwash effects reduced towards the centre span the delay in transition decreased, resulting in the curved line of transition observed. The surface streaklines remained largely unaffected by decreasing the ride height to $0.247c$ (Figure 5.11). This ride height was near to the boundary between force regions *a* and *b*. The centre span location of transition on the main element and flap suction surfaces remained unaffected at $x/c = 0.07$ and 0.54 respectively. As before the lines of transition were slightly curved, moving downstream towards the wing tips. The lower edge vortex was indicated however, the associated streaklines became more vertical.

Figure 5.12 presents the surface streaklines for a the ride height of $0.211c$ (region *c*). The streamwise location of transition was unaffected by the reduction in ride height. The most prominent alteration in the streaklines was observed on the inboard face of the endplate (Figure 5.12(c)). The streaklines no longer indicated a concentrated lower edge vortex. Instead a region of recirculation was indicated reducing in cohesion towards the downstream end of the endplate. Decreasing the ride height to $0.099c$ resulted in a significant alteration in the surface streaklines of both the wing and endplate (Figure 5.13). This ride height was typical for force region *d*. Transition on the main element suction surface moved

downstream with a centre span location of $x/c = 0.12$. The location of transition on the flap suction surface was unaffected. The three-dimensionality of transition of the main element surface flow field increased. The pressure surface streaklines indicated spanwise regions of decelerated flow on the main element originating at $x/c = 0.33$. The streaklines on the endplate (Figure 5.13(c)) indicated a breakdown of any vortical flow.

Reducing the ride height to $0.063c$ for the decreasing ride height case resulted in significant alterations in the surface flow field of the wing (Figure 5.14). This ride height was typical for force region *e*. The pressure surface and endplate streaklines were largely unaffected. However, a region of separation and recirculation was observed on the suction surface of the main element at the trailing edge. The region of separation was off-centre in a spanwise sense, located towards the starboard wing tip. This lack of symmetry was traced back to a flow disturbance originating from a large particle of flow visualisation located at the leading edge towards the port wing tip. The centre span streamwise location of transition on the main element remained constant across the span at $x/c = 0.12$. The flap transition line was straight and located at $x/c = 0.56$. Unlike for higher ride heights the transition lines were straight across the span of the wing.

To investigate the variation in surface flow field due to the direction of ride height variation, an oil flow visualisation was performed at $0.063c$ with increasing ride height (region *f*). The resulting streaklines are shown in Figure 5.15. Compared with Figure 5.14 (region *e*) it was noted that alterations in both the suction surface and pressure surface streaklines were present. A region of deceleration was now present on the main element pressure surface originating at $x/c = 0.36$. In addition to the region of separation on the main element suction surface, a large region of separation was present on the flap suction surface. The flap separation contained two nodes and two regions of counter-rotation. The streaklines on the main element suction surface remained consistent with those observed for the decreasing ride height case. The main element transition line was constant across the span of the wing located at $x/c = 0.12$. Transition was not present on the flap at the wing centre span due to the large region of recirculation. Either side of the recirculation region transition occurred on the flap at $x/c = 0.56$.

Figure 5.16 presents the streaklines obtained for a ride height of $0.039c$ with increasing ride height (region *f*). The pressure surface streaklines indicated a reduction in the width of the deceleration region on the main element. The location of transition on the main element suction surface remained constant at $x/c = 0.12$. Transition on the flap suction

surface was not present at the wing centre span due to the large region of recirculation. Either side of the recirculation region transition occurred on the flap at $x/c = 0.56$. The region of separation on the suction surface of the flap remained unchanged in both size and structure. The region of separation on the main element suction surface originating at $x/c = 0.36$ however, increased in width. The region of separation on the main element was approximately symmetric about the centre span extending from $z/c = -0.31$ to -0.71. Table 5.2 presents quantitative data concerning transition on the suction surfaces of the wing at a centre span location.

5.5 Surface Pressures

Surface pressures were obtained to provide quantitative data concerning the influence of ride height on the surface flow field. Chordwise and spanwise surface pressures were measured on the wing. In addition surface pressures were measured on the inboard face of the port endplate. The ride heights investigated were $0.634c$, $0.317c$, $0.247c$, $0.211c$, $0.141c$, $0.099c$, $0.063c$ and $0.039c$ corresponding to ride heights within each of the six force regions. To investigate force regions e and f the lowest two ride heights were investigated with both increasing and decreasing ride heights.

5.5.1 Chordwise Pressures at Centre Span

Figure 5.17 presents the chordwise surface pressure distribution at the centre span of the wing for various ride heights. For reasons of clarity the surface pressures of the main element and flap are shown separately. For high ride heights (Figure 5.17(a)) variations in ride height predominantly affected the suction surface pressures. The surface pressures on both the main element and flap pressure surfaces remained relatively independent of ride height. Stagnation consistently occurred at $x/c = 0.01$ and 0.46 on the main element and flap respectively. The main element suction surface pressures were strongly dependent on the ride height with lower ride heights generating greater suction. A similar trend was observed within the flap suction surface pressures albeit of reduced magnitude. The main element suction surface pressures indicated a rapid acceleration of the flow obtaining a maximum value of suction (C_{Psuc}) at $x/c = 0.02$ for all high ride heights. A pressure recovery was observed between the location of maximum suction and the main element trailing edge. The rate of pressure recovery and pressure difference at the main element

trailing edge increased with reduced values of ride height. The flap suction surface pressures also indicated a rapid flow acceleration and subsequent pressure recovery, with maximum suction consistently occurring at $x/c = 0.48$. However, a second flow acceleration was observed between $x/c = 0.51$ and 0.52. This streamwise location corresponded to directly downstream of the main element trailing edge. Downstream of $x/c = 0.52$ a pressure recovery was observed increasing in rate with reduced values of ride height.

Greater variation in surface pressures was observed for lower ride heights (Figure 5.17(b)). The surface pressures at a ride height of $0.099c$ (region d) conformed to the trends observed at higher ride heights. The locations of maximum suction and stagnation of both the main element and flap remained independent of ride height. A variation was observed within the initial pressure recovery region on the main element suction surface. The suction on the main element remained constant at a value of $C_P \approx -6.7$ between $x/c = 0.02$ and 0.09. For the lowest two ride heights ($h/c = 0.063$ and 0.039) the trends within the surface pressures and overall shape of the pressure distribution was different.

Very little variation was observed between the surface pressures obtained at $h/c = 0.063$ with increasing and decreasing ride height. In both cases stagnation occurred at $x/c = 0.01$ and 0.46 on the main element and flap respectively. Two stages of flow acceleration were observed on the main element suction surface; an initial high acceleration between the leading edge and $x/c = 0.04$, and a more gradual acceleration between $x/c = 0.04$ and 0.11. Maximum suction occurred at $x/c = 0.11$. This streamwise location corresponded to the lowest point on the main element i.e. the throat of the channel beneath the wing. The chordwise surface pressures indicated that flow beneath the wing accelerated until the throat of the channel then recovered. This behaviour was largely similar to that exhibited by a diffuser in ground effect [7, 43]. It is surmised that for the lowest two ride heights the suction surfaces of the wing acted as a diffuser. The surface pressures obtained at $h/c = 0.099$ represented a transition stage. Downstream of maximum suction the pressure recovered at a greater rate than for $h/c = 0.099$ achieving reduced suction at the main element trailing edge. The flap surface pressures on both the pressure and suction surface were reduced when compared to $h/c = 0.099$. However, the trends within the flap surface pressures remained consistent.

The surface pressures obtained for $h/c = 0.039$ were dependent on the direction of ride height variation (regions e and f). Compared to higher ride heights the pressure surface pressures were reduced, in particular on the main element. Stagnation was observed at

$x/c = 0.01$ and 0.46 on the main element and flap respectively. The pressure surface pressures between $x/c = 0.34$ and the main element trailing edge were significantly increased. A two stage acceleration was observed on the main element suction surface similar to that observed at $h/c = 0.063$. Maximum suction was achieved at $x/c = 0.11$ for both increasing and decreasing ride heights. A high rate of pressure recovery was observed between the location of maximum suction on the main element and $x/c = 0.37$. Directly downstream a region of negligible pressure variation was observed extending to the main element trailing edge. The main element suction surface pressures were less with increasing ride height than for decreasing ride height. Consequently the suction at the main element trailing edge was greater for decreasing ride height. The flap suction surface pressures were independent of ride height variation. Compared to the flap pressures obtained at $h/c = 0.063$ the pressures obtained at $h/c = 0.039$ were reduced between the flap leading edge and $x/c = 0.61$ and increased between $x/c = 0.61$ and the flap trailing edge. Table 5.3 presents quantitative data concerning the chordwise surface pressures obtained at the wing centre span.

5.5.2 Suction Surface Pressure Recovery

To directly compare the rate of pressure recovery along the suction surfaces of the wing a scaled pressure coefficient (C_{Pscale}) was defined. The scaled pressure coefficient was calculated by normalising the suction surface pressures against the peak value of suction (C_{Psuc}). As a result $C_{Pscale} = 0.0$ represented maximum suction and $C_{Pscale} = 1.0$ represented stagnation. The distance downstream of the suction peak (s) was normalised against the distance between the suction peak and the trailing edge (s_t). The variable C_{Pscale} used within this research is identical to the variable $\overline{C_P}$ used by Zerihan [9]. Figures 5.18 presents the scaled pressures on both the main element and flap suction surfaces.

Figure 5.18(a) presents the scaled pressures on the main element suction surface for various ride heights. For the highest ride height the pressure recovery was asymptotic levelling off towards the trailing edge. Reducing the ride height to $0.211c$ decreased the rate of pressure recovery between the suction peak and $s/s_t = 0.73$. The pressure recovery became more linear as the ride height reduced. Reducing the ride height through $0.141c$ to $0.099c$ resulted in the pressure recovery becoming more linear. For a ride height of $0.063c$ the rate of pressure recovery was independent of ride height direction. Initially ($s/s_t = 0.0$ to 0.24) the linear rate of recovery was reduced when compared to higher ride heights. However, downstream of $s/s_t = 0.24$ the recovery rate was significantly increased rounding

off towards the trailing edge. The rate of recovery for $h/c = 0.039$ was dependent on the ride height direction. Greater values of C_{Pscale} were achieved with an increasing ride height. The initial rate of recovery confirmed the trend observed at higher ride heights with a reduced rate of recovery between $s/s_t = 0.0$ and 0.14. Downstream of this location ($s/s_t \leq 0.62$) a maximum rate of recovery was initially observed followed by a rounding off at $C_{Pscale} \approx 0.7$. The suction surface flow field for this ride height (Figure 5.16(b)) indicated a region of separation originating from $x/c = 0.36$ ($s/s_t = 0.68$). The location of separation has been included in Figure 5.18(a).

The scaled centre span suction surface pressures on the flap are presented in Figure 5.18(b). For ride height greater than $0.099c$ reductions in ride height resulted in increased rates of pressure recovery. The pressure recovery in such cases was initially rapid then leveled off towards the flap trailing edge. The rate of pressure recovery for $h/c = 0.063$ was independent of ride height direction. Initially an increased rate of recovery was observed ($s/s_t = 0.0$ to 0.6) in agreement with the trend for higher ride heights. Downstream of this location the recovery rate was significantly reduced when compared to $h/c = 0.099$. Reducing the ride height to $0.039c$ resulted in a further reduced rate of recovery. Dependency on the direction of ride height was observed with greater values of C_{Pscale} obtained for decreasing ride heights.

5.5.3 Chordwise Pressures Near Wing Tip

To quantify the effects of three-dimensionality on the flow field of the wing chordwise surface pressures were measured near the port wing tip ($z/c = -0.088$). Figure 5.19 presents the the chordwise port wing tip pressures for various ride heights and force regions. Reducing the ride height for higher ride heights (Figure 5.19(a)) resulted in increased suction over both the main element and flap. The corresponding pressure surface pressures decreased, in particular on the main element. Stagnation occurred at $x/c = 0.01$ and 0.46 on the main element and flap respectively for the higher ride heights ($h/c \geq 0.141$). The main element suction surface pressures indicated a rapid flow acceleration at the leading edge, albeit of less magnitude when compared to the centre span. A gradual pressure recovery then occurred until $x/c = 0.30$ followed by increased suction extending to the main element trailing edge. For a ride height of $0.141c$ the increased suction towards the main element trailing edge was absent, in contrast to higher ride heights. For the higher ride heights the flap suction surface pressures indicated a flow acceleration and recovery similar to the

centre span.

Reducing the ride height below $0.141c$ (Figure 5.19(b)) resulted in a significant variation in the surface pressure distribution on the main element. The surface pressures on the main element for $h/c = 0.099$ largely conformed to those observed for higher ride heights. Stagnation points remained at $x/c = 0.01$ and 0.46 on the main element and flap respectively. Reduced suction was observed towards the main element trailing edge. The variation in suction over the flap did not conform to the trend observed at higher ride heights. Reduced flap suction was observed for this ride height which further decreased with reductions in ride height. The wing tip flow field indicated that for ride heights below $0.211c$ the lower edge vortex was not present. Therefore the increased suction over the flap, observed at higher ride heights, was not present.

For the lowest two ride heights ($0.063c$ and $0.039c$) stagnation occurred at $x/c = 0.46$ on the flap. These ride heights were typical of force region *e*. However, stagnation on the main element occurred immediately at the leading edge. The chordwise surface pressure distribution on the main element was significantly different to those observed at higher ride heights. Similar to the centre span surface pressures, a two stage flow acceleration was observed on the main element. The peak in suction moved downstream to $x/c = 0.11$ indicating flow behaviour similar to that of a diffuser [7, 43]. A rapid pressure recovery was observed directly downstream of the suction peak followed by a leveling off of suction towards the main element trailing edge. Suction over the flap was decreased in agreement with the trends observed.

For a ride height of $0.063c$ the surface pressures near the wing tip were independent of ride height direction. However the surface pressures were dependent on ride height direction for $h/c = 0.039$. A dependence on the ride height direction was observed in the suction surface pressure in particular. Increased suction was achieved with decreasing ride height. The flap suction surface pressures with increasing ride height indicated a rapid pressure recovery followed directly by a region of constant suction.

Figure 5.20(a) presents chordwise surface pressures for a ride height of $0.317c$ (region *a*) at both the centre span and near the wing tip. Near the wing tip the surface pressures on the pressure surfaces of both the main element and flap were significantly reduced. The main element suction peak near the wing tip and corresponding downstream pressure recovery were also significantly reduced. Decreased suction was observed on the main element between the leading edge and $x/c = 0.35$ when compared to the centre span.

Further downstream increased suction was observed near the wing tip. The flap suction surface pressures were significantly increased for all streamwise locations near the wing tip. These variations in chordwise surface pressures observed for $h/c = 0.317$ were largely consistent with wing tip effects. The upwash generated by the the lower edge vortex reduced the effective incidence of the wing near the wing tip. Accordingly reduced pressure surface pressures were observed. Reduced suction was also observed on the main element. However, increased suction was observed for $x/c > 0.35$ on both the main element and flap. This observation did not conform to an increase in effective incidence near the wing tips. It must be remembered that the port lower edge vortex was present directly beneath the wing, centred at $z/c \approx -0.1$. The corresponding suction generated by the lower edge vortex generated increased suction over the flap and downstream section of the main element, as observed.

Figure 5.20(b) presents chordwise surface pressures at the centre span and wing tip for a ride height of $0.063c$. Both increasing and decreasing ride height cases have been included (regions e and f). For this ride height the wing tip flow field indicated the absence of the lower edge vortex. Accordingly the increased levels of suction over the main element trailing edge and flap were not observed. The suction peak on the main element was consistent at $x/c = 0.11$ at both the centre span and near the wing tip.

5.5.4 Integrated Chordwise Surface Pressures

The integrated chordwise surface pressures are presented in Figure 5.21(a). The sectional downforce at the wing centre span (C_{lc}), near the port wing tip (C_{lt}) and the combined total (C_l) are presented for various ride heights. For all ride heights the centre span sectional downforce was significantly greater than the corresponding wing tip downforce. The total sectional downforce was accordingly the mean value of the centre span and the wing tip downforce. Reducing the ride height from a maximum value to $0.141c$ (region c) resulted in the centre span and wing tip sectional downforce increasing. A linear decrease in wing tip downforce was observed for further reductions in ride height. The centre span downforce increased to a maximum value of $C_{lc} = 3.47$ at $h/c = 0.063$ then decreased abruptly. Below a ride height of $0.099c$ the total sectional downforce was dependent on the ride height direction. Reduced values of total sectional downforce corresponded to increasing ride heights.

The contributions to the centre span and wing tip sectional downforce by the flap and

main element are presented in Figure 5.21(b). The sectional downforce at the centre span was significantly greater than at the wing tip on both the main element and flap. The sectional downforce on the flap was independent of ride height direction at both the centre span and near the wing tip. Ride heights below $0.099c$ resulted in reductions in both the flap centre span and flap wing tip sectional downforce.

The main element centre span downforce increased asymptotically until $h/c = 0.063$. Below this ride height an abrupt reduction in downforce was observed. Greater values of sectional downforce corresponded to decreasing ride heights. The sectional downforce near the wing tip on the main element increased until $h/c = 0.169$. Further reductions in ride height resulted in the sectional downforce decreasing. Below $h/c = 0.063$ the main element sectional downforce near the wing tip was dependent on the ride height direction. Increased downforce was observed with increasing ride height.

5.5.5 Spanwise Pressures

The spanwise distribution of surface pressures on the main element for various ride heights is presented in Figure 5.22. The pressure surface spanwise distribution was largely independent of ride height. The pressure surface pressures gradually decreased from a local maximum at the centre span to a local minimum towards the wing tip. Decreasing the ride height resulted in the pressure surface pressures reducing in magnitude. A much greater dependency on ride height was observed within the suction surface pressures. For ride heights greater than $0.039c$ the suction surface pressures decreased asymptotically from a local maximum at the centre span to a local minimum towards the wing tip. Reducing the ride height resulted in greater suction at the centre span location, a greater rate of spanwise recovery and increased suction at the wing tip.

The surface pressures on the main element obtained for $h/c = 0.063$ were independent of ride height direction. For a ride height of $0.039c$ the pressure surface spanwise pressures were also independent of ride height direction. However, the suction surface pressures were dependent on ride height direction. Decreasing the ride height resulted in decreased suction between the wing tip and $z/c = -0.39$ and increased suction between $z/c = -0.39$ and the centre span. The suction surface pressures obtained at $h/c = 0.039$ with decreasing ride height exhibited trends similar to those observed at higher ride heights. However, between $z/c = -0.88$ and the centre span the suction increased from $C_P = -8.16$ to -8.03. For the case of increasing ride height an identical feature was observed albeit with a greater span

($z/c = -0.53$ to the centre span).

The spanwise surface pressures obtained on the flap for various ride heights are presented in Figure 5.23. For all ride heights the surface pressures on the flap pressure surface decreased gradually from the centre span to $z/c = -0.053$. For spanwise locations closer to the wing tip the pressure surface pressures increased. Reducing the ride height caused the pressure surface pressures to decrease. The suction surface pressures exhibited features significantly different to those observed on the main element. The suction surface pressures obtained at $z/c = -0.70$ did not conform to the overall trends observed. It was noted that this spanwise location was directly downstream of the port wing pillar. For ride heights above $0.211c$ suction increased from the centre span towards the wing tip, in contrast to the main element. This feature was a direct result of the lower edge vortex acting upon the flap suction surface thereby increasing the suction. Reducing the ride height from a maximum value to $0.211c$ resulted in increased suction. Further reductions in ride height resulted in decreased suction over the entire span. The suction surface pressures obtained at a ride height of $0.099c$ exhibited the trends observed for higher ride heights between the centre span and $z/c = -0.35$. Closer to the wing tip reduced suction was observed gradually decreasing towards the wing tip. The surface flow field and wing tip flow field data indicated that the lower edge vortex was absent for this ride height, hence the associated suction was also absent.

The suction surface pressures for $h/c = 0.063$ were greater for the increasing ride height case. The trend within the surface pressures conformed to that observed at $h/c = 0.099$ and was independent of ride height direction. The dependence on ride height direction was more pronounced for the lowest ride height ($h/c = 0.039$). Between the centre span and $z/c = -0.44$ increased suction was observed for increasing ride height. Closer to the wing tip increased suction was observed for the decreasing ride height case.

5.5.6 Endplate Pressures

The surface pressures obtained on the inboard face of the port endplate at various ride heights are presented in Figure 5.24. The location of the lower edge of the endplate has been included. Two distinct trends within the surface pressures were observed; the first for ride heights above $0.247c$, and the second for ride heights below $0.247c$. Reducing the ride height for $h/c \geq 0.247$ caused the suction at a given vertical location to increase. Within this range of ride heights maximum suction was consistently observed at the lowest

vertical location ($y/c = -0.02$). The wing tip flow field data (Table 5.1) indicated that the lower edge vortex was centred close to this vertical location. The corresponding suction generated by the lower edge vortex resulted in the high value of suction observed. Above this vertical location the suction initially decreased then increased towards the flap suction surface. Decreasing the ride height from $0.247c$ (region a) to $0.211c$ (region c) resulted in decreased levels of suction at all vertical locations.

The wing tip flow field for a ride height of $0.211c$ indicated a breakdown of the lower edge vortex. Accordingly the suction on the inboard face of the endplate was reduced when compared to $h/c = 0.247$. However the vertical variation in suction remained consistent with that observed for higher ride heights. It must be noted that the surface pressures on the inboard face were obtained at $x/c = 0.614$ whereas the wing tip flow field data was obtained at $x/c = 0.995$. The surface streaklines obtained for $h/c = 0.211$ (Figure 5.12) indicated the presence of the lower edge vortex at the streamwise location corresponding to the surface pressures. Further downstream the surface streaklines indicated a breakdown of the lower edge vortex. The incomplete breakdown of the lower edge vortex resulted in contradictions between the surface pressures on the endplate and the wing tip flow field, as observed. Further reductions in ride height from $h/c = 0.211$ caused the vertical suction variation to significantly change. A relatively constant level of suction was observed, decreasing in magnitude with reducing ride height. The surface pressure distribution for the lowest two ride heights ($h/c = 0.063$ and 0.039) indicated a lack of dependency on ride height direction.

5.6 Wake Flow Field

The centre span wake flow field of the wing was investigated in two stages using the technique stated in Section 3.6.5. Firstly the influence of ride height on the wake was investigated at a fixed streamwise location ($x/c = 1.127$). Secondly the streamwise development of the wake was investigated for two ride heights, $0.247c$ (region a) and $0.099c$ (region d). The wake flow field was described using the variables defined in Figure 5.25. The minimum streamwise velocities within the main element and flap wakes were defined as u_{low} and u_{top} respectively. The confluence point between the two wakes was defined as the location where a local maximum streamwise velocity was achieved. The upper (δ_{top}) and lower (δ_{low}) boundaries of the wake were defined as the points where $u = 0.99U_\infty$. The main element wake thickness ($(\delta_{99})_{low}$) and flap wake thickness ($(\delta_{99})_{top}$) were then defined. For the cases

in which a single wake flow field was observed the single wake was referred to as the main element wake.

5.6.1 Influence of Ride Height

Centre span wake profiles for various ride heights at a streamwise location of $x/c = 1.127$ are presented in Figure 5.26. The ground plane locations have been included. Table 5.4 presents the corresponding quantitative data. For the majority of ride heights a dual wake structure was observed. A thick main element wake was indicated with a thinner flap wake located directly above. Between the main element and flap wakes a region of confluence was observed. Immediately beneath the main element wake a region of rapid velocity recovery was observed, followed by a region with constant velocity ($u = U_\infty$). Previous investigations indicated the presence of flow acceleration between the lower boundary of the main element wake and the ground plane, a wall jet.

The structure of the flap wake was relatively independent for higher ride heights (Figure 5.26(a)). The minimum streamwise velocity within the flap wake was consistently measured at $0.77U_\infty$, with the corresponding vertical location fixed at $y/c = 0.35$. The upper boundary of the flap wake (δ_{top}) was constant for both high and low ride heights at $y/c = 0.37$. Reducing the ride height from $0.317c$ to $0.141c$ caused the velocity at the confluence point between the wakes (u_{conf}) to gradually decrease from $0.99U_\infty$ to $0.97U_\infty$. The vertical location of confluence was consistently measured at $y/c = 0.32$. The structure of the main element wake was more dependent on ride height, in particular the velocity deficit and lower boundary. The rate of velocity recovery within both the main element and flap wakes was independent of ride height. Reducing the ride height from $0.317c$ (region a) to $0.141c$ (region c) caused the minimum streamwise velocity within the main element wake to decrease from $0.61U_\infty$ to $0.42U_\infty$. The corresponding vertical location remained relatively constant at $y/c \approx 0.28$. The lower boundary of the main element wake moved downwards with reductions in ride height, decreasing from $y/c = 0.24$ to 0.21. Between the main element wake and the ground plane a region of constant velocity was observed. For ride heights less than $0.317c$ velocities less than freestream were observed close to the ground plane, which decreased with reductions in ride height. This feature corresponded to the boundary layer on the ground plane.

The wake flow field obtained at a ride height of $0.099c$ (Figure 5.26(b)) conformed to the structure and trends observed at higher ride heights. This ride height was typical for

force region *d*. The thickness of the ground boundary layer significantly increased. For a ride height to $0.063c$ with decreasing ride height (region *e*), a dual wake flow field was observed. The flap wake was largely unaffected by the reduction in ride height, however the velocity at the confluence point decreased to $0.88U_\infty$. Unlike the higher ride heights the velocity measurements within the main element wake indicated a region of zero pitot pressure extending from $y/c = 0.20$ to 0.28. Due to the measurement technique used to obtain the wake velocity profiles (Section 3.6.5) negative values of streamwise velocity could not be measured. However the velocity profile within the main element wake seemed to suggest a region of flow reversal.

The structure of the wake flow field for $h/c = 0.063$ with increasing ride height (region *f*) was significantly different to that observed with decreasing ride height. A large single wake was observed extending from close to the ground plane to $y/c = 0.36$. A large region of zero pitot pressure was observed from $y/c = 0.05$ to 0.30. A similar wake structure was observed for a ride height of $h/c = 0.039$ with increasing ride height. For this case the region of zero pitot pressure was larger and the lower wake boundary was closer to the ground plane.

5.6.2 Streamwise Development

The streamwise development of the centre span wake flow field was investigated for two ride heights, $h/c = 0.247$ and 0.099. These ride heights were typical for force regions *a* and *d* respectively. Wake flow field data was obtained at four streamwise locations; $x/c = 0.835$, 1.127, 1.268 and 1.532. The most upstream location corresponded to the region directly beneath the flap suction surface.

The wake flow field obtained for a ride height of $0.247c$ is presented in Figure 5.27(a). Corresponding quantitative data is listed in Table 5.5. For streamwise locations greater than $0.835c$ a dual wake flow field was observed. The velocity deficits within the main element and flap wakes recovered downstream with the entire wake structure moving upwards. Although the upper and lower wake boundaries moved upwards with downstream location the thickness of the main element and flap wakes remained relatively constant. The velocity at the confluence point decreased downstream due to the initial merging of the wakes. The wake profile at $x/c = 0.835$ indicated a single wake, the main element wake. For this situation the thickness of the wake was defined as the vertical distance between the lower wake boundary and the local maximum streamwise velocity above the wake. The main

element wake was thin ($0.07c$) when compared to further downstream measurements ($0.12c$). However the corresponding velocity deficit was larger achieving a minimum streamwise velocity of $0.37U_\infty$. Directly above the main element wake at $x/c = 0.835$ the velocity recovered then decreased again. This feature was a result of the boundary layer on the suction surface of the flap. For all streamwise locations at a ride height of $0.247c$ the effects of the ground boundary layer were not present indicating a thin ground boundary layer.

Figure 5.27(b) presents wake profiles at various streamwise locations for a ride height of $0.099c$. Table 5.6 lists the corresponding quantitative data. As for the higher ride height an upwards movement in wake structure was observed downstream with the flap wake thickness remaining constant. However, the main element wake increased in thickness from $(\delta_{99})_{low} = 0.15c$ to $0.19c$. The profiles at $x/c = 1.532$ indicated a merging of the two wakes into a single large wake. The wake profile at $x/c = 0.853$ again indicated a thin main element wake. The associated velocity deficit however, was increased with a region of zero pitot pressure present in the middle of the wake ($y/c = 0.15$ to 0.16). A thick ground boundary layer was detected at all streamwise locations, increasing in thickness downstream.

5.7 Discussion

The force data obtained at various ride heights indicated the presence of six separate force regions (Figure 5.1). For reasons of clarity the flow field within each force region and corresponding variations with ride height will be individually discussed within this section.

5.7.1 Force Region *a*

Force region *a* occurred at ride heights greater than $0.236c$, i.e. high ride heights. Reductions in ride height caused the downforce, drag and pitching moment to increase asymptotically. Accordingly the wing efficiency also increased asymptotically. The results indicated that two force enhancement mechanisms were present within this force region. The first force enhancement mechanism was related to the geometry of the channel created by the ground plane and the suction surfaces of the wing. The channel beneath the wing resembled a diffuser, albeit of high aspect ratio. The inlet corresponded to the streamwise location of the lowest point on the main element. The exit corresponded to the streamwise location of the flap trailing edge. Considering the ratio between the exit area and inlet area of

the diffuser channel, it is clear that reductions in ride height increased the area ratio. In accordance with continuity the velocity underneath the wing subsequently increased with reductions in ride height. The increased flow acceleration was observed as an increase in the magnitude of the suction peak and suction over the entire wing. The increased suction peak caused the pressure recovery downstream of the suction peak to become more adverse with reductions in ride height. Individually this force enhancement mechanism would have resulted in a linear increase in downforce with ride height reductions.

The second force enhancement mechanism was related to the lower edge vortices. The lower edge vortices were a direct result of the finite pressure difference either side of the endplates. Reductions in ride height increased the magnitude of the pressure difference. Accordingly the strength of the lower edge vortices increased. The lower edge vortices were located directly beneath the suction surface of the flap inboard of the endplates. The suction generated within the lower edge vortices therefore acted upon the flap increasing the suction towards the wing tips. Reductions in ride height caused the pressure recovery beneath the wing to become more adverse. Accordingly dilation of the lower edge vortices was observed with ride height reductions. The force enhancement mechanism generated by the lower edge vortices was non-linear in nature.

The two force enhancement mechanisms (linear and non-linear) within this force region caused the downforce to increase asymptotically with reductions in ride height. The increase in flap loading with ride height reductions was observed as increased values of pitching moment. The drag increased with reductions in ride height, however separation was not present within this force region. Figure 5.28 presents the dependency of drag coefficient on the square of the downforce coefficient. The linear dependency observed within force region a indicated that the increase in drag was due primarily to increases within the lift induced drag.

In addition to variations within the forces, variations were observed within the centre span wake flow field. Within force region a the lower boundary of the main element wake translated downwards with reductions in ride height. The flow directly beneath the flap was separated into two regions by the main element wake. The first region was between the lower boundary of the main element wake and ground plane. The second region was between the upper boundary of the main element wake and the flap suction surface. The increased suction generated by decreasing the ride height therefore acted primarily on the lower boundary of the main element wake, causing the downward movement observed.

5.7.2 Force Region *b*

Within force region *b* ($h/c = 0.236$ to 0.218) the downforce and pitching moment decreased abruptly, whereas the drag remained relatively constant. The surface streaklines indicated no variation in the surface flow field of the wing. The chordwise surface pressures indicated increasing flow acceleration and suction over the main element and flap, as within force region *a*. The cause of the sudden reduction in downforce was indicated within the wing tip flow field. Within force region *a* concentrated lower edge vortices were observed. However, within force region *c* the lower edge vortices were absent, indicating the breakdown of the lower edge vortices within force region *b*.

The increased flow acceleration due to reductions in ride height, caused the pressure recovery beneath the wing to become increasingly adverse. As indicated in Table 5.1 the lower edge vortices dilated between $h/c = 0.317$ and 0.247, an indication of imminent vortex breakdown [148]. Within force region *b* the pressure recovery became too adverse for the lower edge vortices to remain cohesive. Figure 5.29 presents streamwise images at a $z/c = -0.05$. Within force region *a* (Figure 5.29(a)) a stable concentrated vortex core was observed, indicated as a dark region. Figure 5.29(b) presents the same spanwise plane within force region *c*. This variation in the flow structure of the lower edge vortex is more readily observed within the computational version of this thesis. It was noted that the concentrated vortex core was absent, replaced by a chaotic region which was observed to oscillated in a streamwise sense. The bursting of the lower edge vortices were observed in the endplate surface pressures and flap spanwise pressures as a reduction in suction. The bursting of the lower edge vortices within force region *b* caused an abrupt reduction in downforce. The associated decrease in flap loading was observed as an abrupt reduction in pitching moment.

5.7.3 Force Region *c*

Force region *c* occurred between $h/c = 0.218$ and 0.134 within which the downforce increased linearly. The drag and pitching moment also increased, both achieving a global maximum value at $h/c = 0.134$. The lower edge vortices were absent within this force region. However, the chordwise surface pressures indicated increased values of flow acceleration and suction with reductions in ride height, similar to force region *a*. The removal of the second force enhancement mechanism observed within force region *a* caused the downforce

to increased more gradual with reductions in ride height. Although the lower edge vortices were absent the flap loading continued to increase with ride height reductions. Increases in pitching moment were therefore observed. Within this force region the drag coefficient was linearly dependent on the square of the downforce coefficient (Figure 5.28), as in force region *a*. Therefore the drag increases observed were primarily a result of increases in lift induced drag.

Within force regions *a* and *b* the lower boundary of the main element wake moved downwards with reductions in ride height. This variation in wake flow field with ride height was also observed within force region *c*.

5.7.4 Force Region *d*

Within force region *d* ($h/c = 0.134$ to 0.081) reductions in ride height caused the downforce to remain constant, whereas the drag and pitching moment decreased. The chordwise surface pressures indicated increased flow acceleration beneath the wing, as for the previous force regions. Reducing the ride height within force region *d* caused the sectional downforce on the main element to increase. Simultaneously the sectional downforce on the flap decreased (Figure 5.21(a)). The wake profile obtained beneath the flap for a ride height of $0.099c$ (Figure 5.27(b)) indicated a region of zero pitot pressure within the centre of the main element wake. This region of zero velocity within the main element wake was due to the pressure recovery beneath the wing becoming too adverse. The suction on the flap accordingly decreased causing the pitching moment to also decrease. The simultaneous increase in main element downforce and decrease in flap downforce caused the total downforce (C_L) to become independent of ride height. The reduction in drag with decreases in ride height was due to the decrease in lift induced drag.

Similar phenomena of flow reversal within the main element wake were reported by Petrov [61, 62] and Drela [63] using aeronautical multi-element wings. However neither quantitatively proved the effect of wake dilation on the forces generated. The results obtained within this research clearly indicated that the primary lift limiting mechanism of a multi-element wing in ground effect is the dilation of the main element wake with the coincidental presence of a region of zero pitot pressure. This finding is novel to this research.

5.7.5 Force Region *e*

Force region *e* occurred at the lowest ride heights ($h/c = 0.081$ to 0.039) for the case with decreasing ride height. Within this force region the downforce, drag and pitching moment decreased with reductions in ride height. The surface flow field (Figure 5.14) indicated that the main element had stalled, observed as a region of separation at the main element trailing edge. The centre span surface pressures indicated a rapid pressure recovery along the main element. Seemingly the rate of pressure recovery was too adverse causing the boundary layer on the main element suction surface to separate. The gradual stall of the main element was most clearly indicated within the downforce. Within this force region the flap loading decreased in conjunction with the total downforce. Accordingly decreases in pitching moment were observed with reductions in ride height.

Within force region *e* the chordwise surface pressure distributions on the main element were significantly different to those observed for higher ride heights. The surface pressures indicated flow behaviour similar to that observed within a diffuser in ground effect. The suction peak on the main element translated downstream to the throat of the channel beneath the wing (Figure 3.1). In addition transition on main element became more uniform across the span of the wing, occurring at a more downstream location. It is surmised that for the lowest ride heights the suction beneath the wing was of great enough magnitude to cause the wing to act similarly to a diffuser of high aspect ratio. This behaviour was also noted within force region *f*.

5.7.6 Force Region *f*

Force region *f* existed over the same ride heights as force region *e*. However force region *f* was observed with increasing ride heights. The downforce obtained within force region *f* was significantly reduced when compared to force region *e*. The surface flow field data (Figures 5.15 and 5.16) indicated the cause. Within force region *f* a large region of separation was observed on the flap suction surface, which was not present within force region *e*. Accordingly the downforce was significantly reduced. The stalling of the flap was also observed within the wake flow field (Figure 5.26(b)). A dual wake structure was observed within force region *e*. However a large single wake was noted within force region *f* corresponding to the regions of separation on the main element and flap merging.

It was noted that the forces obtained for a single static ride height below 0.081c always

reverted to the force values corresponding to region *f*. In addition force region *f* was only present when the ride height was first increased then decreased. The stalling of the flap was attributed to the run-up stage of the wind tunnel, in particular the Reynolds number variation. During the run-up stage of the wind tunnel the wing was subjected to a range of increasing Reynolds numbers. The boundary layers on the suction surfaces of the wing were therefore more prone to separate at lower velocities, as observed on the flap. Once the flap had stalled the region of separation persisted to the higher Reynolds numbers. A similar stall persistence is observed within the stalling of aeronautical wings [4–6].

Within all previous research [9, 96] force region *f* has been detected. However force region *e* has not been previously reported due to the static nature of the experimental test rigs. Since the ride height of the wing was continuously varied in this research the dependency of the forces on the ride height direction could be detected. The dependency of the forces generated by a multi-element wing in ground effect on ride height direction is a novel finding. The main implication of this finding is that care must be taken when testing a multi-element wing at a static ride height. In addition poor agreement between computational results and experimental measurements may be observed due to the lack of the run-up stage within numerical methods.

5.8 Chapter Summary

A systematic experimental investigation into a multi-element wing in ground effect was conducted. The influence of ride height on the performance of the wing was quantified. In addition the flow field mechanisms responsible for the performance variation were identified. The maximum downforce, drag and pitching moment was found to be limited by a region of zero pitot pressure within the main element wake beneath the flap suction surface. At low ride heights the downforce was found to be dependent on the direction of ride height variation due to separation over the flap.

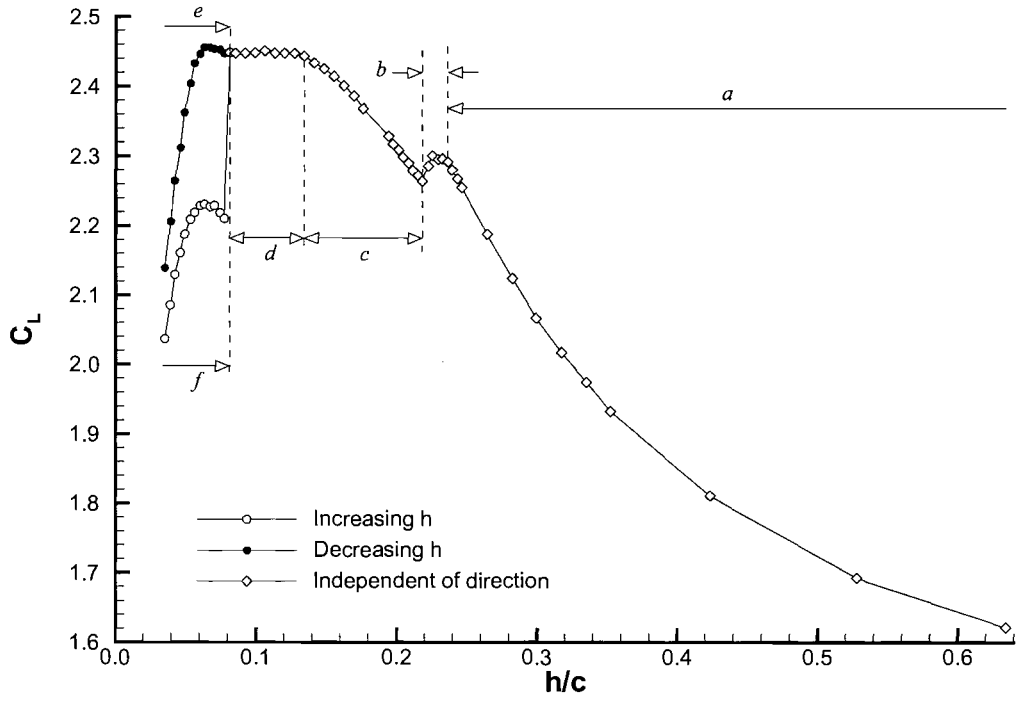

Figure 5.1: Variation of downforce coefficient with ride height.

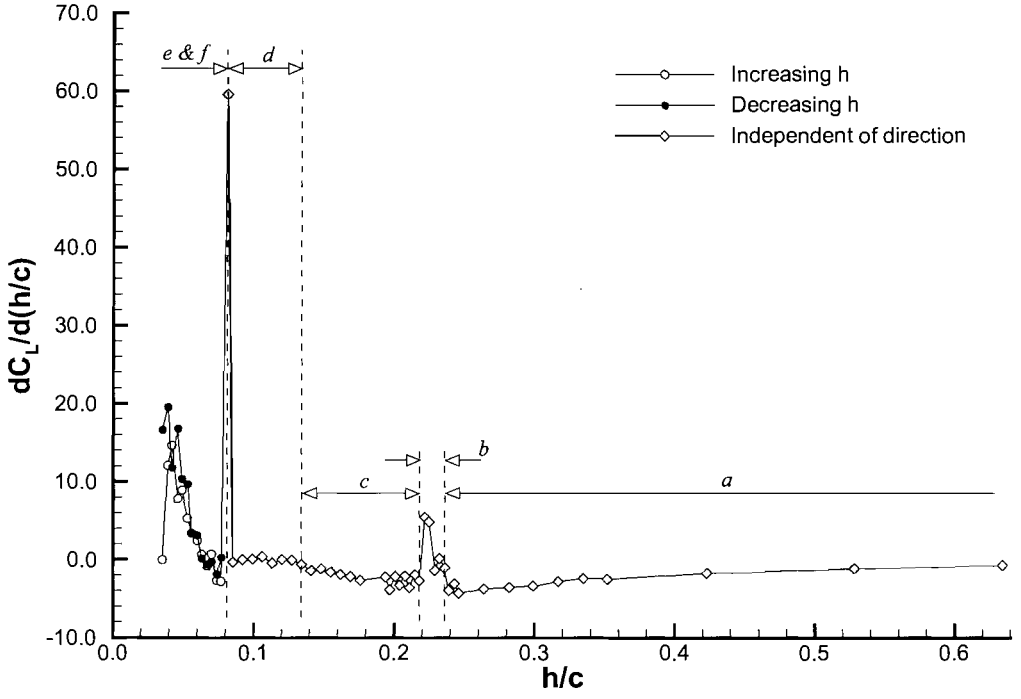

Figure 5.2: Variation of downforce slope with ride height and definition of the force regions.

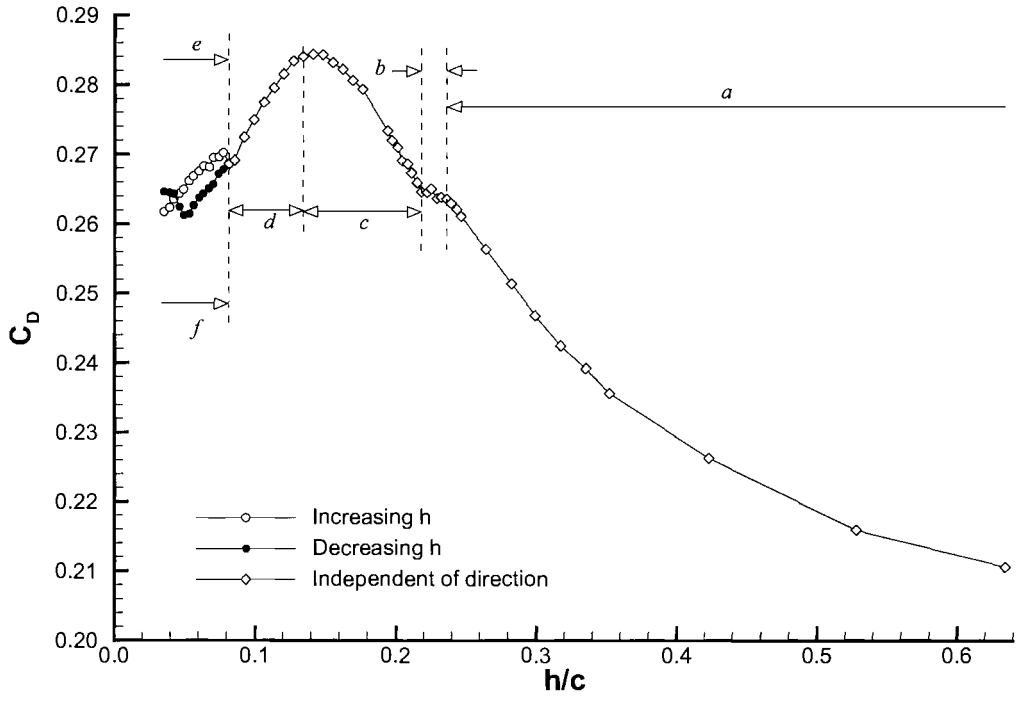

Figure 5.3: Variation of drag coefficient with ride height.

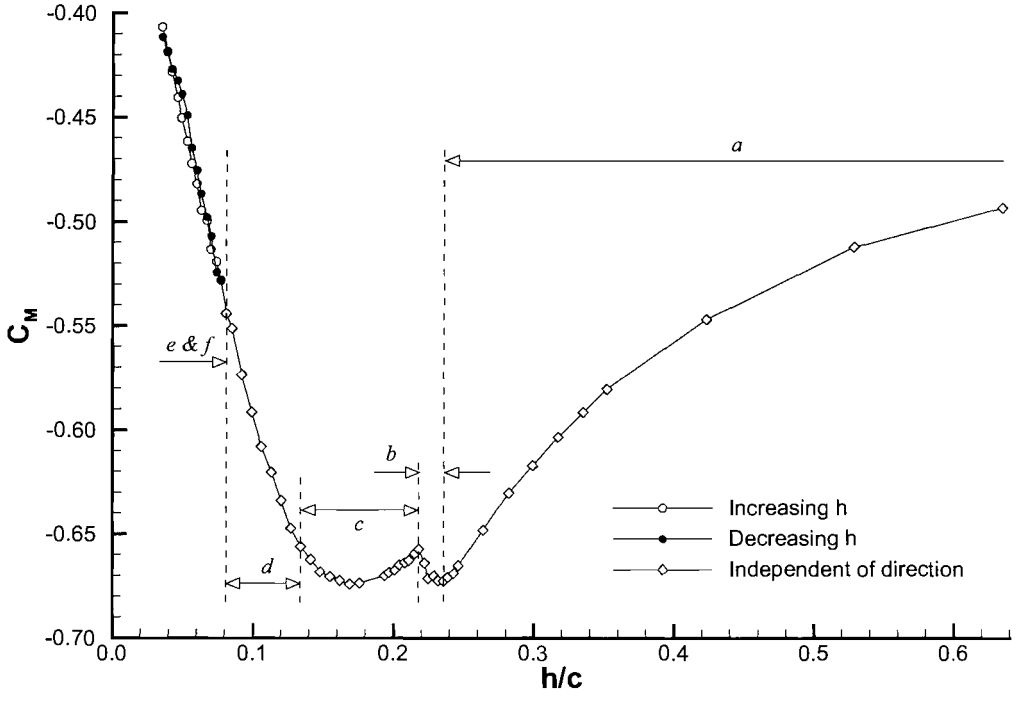

Figure 5.4: Variation of pitching moment coefficient with ride height.

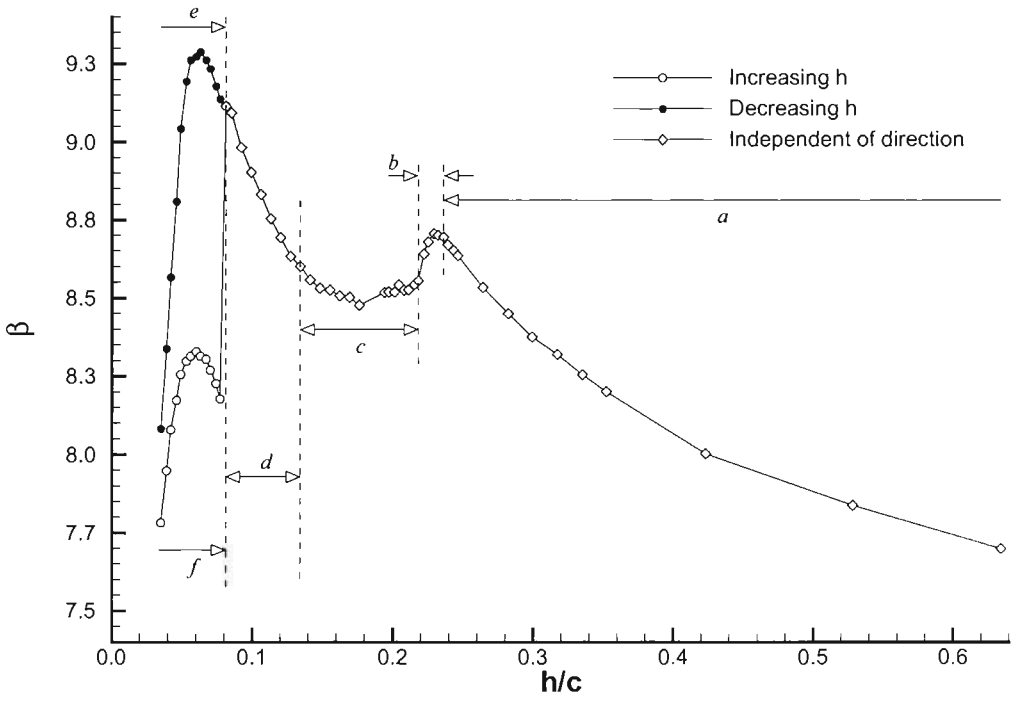

Figure 5.5: Variation of wing efficiency with ride height.

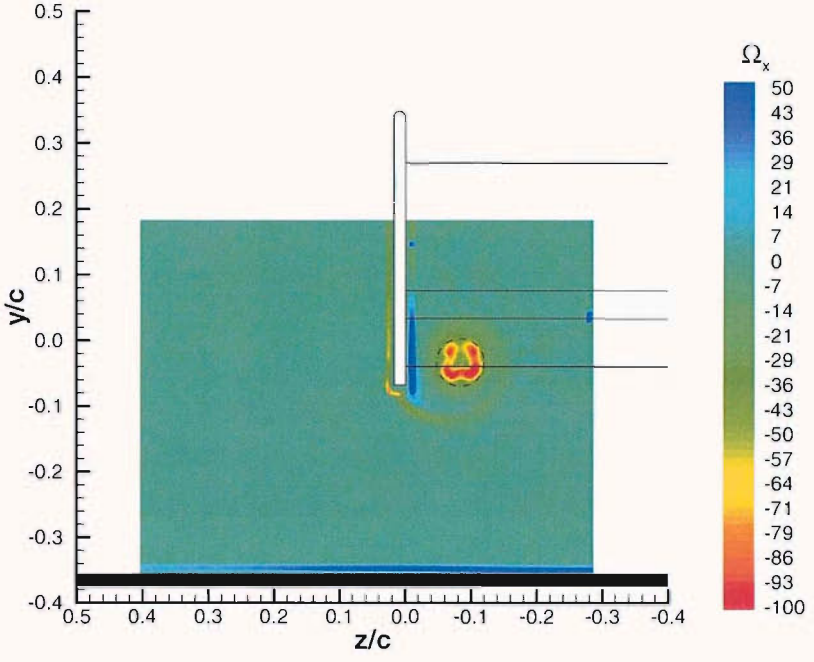

(a)

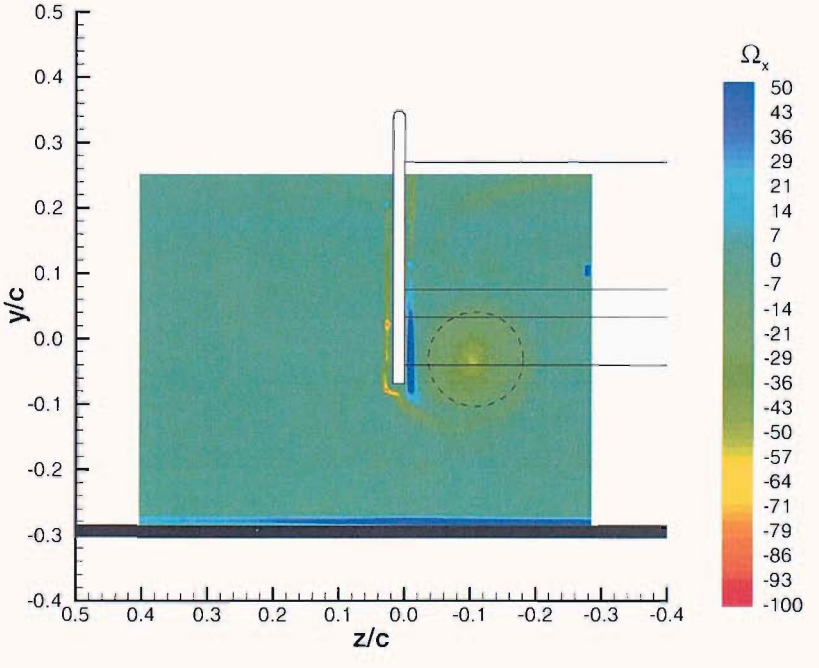

(b)

Figure 5.6: Time-averaged non-dimensional vorticity contours of the port wing tip at $x/c = 0.995$; (a) $h/c = 0.317$ (region a), (b) $h/c = 0.247$ (region a/b boundary).

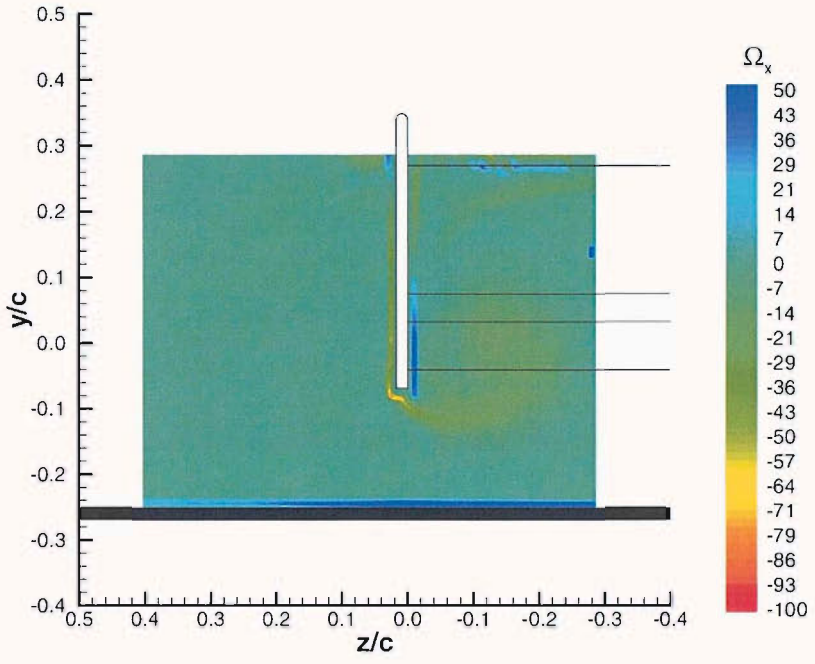

(a)

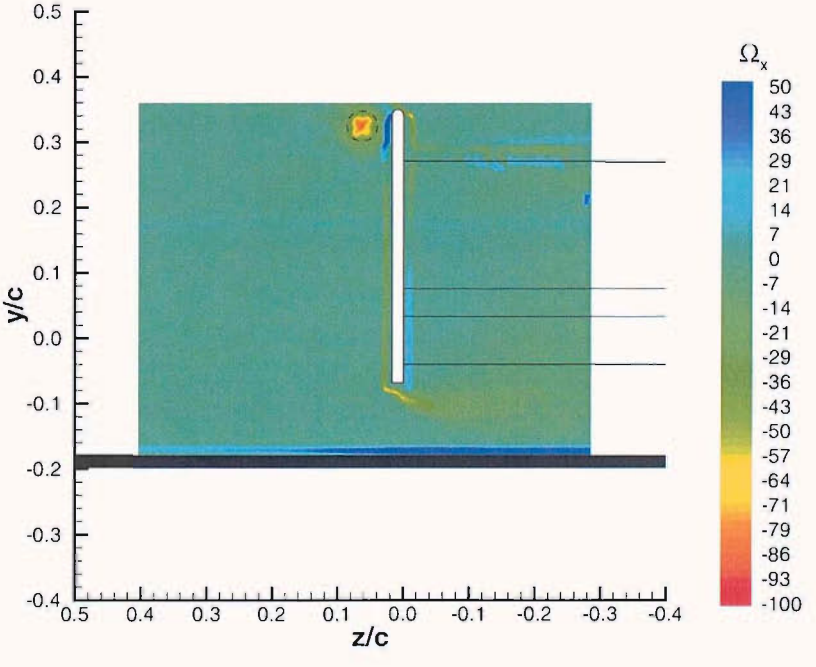

(b)

Figure 5.7: Time-averaged non-dimensional vorticity contours of the port wing tip at $x/c = 0.995$; (a) $h/c = 0.211$ (region b/c boundary), (b) $h/c = 0.141$ (region c/d boundary).

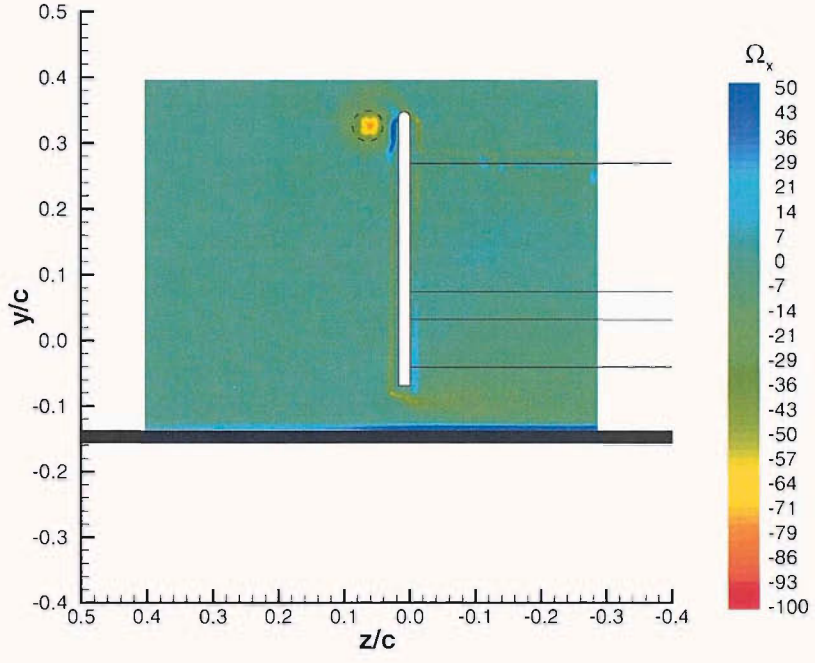

(a)

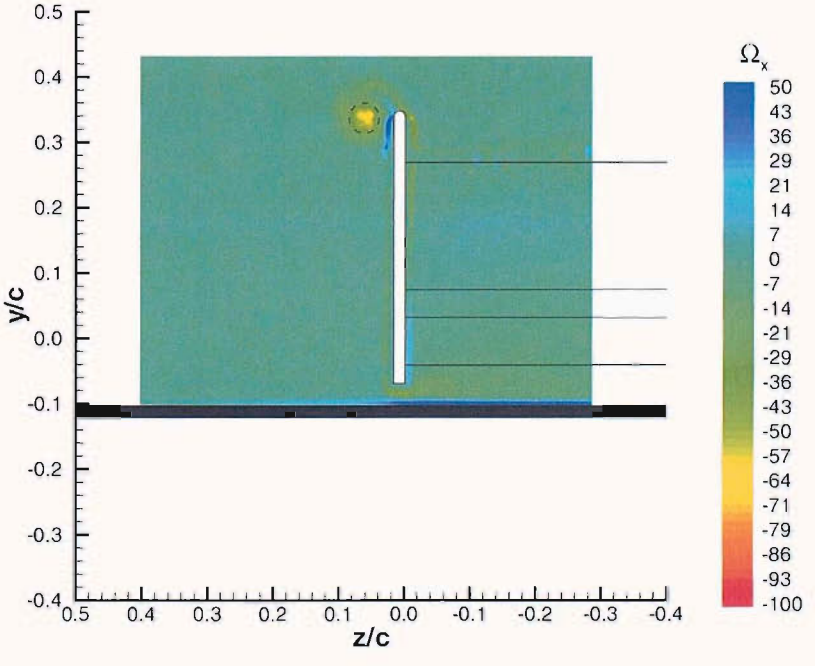

(b)

Figure 5.8: Time-averaged non-dimensional vorticity contours of the port wing tip at $x/c = 0.995$; (a) $h/c = 0.099$ (region d), (b) $h/c = 0.063$, decreasing h (region e).

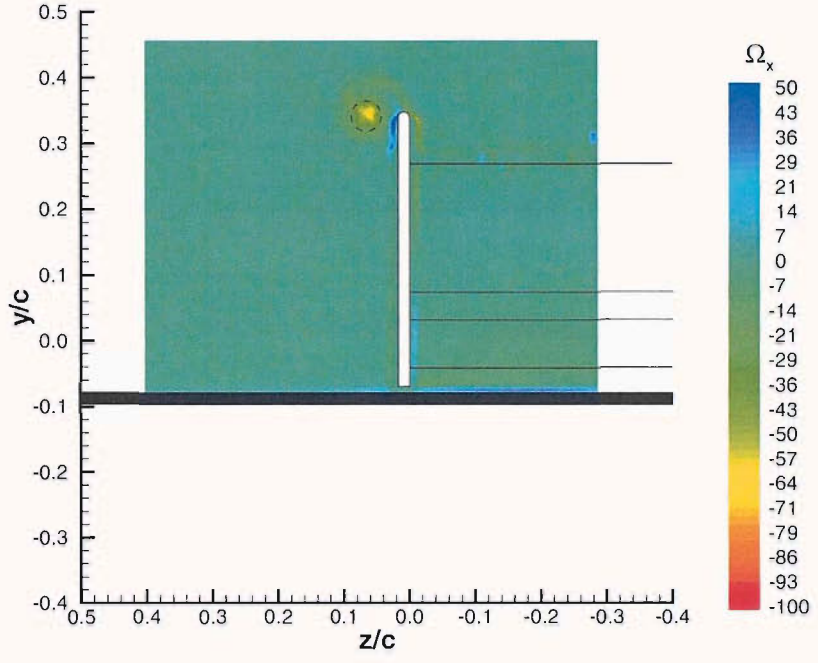

(a)

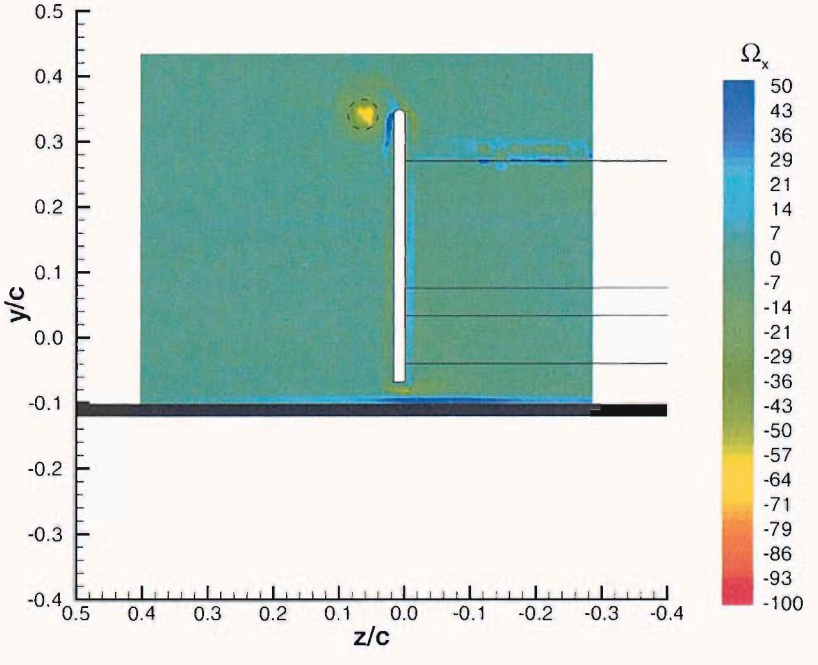

(b)

Figure 5.9: Time-averaged non-dimensional vorticity contours of the port wing tip at $x/c = 0.995$: (a) $h/c = 0.039$, decreasing h (region e). (b) $h/c = 0.063$, increasing h (region f).

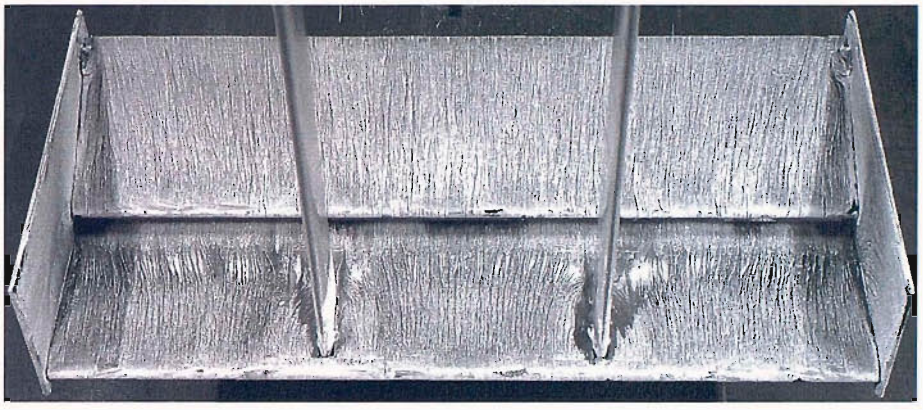

(a) Pressure surface of the wing (leading edge lowest most).

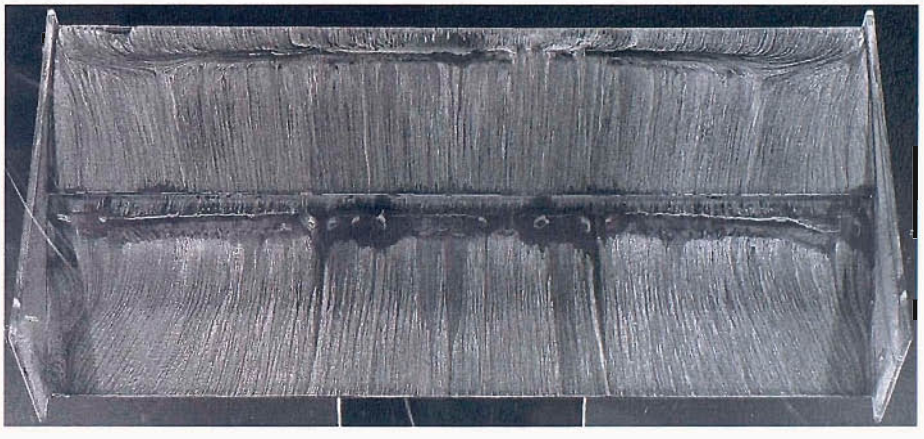

(b) Suction surface of the wing (leading edge upper most).

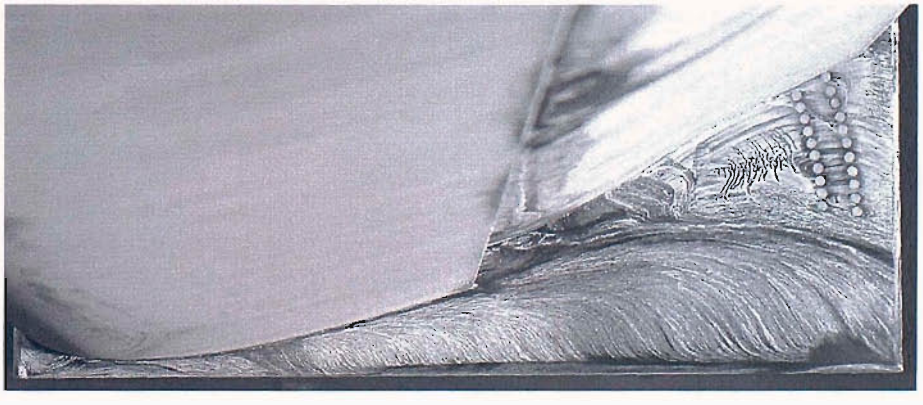

(c) Inboard surface of starboard endplate beneath the suction surfaces of the wing (flow from left to right).

Figure 5.10: Surface streaklines obtained at h/c=0.317 (region a).

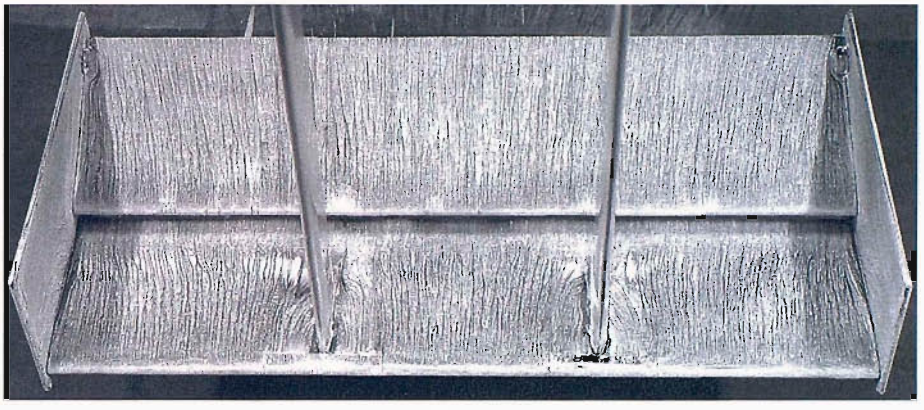

(a) Pressure surface of the wing (leading edge lowest most).

(b) Suction surface of the wing (leading edge upper most).

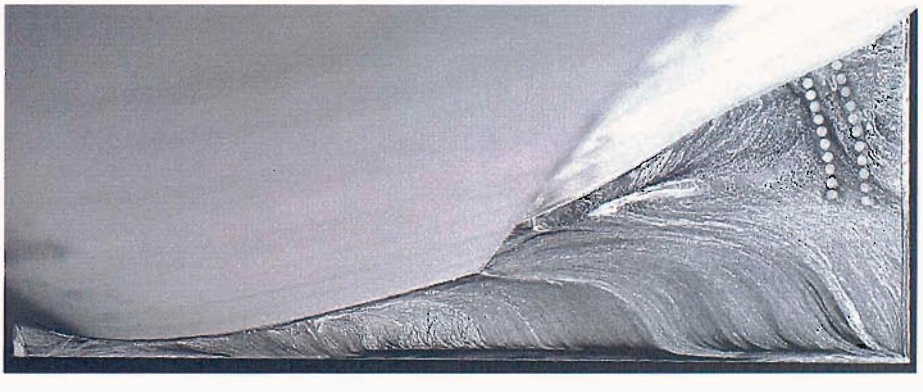

(c) Inboard surface of starboard endplate beneath the suction surfaces of the wing (flow from left to right).

Figure 5.11: Surface streaklines obtained at h/c=0.247 (region a/b boundary).

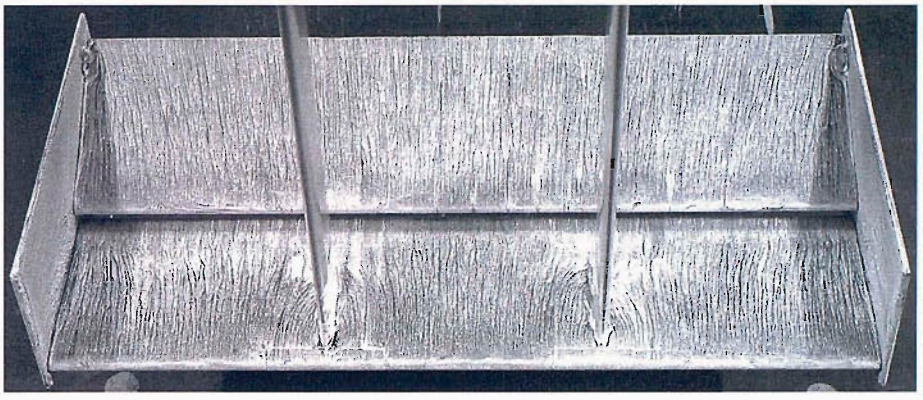

(a) Pressure surface of the wing (leading edge lowest most).

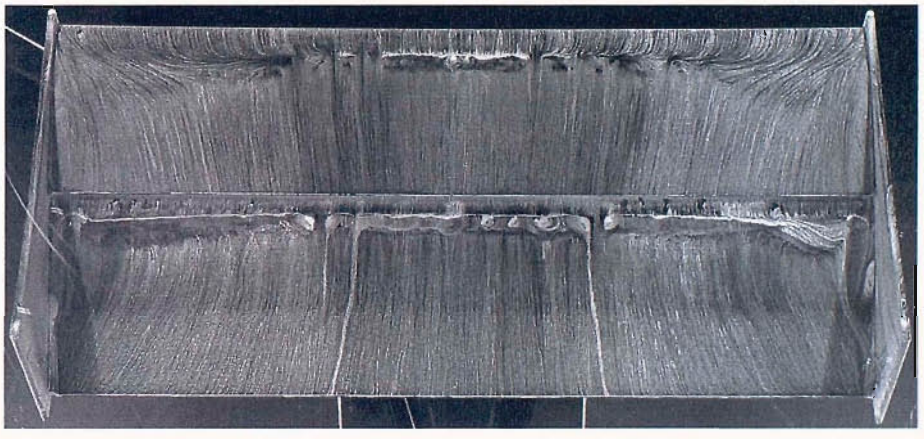

(b) Suction surface of the wing (leading edge upper most).

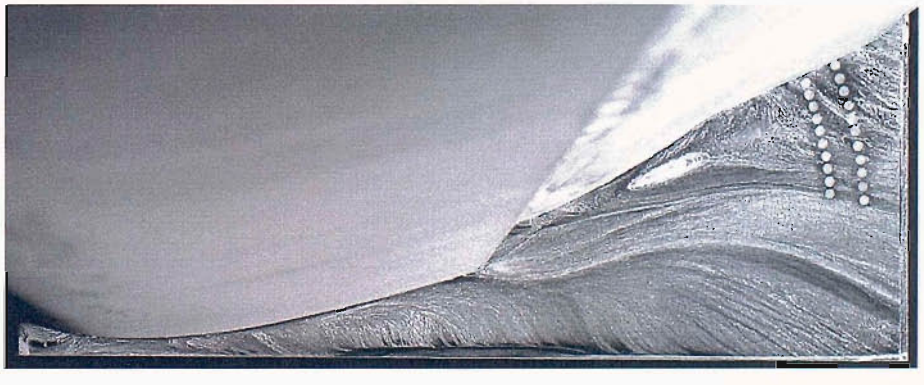

(c) Inboard surface of starboard endplate beneath the suction surfaces of the wing (flow from left to right).

Figure 5.12: Surface streaklines obtained at h/c=0.211 (region b/c boundary).

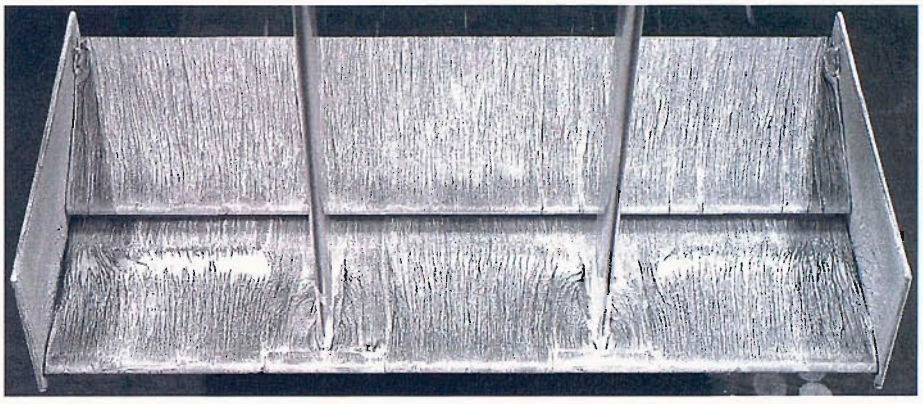

(a) Pressure surface of the wing (leading edge lowest most).

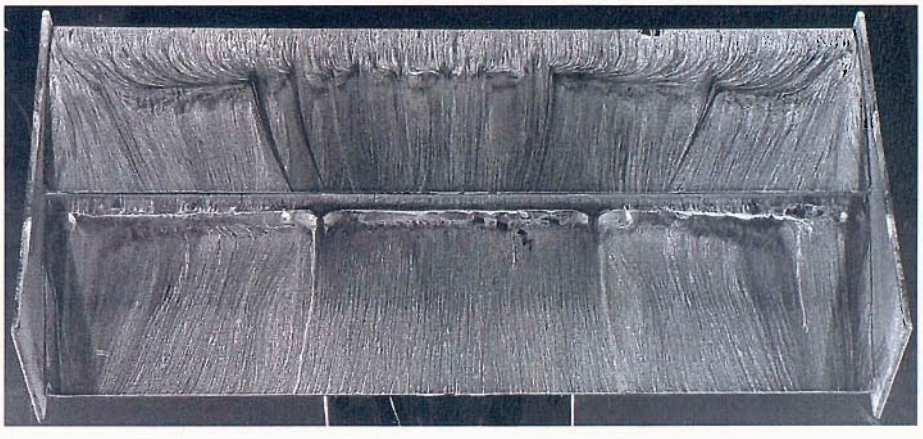

(b) Suction surface of the wing (leading edge upper most).

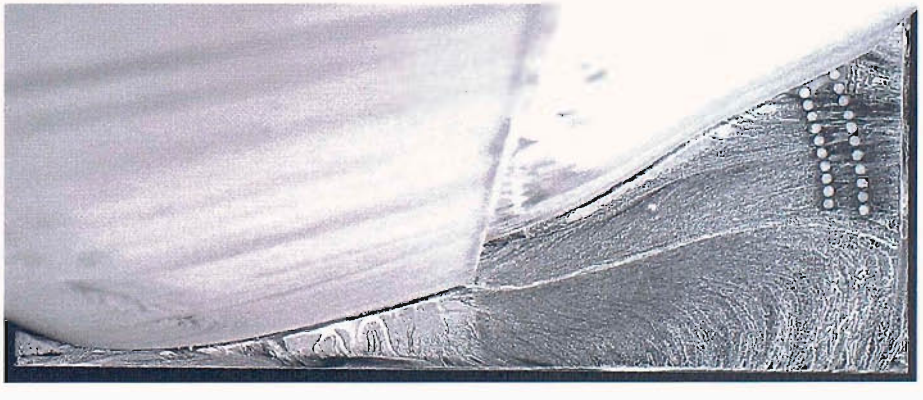

(c) Inboard surface of starboard endplate beneath the suction surfaces of the wing (flow from left to right).

Figure 5.13: Surface streaklines obtained at h/c=0.099 (region d).

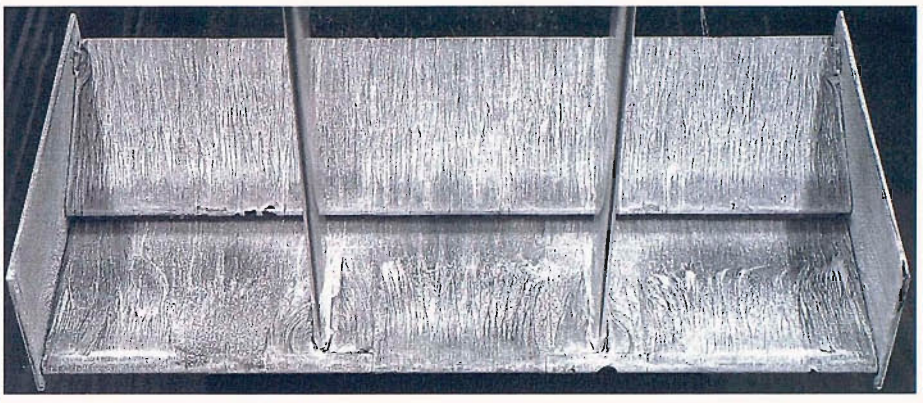

(a) Pressure surface of the wing (leading edge lowest most).

(b) Suction surface of the wing (leading edge upper most).

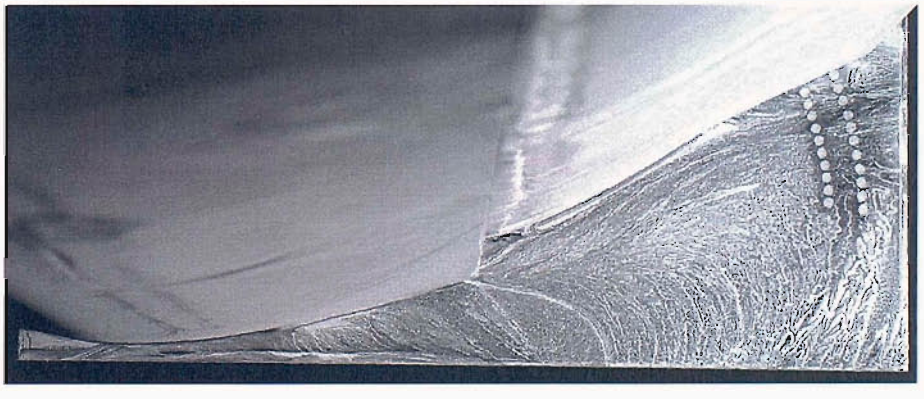

(c) Inboard surface of starboard endplate beneath the suction surfaces of the wing (flow from left to right).

Figure 5.14: Surface streaklines obtained at h/c=0.063, decreasing h (region e).

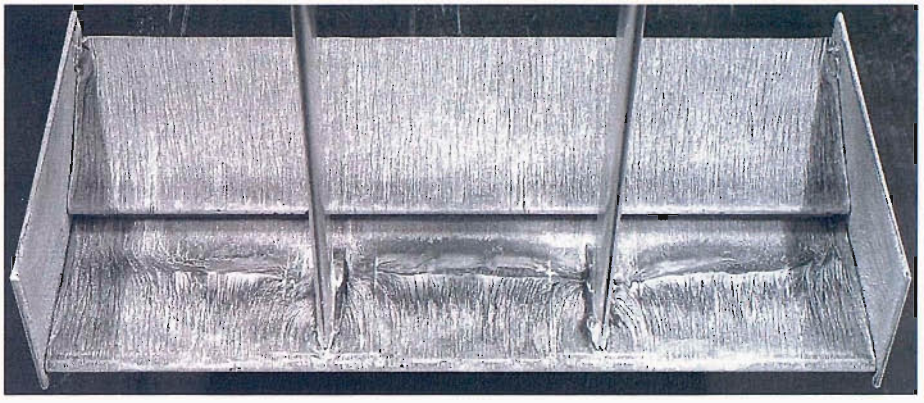

(a) Pressure surface of the wing (leading edge lowest most).

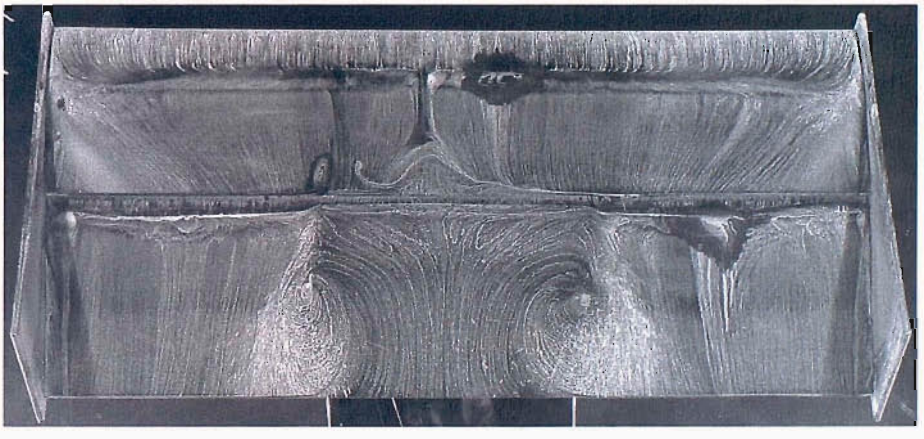

(b) Suction surface of the wing (leading edge upper most).

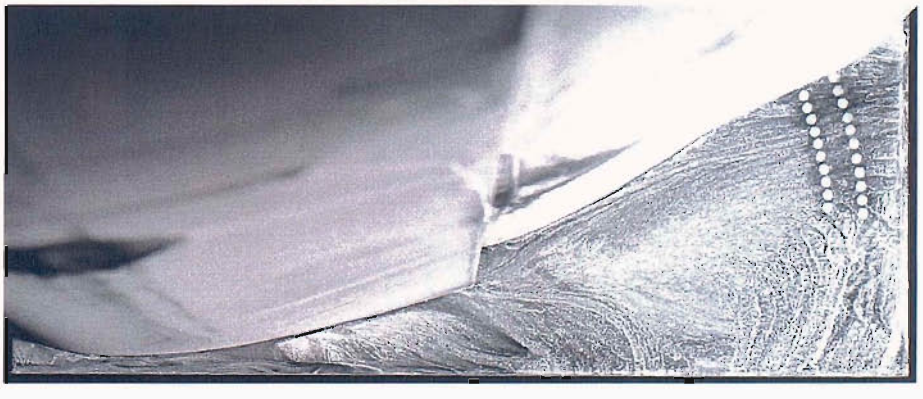

(c) Inboard surface of starboard endplate beneath the suction surfaces of the wing (flow from left to right).

Figure 5.15: Surface streaklines obtained at h/c=0.063, increasing h (region f).

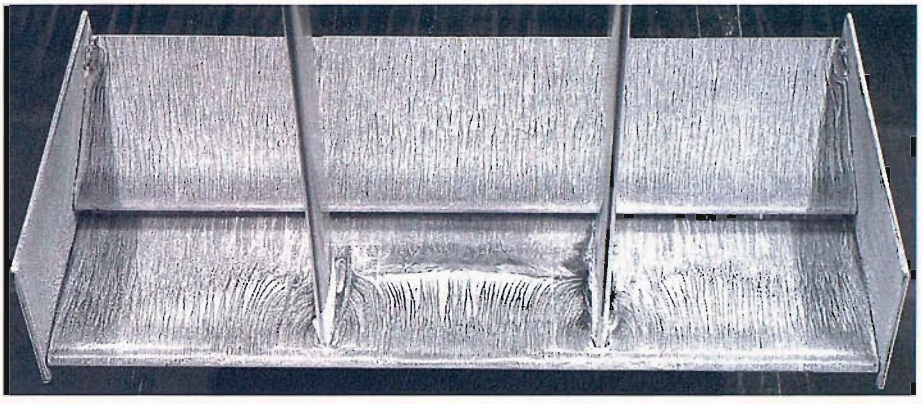

(a) Pressure surface of the wing (leading edge lowest most).

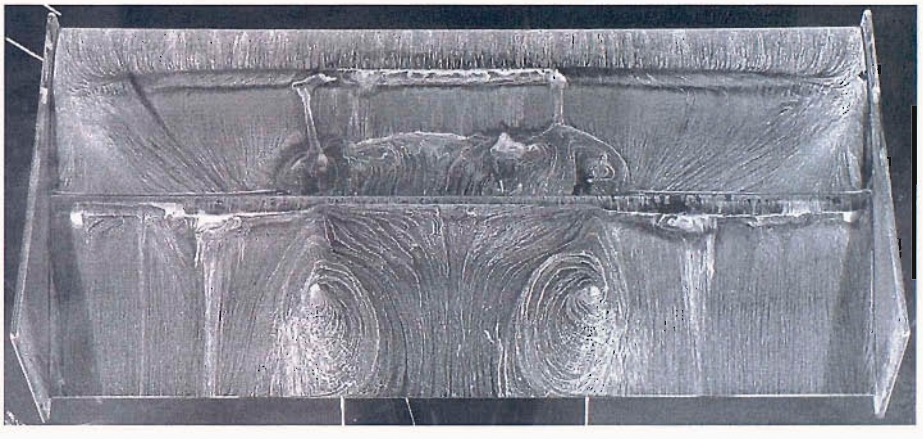

(b) Suction surface of the wing (leading edge upper most).

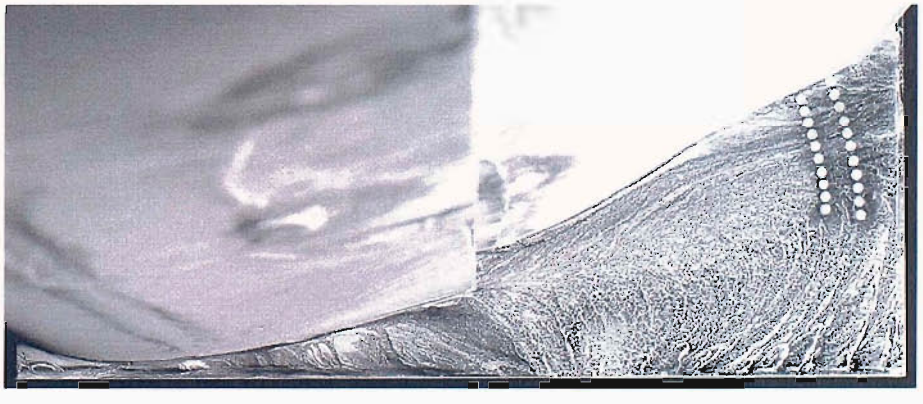

(c) Inboard surface of starboard endplate beneath the suction surfaces of the wing (flow from left to right).

Figure 5.16: Surface streaklines obtained at h/c=0.039, increasing h (region f).

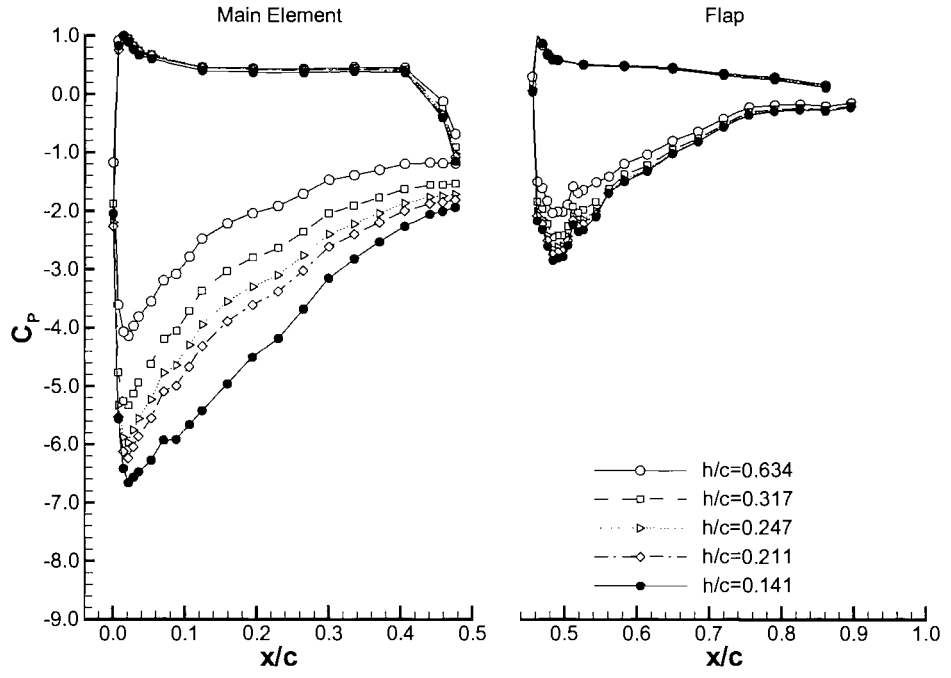

(a)

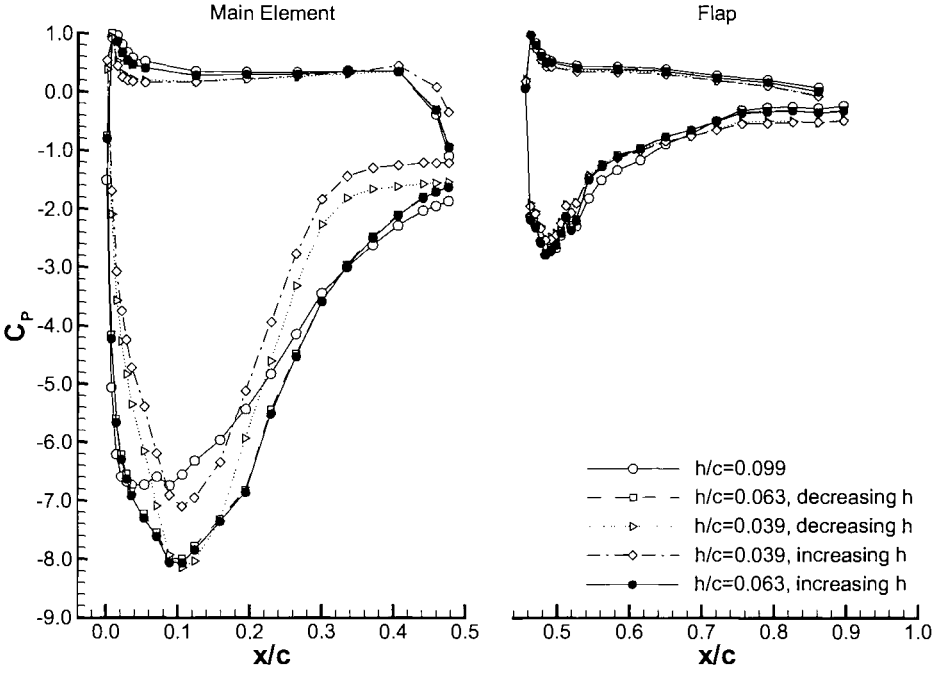

(b)

Figure 5.17: Chordwise surface pressures at wing centre span; (a) high ride heights, (b) low ride heights.

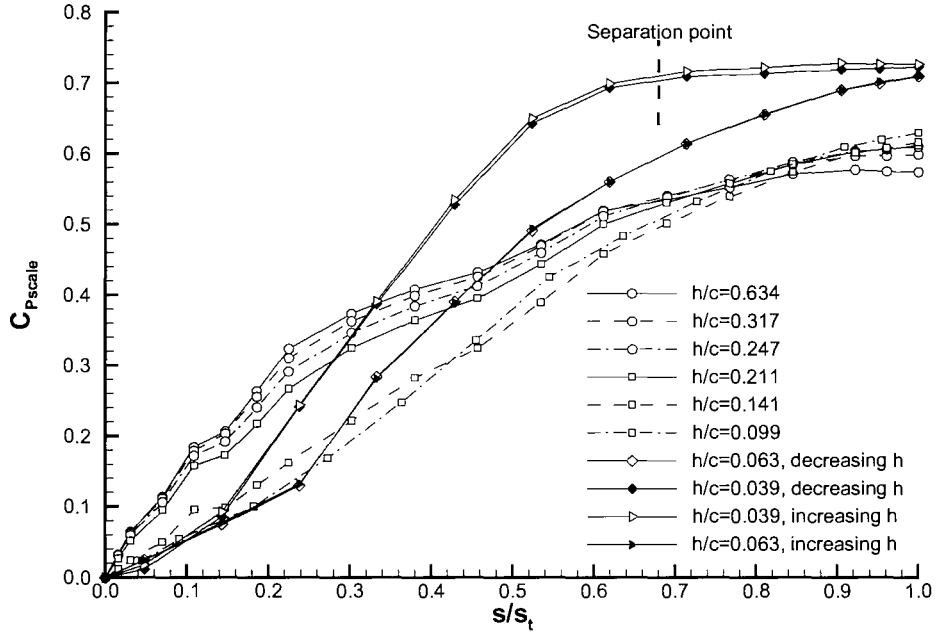

(a)

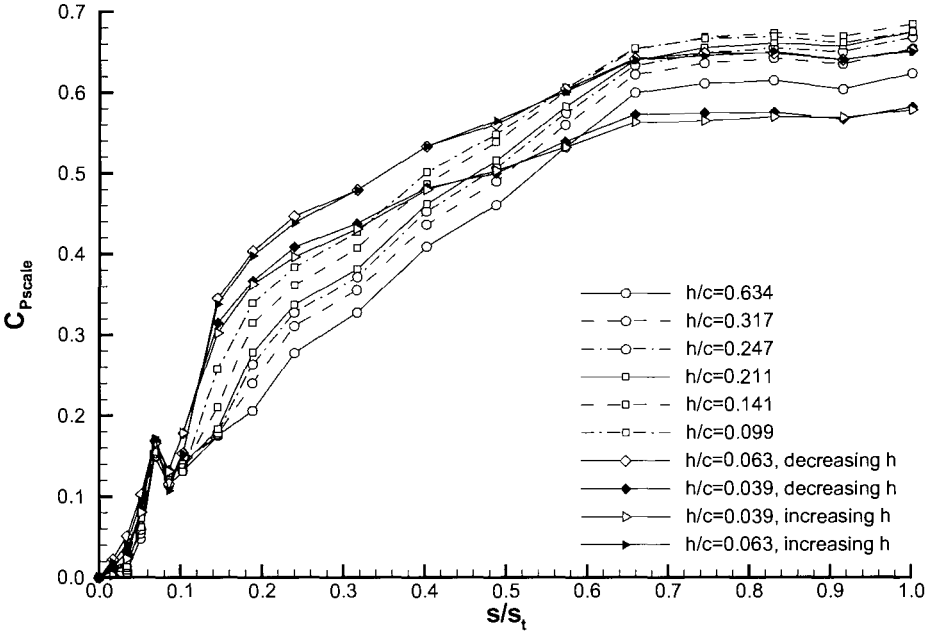

(b)

Figure 5.18: Scaled centre span suction surface pressures; (a) main element, (b) flap.

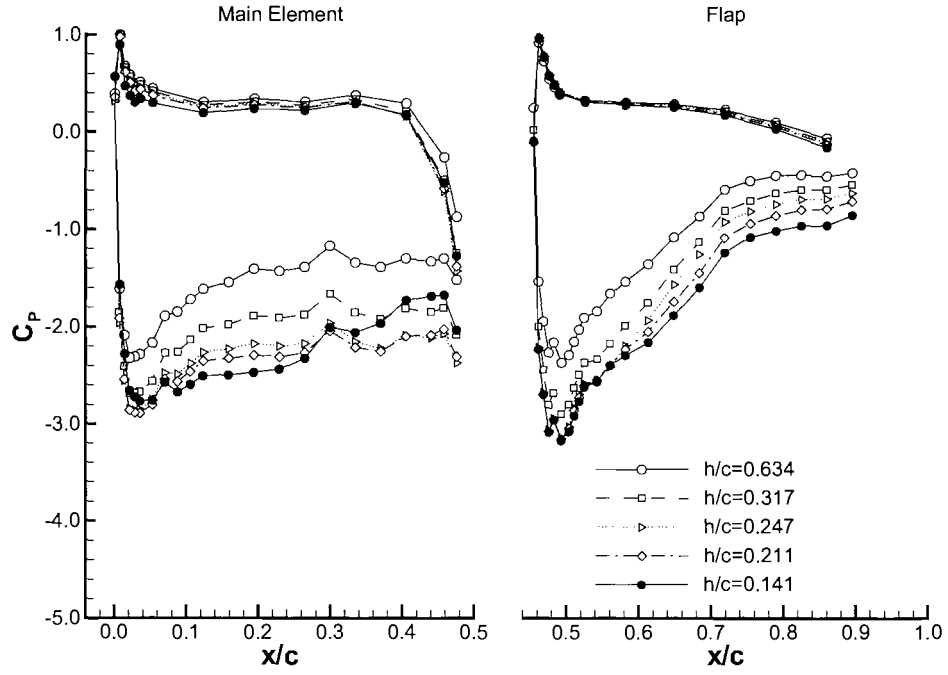

(a)

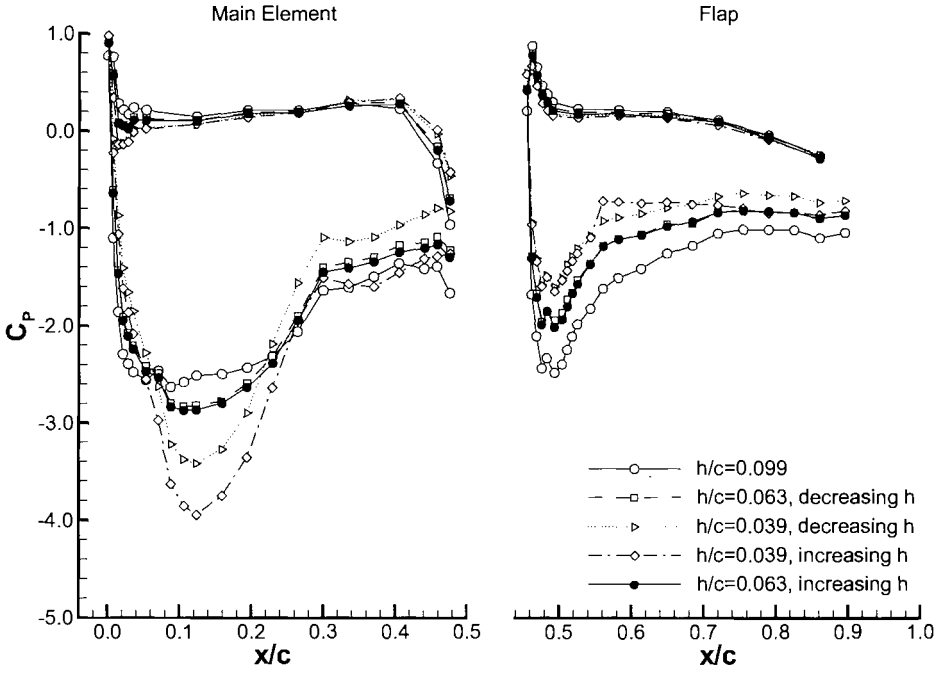

(b)

Figure 5.19: Chordwise surface pressures near port wing tip, $z/c = -0.088$; (a) high ride heights, (b) low ride heights.

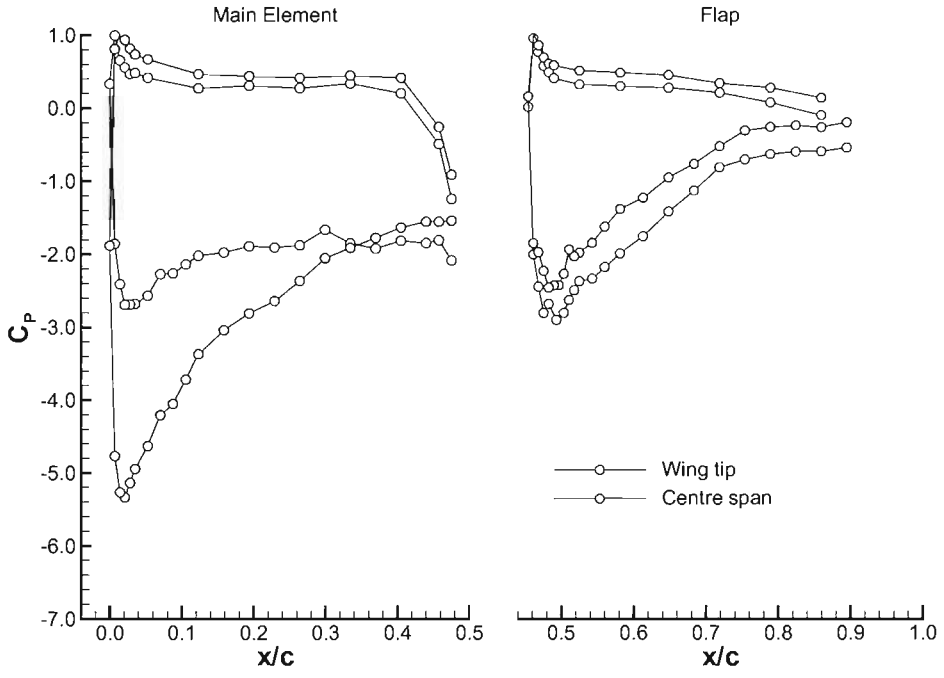

(a)

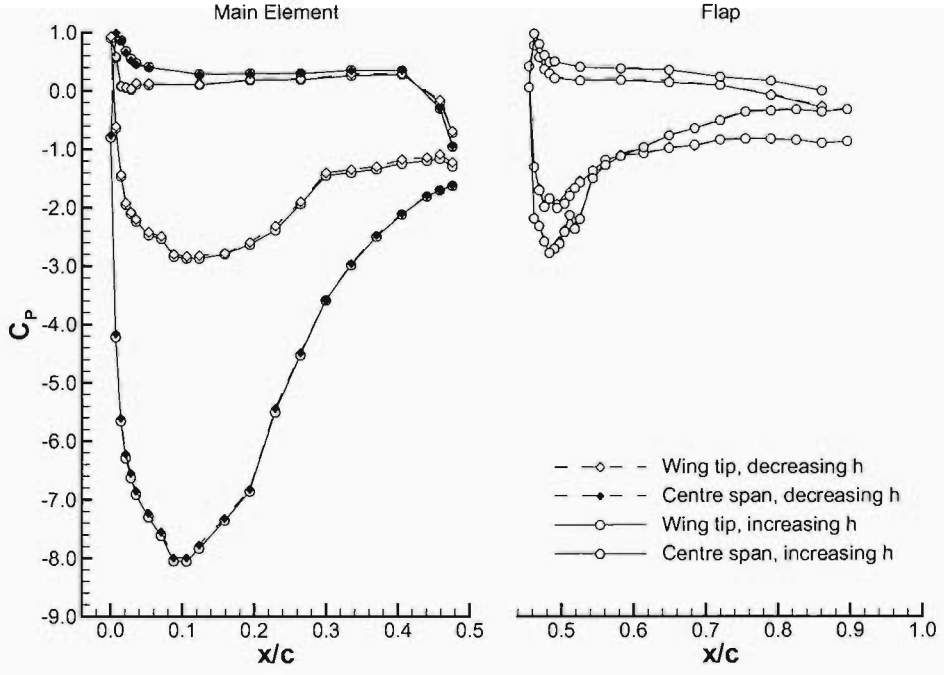

(b)

Figure 5.20: Chordwise surface pressures at centre span and port wing tip; (a) $h/c = 0.317$ (region a), (b) $h/c = 0.063$ increasing h and decreasing h (regions e & f).

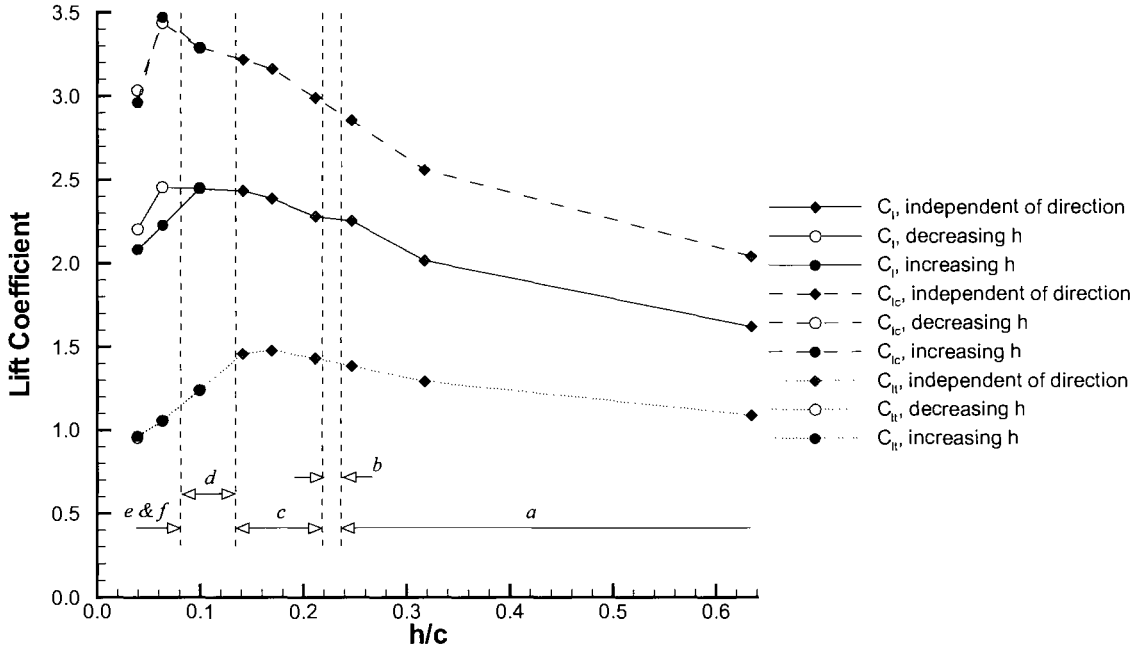

(a)

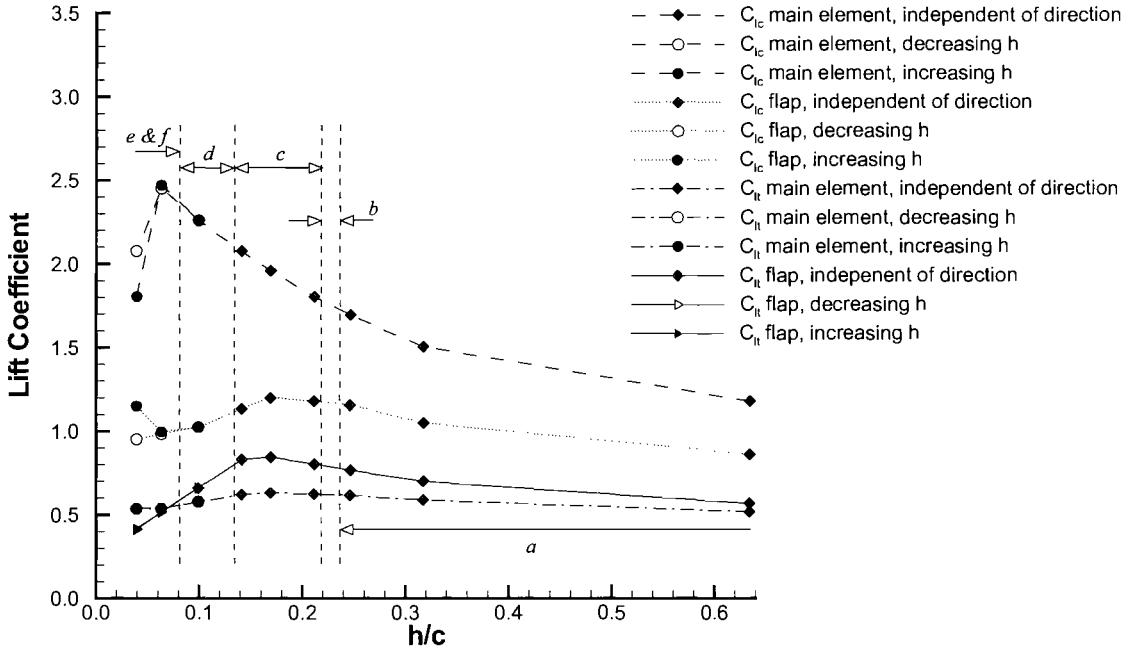

(b)

Figure 5.21: Integrated surface pressures for various ride heights; (a) total downforce at centre span and wing tip, (b) downforce due to main element and flap.

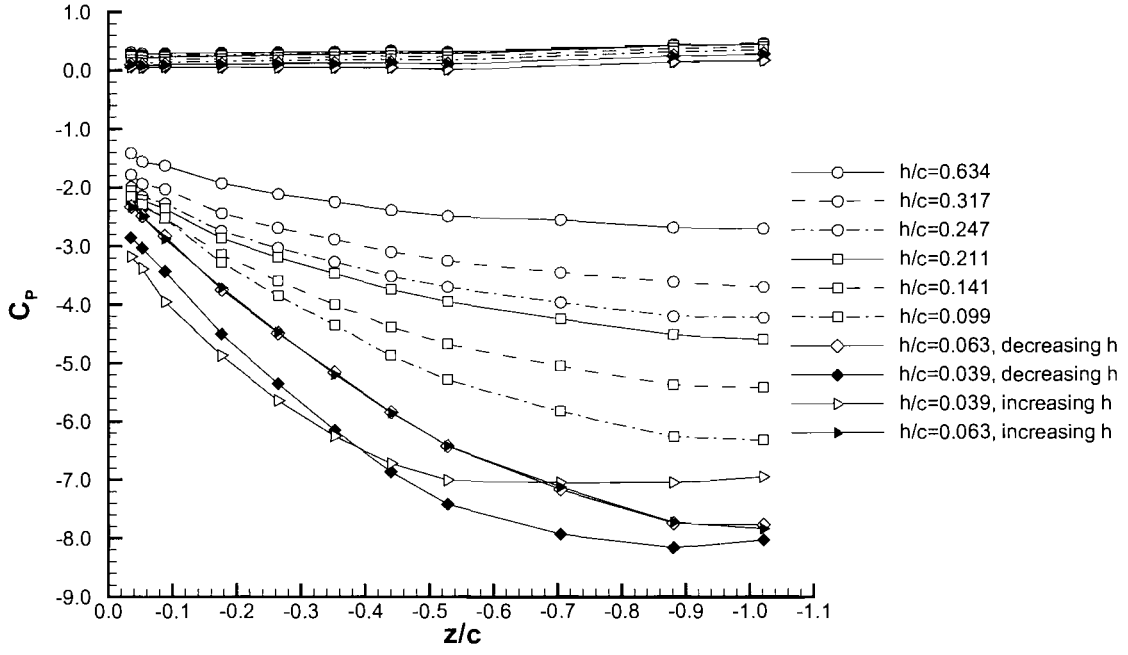

Figure 5.22: Spanwise surface pressure distribution on the main element for various ride heights; $x/c = 0.123$.

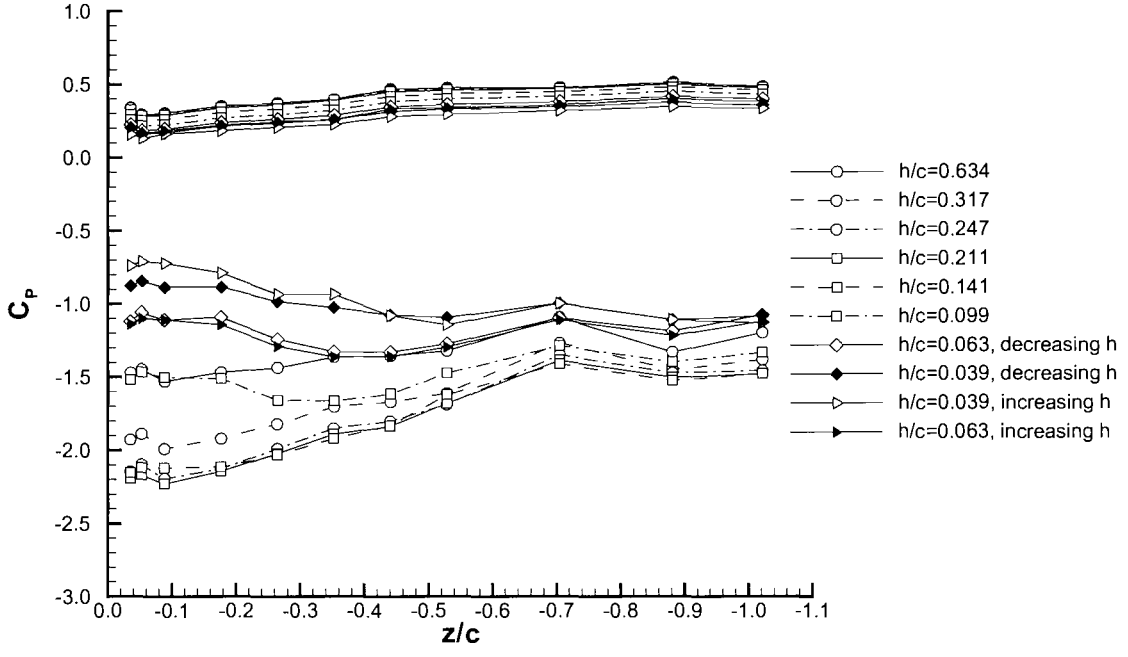

Figure 5.23: Spanwise surface pressure distribution on the flap for various ride heights; $x_f/c = 0.127$.

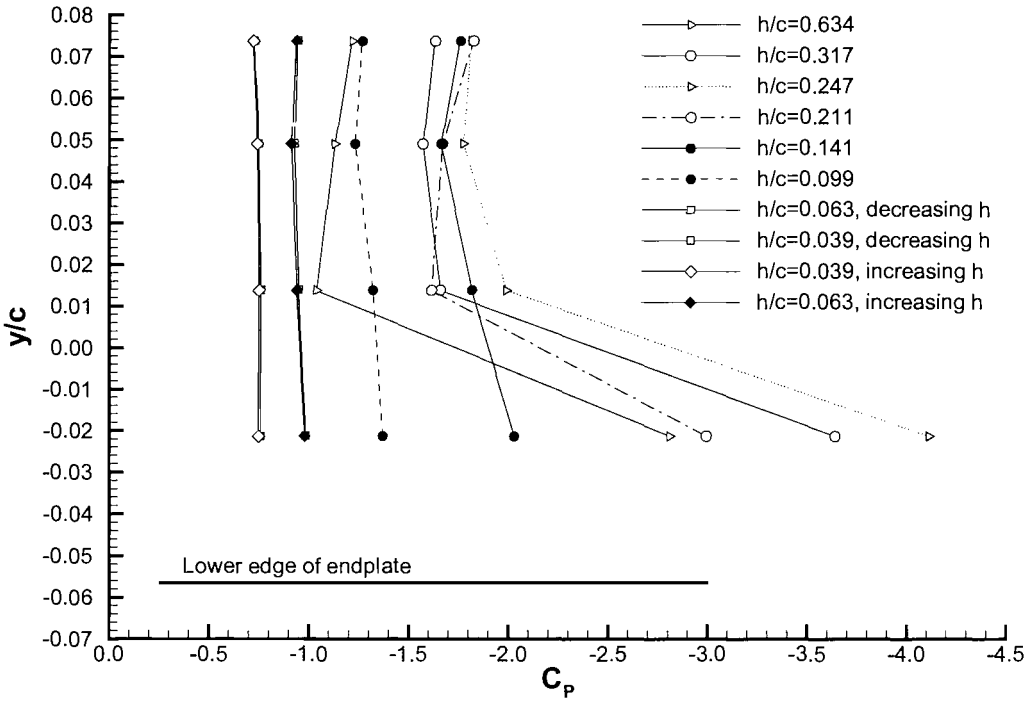

Figure 5.24: Surface pressure distribution on the inboard side of the port endplate for various ride heights; $x/c = 0.614$.

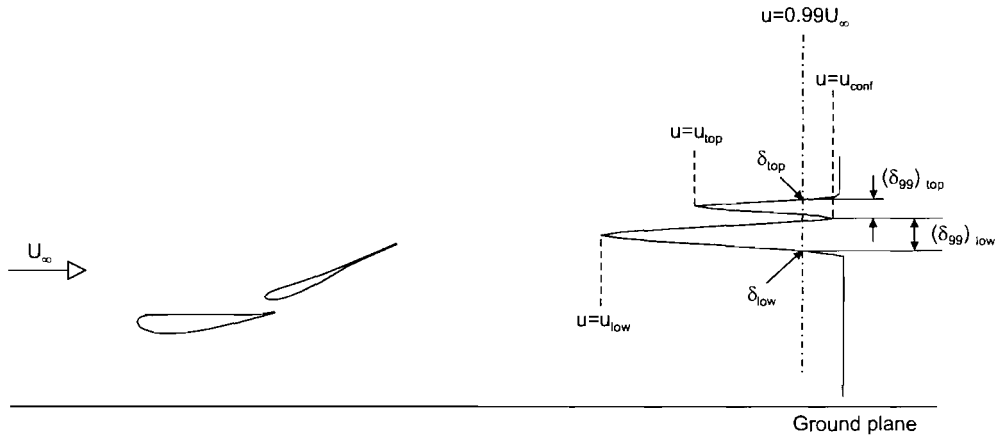

Figure 5.25: Definition of the variables used to describe the wake flow field.

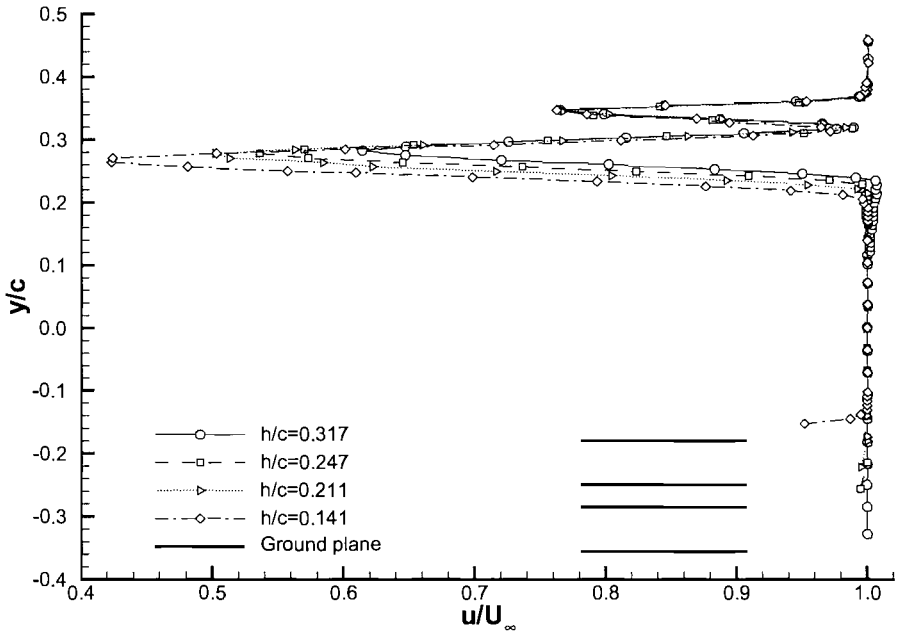

(a)

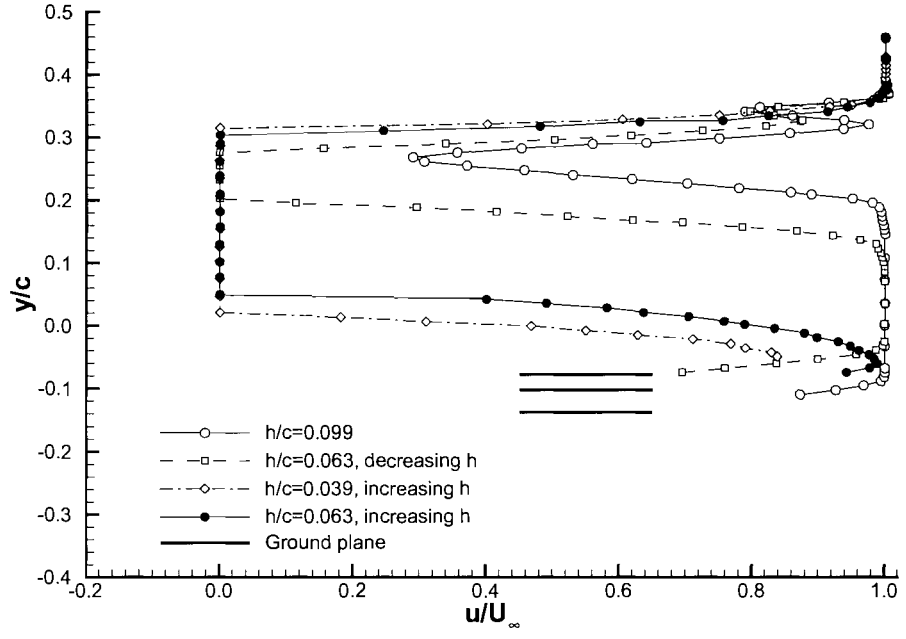

(b)

Figure 5.26: Non-dimensional wake profiles for various ride heights at $x/c = 1.127$, $z/c = -1.021$; (a) high ride heights, (b) low ride heights.

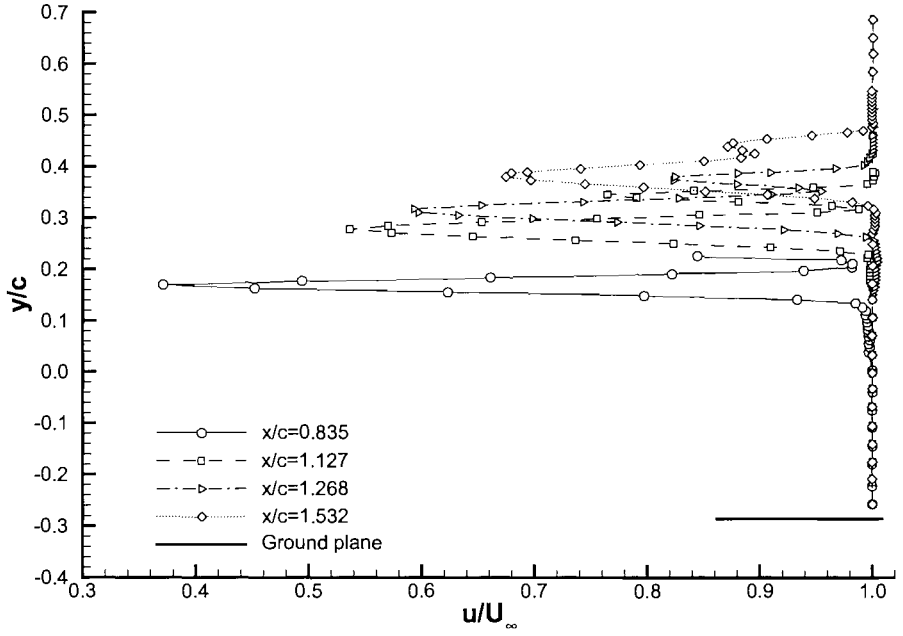

(a)

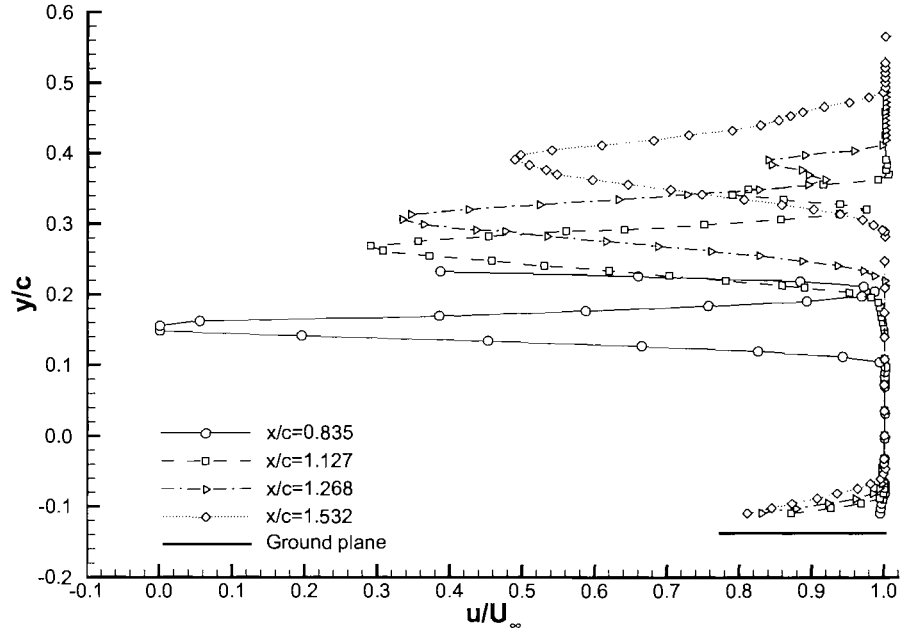

(b)

Figure 5.27: Non-dimensional wake profiles at various streamwise locations, $z/c = -1.021$; (a) $h/c = 0.247$ (region a/b boundary), (b) $h/c = 0.099$ (region d).

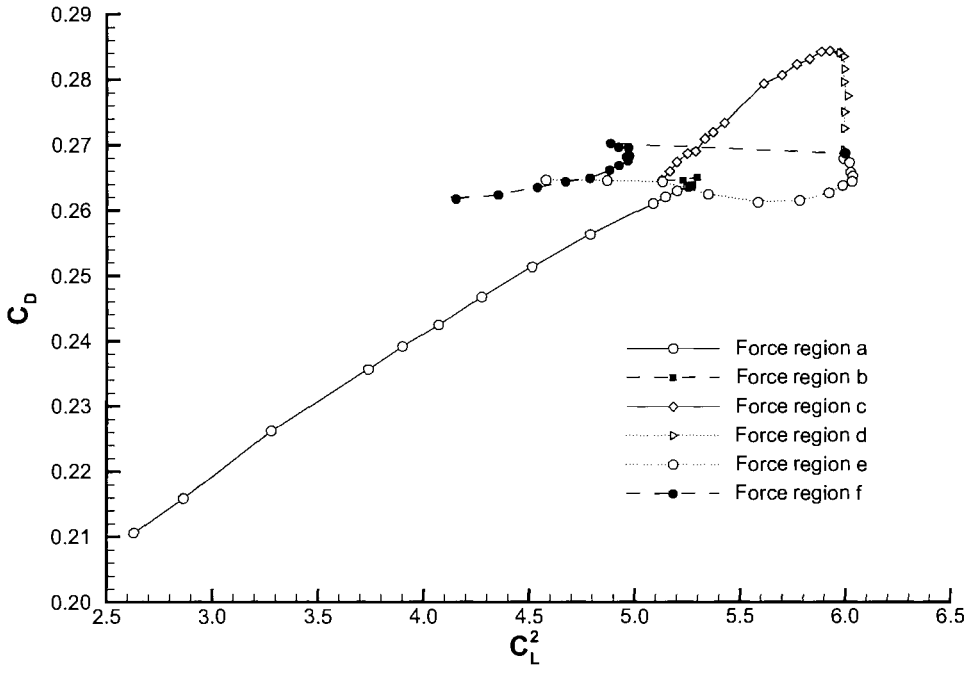

Figure 5.28: Dependency of drag coefficient on the square of the downforce coefficient for various ride heights.

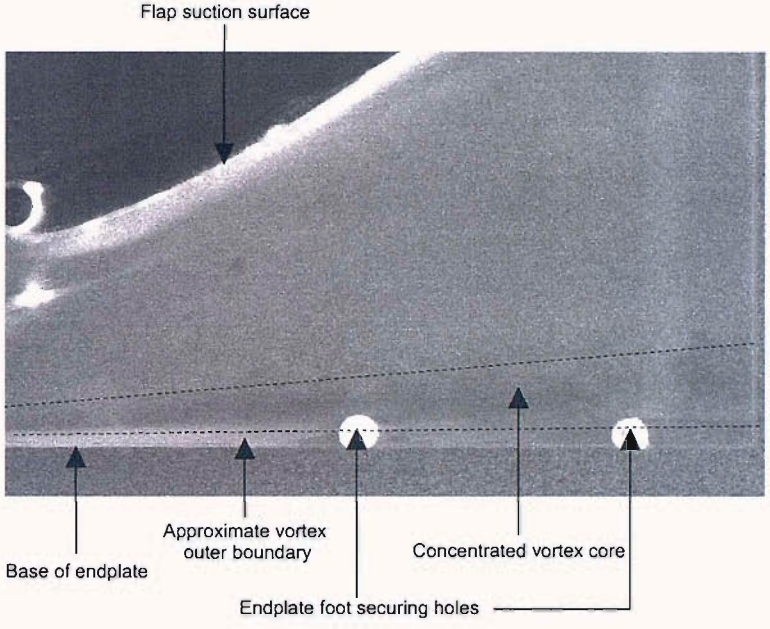

(a)

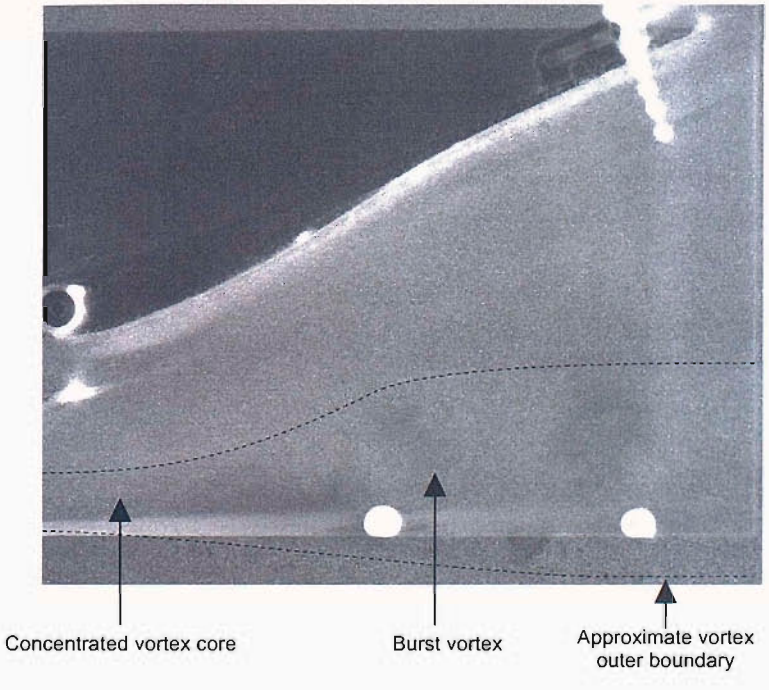

(b)

Figure 5.29: Smoke visualisation of port lower edge vortex core at $z/c = -0.05$; (a) $h/c = 0.247$ (region a), (b) $h/c = 0.211$ (region c). Flow from left to right.

h/c	Upper Edge Vortex				Lower Edge Vortex			
	$(z/c)_v$	$(y/c)_v$	d_h/c	$(\Omega_x)_v$	$(z/c)_v$	$(y/c)_v$	d_h/c	$(\Omega_x)_v$
0.317	NV	NV	NV	NV	-0.08	-0.03	0.04	-116
0.247	NV	NV	NV	NV	-0.11	-0.03	0.07	-54
0.211	NV	NV	NV	NV	-	-	-	-
0.141	0.06	0.32	0.02	-91	-	-	-	-
0.099	0.06	0.32	0.02	-76	-	-	-	-
0.063, decreasing h	0.06	0.34	0.02	-68	-	-	-	-
0.039, decreasing h	0.06	0.34	0.02	-62	-	-	-	-
0.063, increasing h	0.06	0.34	0.02	-69	-	-	-	-

Table 5.1: Properties of the port wing tip vortices at various ride heights. (NV = not visible).

h/c	$(x_t/c)_m$	$(x_t/c)_f$
0.317	0.07	0.54
0.247	0.07	0.54
0.211	0.07	0.54
0.099	0.12	0.54
0.063, decreasing h	0.12	0.56
0.063, increasing h	0.12	0.56
0.039, increasing h	0.12	0.56

Table 5.2: Centre span suction surface transition location for various ride heights.

h/c	Main element			Flap		
	C_{Psuc}	x/c at C_{Psuc}	x/c at C_{Pstag}	C_{Psuc}	x/c at C_{Psuc}	x/c at C_{Pstag}
0.634	-4.15	0.02	0.01	-2.02	0.48	0.46
0.317	-5.35	0.02	0.01	-2.65	0.48	0.46
0.247	-5.95	0.02	0.01	-2.65	0.48	0.46
0.211	-6.25	0.02	0.01	-2.75	0.48	0.46
0.141	-6.54	0.02	0.01	-2.89	0.48	0.46
0.099	-6.67	0.02	0.01	-2.80	0.48	0.46
0.063, decreasing h	-7.99	0.11	0.01	-2.75	0.48	0.46
0.039, decreasing h	-8.13	0.11	0.01	-2.52	0.48	0.46
0.039, increasing h	-7.09	0.11	0.01	-2.53	0.48	0.46
0.063, increasing h	-8.06	0.11	0.01	-2.78	0.48	0.46

Table 5.3: Chordwise centre span surface pressure details for various ride heights.

h/c	u_{min}/U_∞			y/c at u_{min}/U_∞			y/c at δ		δ_{99}/c	
	low	*top*	*conf*	*low*	*top*	*conf*	*low*	*top*	*low*	*top*
0.317	0.61	0.77	0.99	0.28	0.35	0.32	0.24	0.37	0.08	0.05
0.247	0.54	0.77	0.99	0.28	0.35	0.32	0.23	0.37	0.09	0.05
0.211	0.50	0.77	0.98	0.28	0.35	0.32	0.22	0.37	0.10	0.05
0.141	0.42	0.77	0.97	0.26	0.35	0.31	0.21	0.37	0.10	0.06
0.099	0.29	0.79	0.98	0.27	0.34	0.32	0.19	0.37	0.13	0.05
0.063, decreasing h	-0.46	0.80	0.88	0.25	0.34	0.33	0.12	0.36	0.21	0.03
0.039, increasing h	-0.81	-	-	0.18	-	-	-	0.37	-	-
0.063, increasing h	-0.78	-	-	0.21	-	-	-0.06	0.36	0.42	-

Table 5.4: Wake profile information at $x/c = 1.127$ for various ride heights; $z/c = -1.021$.

x/c	u_{min}/U_∞			y/c at u_{min}/U_∞			y/c at δ		δ_{99}/c	
	low	*top*	*conf*	*low*	*top*	*conf*	*low*	*top*	*low*	*top*
0.835	0.37	-	-	0.17	-	-	0.13	0.20	0.07	-
1.127	0.54	0.77	0.99	0.28	0.35	0.32	0.23	0.37	0.09	0.05
1.268	0.59	0.82	0.95	0.32	0.37	0.35	0.27	0.40	0.08	0.05
1.532	0.67	0.87	0.90	0.38	0.44	0.43	0.33	0.47	0.10	0.04

Table 5.5: Wake profile information at various streamwise locations for $h/c = 0.247$ (region *a*); $z/c = -1.021$.

x/c	u_{min}/U_∞			y/c at u_{min}/U_∞			y/c at δ		δ_{99}/c	
	low	*top*	*conf*	*low*	*top*	*conf*	*low*	*top*	*low*	*top*
0.835	-0.28	-	-	0.16	-	-	0.11	0.20	0.09	-
1.127	0.29	0.79	0.98	0.27	0.34	0.32	0.19	0.37	0.13	0.05
1.268	0.33	0.84	0.90	0.31	0.39	0.36	0.22	0.41	0.14	0.05
1.532	0.49	-	-	0.39	-	-	0.30	0.49	0.19	-

Table 5.6: Wake profile information at various streamwise locations for $h/c = 0.099$ (region *d*); $z/c = -1.021$.

Chapter 6

Influence of Flap Incidence on Wing Performance

This chapter discusses experimental results obtained for the wing with various flap incidences. The experimental setup will be stated followed by discussions of the data. The results will then be discussed in combination. The aim of this investigation was to quantify the effect of flap incidence on the performance of the wing. In addition the flow field variations responsible for the alterations in wing performance will be identified. The dependency of the forces on the direction of ride height variation will be investigated and quantified for various flap incidences.

6.1 Experimental Details

During this investigation the incidence of the main element remained constant at $+4^{\circ}$. The incidence of the flap was varied between $+10^{\circ}$ and $+30^{\circ}$ in increments of 2°. The flap gap and overlap were assigned optimum values of $0.042c$ and $0.035c$ respectively. The range of ride heights investigated were consistent with those stated in Chapter 5. The ride height was varied in two stages as described previously (Chapter 5). Downforce, drag and pitching moment data was obtained at all ride heights. Surface pressures were also obtained at ride heights of interest as indicated by the forces.

6.2 Forces

The downforce, drag, pitching moment and wing efficiency at various ride heights are presented in Figures 6.1 to 6.4. For certain flap incidences the force measurements were catagorised into three types; increasing ride height, decreasing ride height and independent of direction. The latter category referred to force data which was independent of the direction of ride height variation. Force regions similar to those identified in Chapter 5 were observed within the forces. However the ride heights over which the force regions were present varied with flap incidence.

Reducing the ride height for flap incidences below $+20°$ resulted in a consistent variation in downforce (Figure 6.1(a)). The downforce increased asymptotically, increased linearly, achieved a maximum value and then decreased. For these low flap incidences the downforce at all ride heights was independent of the direction of ride height variation. Increasing the flap incidence caused the downforce to increase for all ride heights. The ride height at which a maximum value (C_{Lmax}) was achieved increased with increases in flap incidence. The lower boundary of the asymptotic downforce increase (region a) occurred at higher ride heights for increased values of flap incidence (Figure 5.1). The downforce variations for $\alpha_f = +20°$ and $+22°$ were largely similar to those observed for lower flap incidences. However at low values of ride height the downforce was dependent on ride height direction. Reduced values of downforce were obtained with increasing ride heights. The ride height below which the force was dependent on ride height direction (h_{dep}) increased with increased values of flap incidence.

The downforce variation for flap incidences above $+22°$ exhibited a greater dependence on ride height direction. A largely similar downforce variation was observed with flap incidences of $+24°$ and $+26°$. The six force regions defined in Chapter 5 were easily observed. As for lower flap incidences h_{dep} increased with increases in flap incidence. This was also true for $\alpha_f = +28°$. For a flap incidence of $+28°$ the downforce was dependent on ride height direction for a wide range of ride heights ($h_{dep} = 0.342c$). The downforce at all ride heights for $\alpha_f = +30°$ was significantly reduced when compared to $\alpha_f = +28°$. It was noted that the downforce variation for the highest flap incidence conformed to the variations observed with increasing ride heights for lower flap incidences (region f). It has been shown that the force dependency observed for $\alpha_f = +24°$ was a result of the flap stalling (Chapter 5). The downforce variation for $\alpha_f = +30°$ suggested that the flap was stalled

for all ride heights tested.

The variation in drag with ride height for various flap incidences is presented in Figure 6.2. For flap incidences below +30° increased values of flap incidence resulted in increased values of drag at all ride heights. For flap incidences below +20° the drag was independent of ride height direction for all ride heights (Figure 6.2(a)). An asymptotic increase in drag was observed for flap incidences below $\alpha_f = +20°$. Maximum drag (C_{Dmax}) was observed at the lowest ride height for these cases. The drag was dependent on the direction of ride height variation for $\alpha_f = +20°$ and +22° at low ride heights. For these flap incidences a maximum drag value was obtained at ride heights significantly greater than the minimum value. The range of ride heights over which the drag was dependent on ride height direction increased significantly for flap incidences greater that +22° (Figure 6.2(b)). The drag variations for these higher flap incidences were largely similar. Increasing the flap incidence caused the ride height at which C_{Dmax} was achieved to increase. In addition the value of h_{dep} also increased. The drag variation for $\alpha_f = +30°$ did not conform to those observed for lower flap incidences. A more constant drag was observed increasing gradually until $0.113c$ then decreasing.

The variation in pitching moment with ride height for various flap incidences in presented in Figure 6.3. For all ride heights increased values of pitching moment were observed with increased values of flap incidence. The variation in pitching moment was largely similar for all flap incidences. The ride height at which a maximum value of pitching moment (C_{Mmax}) was achieved increased for increased values of flap incidence. For all flap incidences the ride height at which C_{Mmax} was achieved was significantly greater than the ride height at which C_{Lmax} was achieved. The pitching moment was entirely independent of ride height direction for flap incidences below +20° (Figure 6.3(a)). A slight dependency on ride height direction was observed for $\alpha_f = +22°$ and +24° for low ride heights. For greater values of flap incidence a greater dependency on ride height was observed. The ride height below which the pitching moment was dependent on ride height direction increased with increases in flap incidence. For the greatest value of flap incidence the pitching moment remained relatively constant for $h/c \geq 0.106$. Below this ride height a rapid reduction in pitching moment was observed, as for lesser flap incidences. The pitching moment for this case was independent of ride height direction for all ride heights.

Figure 6.4 presents the variation in wing efficiency with ride height for various flap incidences. For all flap incidences the variation in wing efficiency with ride height was

largely similar. Decreased values of wing efficiency were observed with increased values of flap incidence. Since dependent on both the downforce and drag the wing efficiency exhibited a dependency on ride height direction for flap incidences greater than +18°. The ride height at which a maximum value of wing efficiency (β_{max}) was achieved decreased with increased values of flap incidence. Table 6.1 presents quantitative data concerning the forces obtained with various flap incidences.

6.3 Surface Pressures

Surface pressures were obtained to provide quantitative data concerning the influence of flap incidence on the surface flow field. Chordwise and spanwise surface pressures were measured on the wing. In addition surface pressures were measured on the inboard face of the port endplate. Flap incidences of +16°, +20°, +24° and +28° were investigated at two ride heights. The first ride height of $h/c = 0.634$ represented the highest ride height achievable i.e. closest to freestream. The second ride height of $0.063c$ represented a ride height close to the maximum downforce ride height.

6.3.1 Chordwise Pressures at Centre Span

Figure 6.5(a) presents the chordwise surface pressures at the wing centre span for a ride height of $0.634c$. The surface pressure distributions were largely similar in shape for all flap incidences. Increased values of flap incidence caused the circulation of the flap to increase. This was observed as increased values of suction and pressure on the lower and upper surfaces of the flap respectively. Stagnation on the flap moved downstream from $x/c = 0.45$ to 0.46 with increases in flap incidence. The suction peak (C_{Psuc}) on the flap increased in magnitude with increases in flap incidence. The corresponding streamwise location of the suction peak also varied, moving upstream from $x/c = 0.50$ to 0.48 with increases in flap incidence.

The surface pressures on the main element also indicated increased values of circulation with increased values of flap incidence. The increase in flap circulation induced a greater circulation on the main element in accordance the "circulation effect" as stated by Smith [48] (Appendix A). Maximum suction was consistently achieved at $x/c = 0.02$ on the main element, increasing in magnitude with increases in flap incidence. Stagnation on the main element was independent of flap incidence and was consistently observed at $x/c = 0.01$.

Table 6.2 presents quantitative data concerning the centre span chordwise surface pressures for $h/c = 0.634$.

Figure 6.5(b) presents the chordwise surface pressures at the wing centre span for various flap incidences at $h/c = 0.063$. The ride height shown was close to the maximum downforce ride height. For flap incidences of $+16°$, $+20°$ and $+24°$ the variations due to flap incidence were consistent with those observed at the higher ride height. For these three flap incidences the surface pressures were independent of ride height direction. Stagnation consistently occurred at $x/c = 0.01$ on the main element. The streamwise location of stagnation on the flap moved downstream with increases in flap incidence from $x/c = 0.45$ to 0.46. The suction peak on the main element was consistently observed at $x/c = 0.11$ for all flap incidences. However, the suction peak on the flap moved upstream from $x/c = 0.50$ to 0.48 with increased flap incidences. The chordwise surface pressures obtained with a flap incidence of $+28°$ at $h/c = 0.063$ were dependent on ride height direction. Decreased values of suction were observed over the main element for the increasing ride height case. A significant reduction in suction on the flap was observed with increasing ride heights. The constant suction over the majority of the flap suggested that the flap had stalled. Similar observations were noted for lower ride heights with a flap incidence of $+24°$ (Chapter 5).

6.3.2 Chordwise Pressures Near Wing Tip

Figure 6.6 presents the chordwise surface pressures near the port wing tip for various flap incidences. For a ride height of $0.634c$ (Figure 6.6(a)) the variation in surface pressures was consistent with that observed at the centre span. Increased values of flap incidence increased the circulation of the flap which in turn increased the main element circulation. The streamwise locations of stagnation on the main element and flap were identical to the centre span case. In addition the streamwise locations of the suction peaks and corresponding movement were also largely similar.

The surface pressures obtained for all flap incidences on the main element for $h/c = 0.063$ were independent of ride height direction (Figure 6.6(b)). The variations in surface pressures were largely similar to those observed at the higher ride height. The surface pressures on the flap were also independent of ride height direction for $\alpha_f = +16°$, $+20°$ and $+22°$. However for $\alpha_f = +28°$ the suction over the flap was dependent on ride height direction. Significantly reduced values of suction were observed from the flap leading edge to $x/c = 0.54$ with increasing ride height. Further downstream the suction conformed to that

observed for the decreasing ride height case. Due to the large number of pressure tappings the surface pressures over the wing were obtained in three separate runs (Section 3.6.4). The discontinuity within the surface pressures between $x/c = 0.54$ and 0.55 corresponded to the boundary between two separate pressure tapping runs. Conclusive trends within the data can therefore not be drawn due to the anomalous nature of the surface pressures on the flap for $\alpha_f = +28°$ at $h/c = 0.063$ with increasing ride heights.

6.3.3 Integrated Chordwise Surface Pressures

The integrated chordwise surface pressures for $h/c = 0.634$ are presented in Figure 6.7(a). The sectional downforce at the wing centre span (C_{lc}), near the port wing tip (C_{lt}) and the combined total (C_l) are presented for various ride heights. In addition the centre span and wing tip sectional downforce generated solely by the main element and flap are presented. Linear variations in the sectional downforce were observed at this ride height. The chordwise surface pressures indicated increased values of circulation for higher flap incidences. Accordingly increased values of sectional downforce were observed with increased values of flap incidence. For all flap incidences the majority of the sectional downforce was generated by the main element. In addition the centre span sectional downforce was significantly greater than the corresponding wing tip downforce.

Figure 6.7(b) presents the sectional downforce obtained at $h/c = 0.063$ for various flap incidences. For reasons of clarity only the centre span, wing tip and total sectional downforce are presented. As for the higher ride height a linear increase in sectional downforce was observed at all flap incidences for the decreasing ride height case. A dependency between the sectional downforce and direction of ride height variation was observed for flap incidences greater that +20°. Reduced values of overall sectional downforce were observed with increasing ride heights. The dependency within the wing tip sectional downforce occurred at flap incidences greater than +24°.

6.3.4 Spanwise Pressures

The spanwise surface pressures on the main element for ride heights of $0.634c$ and $0.063c$ are presented in Figure 6.8. For the higher ride height (Figure 6.8(a)) a consistent spanwise variation was observed for flap incidences less than +28°. The pressure surface pressures linearly decreased from a local maximum at the centre span to the wing tip. The suction also decreased from the centre span to the wing tip albeit asymptotically. For flap incidences

greater than $+28°$, increased circulation was observed over the span of the main element with increases in flap incidence. This was observed as increased values of suction and pressure on the lower and upper surfaces of the main element respectively. The spanwise surface pressures for $\alpha_f = +28°$ largely conformed to the trends observed with lower flap incidences. However, reduced suction was observed from the centre span to $z/c = -0.53$ on the suction surface. The exact cause of the reduction in suction was unclear since the chordwise centre span surface pressures conformed to trends observed. Without a more in-depth investigation into the surface flow field definitive conclusions may not be drawn.

The spanwise surface pressures obtained on the main element at the lower ride height ($h/c = 0.063c$) are presented in Figure 6.8(b). The variations in spanwise pressures with flap incidence were consistent with those observed for the higher ride height. The surface pressures obtained for flap incidences less than $+28°$ were independent of the direction of ride height variation. However, significantly reduced suction was observed over the span of the main element for $\alpha_f = +28°$ with increasing ride heights. For all flap incidences at the lower ride height the spanwise distribution of surface pressures conformed to that observed at the higher ride height.

The spanwise distribution of surface pressures on the flap for various flap incidences are presented in Figure 6.9. For a ride height of $0.634c$ a consistent spanwise variation in surface pressures was observed with all flap incidences (Figure 6.9(a)). Increases in flap incidence resulted in increased circulation of the flap. The spanwise distribution of suction indicated the presence of the lower edge vortex, observed as increased suction towards the wing tip (Chapter 5). The variation in spanwise surface pressures on the pressure surface of the flap at a ride height of $0.063c$ (Figure 6.9(b)) were consistent with that observed at the higher ride height. However, a significant variation in suction was observed. Increases in flap incidence resulted in increased suction between the centre span and $z/c = -0.18$. Closer to the wing tip the suction was relatively independent of flap incidence. It has been shown that for $\alpha_f = +24°$ the lower edge vortex was absent at $h/c = 0.063c$. Accordingly the suction towards the wing tip was reduced. The spanwise surface pressures obtained for $\alpha_f = +24°$ were independent of the direction of ride height variation. However, the spanwise distribution of suction for $\alpha_f = +28°$ was dependent. Between the centre span and $z/c = -0.35$ decreased suction was observed with increasing ride heights. Closer to the wing tip decreased suction was observed with decreasing ride heights.

6.3.5 Endplate Pressures

The surface pressures obtained on the inboard face of the port endplate for various flap incidences are presented in Figure 6.10. The results obtained at a ride height of $0.634c$ are shown. Suction was present for all flap incidences and at all vertical locations. Increasing the flap incidence resulted in increased values of suction at all vertical locations, due to the increased circulation of the wing. Maximum suction was consistently observed at the lowest vertical location. It has been shown previously (Chapter 5) that the significantly greater value of suction observed at $y/c = -0.02$ was a result of the lower edge vortex. The endplate surface pressures presented here indicated the presence of the lower edge vortex for all flap incidences. The endplate surface pressures obtained at a ride height of $0.063c$ are not presented. For the lower ride height constant suction ($C_P \approx -0.75$) was observed over the inboard face of the endplate for all flap incidences. Previously it has been shown that for low ride heights that lower edge vortex was absent. Accordingly reduced suction was observed, as is the case here.

6.4 Discussion

The force and surface pressure measurements obtained within this investigation indicated that alterations in flap incidence significantly affected the forces generated by the wing. In addition the force variations due to ride height were also influenced by flap incidence. For higher ride heights increases in flap incidence resulted in greater values of flap circulation. This was observed as increased suction over the lower surface of the flap and increased pressure over the upper surface of the flap. Greater values of main element circulation were also observed in accordance with the "circulation effects" as stated by Smith [48]. Due to the increased circulation over the wing greater downforce was observed at all ride heights with larger values of flap incidence. The increased suction over the flap also resulted in increasingly negative values of pitching moment. Increases in flap incidence caused increased values of drag. It was noted that the induced drag factor (k_i) was relatively independent of flap incidence with a value of approximately 7.22. Therefore greater values of downforce, as observed with higher values of flap incidence, resulted in increased values of drag at all ride heights.

The influence of flap incidence for lower ride heights was largely similar to that observed at higher ride heights. It was noted that the ride height below which the forces were

dependent on ride height direction (h_{dep}), increased with flap incidence increases. It has been previously shown (Chapter 5) that the dependency of the forces on ride height direction was due to the flap stalling. It was surmised that the stalling of the flap was a direct result of the Reynolds number variation endured by the wing during the run-up stage of the wing tunnel. Physically h_{dep} represented the ride height where the adverse pressure gradient beneath the wing was weak enough to allow for the flap suction surface boundary layer to reattach. Increases in flap incidence increased the magnitude of the adverse pressure gradient over the suction surfaces of the wing. It is therefore surmised that increased values of flap incidence delayed boundary layer reattachment on the flap suction surface therefore increasing the value of h_{dep}, as observed.

6.5 Chapter Summary

An experimental investigation into the influence of flap incidence on a multi-element wing in ground effect was conducted. The flap incidence was found to significantly affect the forces generated by the wing. The alterations in forces were consistent with variations in "circulation effects" [48]. The "dumping effects", "off-surface pressure recovery" and "fresh boundary layer effects" remained relatively consistent with variations in flap incidence. "Slat effects" were not present. The ride height below which the forces were dependent on ride height direction also varied with flap incidence. Higher values of flap incidence resulted in an increased range of ride heights over which the forces were dependent on ride height direction.

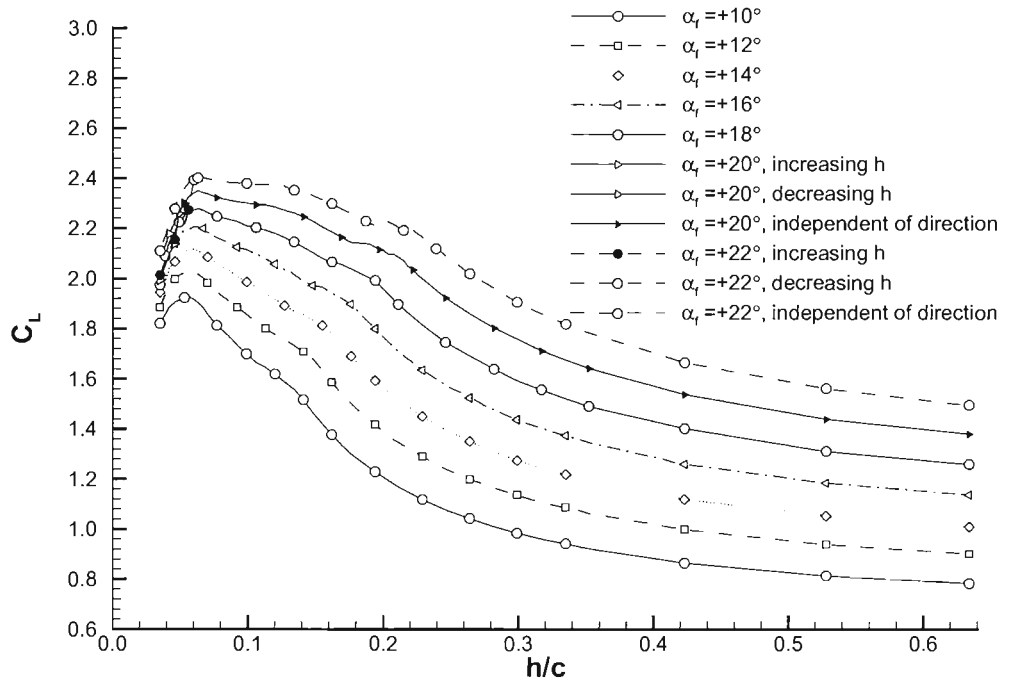

(a)

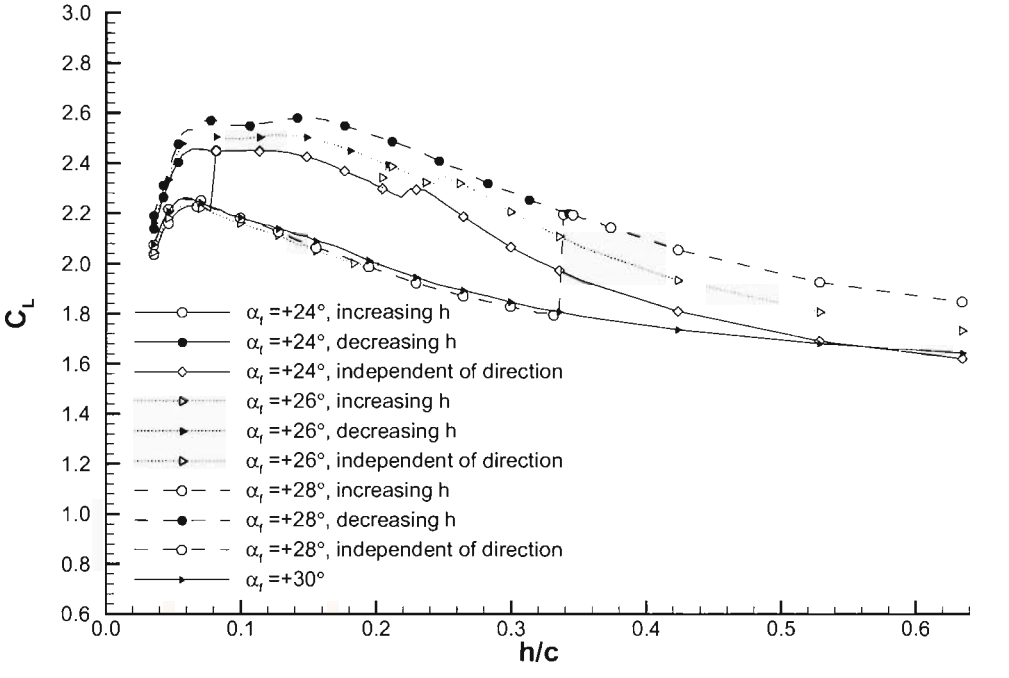

(b)

Figure 6.1: Variation of downforce coefficient with ride height for various flap incidences; (a) low flap angles, (b) high flap angles.

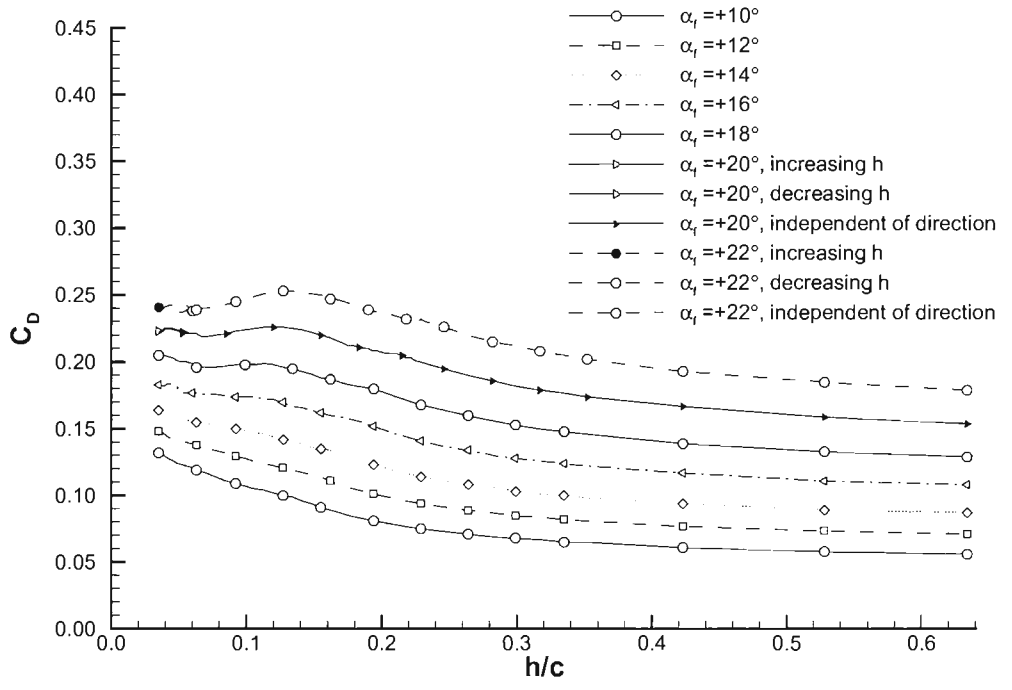

(a)

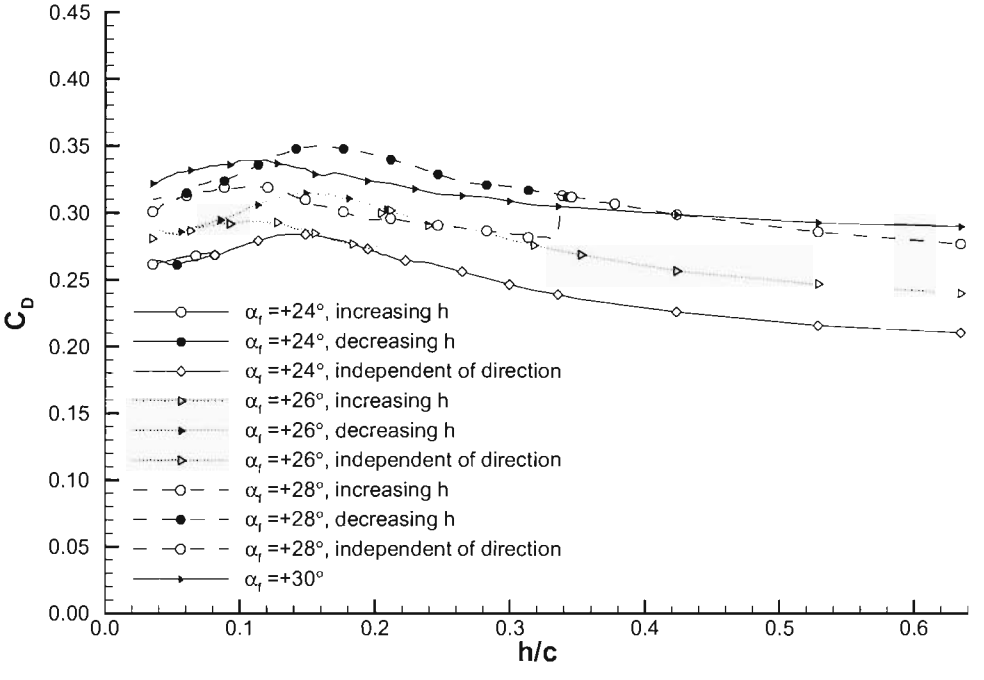

(b)

Figure 6.2: Variation of drag coefficient with ride height for various flap incidences: (a) low flap angles, (b) high flap angles.

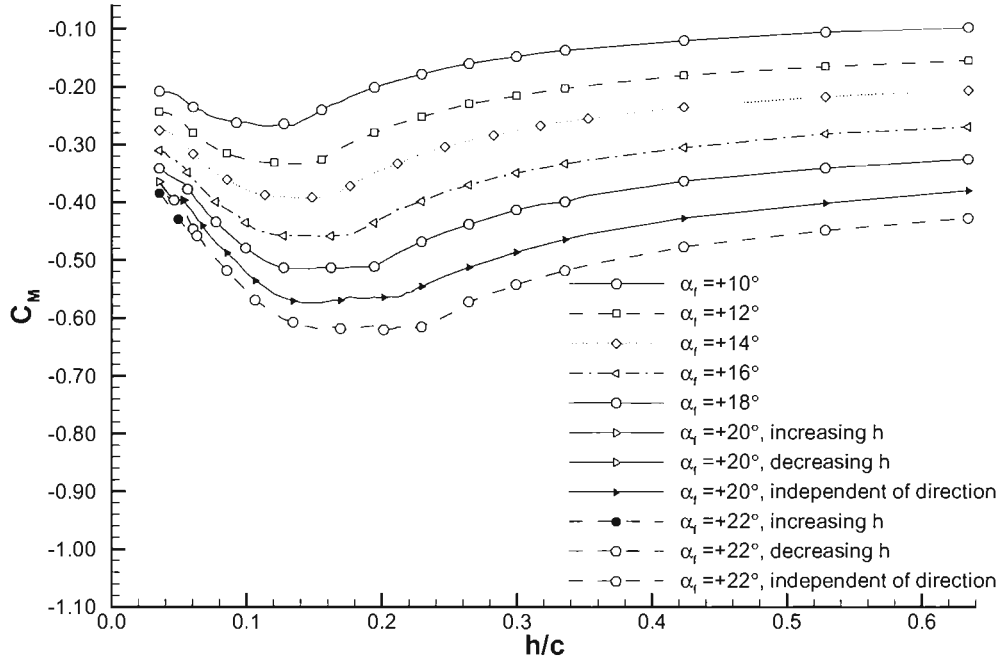

(a)

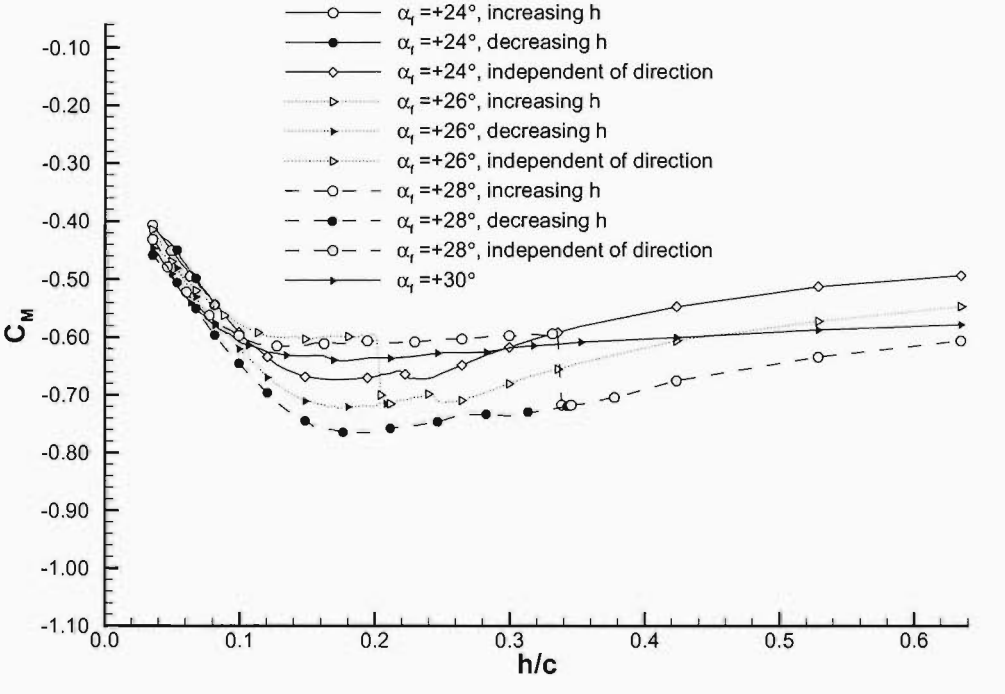

(b)

Figure 6.3: Variation of pitching moment coefficient with ride height for various flap incidences; (a) low flap angles, (b) high flap angles.

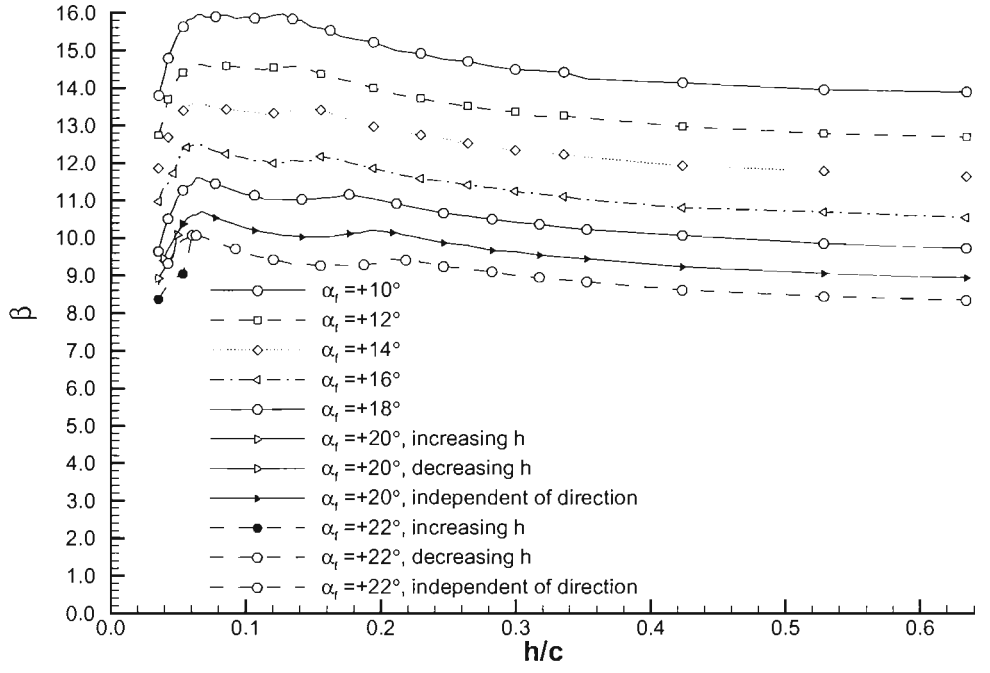

(a)

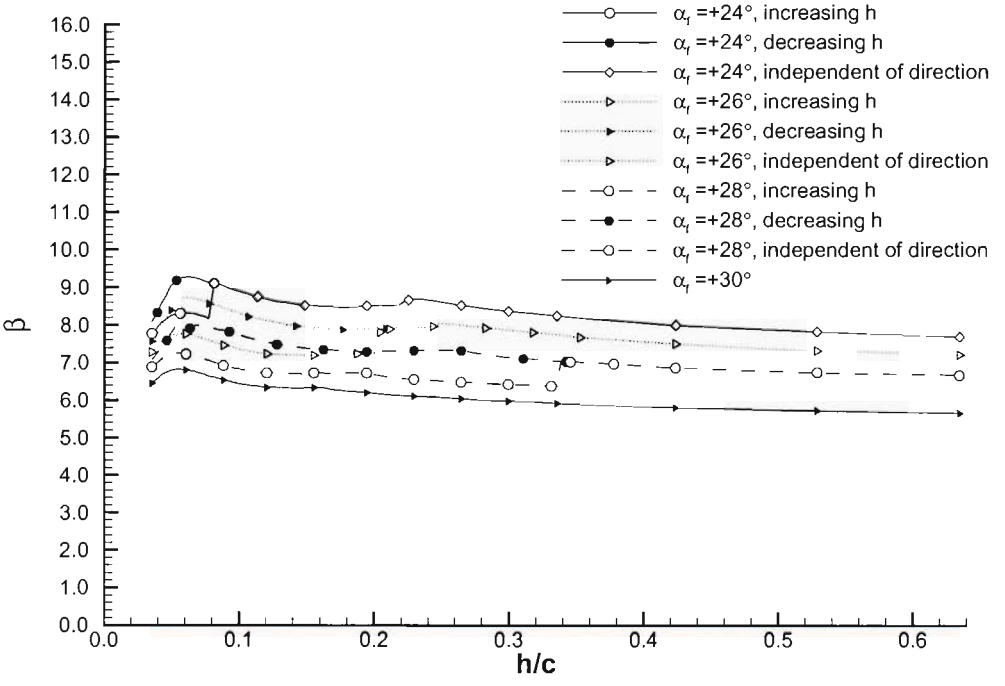

(b)

Figure 6.4: Variation of wing efficiency with ride height for various flap incidences; (a) low flap angles, (b) high flap angles.

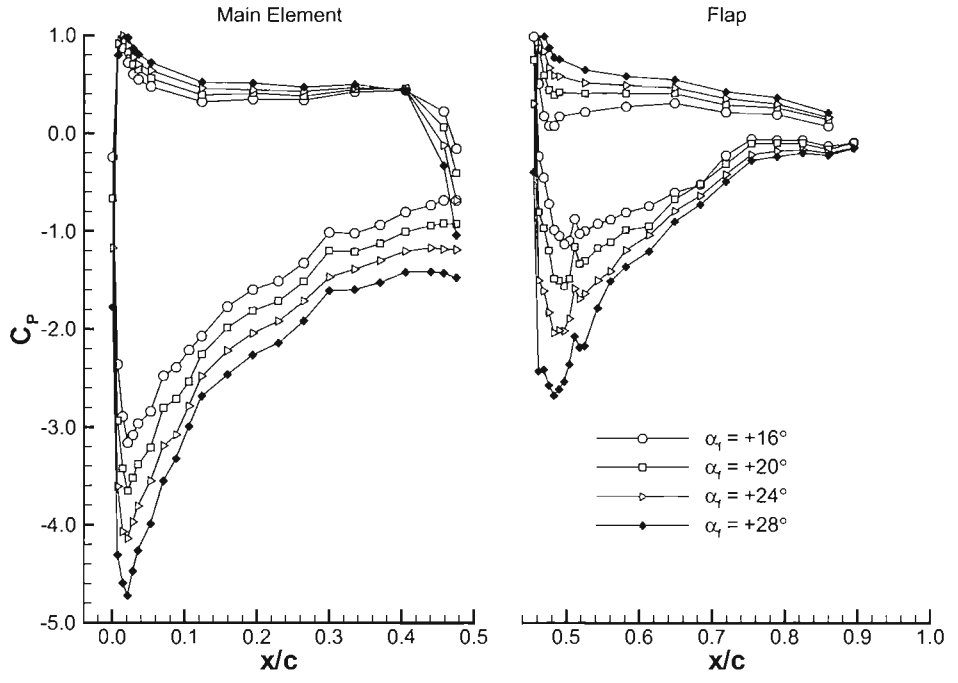

(a)

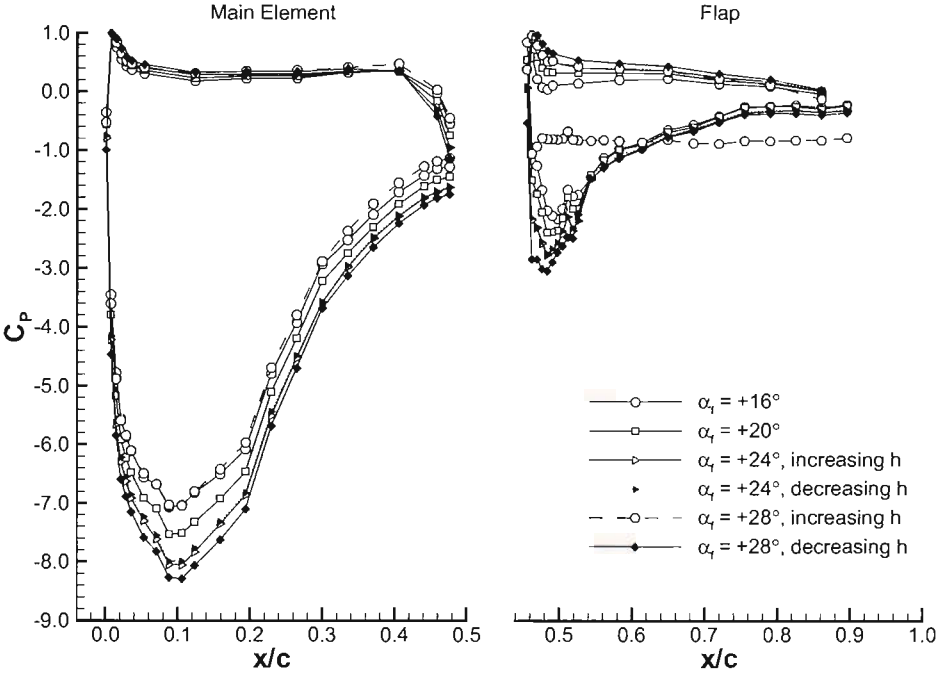

(b)

Figure 6.5: Chordwise surface pressure distributions at wing centre span for various flap incidences; (a) $h/c = 0.634$, (b) $h/c = 0.063$.

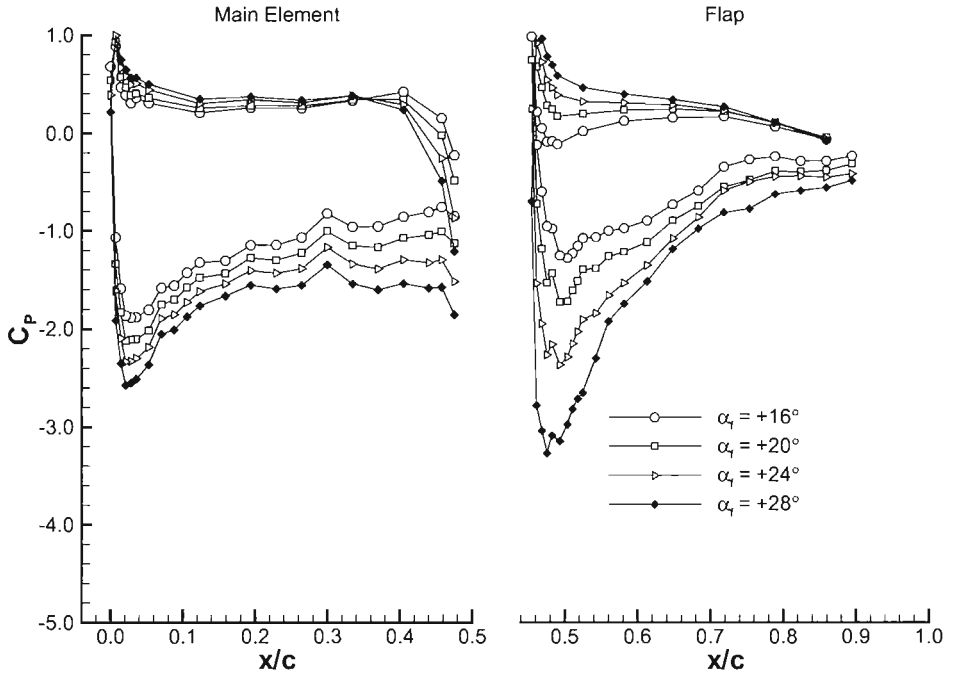

(a)

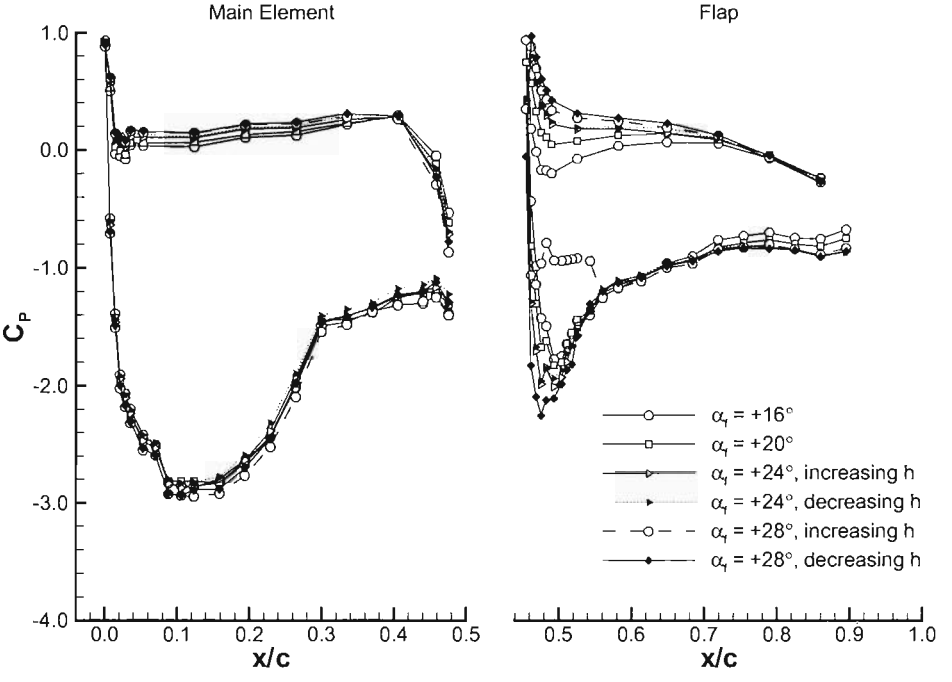

(b)

Figure 6.6: Chordwise surface pressure distributions near port wing tip for various flap incidences, $z/c = -0.088$; (a) $h/c = 0.634$, (b) $h/c = 0.063$.

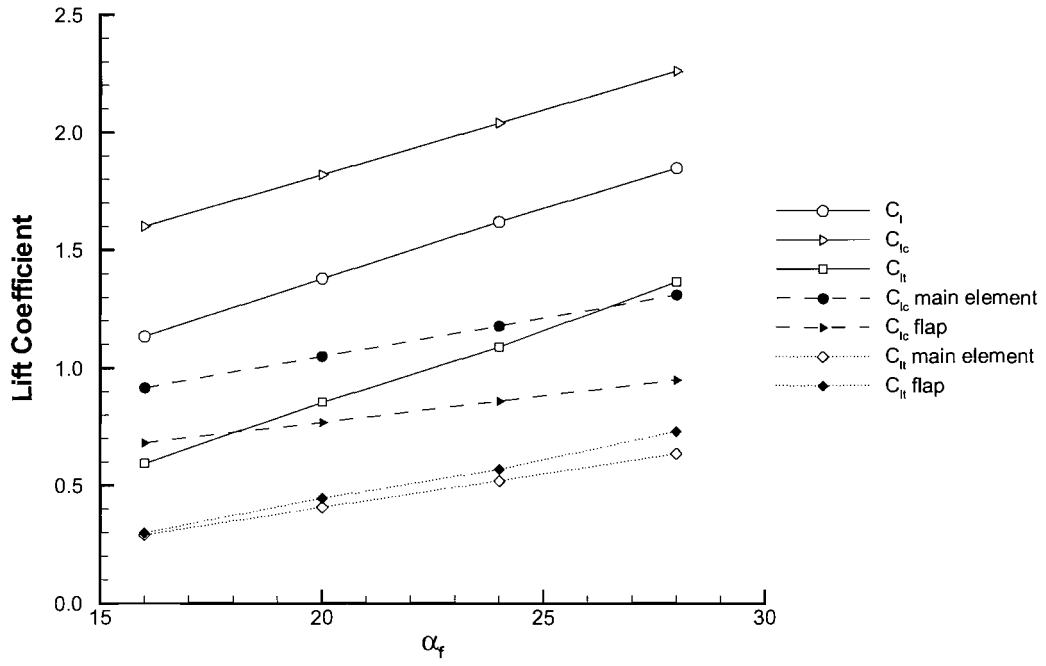

(a)

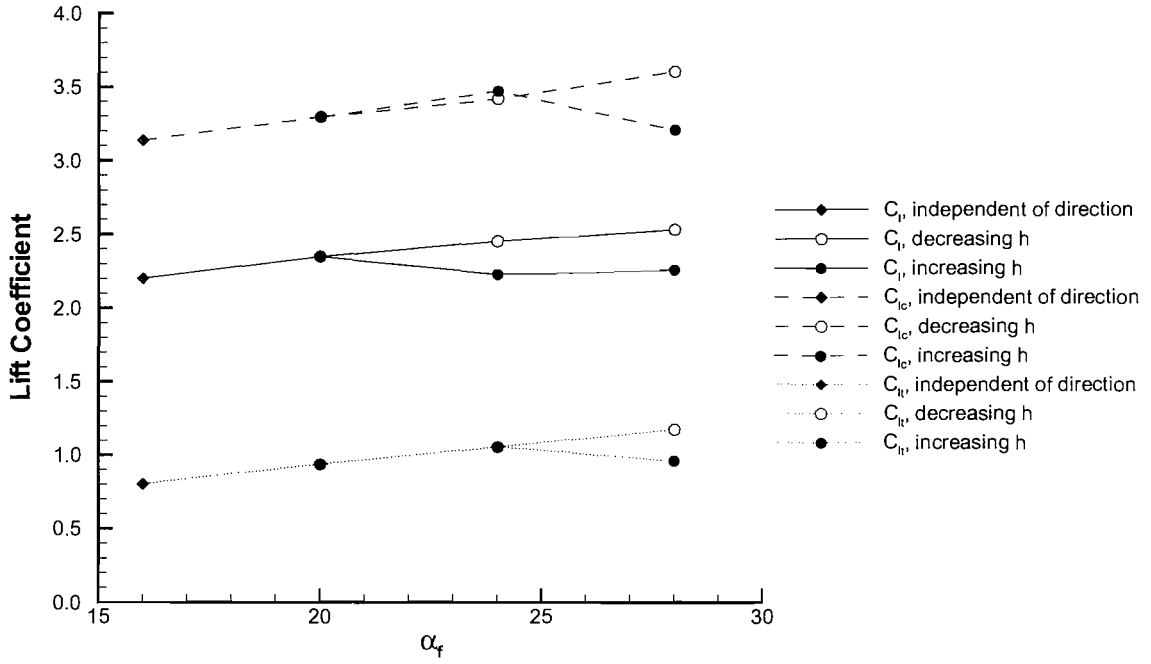

(b)

Figure 6.7: Integrated surface pressures for various flap incidences; (a) $h/c = 0.634$, (b) $h/c = 0.063$.

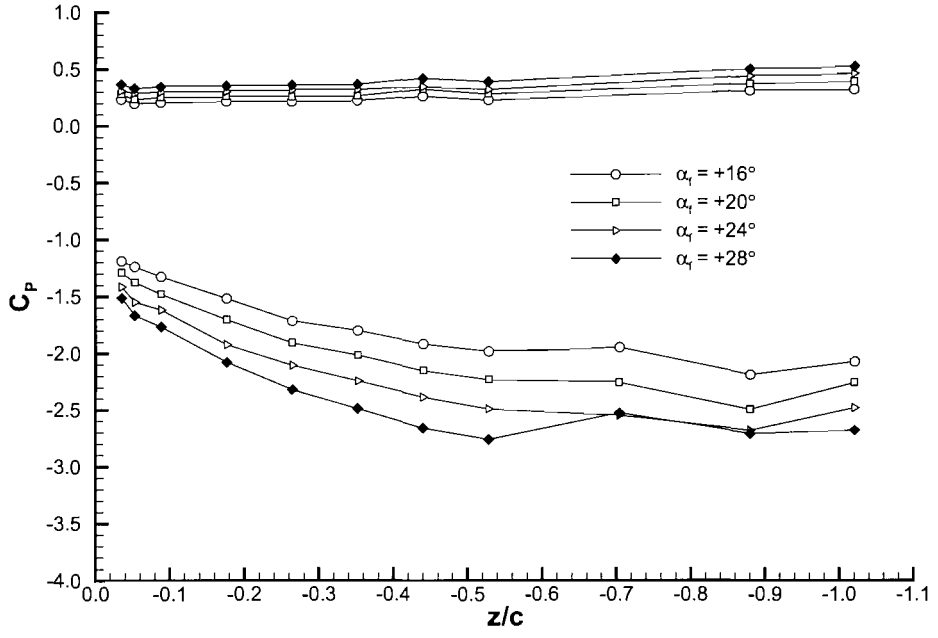

(a)

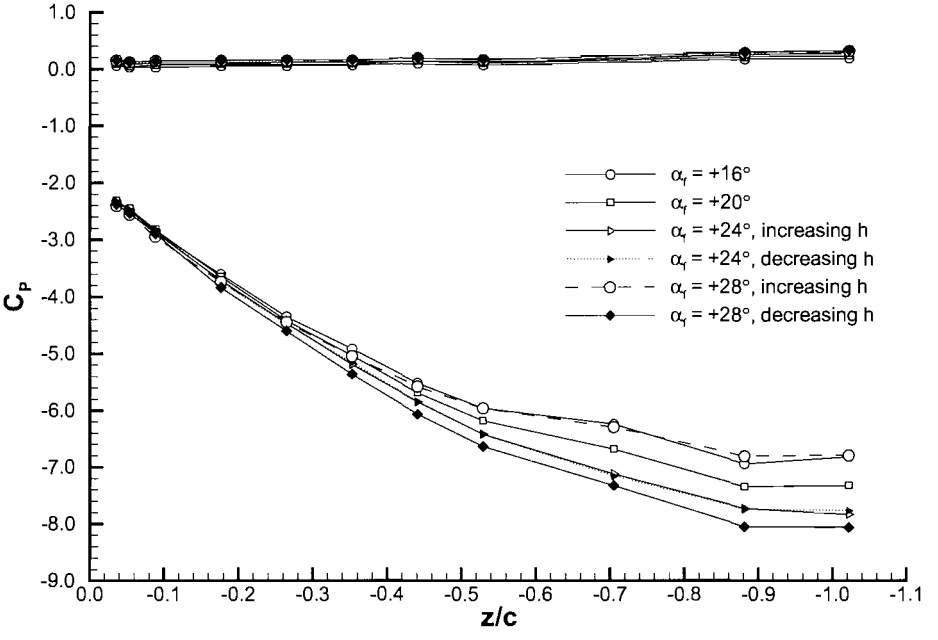

(b)

Figure 6.8: Spanwise surface pressure distribution on the main element for various flap incidences at $x/c = 0.123$; (a) $h/c = 0.634$, (b) $h/c = 0.063$.

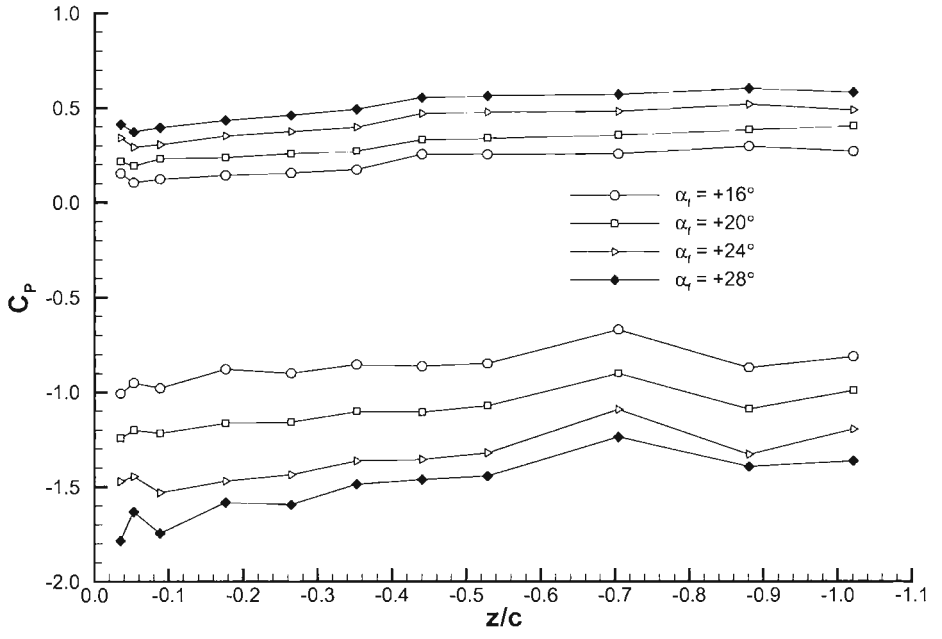

(a)

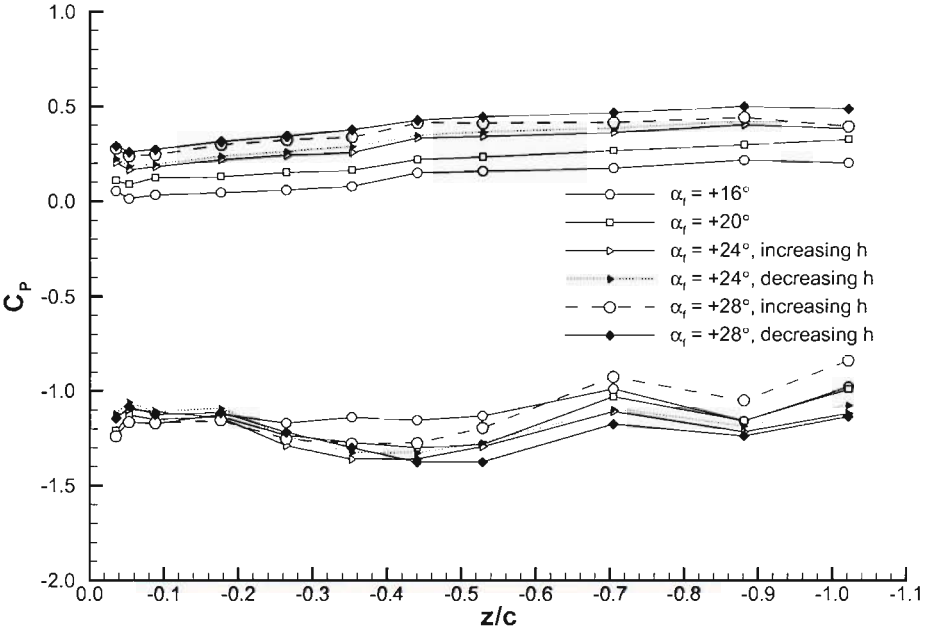

(b)

Figure 6.9: Spanwise surface pressure distribution on the flap for various flap incidences at $x/c_f = 0.127$; (a) $h/c = 0.634$, (b) $h/c = 0.063$.

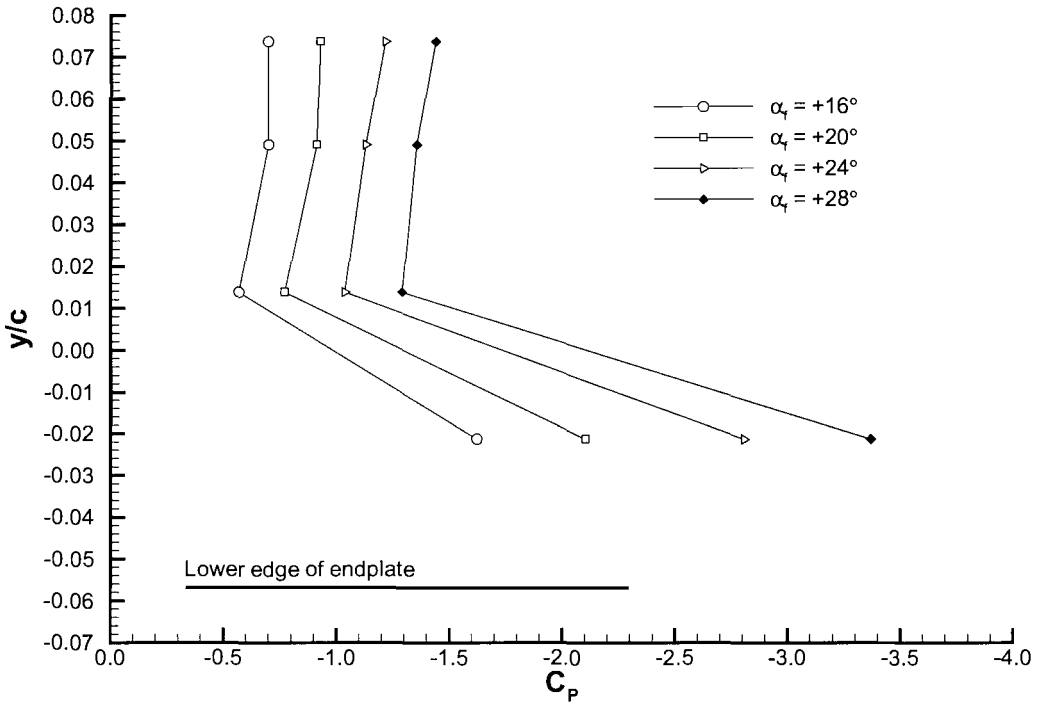

Figure 6.10: Surface pressure distribution on the inboard side of the port endplate for various flap incidences; $x/c = 0.614$, $h/c = 0.634$.

α_f	C_{Lmax}	C_{Dmax}	C_{Mmax}	β_{max}	h/c at				h_{dep}/c
					C_{Lmax}	C_{Dmax}	C_{Mmax}	β_{max}	
+10°	1.93	0.132	-0.268	15.95	0.056	0.035	0.113	0.085	-
+12°	2.03	0.148	-0.334	14.63	0.060	0.035	0.134	0.063	-
+14°	2.12	0.164	-0.393	13.60	0.060	0.035	0.141	0.063	-
+16°	2.21	0.183	-0.459	12.50	0.063	0.035	0.115	0.063	-
+18°	2.28	0.205	-0.515	11.61	0.063	0.035	0.141	0.063	-
+20°	2.35	0.225	-0.574	10.71	0.063	0.042	0.148	0.067	0.053
+22°	2.40	0.253	-0.621	10.08	0.067	0.134	0.176	0.060↓	0.063
+24°	2.46	0.284	-0.674	9.29	0.067↓	0.141	0.169	0.063↓	0.081
+26°	2.51	0.315	-0.723	8.72	0.067↓	0.148↓	0.173↓	0.060↓	0.208
+28°	2.58	0.350	-0.765	8.08	0.141↓	0.155↓	0.194↓	0.056↓	0.342
+30°	2.26	0.339	-0.641	6.84	0.056	0.113	0.176	0.053	-

Table 6.1: Force data for various for various flap incidences. (↓= decreasing h).

α_f	Main element			Flap		
	C_{Psuc}	x/c at C_{Psuc}	x/c at C_{Pstag}	C_{Psuc}	x/c at C_{Psuc}	x/c at C_{Pstag}
+16°	-3.16	0.02	0.01	-1.13	0.50	0.45
+20°	-3.65	0.02	0.01	-1.56	0.50	0.46
+24°	-4.15	0.02	0.01	-2.02	0.48	0.46
+28°	-4.72	0.02	0.01	-2.67	0.48	0.46

Table 6.2: Chordwise centre span surface pressure details for various flap incidences; $h/c = 0.634$.

Chapter 7

Influence of Endplate Feet on Wing Performance

This chapter discusses experimental results obtained at various ride heights for the wing equipped with endplate feet. The experimental setup will be stated followed by discussions of the data. The results will then be discussed in combination. The aim of this investigation was to quantify the effect of endplate feet on the performance of the wing. In addition the flow field variations responsible for the alterations in wing performance will be identified.

7.1 Experimental Details

During this investigation the incidences of the main element and flap were $+4^\circ$ and $+24^\circ$ respectively. The flap gap and overlap were assigned optimum values of $0.042c$ and $0.035c$ respectively. The wing was equipped with endplate feet as described in Section 3.2.3. Within a single test run the ride height of the wing was varied in two stages: first an upstroke stage (increasing h) followed by a downstroke stage (decreasing h). During the upstroke stage the ride height was increased from 15mm ($0.053c$) to 180mm ($0.634c$) with the wing in situ in a continuous wind-on state. During the downstroke stage the ride height was decreased from 180mm to 15mm again with the wing in situ in a continuous wind-on state. The incremental variation in ride height was set according to the variations in the forces and refined in areas of importance. Downforce, drag and pitching moment data was obtained at all ride heights. On-surface and off-surface data was then obtained at ride heights of importance as identified by the forces.

7.2 Forces

The downforce, drag, pitching moment and wing efficiency at various ride heights are presented in Figures 7.1, 7.3, 7.4 and 7.5 respectively. Force data obtained without endplate feet has been included for comparison reasons. The force measurements were catagorised into three types; increasing ride height, decreasing ride height and independent of direction. The latter category referred to force data which was independent of the direction of ride height variation. Figure 7.2 presents the variation in downforce slope ($dC_L/d(h/c)$) with ride height for the wing equipped with endplate feet. Upon inspection four regions were identified and labelled force regions g, i, j and n.

Figure 7.1 presents the variation in downforce coefficient (C_L) with ride height. Reducing the ride height from a maximum value resulted in an asymptotic increase in downforce until a ride height of $0.158c$ ($C_L = 3.16$). This region was labelled force region g. For ride heights between $0.634c$ and $0.236c$ a offset of approximately 10% was observed between the downforce obtained with and without endplate feet. Increased values of downforce were achieved with the addition of endplate feet. Decreasing the ride height from $0.158c$ to $0.127c$ resulted in a linear increase in downforce (region i). Below a ride height of $0.127c$ the downforce was dependent on the ride height direction. Decreasing the ride height from $0.127c$ (region j) resulted in the downforce increasing initially reaching a global maximum (C_{Lmax}) of 3.46 at $h/c = 0.106$. The downforce decreased for lower ride heights, gradually at first then rapidly. The downforce obtained for ride heights below $0.127c$ was significantly reduced for the increasing ride height case (region n). Within force region n increasing the ride height from a minimal value resulted in the downforce increasing rounding off at $h/c = 0.092$. An abrupt increase in downforce was observed between $h/c = 0.113$ and 0.127 during which the downforce increased by 23% from $C_L = 2.73$ to 3.36.

The variation in drag with ride height is presented in Figure 7.3 for the wing with and without endplate feet. Reducing the ride height from a maximum value to $0.158c$ resulted in an asymptotic increase in drag (region g). The variation in drag for $h/c \leq 0.236$ with endplate feet was largely similar to that observed without endplate feet. Reduced values of drag were achieved for the wing equipped with endplate feet. Reducing the ride height from $0.158c$ to $0.127c$ (region i) resulted in the drag decreasing initially then increasing linearly. For ride heights below $0.127c$ the drag was dependent on the direction of ride height variation. A similar variation in drag was observed for both increasing and decreasing ride

height cases. Reducing the ride height from $0.127c$ (region j) caused the drag to increase reaching a global maximum value (C_{Dmax}) of 0.29 at $h/c = 0.088$. Below this ride height the drag decreased linearly until a minimal ride height was achieved. Increasing the ride height from $0.053c$ (region n) caused the drag to increase initially then decrease until $h/c = 0.113$. Between ride heights of $0.113c$ and $0.127c$ the drag increased abruptly from $C_D = 0.26$ to 0.28, an increase of 4%.

Figure 7.4 presents the variation in pitching moment coefficient (C_M) with ride height. Reducing the ride height from $0.634c$ to $0.158c$ (region g) caused the pitching moment to increase asymptotically, i.e. become more negative. The variation in pitching moment for $h/c \geq 0.236$ for the wing equipped with endplate feet was similar to that observed without endplate feet. The addition of endplate feet generated increased values of pitching moment. Reducing the ride height from $0.158c$ to $0.127c$ (region i) resulted in the pitching moment increasing initially achieving a global maximum value (C_{Mmax}) of -0.89 at $h/c = 0.155$. Below this ride height a linear reduction in pitching moment was observed. For ride height below $0.127c$ the pitching moment was dependent on the direction of ride height variation. This feature was in contrast to the pitching moment obtained for the wing without endplate feet. Decreasing the ride height from $0.127c$ (region j) caused the pitching moment to decrease gradually at first until a minimum ride height was achieved. Increasing the ride height from $0.053c$ (region n) resulted in the pitching moment increasing until $h/c = 0.106$. Above this ride height the pitching moment decreased initially then increased abruptly between $h/c = 0.113$ and 0.127 by 18%.

The variation in wing efficiency (β) with ride height is presented in Figure 7.5. For all ride heights the efficiency of the wing was significantly increased through the addition of endplate feet. The variation in wing efficiency with ride height possessed features of both the downforce and drag variation. An asymptotic increase in efficiency was observed for high ride heights followed by a linear increase and subsequent reduction. The maximum value of wing efficiency (β_{max}) achieved was 12.27 at a ride height of $0.113c$ (region j).

7.3 Wing Tip Flow Field

The flow field of the port wing tip was visualised using PIV (Section 3.6.2). Ride heights of $0.317c$, $0.211c$, $0.169c$, $0.141c$, $0.099c$ and $0.063c$ were investigated, corresponding to ride heights within each of the four force regions. Figures 7.6 to 7.9 present contours of time-

averaged non-dimensional vorticity (Ω_x) at $x/c = 0.995$ for various ride heights. Positive and negative vorticity was defined as clockwise and anti-clockwise rotations respectively. Where applicable the boundaries of the vortices have been included as dashed lines. The vortex identification method of Jeong & Hussain [147] was used.

Figure 7.6(a) presents the wing tip flow field for a ride height of $0.317c$ (region g). The most prominent features of the flow are two vortices, one located inboard of the endplate (lower edge vortex) and the other located beneath the endplate foot. The vortex beneath the endplate foot will be referred to as the 'foot vortex'. A shear layer, originating from the outboard edge of the endplate foot, was entrained into the foot vortex. The foot vortex was centred at $z/c = 0.12$, $y/c = -0.11$ with a hydraulic diameter of $0.02c$. The maximum vorticity (Ω_x) within foot vortex was -72. The lower edge vortex was located close to the inboard face of the endplate at $z/c = -0.05$, $y/c = 0.01$. It was noted that the addition of the endplate feet (Figure 5.6(a)) seemingly moved the lower edge vortex outwards and upwards while reducing the hydraulic diameter. The hydraulic diameter of the lower edge vortex was $0.03c$ with a maximum vorticity of $\Omega_x = -91$. Without endplate feet the hydraulic diameter of the lower edge vortex and corresponding maximum vorticity were $0.04c$ and -116 respectively. A shear layer originating from the lower edge of the endplate was entrained into the lower edge vortex. The boundary layer along the ground plane was observed as a region of positive vorticity.

Decreasing the ride height to $0.211c$ resulted in the flow field remaining largely unchanged (Figure 7.6(b)). The foot vortex, lower edge vortex and associated shear layers were present. The vertical location and hydraulic diameter of the lower edge vortex remained constant however the centre of the vortex moved inboard to $z/c = -0.07$. The increased pressure difference between the freestream flow and underneath the wing resulted in the vorticity within the lower edge vortex increasing, achieving a maximum of $\Omega_x = -116$. The foot vortex dilated ($d_h = 0.03c$) moving inboard and downward. The vorticity within the foot vortex significantly decreased to $\Omega_x = -30$. The vorticity within the centre of the lower edge vortex was seemingly less than the surrounding area. It was noted during the investigation that the centrifugal forces within the core of the vortex forced the seeding particles outwards. The lack of seeding within the vortex core consequently resulted in an artificially low value of vorticity.

Figure 7.7(a) presents the wing tip flow field for a ride height of $0.169c$ (near region g/i boundary). For this ride height and below a breakdown of the foot vortex was observed.

The lower edge vortex dilated with a hydraulic diameter of $0.04c$. The vertical location of the vortex was constant however the centre of the vortex moved inboard to $z/c = -0.08$. As before the lack of seeding within the core of the lower edge vortex resulted in an artificially low value of vorticity. Figure 7.7(b) presents the wing tip flow field for a ride height of $0.141c$. Reducing the ride height to $0.141c$ (region i) caused the lower edge vortex to significantly dilate ($d_h = 0.07c$). The lower edge vortex moved inboard and upward with the vorticity significantly reducing to $\Omega_x = -45$. The upper edge vortex was present for this ride height located outboard of the top of the endplate. Above this ride height the upper edge vortex was present. However, the physical dimensions of the data field prevented the vortex being detected.

The wing tip flow field obtained for $h/c = 0.099$ with decreasing ride height (region j) indicated a breakdown of the lower edge vortex (Figure 7.8(a)). For this ride height and below the lower edge vortex was not present. A region of anti-clockwise recirculation was present in place of the lower edge vortex. The upper edge vortex was centred at $z/c = 0.07$, $y/c = 0.33$ with a hydraulic diameter of $0.02c$. Decreasing the ride height further through $0.063c$ (Figure 7.8(b)) to $0.053c$ (Figure 7.9(a)) resulted in the wing tip flow field remaining largely unchanged. The lower region of recirculation became increasingly elongated in a spanwise sense. The upper edge vortex was unaffected.

Figures 7.9(b) presents the wing tip flow field for $h/c = 0.063$ with increasing ride height (region n). When compared to Figure 7.8(b) minimal variations in flow field were observed. The upper edge vortex and lower recirculation region were seemingly independent of ride height direction. Table 7.1 presents quantitative data concerning the upper and lower edge vortices and the foot vortex for various ride heights.

7.4 Surface Flow Field

Figures 7.10 to 7.15 present surface streaklines obtained at various ride heights using an oil flow visualisation technique (Section 3.6.3). Ride heights of $0.317c$, $0.169c$, $0.141c$, $0.099c$ and $0.063c$ were investigated, corresponding to ride heights within each of the four force regions. To investigate force regions j and n a ride height of $0.063c$ was investigated with both increasing and decreasing ride heights. Within each figure the subfigures (a), (b) and (c) present the streaklines on the suction surface, inboard surface of the starboard endplate and lower surface of the starboard foot respectively. The streaklines obtained on

the pressure surfaces of the wing were largely similar to those observed without endplate feet. The variations within the pressure surface streaklines with ride height were seemingly independent of the presence of endplate feet.

The streaklines obtained at a ride height of $0.317c$ (region g) are presented in Figure 7.10. The streaklines on the surfaces of the wing indicated a fully attached flow field. Transition at the centre span of the main element and flap occurred at $x/c = 0.10$ and 0.53 respectively. The lines of transition were slightly curved, with transition moving downstream towards the wing tips. The streaklines on the inboard face of the endplate (Figure 7.10(b)) indicated the presence of a rotating flow, the lower edge vortex. The vortex extended along the full length of the endplate. The lower boundary of the vortex was distinct within the streaklines, inclined to the base of the endplate. The vortex was smaller and located higher on the endplate when compared to the situation without endplate feet (Figure 5.10(a)). The streaklines on the lower surface of the endplate foot (Figure 7.10(c)) indicated the foot vortex originating from the upstream, outboard edge of the foot. The foot vortex translated inboard with downstream location. Inboard of the foot vortex the streaklines indicated a change in flow direction from streamwise to spanwise.

Figure 7.11 presents the streaklines obtained at a ride height of $0.169c$. This ride height was near the boundary between force regions g and i. The streaklines over all surfaces were largely similar to those obtained at $h/c = 0.317$. The three-dimensionality within the main element transition line was increased, in particular near the wing tips. Transition occurred on the main element suction surface at $x/c = 0.10$ for the centre span location. The streamwise location of transition on the flap suction surface remained consistent with that observed at the $h/c = 0.317$. The streaklines on the endplate (Figure 7.11(b)) indicated a dilation of the lower edge vortex. The endplate foot streaklines again indicate the foot vortex originating from the upstream, outboard edge of the endplate foot as before.

Decreasing the ride height to $0.141c$ resulted in increased three-dimensionality within transition on the main element (Figure 7.12(a)). This ride height was typical for force region i. The centre span locations of transition on the main element and flap were consistent with those observed for $h/c = 0.317$. However, the curvature of the line of transition on the main element was significantly increased. The endplate streaklines again indicated the presence of the lower edge vortex. The streaklines on the endplate foot indicated the presence of the foot vortex initially. However, towards the downstream edge of the foot the vortex seemingly burst.

Figures 7.13 and 7.14 present surface streaklines for ride height of $0.099c$ and $0.063c$ respectively. In both cases results were obtained with a decreasing ride height (region j). The streaklines on the suction surfaces of the wing remained largely constant. At the centre span of the wing transition occurred at $x/c = 0.10$ and 0.53 on the main element and flap respectively for both ride heights. The endplate streaklines indicated the absence of the lower edge vortex with the surface flow field becoming less stable for $h/c = 0.063$. For both ride height the foot vortex was indicated on the upstream section of the endplate foot. Further downstream the foot vortex burst. A small region of separation was observed on the main element suction surface for $h/c = 0.063$ with decreasing ride height. The region of separation was located at the centre span, originating from $x/c = 0.42$ and extending to the main element trailing edge.

Figure 7.15 presents streaklines obtained for a ride height of $0.063c$ with increasing ride height (region n). When compared to Figure 7.14 the most prominent alteration in surface flow field was on the suction surfaces of the wing and the endplate foot. A large region of separation was present on the flap with increasing ride height (Figure 7.15(a)), a feature which was not present with decreasing ride height. The separation on the flap contained two nodes and two regions of counter-rotation. A smaller region of separation was observed on the main element close to the trailing edge originating from $x/c = 0.41$. Transition on the main element was more uniform across the main element with increasing ride height. Transition occurred at $x/c = 0.12$ on the main element. The streaklines on the endplate were independent of ride height direction. The streaklines on the foot indicated the absence of the foot vortex, instead a fully attached flow was observed.

7.5 Surface Pressures

Surface pressures were obtained to provide quantitative data concerning the influence of endplate feet on the surface flow field. Chordwise and spanwise surface pressures were measured on the wing. In addition surface pressures were measured on the inboard face of the port endplate and the lower face of the port endplate foot. The ride heights investigated were $0.634c$, $0.317c$, $0.211c$, $0.141c$, $0.099c$, $0.063c$ and $0.053c$. These ride heights corresponded to a combination of ride heights investigated without endplate feet and ride heights within each of the four force regions previously identified. To investigate force regions j and n the lowest three ride heights were investigated with both increasing and

decreasing ride heights.

7.5.1 Chordwise Pressures at Centre Span

The chordwise centre span surface pressures at various ride heights for the wing equipped with endplate feet are presented in Figure 7.16. For high ride heights (Figure 7.16(a)) the chordwise distribution of surface pressures on the wing was largely similar to those obtained without endplate feet (Section 5.5.1). A rapid flow acceleration and subsequent pressure recovery was observed on the wing, as for the case without endplate feet. Identical variations within the surface pressures with ride height were also observed. For such ride heights stagnation was consistently located at $x/c = 0.01$ and 0.46 on the main element and flap respectively. In addition maximum suction was consistently observed at $x/c = 0.02$ and 0.48 on the main element and flap respectively.

Decreasing the ride height to $0.099c$ resulted in significant variations within the surface pressures on the main element (Figure 7.16(b)). This ride height was typical for force region *j*. As for the case without endplate feet a plateau of suction was observed directly downstream of the main element. The suction over the flap was reduced when compared to $h/c = 0.141$ in contrast to the trend observed for high ride heights. The flap surface pressures and main element pressure surface pressures were independent of ride height direction. However the main element suction was significantly affected with increased suction observed for decreasing ride heights. This dependency of the main element suction on ride height direction was also observed for $h/c = 0.063$. Compared to higher ride heights, a reduction in the pressure surface pressures was observed. As for the case without endplate feet the distribution of main element suction was largely altered for the lowest two ride heights. The suction peak moved downstream followed by a rapid pressure recovery.

In addition to the dependency of main element suction on ride height direction, the flap suction was also dependent for $h/c = 0.053$. The flap suction distribution with decreasing ride height conformed to the trends observed for higher ride heights. However, with increasing ride height the flap suction was significantly decreased from the flap leading edge to $x/c = 0.58$. Further downstream a constant level of suction was observed ($C_P \approx -1.2$). The streaklines obtained on the flap suction surface for $h/c = 0.063$ within force region *n* (Figure 7.15) indicated the presence of a large region of separation. The reduced suction over the centre span of the flap at $h/c = 0.053$ suggested that the region of separation persisted to lower ride heights.

For all ride heights the addition of endplate feet increased the suction and reduced the pressure surface pressures on both the main element and flap (Figure 7.17). Table 7.2 lists the quantitative data concerning the chordwise surface pressures at the wing centre span.

7.5.2 Chordwise Pressures Near Wing Tip

Figure 7.18 presents the chordwise surface pressure obtained near the wing tip for $h/c = 0.317$. For comparison reasons the surface pressures obtained with and without endplate feet are presented. The addition of endplate feet caused a reduction in the pressures surface pressures on both the main element and flap. In addition increased suction was observed with the addition of endplate feet, again on both the main element and flap. The distribution of the surface pressures was identical to that observed without endplate feet. For high ride heights (Figure 7.19(a)) the variation the in surface pressures due to the addition of endplate feet was similar to that observed for $h/c = 0.317$. Stagnation was consistently achieved at $x/c = 0.01$ and 0.46 on the main element and flap respectively. The variations in surface pressures with ride height were consistent with those observed without endplate feet (Section 5.5.3).

The chordwise surface pressures obtained at low ride height are presented in Figure 7.19(b). The variation in surface pressures due to the addition of the endplate feet remained consistent with that observed for higher ride heights. Stagnation for low ride heights was located at $x/c = 0.01$ and 0.46 on the main element and flap respectively. The surface pressures on both the main element and flap were independent of the ride height direction for $h/c = 0.099$ and 0.063. The surface pressures on the main element were also independent of ride height direction for $h/c = 0.053$. However, the suction surface pressures on the flap indicated a dependency on ride height direction. The suction surface pressures for the decreasing ride height case (region j) conformed to the trends observed at higher ride heights. However, with increasing ride heights (region n) decreased suction was observed between the flap leading edge and $x/c = 0.56$. Further downstream the suction conformed to that observed with decreasing ride heights.

7.5.3 Integrated Chordwise Surface Pressures

The integrated chordwise surface pressures are presented in Figure 7.20(a). The sectional downforce at the wing centre span (C_{lc}), near the port wing tip (C_{lt}) and the combined total (C_l) are presented for various ride heights. For all ride heights the centre span sectional

downforce was significantly greater than the wing tip sectional downforce. Reducing the ride height for $h/c > 0.141$ resulted in the centre span and wing tip sectional downforce increasing asymptotically. Below a ride height of $0.141c$ reducing the ride height resulted in the wing tip sectional downforce decreasing. The centre span sectional downforce was dependent on ride height direction for ride heights below $0.141c$. Accordingly the total sectional downforce was also dependent on ride height direction. The centre span sectional downforce was significantly reduced for the increasing ride height case (region n). Decreasing the ride height from $0.141c$ (region j) caused the centre span sectional downforce to increase, achieve a maximum at a ride height of $0.099c$, then decrease.

The contributions to the centre span and wing tip sectional downforce by the flap and main element are presented in Figure 7.20(b). For all ride heights the wing tip sectional downforce generated by the main element and flap was independent of ride height direction. The centre span sectional downforce however, was dependent on ride height direction for $h/c \leq 0.141$. The centre span sectional downforce on the main element was particularly dependent on ride height direction.

7.5.4 Spanwise Pressures

The spanwise surface pressures on the main element for various ride heights are presented in Figure 7.21. The spanwise surface pressures obtained for $h/c = 0.634$ without endplate feet have been included for comparison reasons. The addition of endplate feet decreased the pressure surface pressures and significantly increased the suction surface pressures over the entire wing span. This variation was true for all ride heights.

The main element pressure surface spanwise distribution was independent of ride height, decreasing linearly from the centre span towards the wing tips. Reducing the ride height resulted in the pressure surface pressures decreasing in magnitude. The suction surface distribution was more dependent on ride height. For ride heights above $0.099c$ the suction asymptotically decreased from a local maximum at the centre span. The corresponding local minimum was achieved at the spanwise location closest to the wing tip. Reducing the ride height for $h/c > 0.099$ resulted in increased values of suction across the entire span of the wing.

For all ride heights the pressures surface pressures on the main element were independent of ride height direction. However, a dependency on ride height direction was observed in the main element suction surface pressures for $h/c \leq 0.099$. For a ride height of $0.099c$

the overall spanwise distribution was largely similar to that observed at higher ride heights. Decreased values of suction were observed for increasing ride heights (region n), particularly towards the centre span location. The centre span chordwise surface pressures indicated a significant variation in the surface pressures obtained with increasing and decreasing ride height (Figure 7.16(b)). The dependency on ride height was therefore present within the spanwise surface pressures. However, the spanwise surface pressures indicated that this dependency on ride height variation for $h/c = 0.099$ was limited to the region close to the centre span of the wing.

The spanwise distribution of suction obtained at $0.063c$ with decreasing ride height (region j) conformed to the trends observed at higher ride heights. However, the increasing ride height case did not conform (region n). A region of constant suction was noted between $z/c = -0.53$ and the centre span. In addition decreased values of suction were observed between $z/c = -0.18$ and the centre span for the increasing ride height case. For the lowest ride height ($h/c = 0.053$) a region of constant suction close to the centre span was observed for both the increasing and decreasing ride heights. Increased suction was observed between the wing tip and $z/c = -0.26$ for the increasing ride height case. However, decreased suction was observed between $z/c = -0.26$ and the centre span for the increasing ride height case.

The spanwise distribution of surface pressures on the flap at various ride heights is presented in Figure 7.22. The spanwise surface pressures obtained for $h/c = 0.634$ without endplate feet have been included. Similar to the main element, the addition of endplate feet decreased the pressure surface pressures and increased the suction surface pressures over the entire wing span. This variation was true for all ride heights.

The spanwise distribution of pressure surface pressures remained consistent with that observed without endplate feet. Reductions in ride height caused the pressure surface pressures to decrease over the entire wing span. The suction surface pressures were more dependent on ride height. For higher ride heights ($h/c \geq 0.141$) the spanwise distribution of suction could be separated into two regions. Between the centre span and $z/c = -0.44$ a region of relatively constant suction was observed. Towards to the wing tip the suction increased. Within this range of ride heights the suction increased in magnitude with reductions in ride height, especially near to the wing tip. The increased suction towards the wing tip was a direct result of the lower edge vortex. The increases in suction with ride height reductions were a result of the lower edge vortex increasing in strength (Table 7.1).

Reducing the ride height below $0.141c$ resulted in decreased values of suction. The

wing tip flow field indicated that for $h/c \leq 0.141$ the lower edge vortex was absent. The corresponding suction near to the tip of the flap was therefore significantly reduced, as observed. For the lowest three ride heights ($h/c = 0.099$, 0.063 and 0.053) the spanwise surface pressures on the flap were independent of ride height direction. The pressure surface pressures conformed to the trends observed for higher ride heights. The suction decreased in magnitude with reductions in ride height as before. At the lowest ride height a relatively constant level of suction was observed over the span of the wing.

7.5.5 Endplate Pressures

The surface pressures obtain on the inboard face of the port endplate for various ride heights are presented in Figure 7.23. Two trends in suction variation were observed; the first for higher ride heights ($h/c \geq 0.141$), and the second for lower ride heights ($h/c < 0.141$). For higher ride heights (regions g and i) reducing the ride height resulted in increased suction at all vertical locations. Within this range of ride heights maximum suction was consistently observed at the lowest vertical location. This location corresponded to the lower edge vortex. Decreasing the ride height below $0.141c$ resulted in decreased suction at all vertical locations. The wing tip flow field indicated that the lower edge vortex was absent for ride heights below $0.141c$. Accordingly the suction decreased, in particular at the lowest vertical location. For the lowest three ride heights (regions j and n) the suction observed was independent of ride height direction. The suction was relatively constant, decreasing in magnitude with reductions in ride height. The addition of endplate feet at ride heights below $0.317c$ increased the suction at all vertical locations. For ride heights above $0.317c$ the suction at the lowest vertical location decreased with the addition of endplate feet.

7.5.6 Endplate Foot Pressures

The surface pressures obtained on the lower surface of the port endplate foot for various ride heights are presented in Figure 7.24. Suction was present over the span of the foot for all ride heights. Reductions in ride height between $0.634c$ and $0.053c$ (regions g to j) resulted in increased suction at all spanwise locations. The spanwise distribution also remained constant. Initially the suction increased from the outboard edge of the foot to $z/c = 0.094$. Further inboard the suction remained relatively constant until $z/c = 0.135$. The wing tip flow field and surface flow field indicated the presence of a vortex, the foot vortex, centred within this spanwise region. The increased values of suction corresponded

to the influence of the foot vortex. Further inboard the suction on the foot decreased. For ride heights below $0.211c$ the wing tip flow field indicated the absence of the foot vortex (Table 7.1). However, the surface streaklines indicated the presence of the foot vortex at the streamwise location at which the surface pressures were measured. The suction generated by the foot vortex was accordingly observed within the surface pressures.

The surface pressures for the lowest three ride heights indicated a dependency on the direction of ride height variation. In all cases decreased suction was observed over the span of the foot with increasing ride height (region n). The surface flow field at $h/c = 0.063$ with increasing ride height (Figure 7.15(c)) indicated the absence of any vortical flow. Accordingly the spanwise suction distribution was of a more constant value when compared the the decreasing ride height cases.

7.6 Discussion

The discussion of the results obtained for the wing equipped with endplate feet will be divided into individual sub-sections. The influence of endplate feet on the flow field generated by the wing and corresponding force variations will be discussed first. The individual force regions identified within the downforce (Figure 7.1) will then be discussed.

7.6.1 Influence of Endplate Feet

The addition of endplate feet to the wing resulted in significant variations within the forces and flow field generated by the wing. The downforce and pitching moment was increased through the addition of endplate feet for all ride heights. For lower ride heights ($h/c \leq 0.236$) a much greater increase in downforce and pitching moment was observed. The streaklines on the surfaces of the wing were largely unaffected by the addition of endplate feet. However, the chordwise surface pressures indicated increased flow acceleration beneath the wing with endplate feet (Figure 7.17). Accordingly increased suction was observed over the entire span of both the main element and flap. In addition increased suction was observed on the inboard face of the port endplate. The cause of the increased suction beneath the wing was indicated within the wing tip flow field. Figure 7.25 presents velocity vectors downstream of the port wing tip at $x/c = 0.995$ for $h/c = 0.317$. The presence of the endplate foot and the foot vortex seemingly constrained the flow beneath the endplate foot. The resulting convergent-divergent channel accelerated the flow beneath the endplate

foot increasing the suction beneath the wing as observed. This spanwise pumping effect will be referred to as the 'foot pumping mechanism'.

The surface pressures on the lower surface of the port endplate foot indicated suction for all ride heights. The wing tip flow field (Figure 7.25) indicated that the flow drawn underneath the endplate feet was accelerated. The corresponding suction acted upon the endplate feet as observed. Additional suction was also generated by the foot vortex. The suction generated by the endplate feet operated in conjunction with the increased suction beneath the wing. The additional suction generated by the presence of the endplate feet resulted in the fixed downforce and pitching moment increase observed. In summary the presence of endplate feet enhanced the downforce and pitching moment generated by the wing through two force enhancement mechanisms.

The drag generated by the wing was decreased with the addition of endplate feet. It has been shown in Chapter 5 that the lift induced drag contributed greatly to the overall drag observed. Figure 7.26 presents the dependency of drag on the square of the downforce for the wing equipped with endplate feet within various force regions. Through comparisons with Figure 5.25 it was noted that the gradient of the variation within force region g was reduced when compared to force region a. The induced drag factor (k_i) was calculated at 7.80 and 16.78 for the wing without and with endplate feet respectively (Section 2.1.2). The cause of the increase in k_i was attributed to the variation in wing tip flow field. The addition of endplate feet decreased the strength of the lower edge vortex from $\Omega_x = -116$ to -90 at a ride height of $0.317c$. Accordingly the upwash generated by the wing was reduced hence the induced drag was also reduced. Therefore the reduction in drag observed with the addition of endplate feet was caused by a reduction in the upwash of the wing.

The influence of endplate feet on the performance of a multi-element wing in ground effect is a topic novel to this research. The effects of such flow control devices on the flow field generated by a wing in ground effect have not previously been reported.

7.6.2 Force Region *g*

Force region g occurred at ride heights greater than $0.158c$. Reductions in ride height caused the downforce, drag, pitching moment and wing efficiency to increase asymptotically. For ride height above $0.236c$ the force variations were largely similar to those observed without endplate feet (region a). The surface data and off-surface flow field indicated largely similar force enhancement mechanisms to those observed within force region a. Accordingly the

force variations were similar. A relatively constant offset was observed between forces obtained with and without endplate feet due to the additional force enhancement mechanisms generated by the endplate feet.

It was noted that force region *g* persisted to a lower ride height when compared with force region *a*. It has been shown that the lower boundary of force region *a* was caused by the breakdown of the lower edge vortex (Chapter 5). The wing tip flow field obtained with endplate feet indicated the presence of the lower edge vortex beyond the lower boundary of force region *a*. As mentioned previously the addition of endplate feet significantly reduced the strength of the lower edge vortex. In addition it was noted that the addition of endplate feet increased the adverse pressure gradient over the suction surfaces of the wing. This persistence of the lower edge vortex in a increasingly adverse pressure gradient may appear to be unrealistic. An explanation for this seemingly unrealistic behaviour of the lower edge vortex was offered by Spall *et al* [149] in terms of the Rossby number (R_s). The Rossby number for an isolated wing tip vortex is presented in Equation 7.1 [149].

$$R_s = \frac{u}{r^* \, \omega} \tag{7.1}$$

where ω represents the maximum rotation rate within the vortex and r^* is the radial distance from the vortex centre at which the maximum rotation rate occurs. Spall *et al* noted that for a fixed Reynolds number the breakdown of a wing tip vortex was directly dependent on the Rossby number. Vortex breakdown occurred with low values of Rossby number ($R_s < 0.5$) whereas high values of Rossby number ($R_s > 0.6$) corresponded to stable wing tip vortices. It was noted that the addition of endplate feet increased the velocity beneath the wing and decreased the rotation rate within the lower edge vortex. Assuming negligible variation in r^*, it is hypothesised that the addition of endplate feet increased the Rossby number of the lower edge vortex. Accordingly the lower edge vortex persisted to a lower ride height with endplate feet even though the strength of the lower edge vortex was reduced and the imposed pressure gradient was more adverse, as observed.

The presence of the force enhancement mechanisms until a lower ride height resulted in increased values of downforce, particularly towards the lower boundary of region *g*. Within force region *g* the drag was observed to be linear dependent on the square of the downforce (Figure 7.26). The increases in drag with ride height reductions were therefore primarily due to increases in lift induced drag. The increased downforce on the flap resulted in increased values of pitching moment with ride height reductions.

7.6.3 Force Region *i*

Within force region *i* ($h/c = 0.158$ to 0.127) reductions in ride height caused the downforce to increase linearly. The drag also increased however, reductions in pitching moment were observed. A distinct transition between force regions *g* and *i* was observed. The streaklines obtained within force region *i* indicated that the surface flow field remained largely unchanged when compared to force region *g*. The chordwise surface pressures indicated increased levels of suction with reductions in ride height, as for higher ride heights. A contributing factor to the reduced rate of downforce enhancement was observed within the wing tip flow field. It was noted that the lower edge vortex dilated significantly between $h/c = 0.169$ (region *g*) and $h/c = 0.141$ (region *i*), a sign of imminent breakdown [148].

It was observed that the sectional downforce generated by the main element within force region *i* increased with reductions in ride height. However the flap sectional downforce reduced slightly, particularly near the wing tip. The spanwise surface pressures on the flap indicated a slight reduction in suction however, the endplate pressure indicated an increase in suction. It is surmised that the reduced rate of downforce enhancement within force region *i* was a result of the gradual breakdown of the lower edge vortex. The removal of the force enhancement mechanism due to the lower edge vortex caused a reduced rate of downforce increase. The flap loading decreased, observed as reductions in pitching moment while increased values of drag were observed due to increased values of lift induced drag.

7.6.4 Force Region *j*

Force region *j* occurred at ride heights below $0.127c$ for the case with decreasing ride height. The downforce and drag increased initially then decreased until a minimum ride height was achieved. The pitching moment decreased rapidly within this force region. The wing tip flow field, surface streaklines indicated an absence of the lower edge vortex. Within this force region the sectional downforce due to the flap decreased. The main element sectional downforce increased initially due to increased flow acceleration beneath the wing, as indicated in the chordwise surface pressures. The streaklines obtained at $h/c = 0.063$ with decreasing ride height indicated a region of separation at the trailing edge of the main element. This stalling of the main element caused the downforce to decrease significantly. Reductions in drag were observed due to reductions in the lift induced drag component. The reduction in flap loading caused the pitching moment to decrease significantly, as observed.

In summary the reduction in forces within force region j was due primarily to stalling of the main element.

7.6.5 Force Region n

Force region n occurred at the same ride heights as force region j. However force region n was observed with increasing ride heights. The downforce obtained within force region n was significantly reduced when compared to force region j. A similar variation was observed without endplate feet (force regions e and f). The streaklines indicated that within force region n a large region of separation was present on the flap suction surface (Figure 7.15). This flow feature was not present within force region j. The stalling of the flap was observed within the sectional downforce, particularly on the main element at the centre span location.

The stalling of the flap resulted in a reduction in drag, in contrast to stalling of a wing in freestream. However it must be noted that the significant reduction in downforce caused a significant reduction in lift induced drag. Hence a reduction in drag was observed. The stalling of the flap also resulted in a significant reduction in pitching moment due to the reduction in flap loading.

It was noted that the forces obtained for a single static ride height below $0.127c$ always reverted to the force values corresponding to region n. In addition force region j was only present when the ride height was first increased then decreased. As for the case without endplate feet (Chapter 5) the stalling of the flap was attributed to the run-up stage of the wind tunnel, in particular the Reynolds number variation.

7.7 Chapter Summary

A systematic experimental investigation into a multi-element wing equipped with endplate feet in ground effect was conducted. The influence of endplate feet on the performance of the wing was quantified. In addition the flow field mechanisms responsible for the performance variation were identified. The addition of endplate feet was found to increase the downforce generated by the wing while significantly reducing the drag. The endplate feet generated additional force enhancement mechanisms while strengthening the preexisting force enhancement mechanisms. At low ride heights the downforce was found to be dependent on the direction of ride height variation due to separation over the flap.

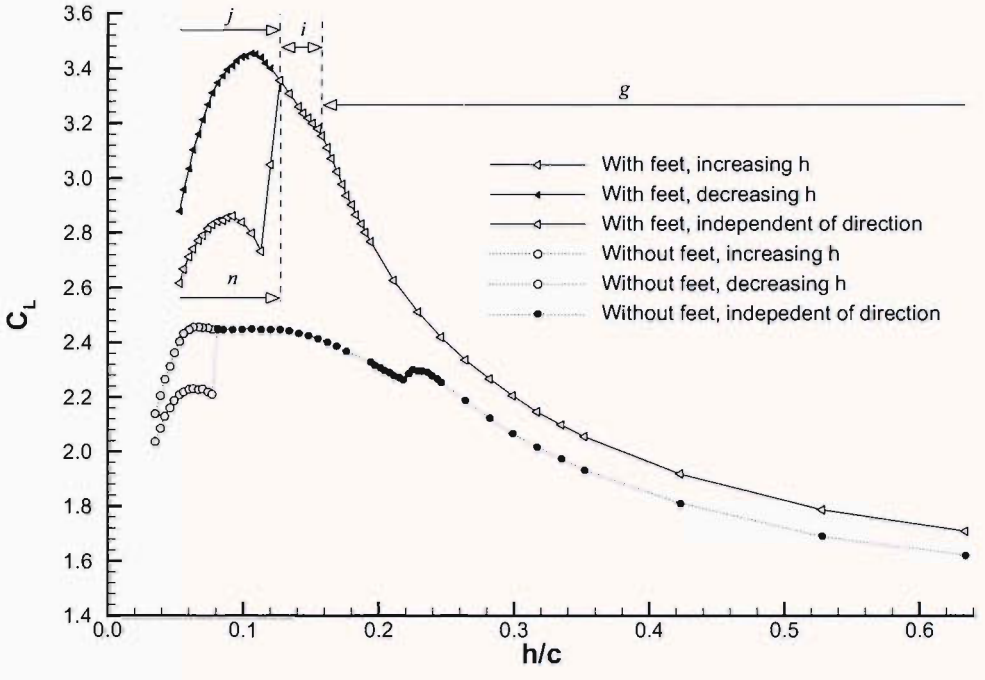

Figure 7.1: Variation of downforce coefficient with ride height. Wing equipped with endplate feet.

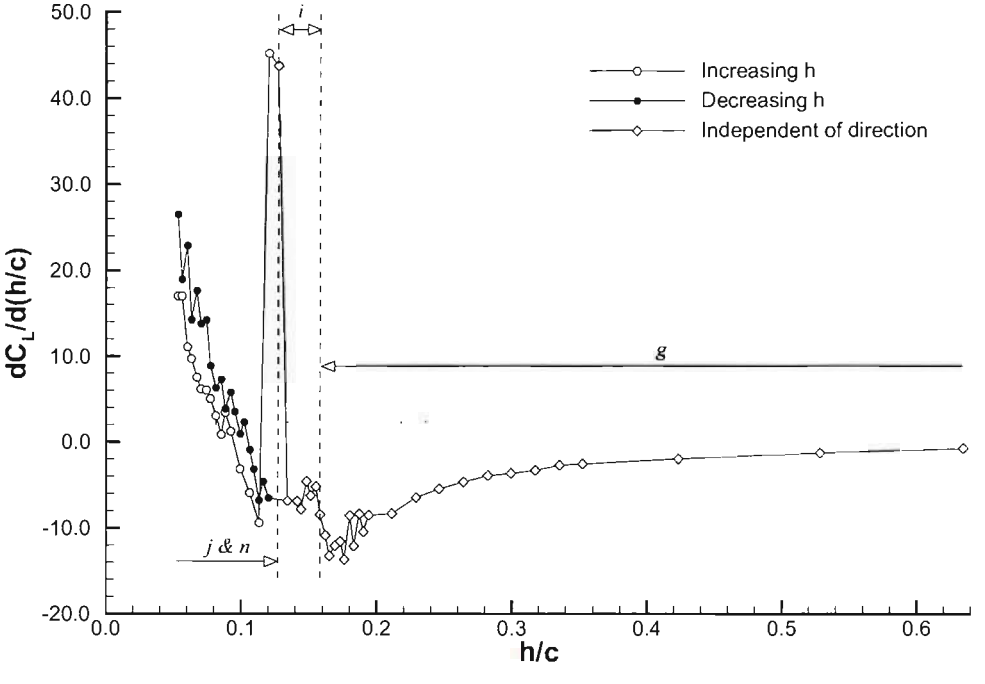

Figure 7.2: Variation of downforce slope with ride height and definition of the force regions. Wing equipped with endplate feet.

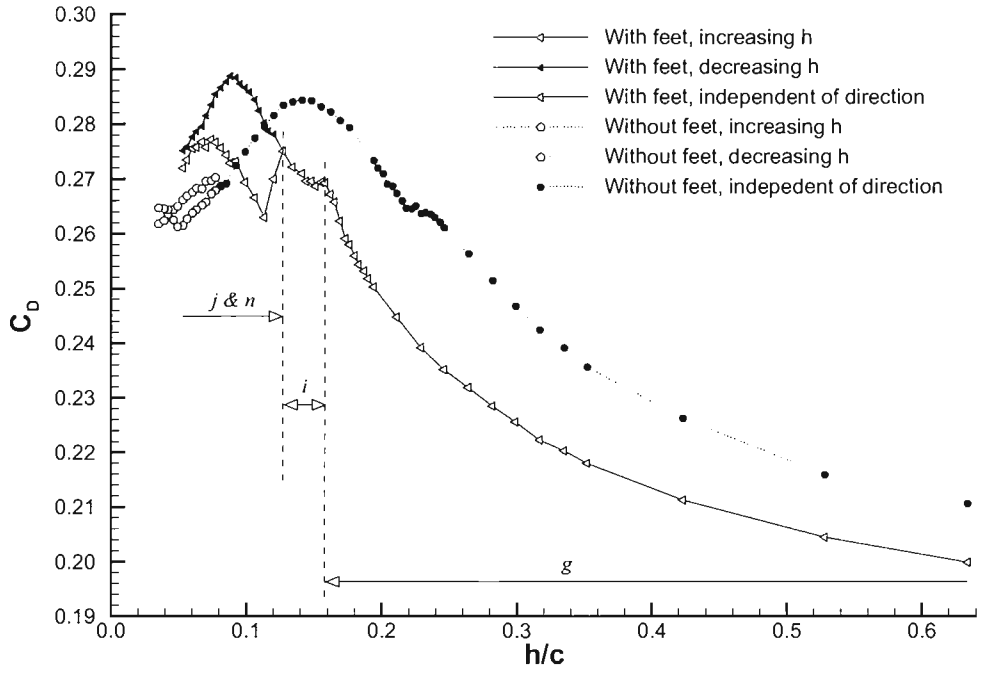

Figure 7.3: Variation of drag coefficient with ride height. Wing equipped with endplate feet.

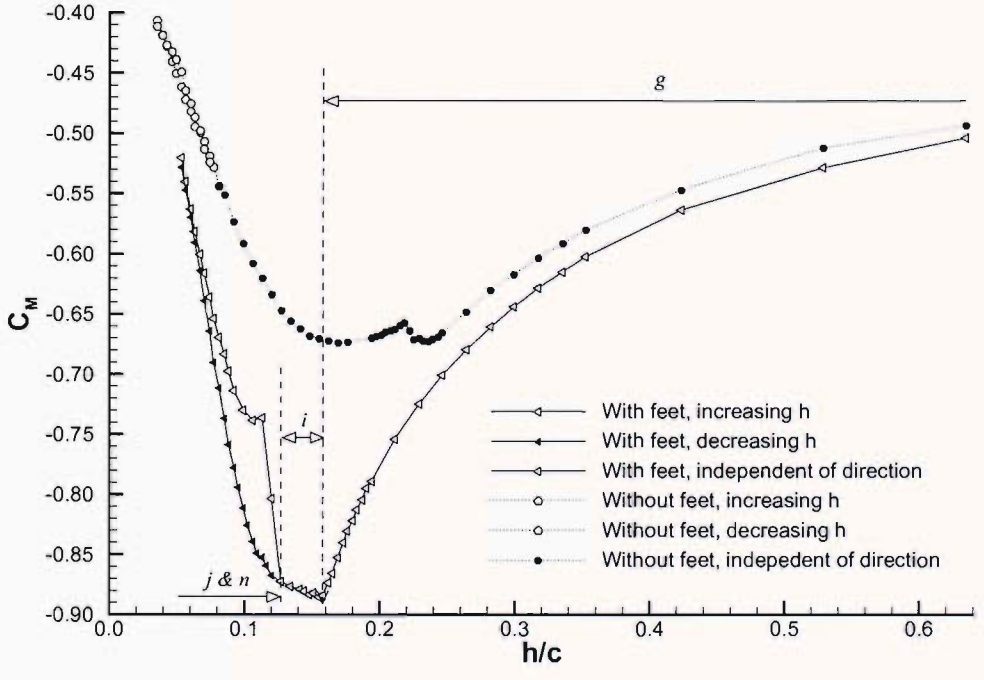

Figure 7.4: Variation of pitching moment coefficient with ride height. Wing equipped with endplate feet.

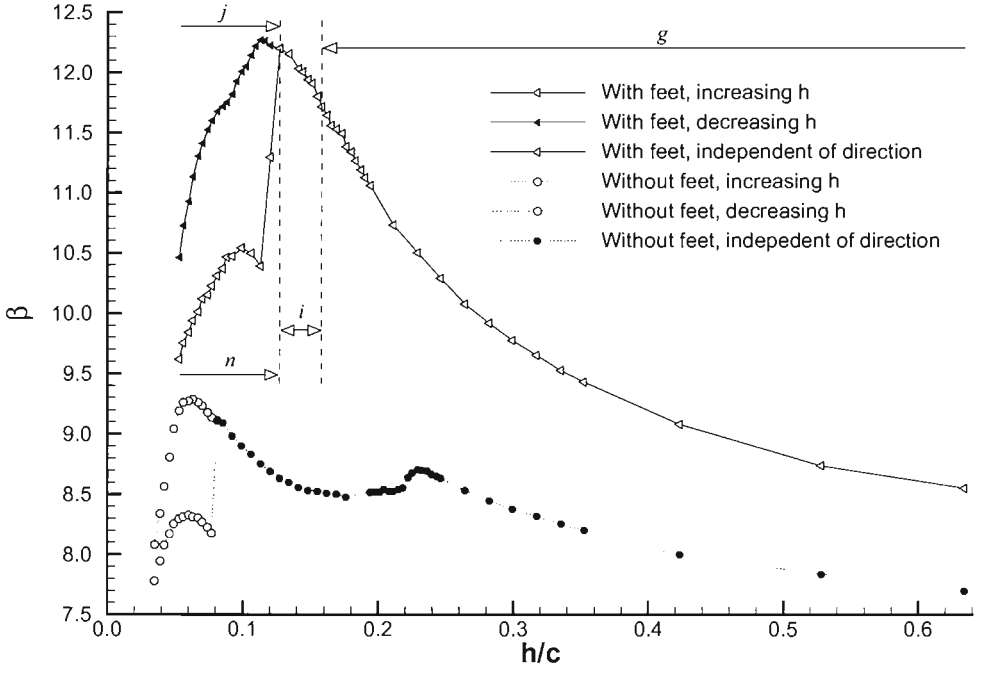

Figure 7.5: Variation of wing efficiency with ride height. Wing equipped with endplate feet.

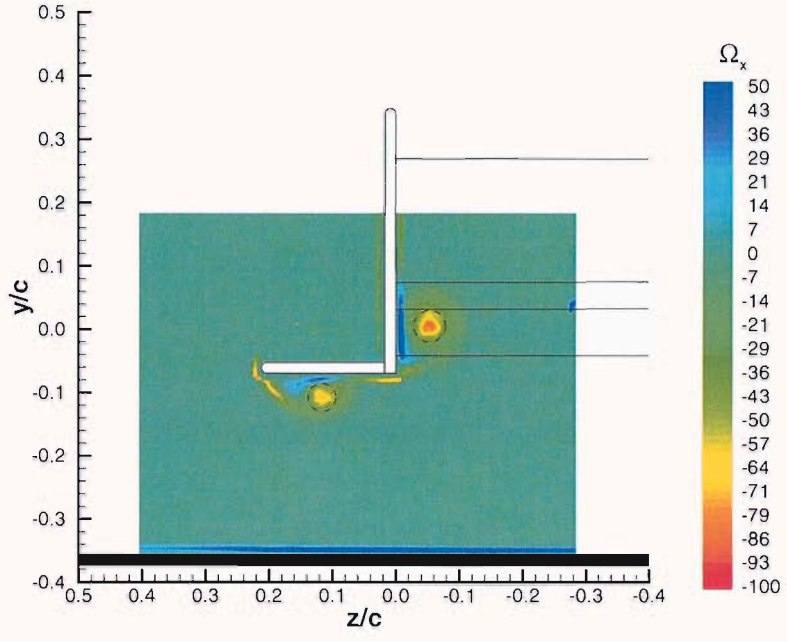

(a)

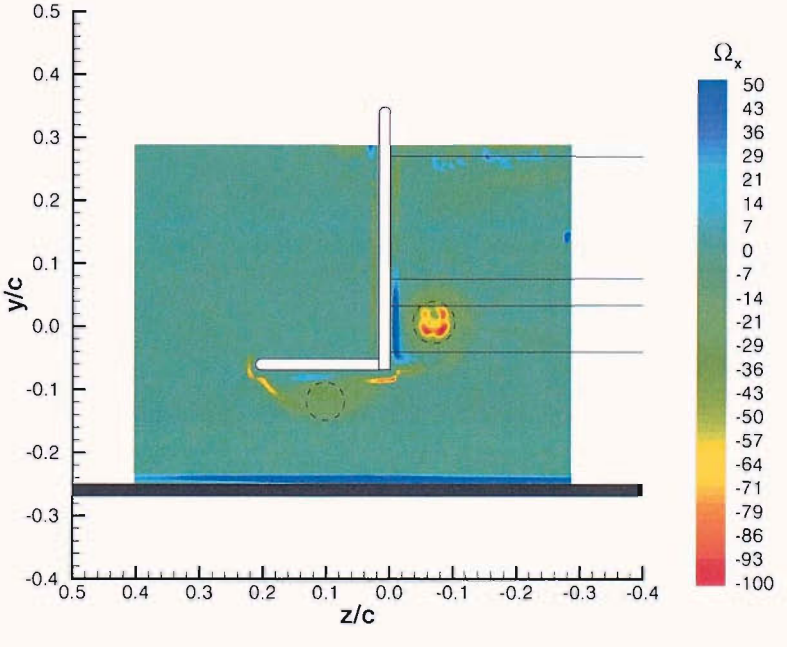

(b)

Figure 7.6: Time-averaged non-dimensional vorticity contours of the port wing tip at $x/c = 0.995$ with endplate feet; (a) $h/c = 0.317$ (region g). (b) $h/c = 0.211$ (region g).

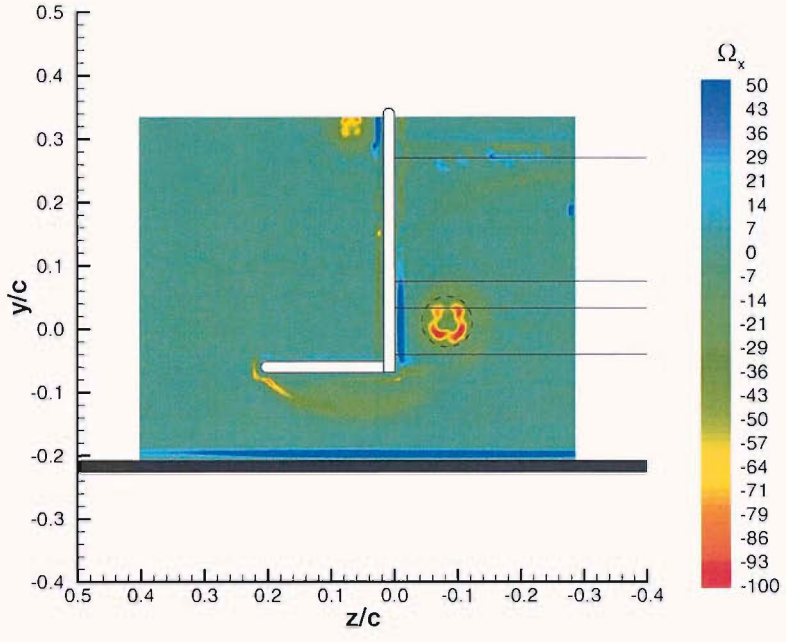

(a)

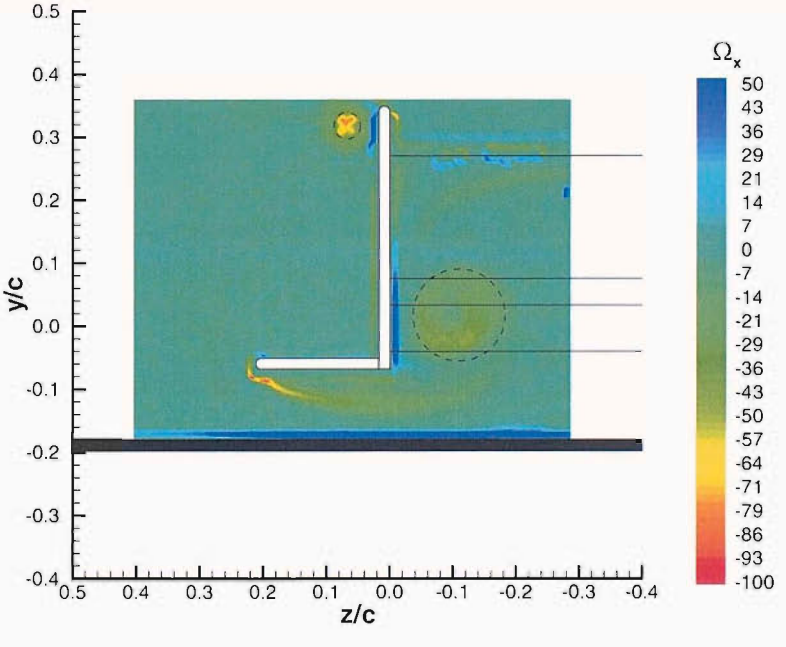

(b)

Figure 7.7: Time-averaged non-dimensional vorticity contours of the port wing tip at $x/c = 0.995$ with endplate feet; (a) $h/c = 0.169$ (region g/i boundary), (b) $h/c = 0.141$ (region i).

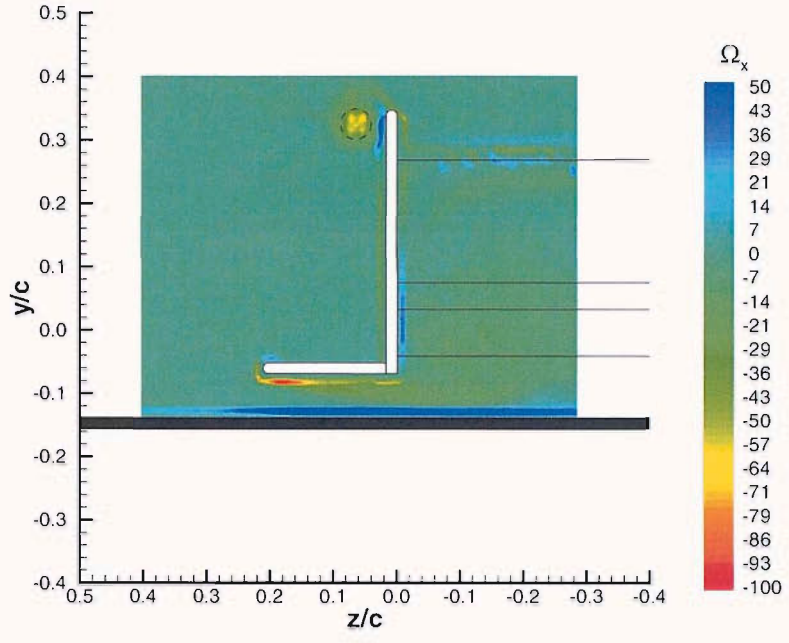

(a)

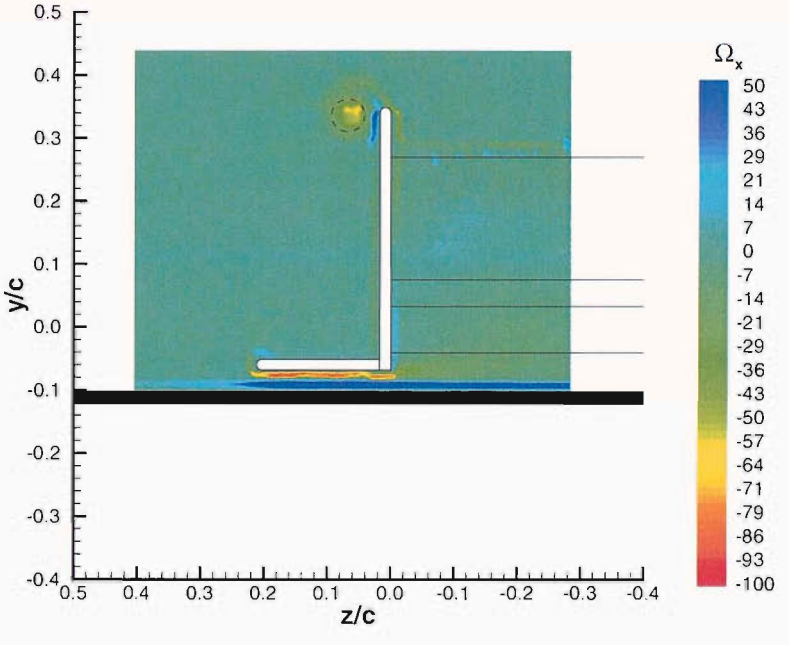

(b)

Figure 7.8: Time-averaged non-dimensional vorticity contours of the port wing tip at $x/c = 0.995$ with endplate feet; (a) $h/c = 0.099$ decreasing h (region j), (b) $h/c = 0.063$ decreasing h (region j).

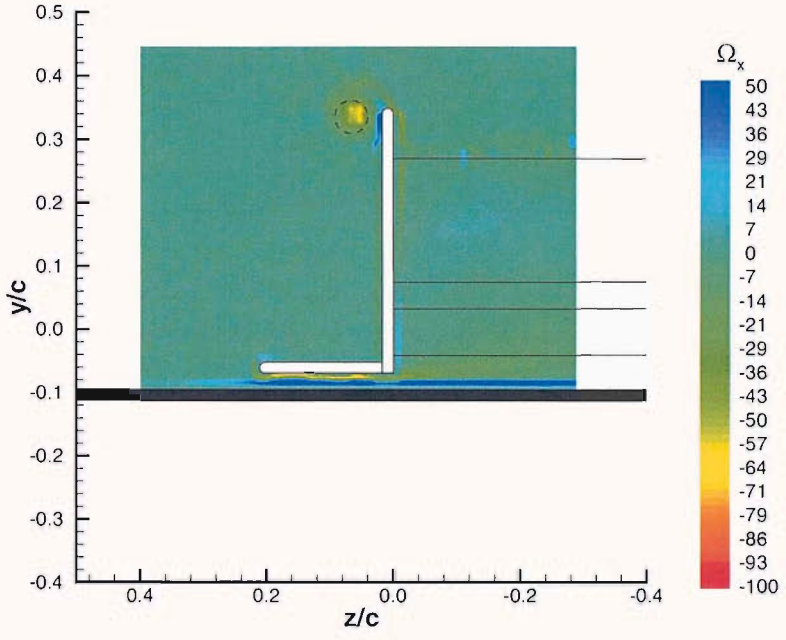

(a)

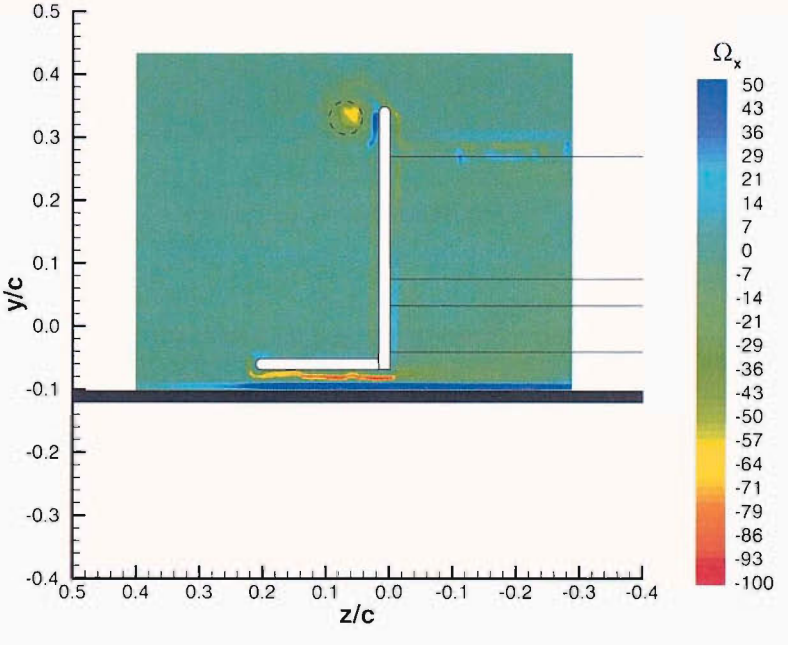

(b)

Figure 7.9: Time-averaged non-dimensional vorticity contours of the port wing tip at $x/c = 0.995$ with endplate feet; (a) $h/c = 0.053$ decreasing h (region j). (b) $h/c = 0.063$ increasing h (region n).

(a) Suction surface of the wing (leading edge upper most).

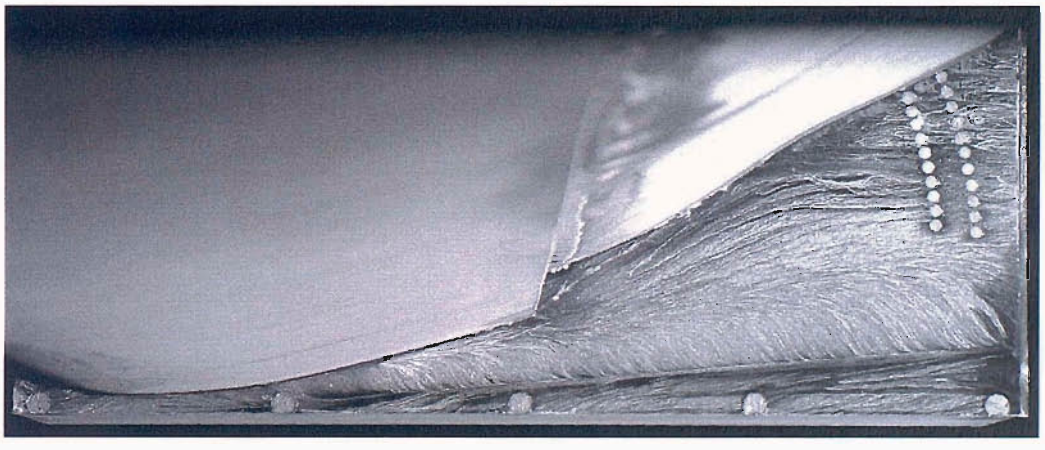

(b) Inboard surface of starboard endplate beneath the suction surfaces of the wing (flow from left to right).

(c) Underside of the starboard endplate foot (flow from left to right).

Figure 7.10: Surface streaklines obtained at h/c=0.317 (region g). Wing equipped with endplate feet.

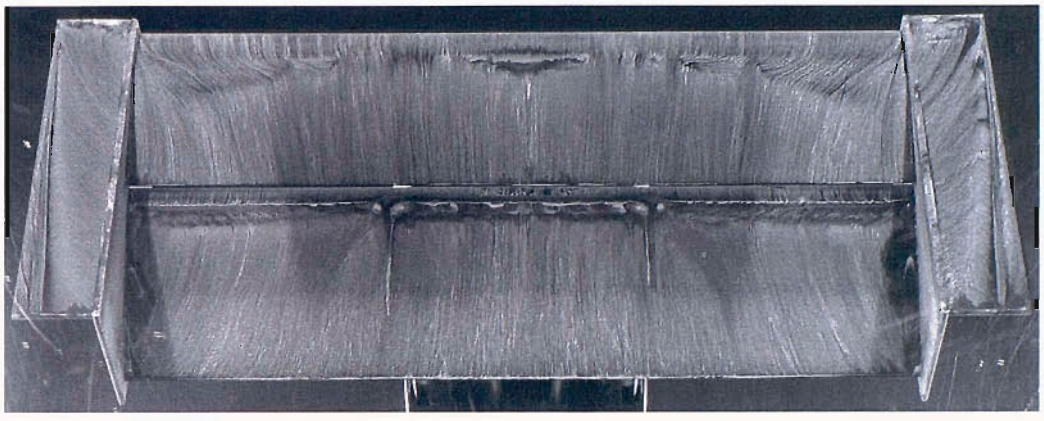

(a) Suction surface of the wing (leading edge upper most).

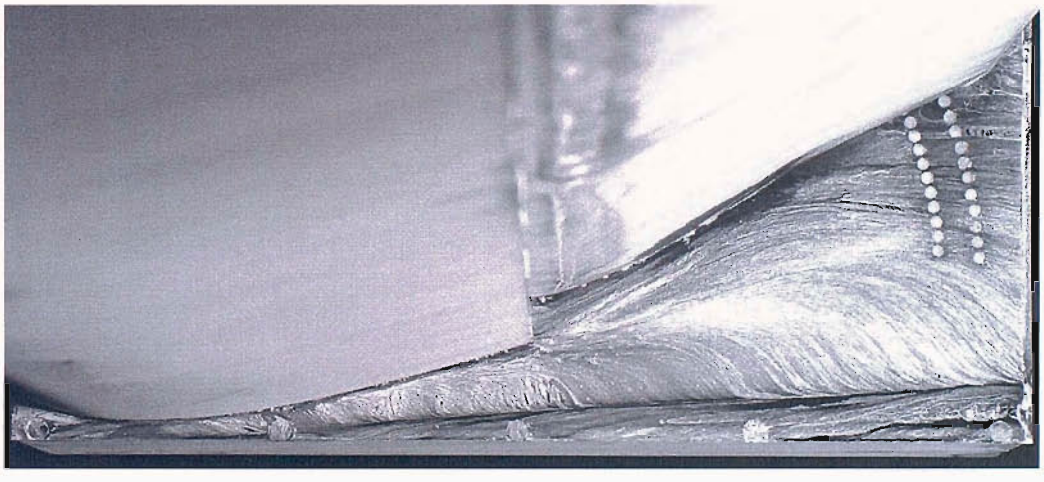

(b) Inboard surface of starboard endplate beneath the suction surfaces of the wing (flow from left to right).

(c) Underside of the starboard endplate foot (flow from left to right).

Figure 7.11: Surface streaklines obtained at h/c=0.169 (region g/i boundary). Wing equipped with endplate feet.

(a) Suction surface of the wing (leading edge upper most).

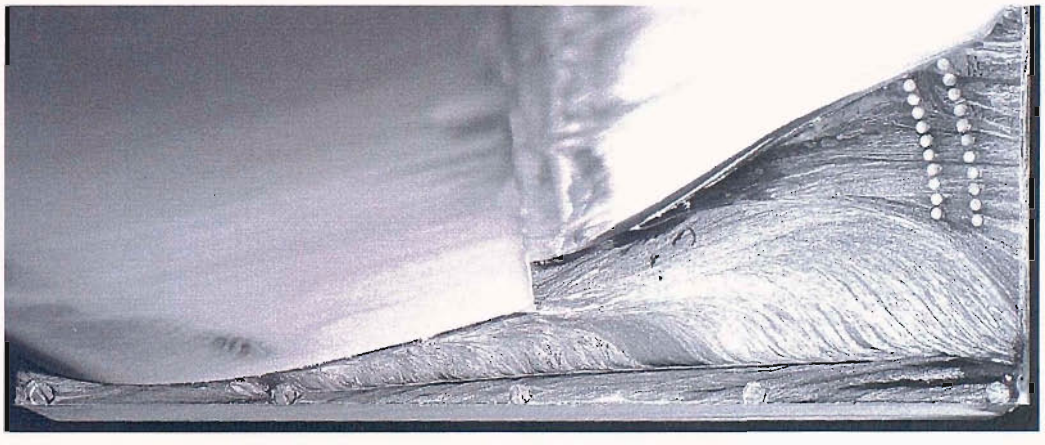

(b) Inboard surface of starboard endplate beneath the suction surfaces of the wing (flow from left to right).

(c) Underside of the starboard endplate foot (flow from left to right).

Figure 7.12: Surface streaklines obtained at h/c=0.141 (region i). Wing equipped with endplate feet.

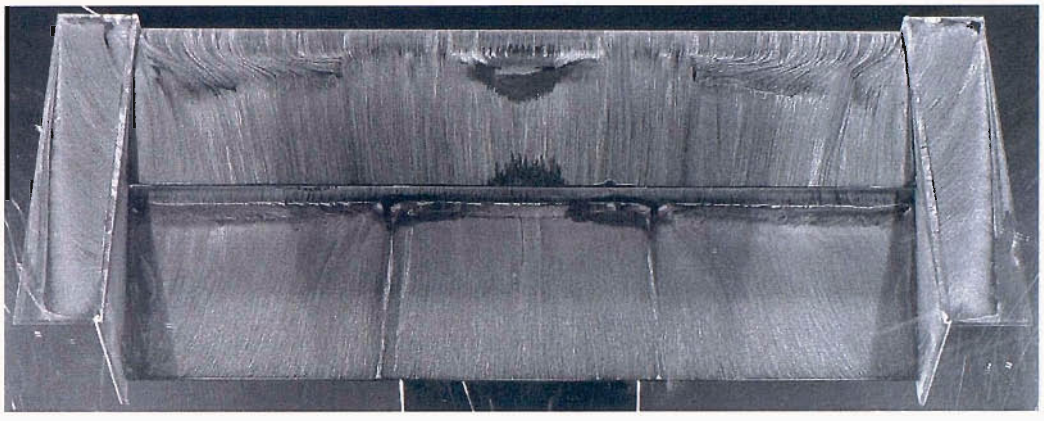

(a) Suction surface of the wing (leading edge upper most).

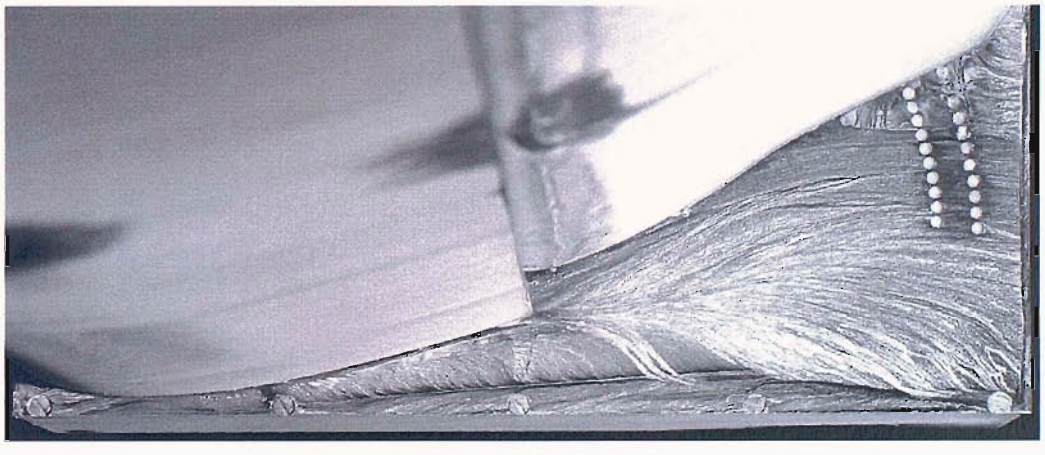

(b) Inboard surface of starboard endplate beneath the suction surfaces of the wing (flow from left to right).

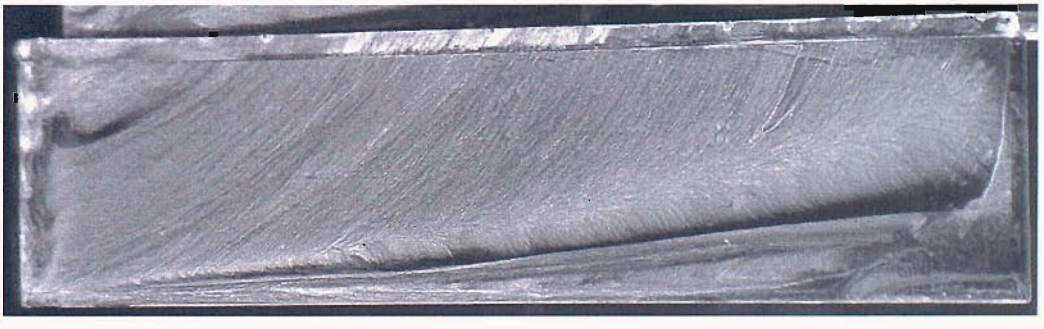

(c) Underside of the starboard endplate foot (flow from left to right).

Figure 7.13: Surface streaklines obtained at h/c=0.099, decreasing h (region j). Wing equipped with endplate feet.

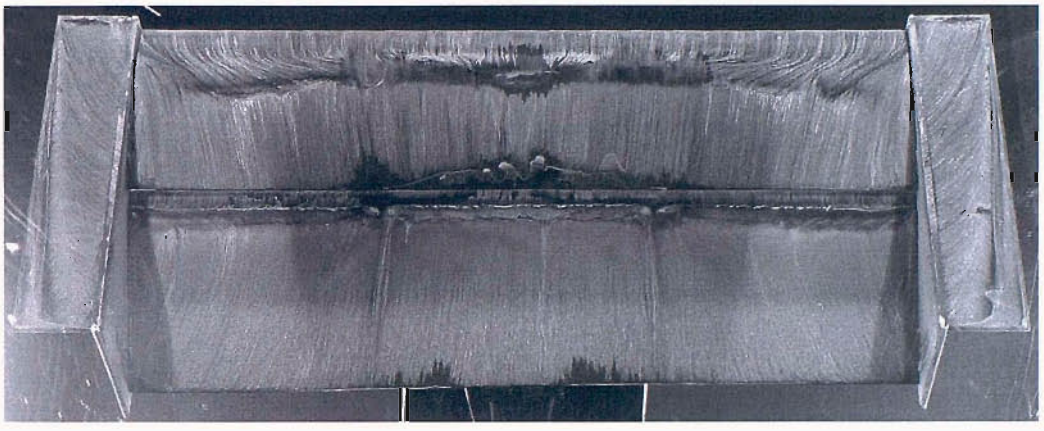

(a) Suction surface of the wing (leading edge upper most).

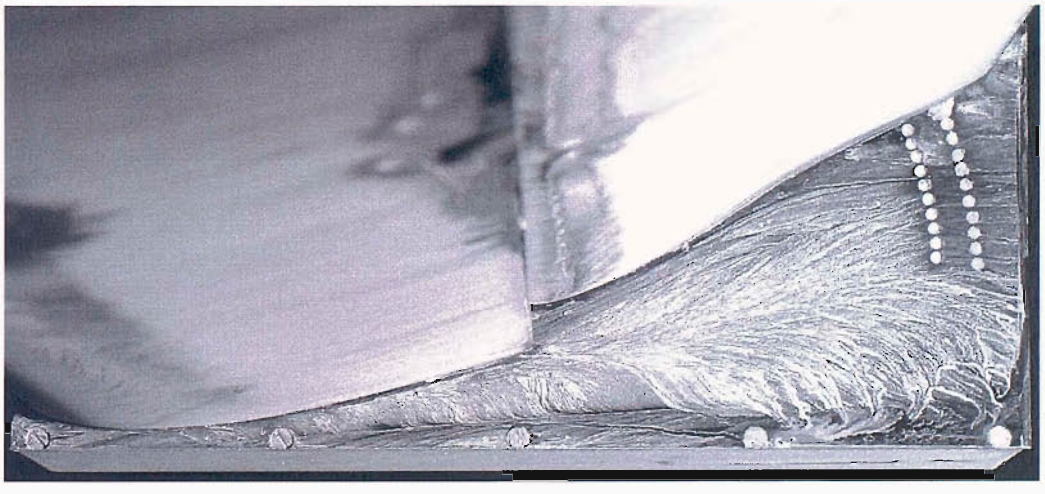

(b) Inboard surface of starboard endplate beneath the suction surfaces of the wing (flow from left to right).

(c) Underside of the starboard endplate foot (flow from left to right).

Figure 7.14: Surface streaklines obtained at h/c=0.063, decreasing h (region j). Wing equipped with endplate feet.

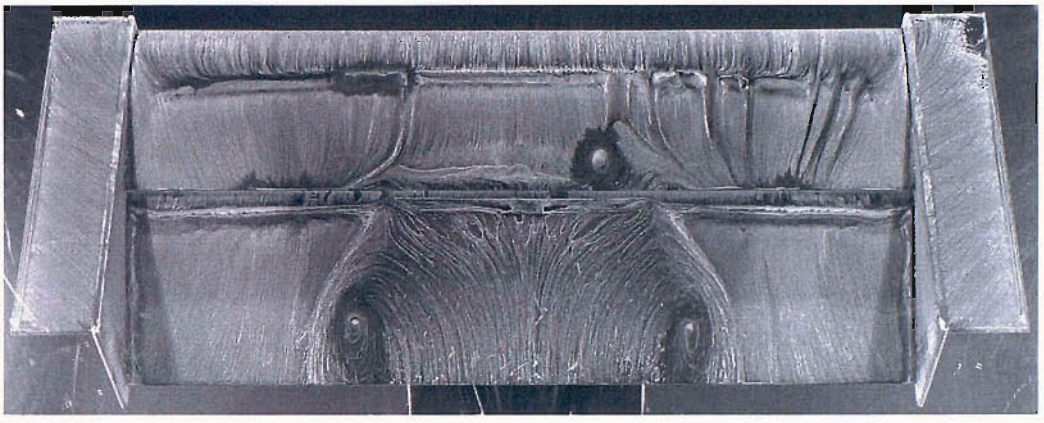

(a) Suction surface of the wing (leading edge upper most).

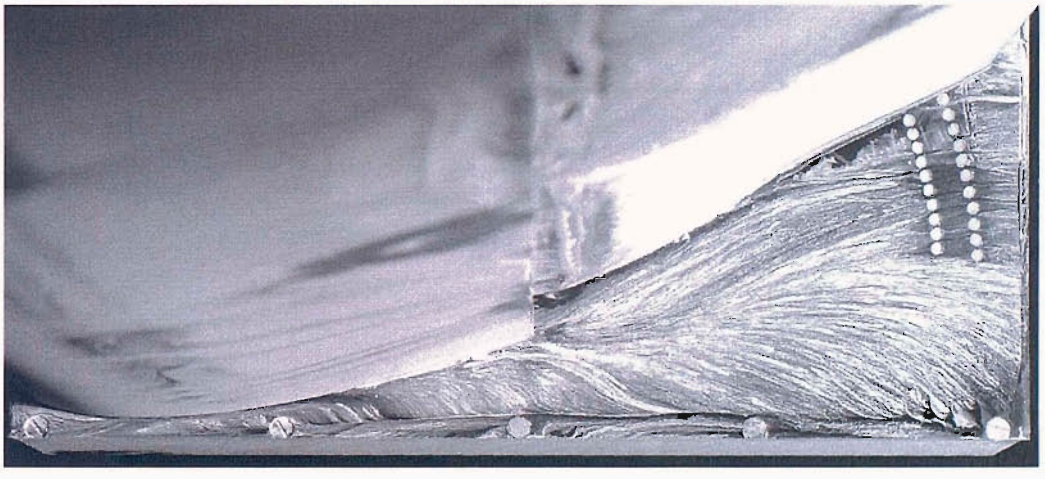

(b) Inboard surface of starboard endplate beneath the suction surfaces of the wing (flow from left to right).

(c) Underside of the starboard endplate foot (flow from left to right).

Figure 7.15: Surface streaklines obtained at h/c=0.063, increasing h (region n). Wing equipped with endplate feet.

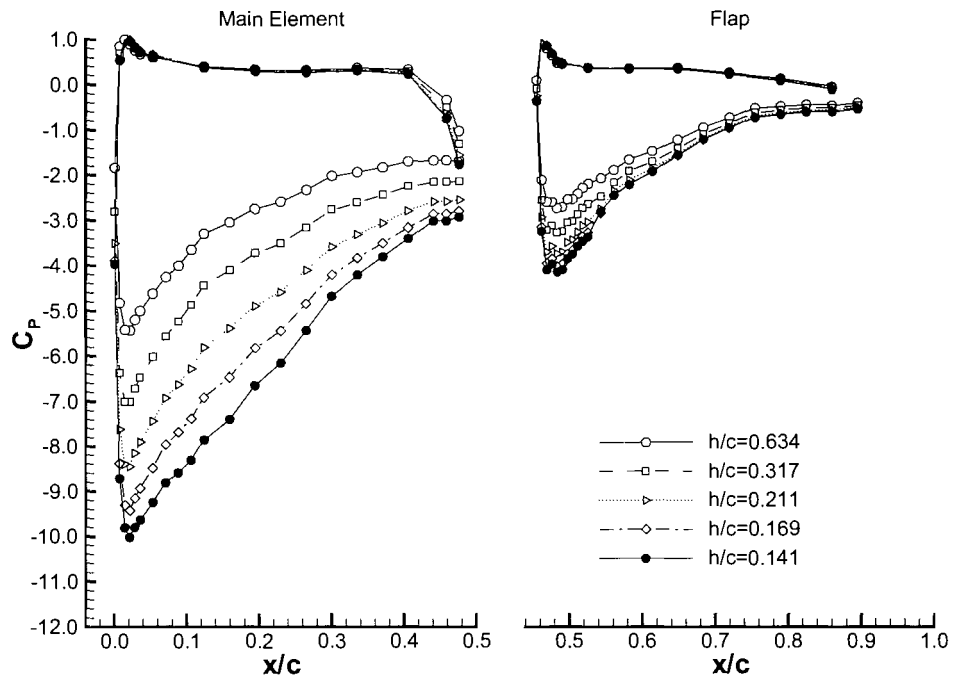

(a)

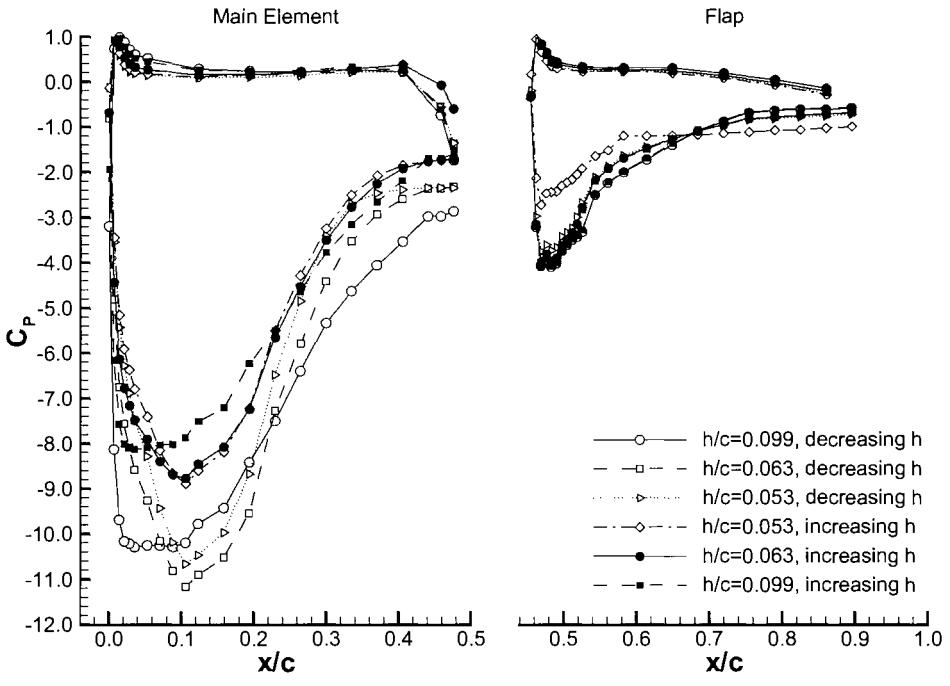

(b)

Figure 7.16: Chordwise surface pressure distributions at wing centre span for wing equipped with endplate feet; (a) high ride heights, (b) low ride heights.

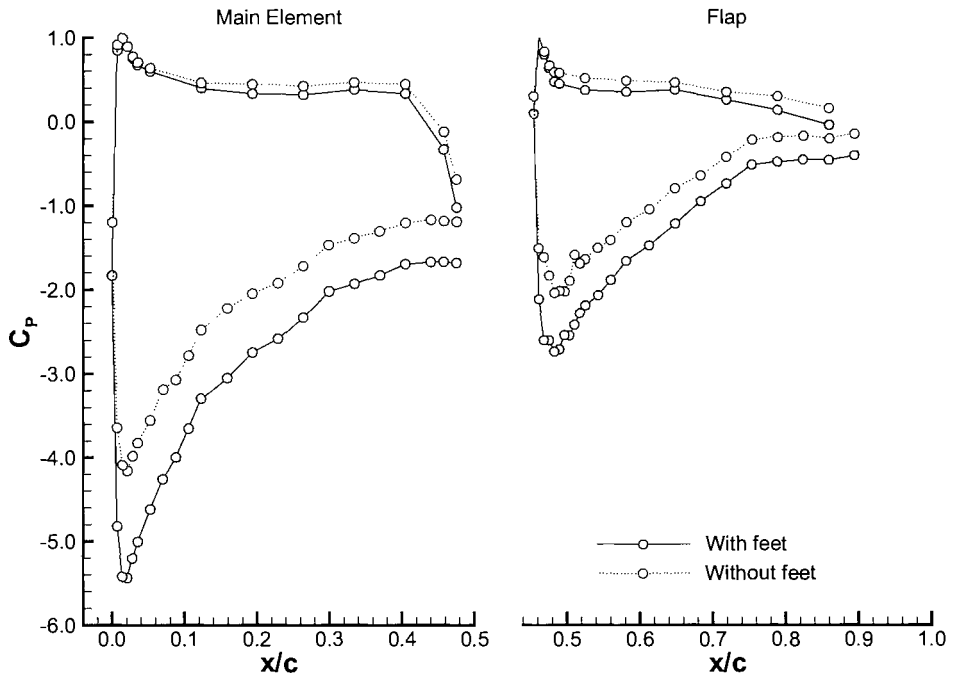

Figure 7.17: Chordwise surface pressure distributions at wing centre span for wing equipped with and without endplate feet; $h/c = 0.317$ (region g).

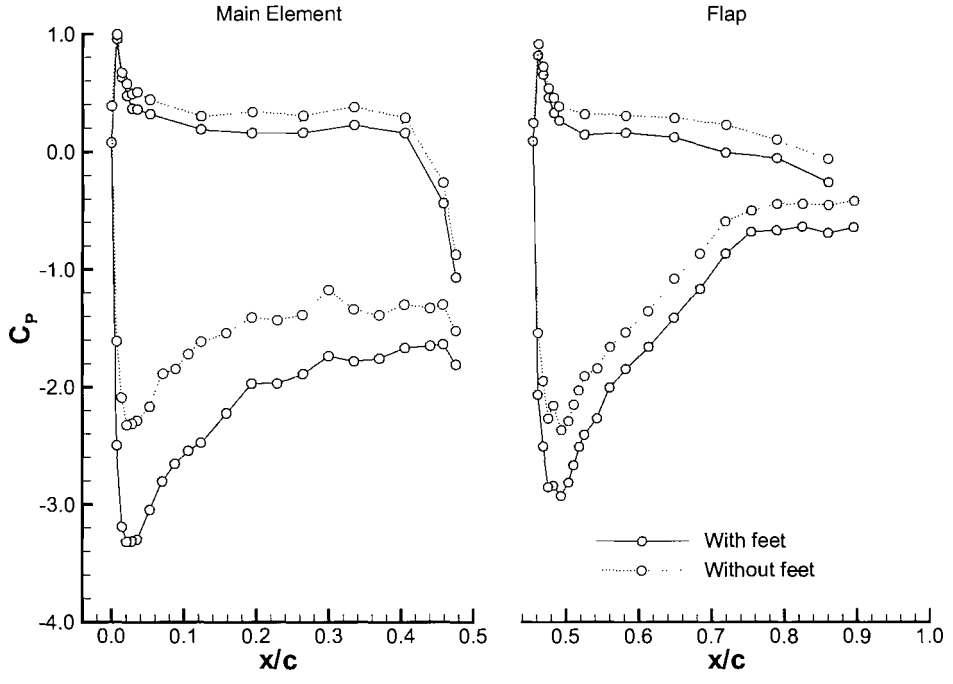

Figure 7.18: Chordwise surface pressure distributions near port wing tip for wing equipped with and without endplate feet; $h/c = 0.317$ (region g), $z/c = -0.088$.

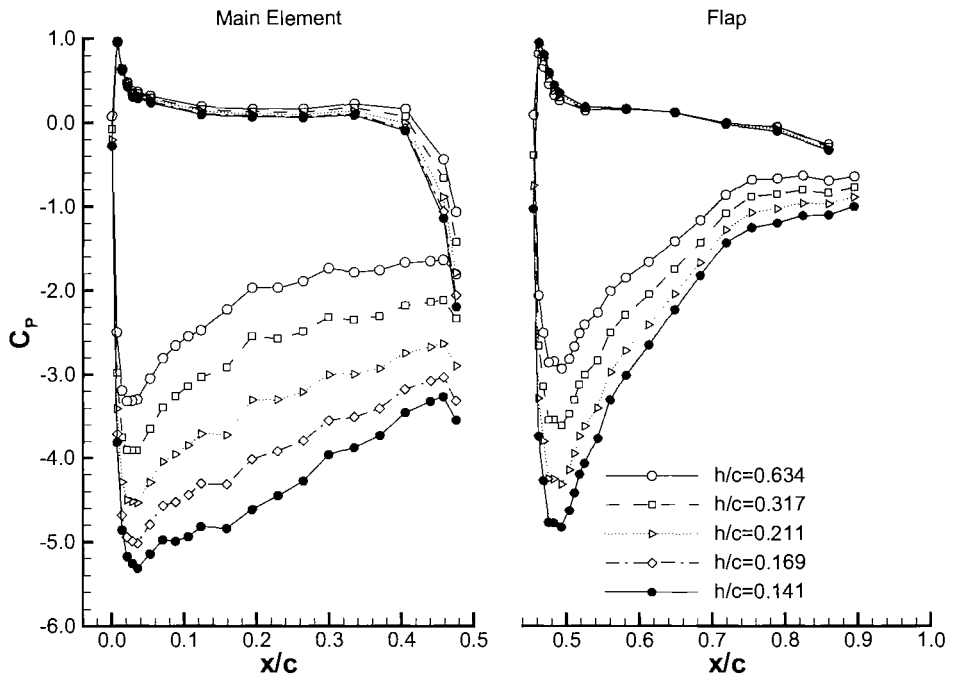

(a)

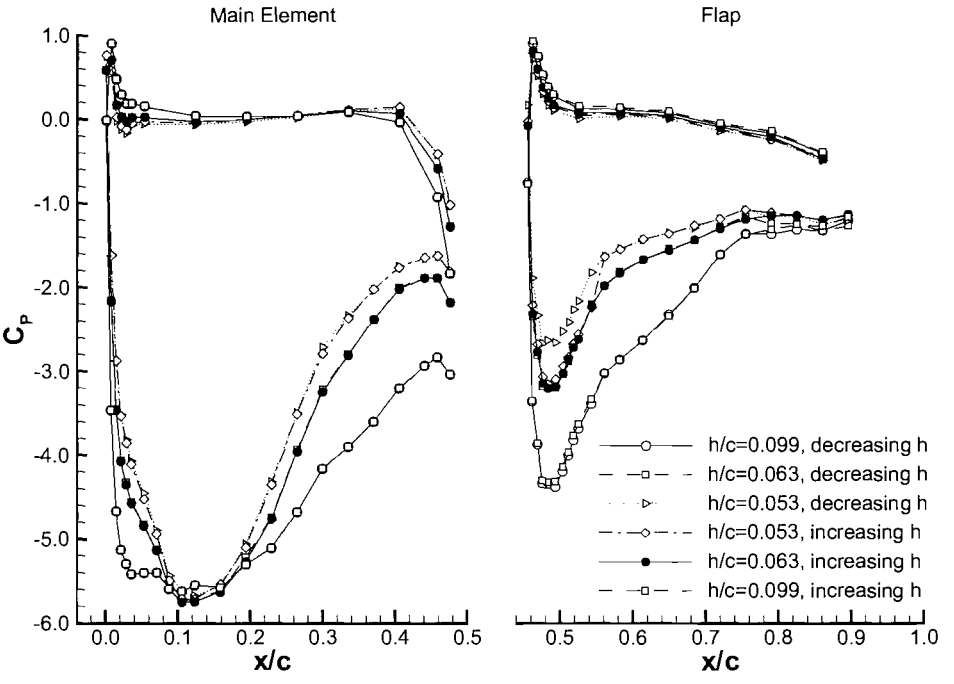

(b)

Figure 7.19: Chordwise surface pressure distributions near port wing tip for wing equipped with endplate feet, $z/c = -0.088$; (a) high ride heights, (b) low ride heights.

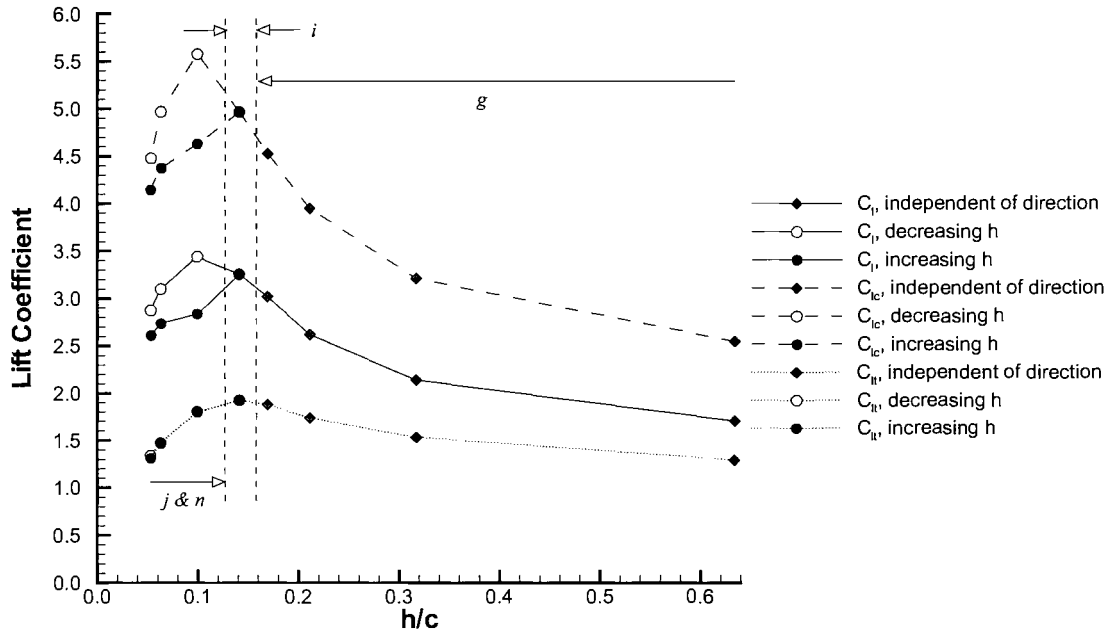

(a)

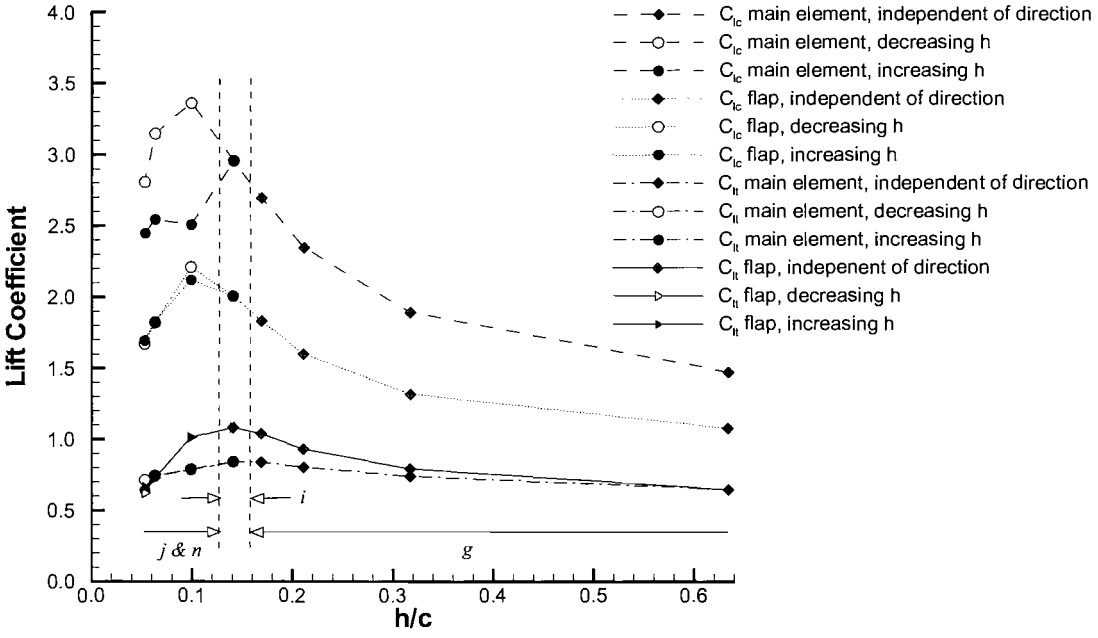

(b)

Figure 7.20: Integrated surface pressures for various ride heights. Wing equipped with endplate feet; (a) total downforce at centre span and wing tip, (b) downforce due to main element and flap.

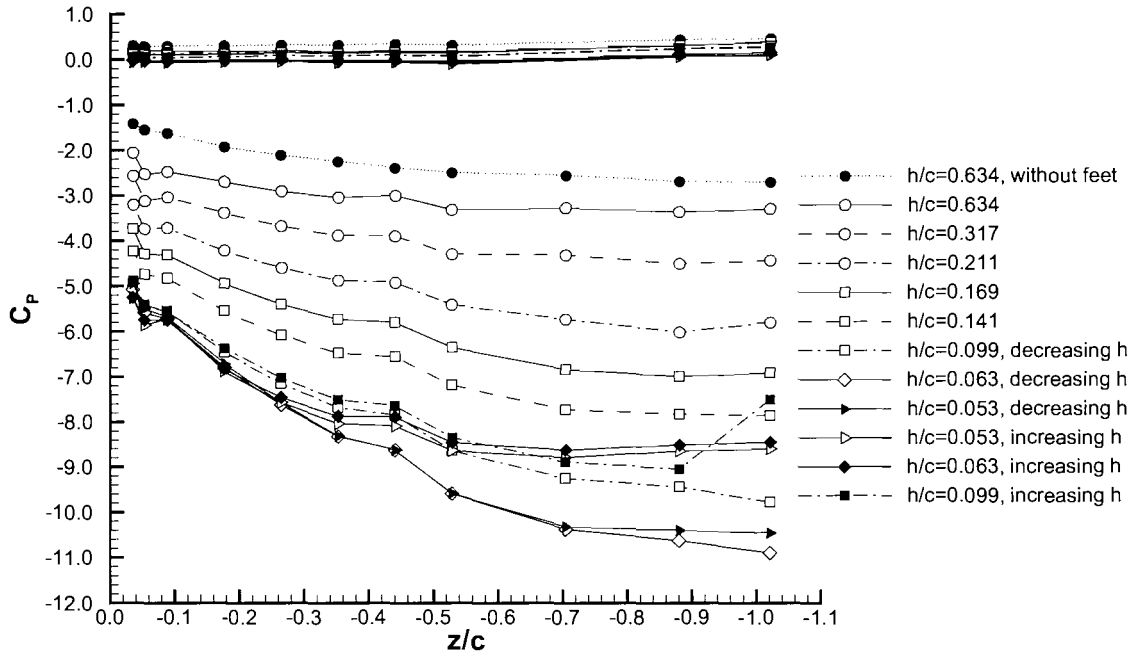

Figure 7.21: Spanwise surface pressure distributions on the main element for wing equipped with endplate feet; $x/c = 0.123$.

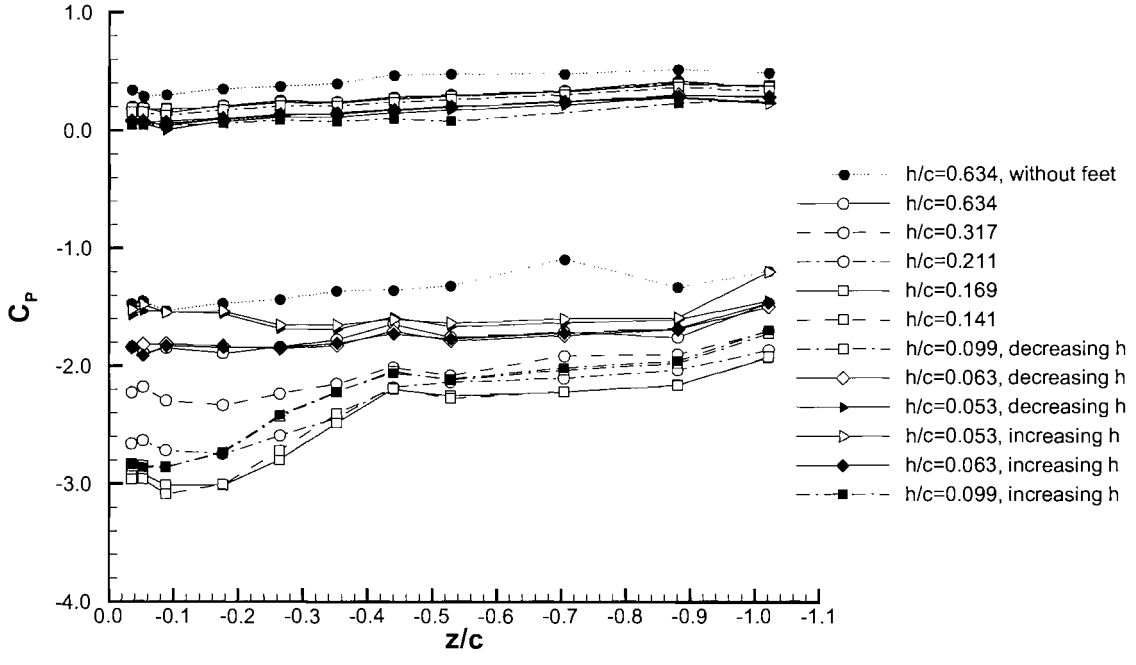

Figure 7.22: Spanwise surface pressure distributions on the flap for wing equipped with endplate feet; $x_f/c = 0.127$.

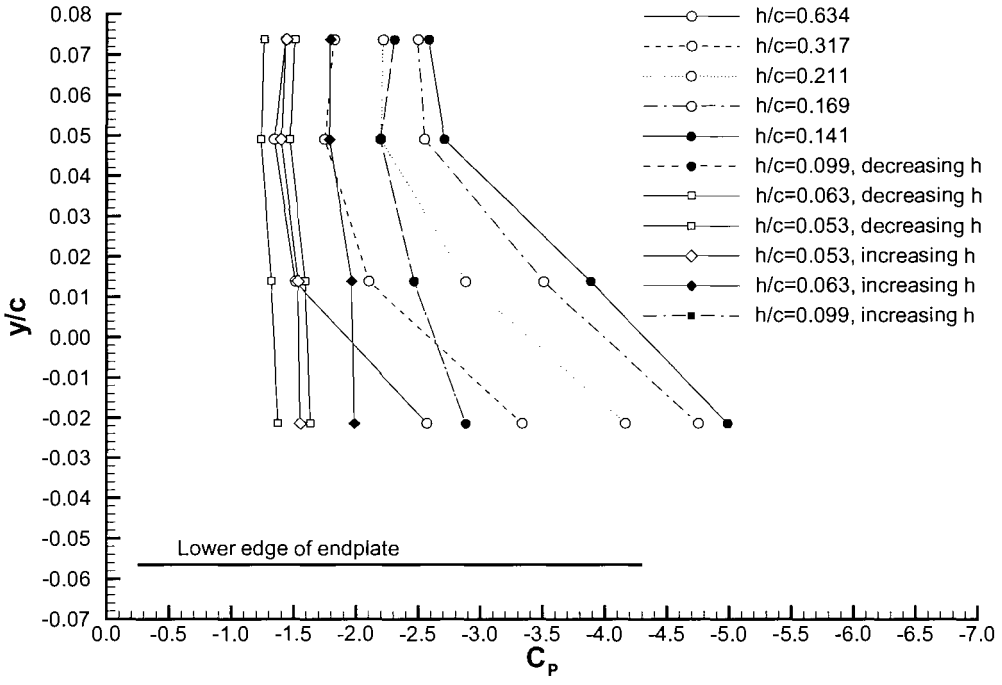

Figure 7.23: Surface pressure distributions on the inboard side of the port endplate for wing equipped with endplate feet; $x/c = 0.614$.

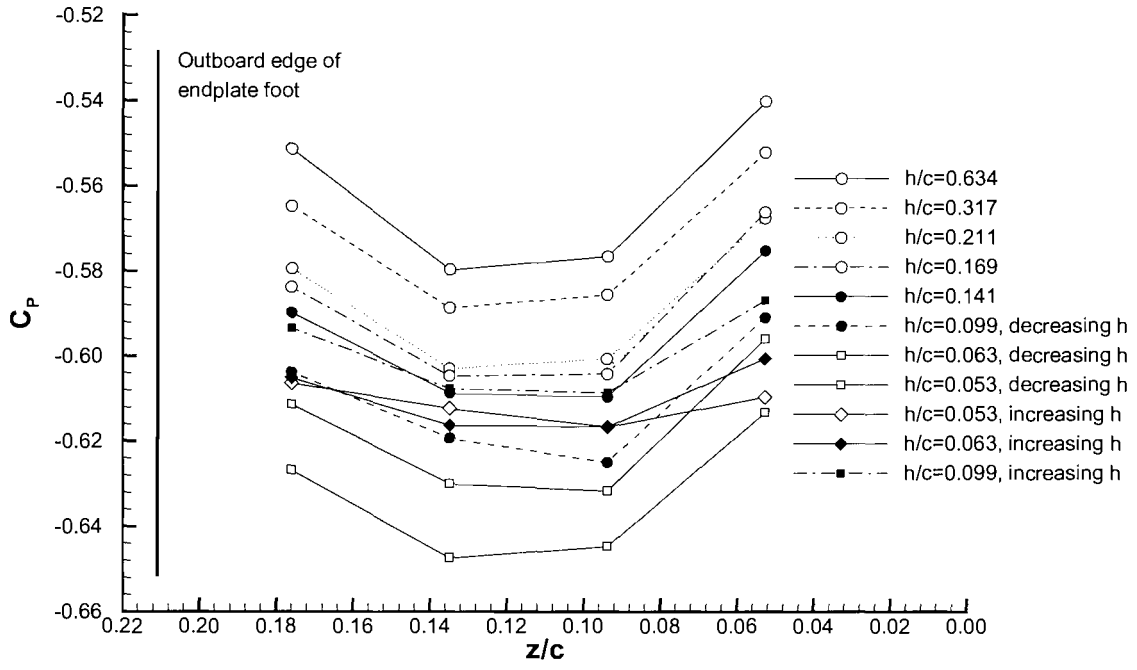

Figure 7.24: Surface pressure distributions on the lower surface of the port endplate foot; $x/c = 0.614$.

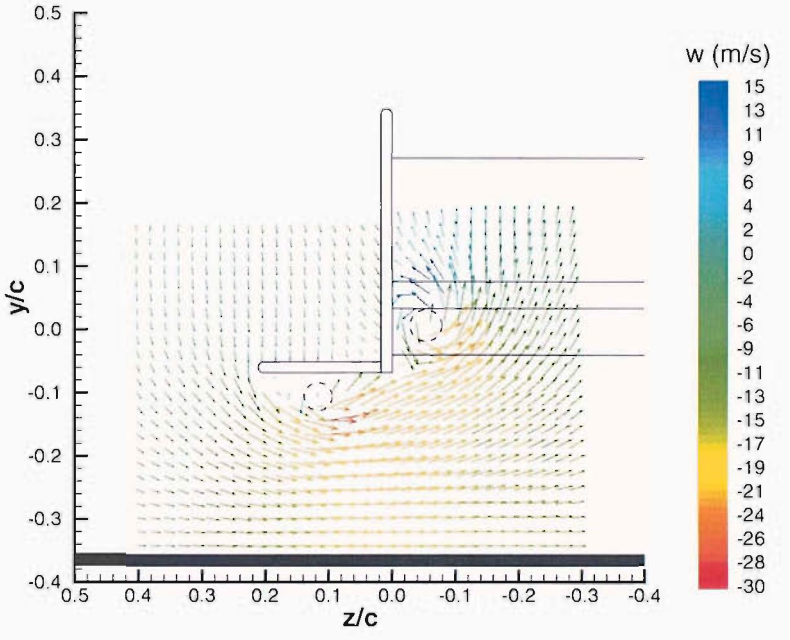

Figure 7.25: Spanwise velocity vectors at port wing tip at $x/c = 0.995$ (every fifth vector shown). Wing equipped with endplate feet: $h/c = 0.317$ (region g).

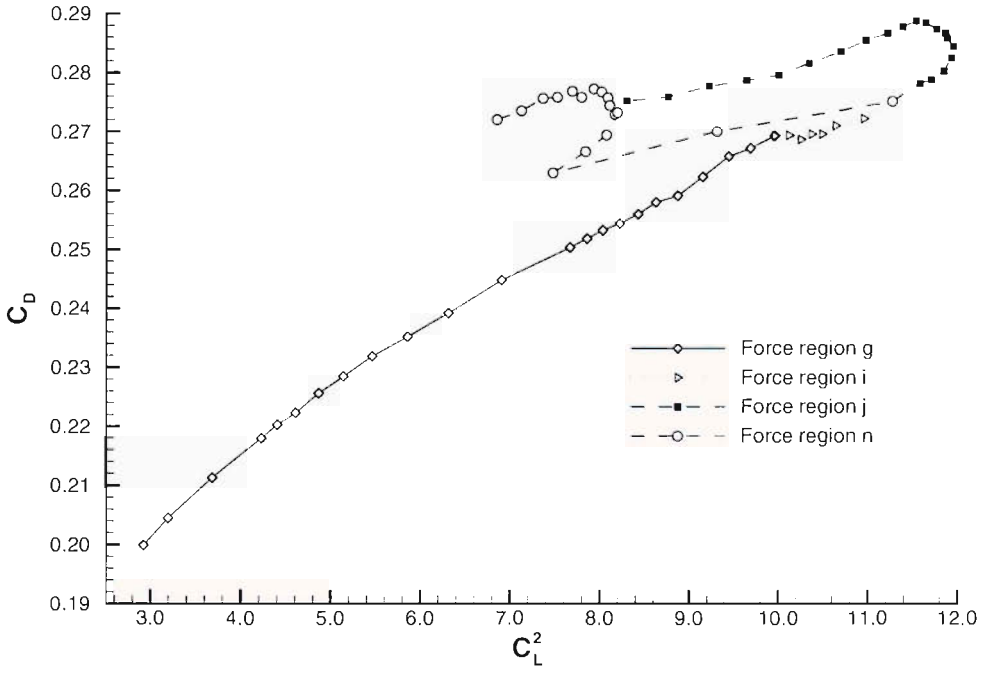

Figure 7.26: Dependency of drag coefficient on the square of the downforce coefficient for various ride heights. Wing equipped with endplate feet.

h/c	Upper Edge Vortex				Lower Edge Vortex				Foot Vortex			
	$(z/c)_v$	$(y/c)_v$	d_h/c	$(\Omega_x)_v$	$(z/c)_v$	$(y/c)_v$	d_h/c	$(\Omega_x)_v$	$(z/c)_v$	$(y/c)_v$	d_h/c	$(\Omega_x)_v$
0.317	NV	NV	NV	NV	-0.05	0.01	0.03	-90	0.12	-0.11	0.02	-72
0.211	NV	NV	NV	NV	-0.07	0.01	0.03	-116	0.10	-0.12	0.03	-30
0.169	NV	NV	NV	NV	-0.08	0.01	0.04	-135	-	-	-	-
0.141	0.07	0.32	0.02	-80	-0.11	0.02	0.07	-45	-	-	-	-
0.099, decreasing h	0.07	0.33	0.02	-71	-	-	-	-	-	-	-	-
0.063, decreasing h	0.07	0.34	0.03	-66	-	-	-	-	-	-	-	-
0.053, decreasing h	0.07	0.34	0.03	-63	-	-	-	-	-	-	-	-
0.063, increasing h	0.07	0.33	0.03	-71	-	-	-	-	-	-	-	-

Table 7.1: Properties of the port wing tip vortices at various ride heights. Wing equipped with endplate feet. (NV = not visible).

h/c	Main element			Flap		
	C_{Psuc}	x/c at C_{Psuc}	x/c at C_{Pstag}	C_{Psuc}	x/c at C_{Psuc}	x/c at C_{Pstag}
0.634	-5.43	0.02	0.01	-2.73	0.48	0.46
0.317	-7.01	0.02	0.01	-3.27	0.48	0.46
0.211	-7.84	0.02	0.01	-3.56	0.48	0.46
0.169	-9.42	0.02	0.01	-4.02	0.48	0.46
0.141	-10.01	0.02	0.01	-4.14	0.48	0.46
0.099, decreasing h	-10.28	0.09	0.01	-4.09	0.48	0.46
0.063, decreasing h	-11.16	0.11	0.01	-4.00	0.48	0.46
0.053, decreasing h	-10.65	0.11	0.01	-3.72	0.48	0.46
0.053, increasing h	-8.88	0.11	0.01	-2.72	0.47	0.46
0.063, increasing h	-8.76	0.11	0.01	-3.98	0.47	0.46
0.099, increasing h	-8.09	0.05	0.01	-4.08	0.47	0.46

Table 7.2: Chordwise centre span surface pressure details for various ride heights. Wing equipped with endplate feet.

Chapter 8

Computational Fluid Dynamics Model

This chapter discusses the computational fluid dynamics model and computational strategy used within this research. The setup of the numerical solver will be stated followed by the design of the computational grids. Features implemented for realistic modeling of the flow field will also be discussed.

8.1 Computational Strategy

To gain a more in depth insight into the flow field of a multi-element wing in ground effect, computational investigations were conducted in conjunction with the experimental investigations. The experimental and computational aspects of this research were conducted in parallel and designed to complement each other. The computational studies allowed for features of the flow field, difficult to measure experimentally to be quantified. Previous computational investigations into wings in ground effect have been shown to be limited, offering incomplete results (Section 2.4). A logical progressive strategy was therefore required developing from basic building block simulations into the final complex three-dimensional investigation. Three separate investigations were defined and conducted sequentially. Initially a single element aerofoil in ground effect was investigated followed by a multi-element aerofoil in ground effect. Finally a multi-element wing in ground effect equipped with endplates was investigated.

The importance of viscous effects in both ground effect and multi-element wing flow fields has been highlighted by previous investigations (Sections 2.2.6 and 2.3.4). Within

all three computational investigations solutions were obtained by solving the Reynolds Averaged Navier-Stokes (RANS) equations thereby obtaining both on-surface and off-surface flow field data. The effects of turbulence were included through the use of turbulence models. The dependency of the solutions on solver setup and grid resolution were addressed and quantified.

The experimental and computational investigations were conducted in parallel. Therefore validation of the two-dimensional computational data using the experimental data obtained in this research could not be conducted. The two-dimensional computational investigations were therefore based on and validated against previously obtained data [9]. The single element and multi-element wings investigated by Zerihan possessed similar attributes to the wing investigated in this research. The two-dimensional computational solutions were therefore directly applicable to this research. The three-dimensional computational simulations were conducted when experimental data from this research was available. Accordingly the wing experimentally investigated in this research was computationally investigated.

8.2 Governing Equations

Simulations were performed using a RANS solver [150] and were calculated on a linux based cluster. In all calculations the numerical solver was setup in a steady-state segregated configuration which utilised an implicit formulation. In such a configuration solutions at each iteration were obtained by solving the Reynolds Averaged Navier-Stokes equations:

$$\frac{\partial \overline{u}_j}{\partial x_j} = 0 \tag{8.1}$$

$$\frac{\partial}{\partial t}(\rho \overline{u}_i) + \frac{\partial}{\partial x_j}(\rho \overline{u}_i \overline{u}_j) = -\frac{\partial \overline{p}}{\partial x_i} + \frac{\partial}{\partial x_j}(\overline{\tau}_{ij} - \rho \overline{u'_i u'_j}) \tag{8.2}$$

$$\frac{\partial}{\partial t}(\rho c_{ph} \overline{T}) + \frac{\partial}{\partial x_j}(\rho c_{ph} \overline{T} \overline{u}_j) = \frac{\partial \overline{p}}{\partial t} + \overline{u}_j \frac{\partial \overline{p}}{\partial x_j} + \overline{u'_j \frac{\partial p'}{\partial x_j}} + \frac{\partial}{\partial x_j}\left(k \frac{\partial \overline{T}}{\partial x_j} - \rho c_{ph} \overline{T' u'_j}\right) + \overline{\Phi} \tag{8.3}$$

where:

$$\overline{\tau}_{ij} = \mu \left(\frac{\partial \overline{u}_i}{\partial x_j} + \frac{\partial \overline{u}_j}{\partial x_i}\right) \tag{8.4}$$

and:

$$\overline{\Phi} = \tau_{ij}\overline{\frac{\partial u_i}{\partial x_j}} \tag{8.5}$$

Where u_i and x_i represent the instantaneous velocity component and position vector in tensor notation respectively. In addition an over-bar indicates a temporal average of fluctuating properties (e.g. $\overline{p}$). An upwind discretization scheme was used for all flow variables which yielded second order spatial accuracy. The SIMPLEC pressure-velocity coupling algorithm was used. To aid the rate of convergence V-Cycle and flexible multi-grid schemes were used for pressure and momentum respectively.

8.3 Turbulence Modelling

Currently the applicability of specific turbulence models to a wing in ground effect is unclear. Therefore the performance and applicability of each turbulence model in a ground effect situation needed be quantified. The process of quantifying the performance of each turbulence model was repeated for the single element aerofoil, multi-element aerofoil and multi-element wing cases.

Within the two-dimensional simulations turbulence within the computed flow field was modelled using one of six turbulence models. The turbulence models used were the one equation Spalart-Allmaras model [151], the standard $k-\varepsilon$ model [152], the standard $k-\omega$ model [153], the $k-\omega$ SST model [154], the $k-\varepsilon$ RNG model [155] and the Realizable $k-\varepsilon$ model [156]. Turbulence within the three-dimensional computed flow field was only modelled using the Spalart-Allmaras and $k-\omega$ SST models. Convergence could not be obtained with the remaining four turbulence models. The cause of the divergent solution was attributed to the design of the three-dimensional computational grid in particular the hybrid nature of the grid. The performance of the turbulence models stated within the three computational investigations will be discussed separately in each of the corresponding chapters.

8.4 Computational Grids

Three designs of computational grid were used within the numerical section of this research corresponding to a single element aerofoil, multi-element aerofoil and multi-element wing. A multi-block hybrid grid design was used in all cases, containing both structured and unstructured blocks. In a ground effect situation the most important variable is ride height. For each ride height a separate computational grid was required. To maintain the grid topology and structure for different ride heights and wing configurations an automated grid generation method was developed. Using scripting functions within the grid generator [157] it was possible to vary all aspects of the wing configuration automatically, in particular ride height. The following subsections will discuss the three grid strategies used within this research.

8.4.1 Single Element Aerofoil

The single element aerofoil computational grid was the least complex in design containing 8 two-dimensional blocks. A schematic of the computational domain is shown in Figure 8.1(a). To capture the boundary layer of the aerofoil accurately a hyperbolically extruded structured grid was used. A conventional structured block was used to capture the ground boundary layer. A separate structured block was positioned directly downstream of the aerofoil with the purpose of capturing the wake. The remainder of the computational domain was unstructured and refined in areas of importance. Within the ground and aerofoil boundary layer blocks the initial cell spacing, normal to the wall, was set such that $y^+ \approx 1$. The exact number of cells varied according to the ride height. Typically the grids contained of the order of 350,000 cells with the majority of those located towards the trailing edge of the aerofoil and within the wake block. Figures 8.1(b), 8.1(c) and 8.1(d) illustrate the design and resolution of the computational grid.

8.4.2 Multi-Element Aerofoil

The computational domain for the multi-element aerofoil was more complex than the single-element aerofoil domain, containing 10 two-dimensional blocks. A schematic of the computational domain is shown in Figure 8.2(a). To capture the boundary layer of each element of the aerofoil accurately, a hyperbolically extruded structured grid was used (Figure 8.2(b)). A conventional structured block was used to capture the ground boundary layer. Within

the ground and aerofoil boundary layer blocks the initial cell spacing, normal to the wall, was set such that $y^+ \approx 1$. To allow the overlap region between the two elements of the aerofoil to be modelled accurately, the boundary layer blocks of each element were divided and redesigned (Figure 8.2(c)). The gap between the elements was modelled using a single structured block located between the trailing edge of the main element pressure surface and the suction surface of the flap. An unstructured block was located directly upstream of the overlap region with the purpose of joining the pressure surface boundary layer blocks while closely following the streamlines of the flow. A structured block was located directly beneath the flap in order to capture the initial main element wake development. A separate structured block was positioned directly downstream of the aerofoil with the purpose of capturing the development of the wakes from both the main element and flap. The remainder of the computational domain was unstructured and refined in areas of importance. The exact number of cells varied according to the ride height. Typically the grids contained of the order of 200,000 cells with the majority of those located towards the trailing edge of each element of the aerofoil and within the near field and far field wake blocks. Figure 8.2(d) presents the entire computational grid for the multi-element aerofoil.

8.4.3 Multi-Element Wing

The computational grid for the multi-element wing was the most complex containing 16 three-dimensional blocks. The experimental results indicated that the flow field was symmetric about the centre span of the wing. Therefore a half-span wing and wind tunnel was modelled computationally. The starboard face of the computational domain modelled as a symmetry plane. This feature reduced the computational cost and allowed for greater grid resolution in areas of importance. Figure 8.3 presents a schematic of the three-dimensional computational domain.

The primary area of complexity within the three-dimensional grid was the interface between the elements of the wing and the port endplate. Structured blocks were required for accurate resolution of the wing boundary layers. The blocks had to follow the profiles of each element and map onto the inboard face of the endplate (Figure 8.4(a)). For this reason extruded blocks could not be used. The blocks on the pressure surfaces of the wing were generated by offsetting the pressure surfaces of each element. The overlap region was modelled using a single structured block (Figure 8.4(b)). Mapping the wing suction surface connectors onto the base of the endplate created a fully structured block directly beneath

the wing. The leading edge of the main element was modelled using an offset surface. Towards the endplate the leading edge offset was reduced to allow the main element leading edge block to be mapped directly onto the inboard face of the endplate. Within the wing boundary layer blocks the initial cell spacing, normal to the wall, was set such that $y^+ \approx 1$. A glue block was placed directly downstream of the flap trailing edge with the purpose of mapping the wing boundary layer blocks onto the downstream face of the endplate. The remainder of the inboard face of the endplate was modelled using an unstructured domain.

The cells within the wing boundary layer domains were concentrated towards the port endplate (Figures 8.4(c)) and 8.4(d)). This feature allowed the lower edge vortex to be resolved accurately. The experimental results indicated that the shear layer associated with the lower edge vortex originated from the outboard edge of the endplate and developed diagonally downwards. To correctly capture this feature a conventional structured block was created directly beneath the wing and endplate. Figure 8.5(a) illustrates the mapping of the wing boundary layer blocks and the lower edge vortex block onto the symmetry plane. To capture the upper edge vortex a structured block was created directly outboard of the port endplate. This block was designed to capture both the upper edge vortex and the associated shear layer. The upper vortex block connected to a structured block placed directly downstream of the wing designed to capture the wake of the wing. The wake block extended from the wing to the downstream outlet face of the computational domain.

To accurately resolve the boundary layer developing along the ground plane a conventional structured block was created. The experimental results indicated that the ground boundary layer did not extend across the entire span of the moving ground. The structured block was therefore located directly beneath the wing offset from the port tip of the wing. The remainder of the ground plane was modelled using an unstructured block to further reduce the computational costs, as illustrated in Figure 8.5(b). The inlet, outlet, port wind tunnel wall, wind tunnel roof, upper fillet and lower fillet were all modelled as unstructured blocks. Figure 8.5(c) presents the entire computational domain. The exact number of cells varied according to the ride height. Typically the grids contained of the order of 3,000,000 cells with the majority of those located in the boundary layer blocks and vortex blocks.

8.5 Boundary Conditions

In all the computational investigations the boundary conditions were configured to replicate the experimental conditions. The inlet of each computational domain was modelled using a velocity inlet boundary condition. The inlet velocity was set at 30m/s in a positive streamwise direction with a uniform vertical distribution. The downstream boundary was modelled using a pressure outlet boundary condition. The gauge pressure was set at zero. The surfaces of the aerofoil/wing and ground plane were all modelled as solid walls with a no-slip condition enforced. In addition the ground surface was provided with a translational velocity equal to freestream.

Within all simulations the height of the upper edge of the domain above the ground plane corresponded to the height of the wind tunnel test section. A slip wall boundary condition was imposed therefore imposing a zero cross-flow condition and removing the requirement of additional boundary layer resolution. This formulation was set in order to replicate the experimental conditions imposed by the roof of the wind tunnel test section. Additional boundary condition were required with the three-dimensional computational domain. The centre span plane was modelled as a symmetry plane. The roof, port wall, upper fillet and lower fillet of the wind tunnel were all modelled as slip walls. The surfaces of the port endplate were all modelled as walls with a no-slip condition enforced.

In all cases initial levels of turbulence within the flow was prescribed via values of turbulence intensity and length scale. The freestream turbulence intensity level within the 2.1m×1.7m wind tunnel facility has been experimentally measured at 0.3% with a freestream velocity of 30m/s. This value was used in combination with a length scale of 0.039m (Section 3.5).

8.6 Boundary Layer Transition

Transition within boundary layers is an aerodynamic feature present on most wings. The location of transition on a wing in ground effect has been shown to alter with ride height (Section 5.4). The formulation of the RANS solver used assumed a fully turbulent boundary layer and excluded the prediction of transition. Within the computational investigations transition was included through the use of laminar blocks located at the leading edge of the aerofoil/wing. This feature allowed the boundary layer to initially develop as a laminar boundary layer followed by an immediate transition to turbulence. The downstream

location at which the laminar block terminated was set apriori using experimental data. The streamwise locations of transition within the three computational investigations will be discussed separately in each of the corresponding chapters.

8.7 Convergence Criteria

The final aspect of the computational model which needed to be quantified was the convergence of the iterative solution. A composite criterion for convergence was defined taking into account the convergence of both the residual values and the forces. The composite convergence criterion was defined as follows.

- The scaled residual values were reduced by at least a magnitude of three.
- The scaled residual values were of fixed value with respect to iteration number.
- The lift and drag forces generated by the aerofoil/wing were of fixed value with respect to iteration number.

It was noted that the number of iterations required for convergence increased with decreased values of ride height. Figure 8.6 presents the convergence of the scaled residuals (R/R_0) and downforce coefficient (C_L) for the three-dimensional wing at a ride height of $0.317c$ using the Spalart-Allmaras turbulence model.

8.8 Chapter Summary

A logical progressive computational strategy has been devised to investigate aerofoils/wings in ground effect. Computational grids have been designed combining design requirements for accurate flow simulations with flexibility. Modelling of boundary layer transition has been included through the use of laminar blocks. A combination criteria for convergence has been stated taking into account both residual values and force coefficients.

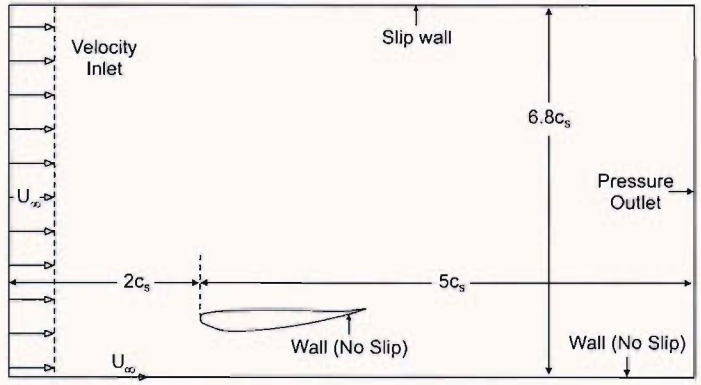

(a)

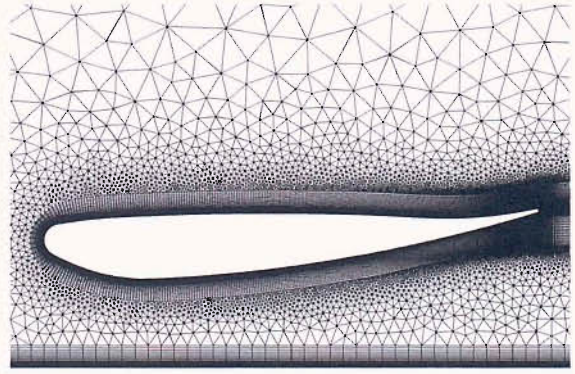

(b)

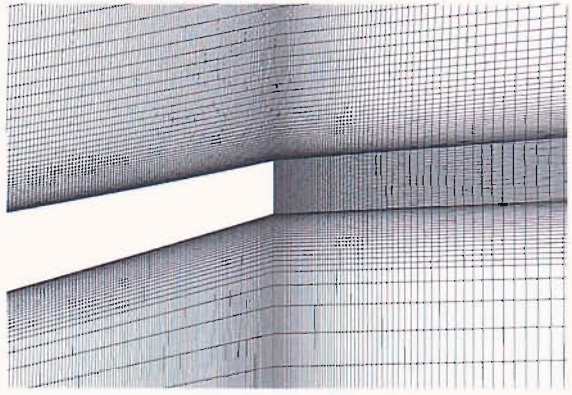

(c)

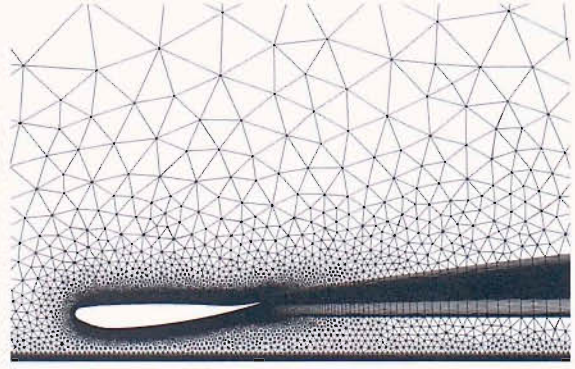

(d)

Figure 8.1: Computational grid for the single element aerofoil; (a) schematic of the computational domain, (b) boundary layer grid, (c) aerofoil trailing edge grid, (d) aerofoil and wake domains.

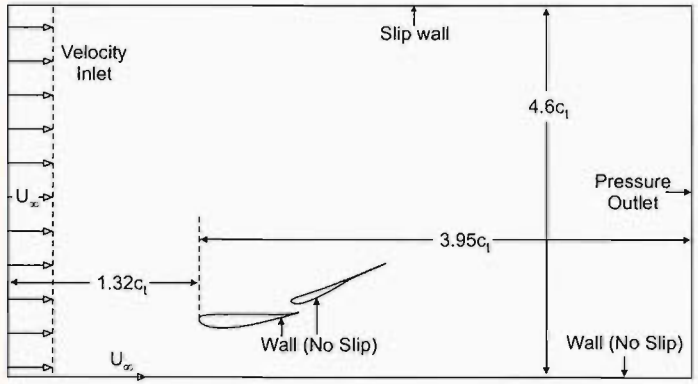

(a)

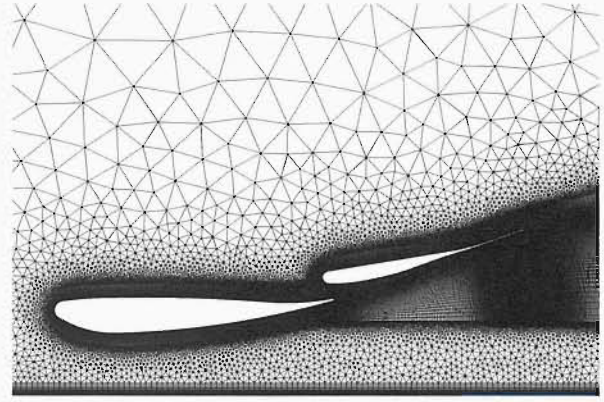

(b)

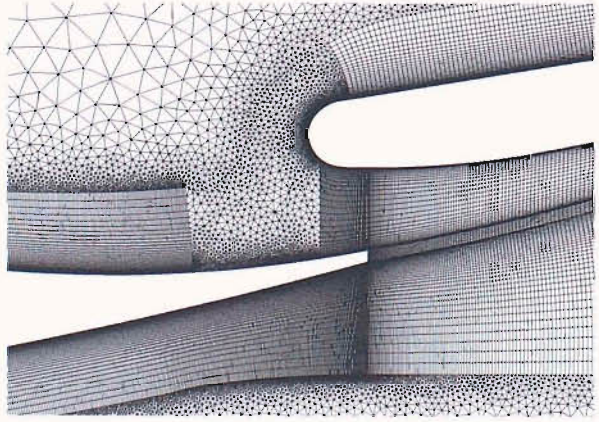

(c)

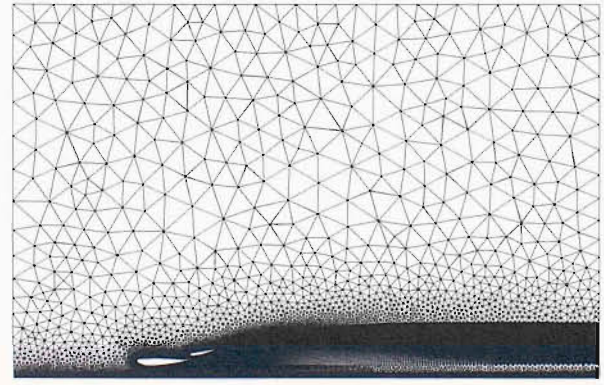

(d)

Figure 8.2: Computational grid for the multi-element aerofoil; (a) schematic of the computational domain, (b) boundary layer grid, (c) overlap region, (d) entire computational domain.

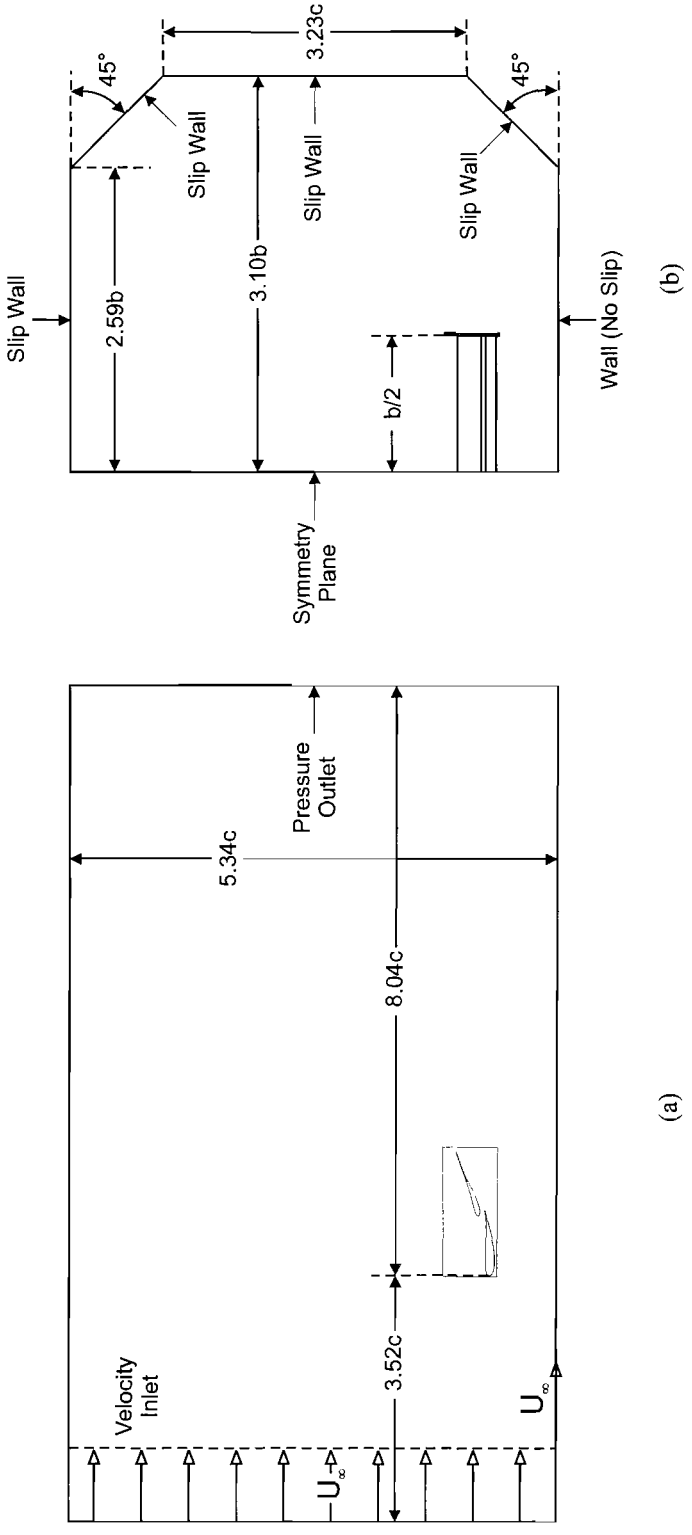

Figure 8.3: Schematic of the multi-element wing computational domain; (a) side view (b) frontal view.

Figure 8.4: Computational grid on the surfaces of the wing and port endplate; (a) inboard face of the port endplate, (b) flap overlap region, (c) wing pressure surfaces, (d) wing suction surfaces.

(a)

(b)

(c)

Figure 8.5: Computational grid on the surfaces of the three-dimensional computational domain; (a) symmetry plane, (b) wing surfaces and ground plane, (c) wind tunnel walls.

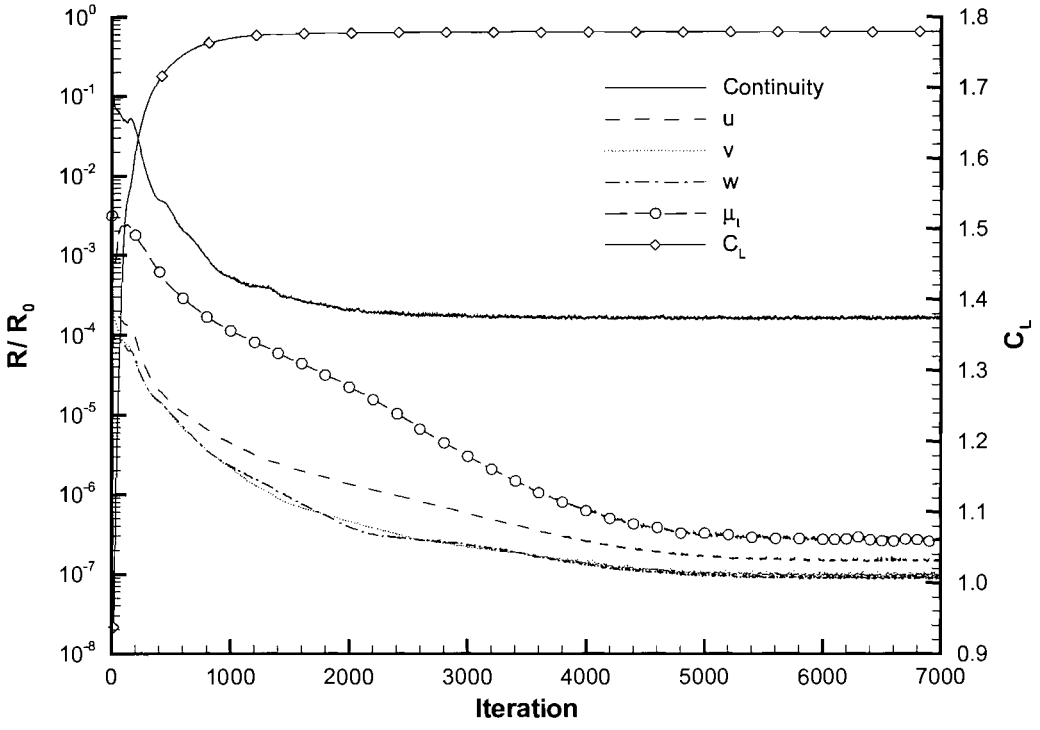

Figure 8.6: Convergence history for the three-dimensional wing with the Spalart-Allmaras turbulence model; $h/c = 0.317$.

Chapter 9

RANS Simulations of a Single Element Aerofoil in Ground Effect

This chapter presents and discusses computational results for a single element aerofoil in ground effect. The applicability of the six turbulence models listed in Section 8.3 will be quantified initially. Results obtained at various ride heights will then presented and quantitatively compared to experimental data.

9.1 Aerofoil Geometry

The aerofoil geometry investigated was a derivative of the LS(1)-0413 MOD profile which had been previously researched. Detailed listing of the profile can be found in Zerihan [9]. The aerofoil was inverted such that the suction surface was closest to the ground. The chord (c_s) and incidence (α_s) of the aerofoil were 223.4mm and +3.6° respectively. The profile possessed a finite trailing edge of $0.007c_s$. All computations were performed at a Reynolds number of 4.6×10^5 based on the chord of the aerofoil. In accordance with experimental data [9], transition was fixed for all ride heights at $x/c_s = 0.1$ on both the pressure and suction surfaces of the aerofoil.

9.2 Grid Independence Study

Prior to conducting investigations at different ride heights the dependence of the solution on the resolution of the computational grid was quantified. A grid sensitivity study was performed at a ride height of $h/c_s = 0.224$, a typical ride height in the force enhancement

region [9]. Three grids were constructed: a coarse grid of 250,000 cells, a medium grid of 350,000 cells and a fine grid of 450,000 cells. The variations in grid density were focused in the wing boundary layer block and wake block. Turbulence was modelled using the Realizable $k-\varepsilon$ model. The surface pressures and wake profiles at $x/c_s = 1.2$ are presented in Figure 9.1. Very little variation was observed between the results obtained with the medium and fine grid resolutions. The surface pressures were predicted more accurately with the coarse grid however discrepancies were observed within the wake profile. The medium grid resolution was used within the remaining single element aerofoil simulations.

9.3 Turbulence Model Comparison

A quantitative comparison of the six turbulence models was conducted. Two cases were selected ($h/c_s = 0.224$ and 0.09). $h/c_s = 0.224$ represented a typical flow condition where the ride height of the aerofoil was in the force enhancement region [42] but separation had started to appear on the suction surface near the trailing edge. At $h/c_s = 0.09$ a large separation region was present on the suction surface. The suitability of each turbulence model was quantitatively assessed using the surface flow features and wake characteristics.

At $h/c_s = 0.224$ (Figure 9.2(a)) all the turbulence models captured the general features of the surface pressures. The leading edge stagnation pressure was accurately predicted by all the turbulence models at $x/c_s = 0.003$ on the pressure surface. Discrepancies were observed in the prediction of the suction peak (C_{Psuc}) and subsequent pressure recovery along the suction surface. The term suction peak refers to the value of maximum suction. No single turbulence model captured the entire surface pressure distribution perfectly. However specific features were captured accurately with various models. At this ride height ($0.224c_s$) the surface pressures were most accurately predicted with the $k-\omega$ SST model. The quantitative features of the surface pressures predicted by each turbulence model are listed in Table 9.1.

Comparisons between the numerical and experimental wake data at $x/c_s = 1.2$ are presented in Figure 9.2(b). The experimental wake profile was measured by Zhang & Zerihan [109] using Laser Doppler Anemometry in a separate wind tunnel study. Unlike the surface pressures a wide variation in the prediction of the wake profile was observed. It was noted that towards the ground plane the non-dimensional velocity (u/U_∞) decreased to approximately 0.89 then sharply increases to a value of unity. This feature was generated

by the ground plane boundary layer.

The standard $k-\varepsilon$ model failed to capture the vertical location of the lower boundary of the wake (δ_{bottom}) and the corresponding velocity recovery resulting in an unrealistic velocity profile. The standard $k-\omega$, $k-\omega$ SST and Spalart-Allmaras models all captured the velocity deficit (u_{min}) accurately, however they did not accurately predict the velocity recovery at the lower wake boundary. The $k-\varepsilon$ RNG and Realizable $k-\varepsilon$ models provided accurate predictions of the lower boundary, however the $k-\varepsilon$ RNG model underpredicted the velocity deficit. The most accurate prediction of the wake profile was obtained with the Realizable $k-\varepsilon$ model, which correctly predicted the velocity deficit, wake thickness and corresponding boundaries. Table 9.2 lists quantitative data concerning the wake profiles predicted by each turbulence model.

At $h/c_s = 0.09$ (Figure 9.2(c)), separation occurred well ahead of the trailing edge and posed an additional challenge to the numerical model. The surface pressures again suggested that the $k-\omega$ SST model gave the best prediction, with the variation between turbulence models observed at the higher ride height amplified. There were no wake measurements at this height, but we note that the variations between the turbulence models were similar to those observed at the higher ride height (Figure 9.2(d)).

9.4 Surface Pressures

The effect of ride height was investigated using the two best turbulence models, the $k-\omega$ SST and Realizable $k-\varepsilon$ models. Calculations were performed at $h/c_s = 0.448$, 0.313, 0.224, 0.179, 0.134, 0.112 and 0.09. Quantitative data concerning the general flow field, surface pressures, wake characteristics and sectional forces was extracted.

The predicted surface pressures and the measured values are shown in Figure 9.3. Only two heights are included for clarity. The agreement between the computational and experimental pressures on the pressure surface of the aerofoil was good. The leading edge stagnation point was accurately predicted at x/c_s=0.003 for all ride heights with both turbulence models. As the ride height was reduced discrepancies were observed in the pressure surface pressures between $x/c_s = 0.024$ and 0.134, where the pressures were over predicted. This was attributed to a spike in the curvature of the aerofoil at $x/c_s = 0.016$ which resulted in a sudden deceleration in the flow. The experimental data illustrated a gradual increase in the surface pressures within this region possibly due to the spike in

curvature being absent, due to manufacturing techniques.

The suction surface pressures were slightly overpredicted with the overprediction increasing with decreasing ride height. A suction spike was observed at $x/c_s = 0.013$, the magnitude of which increased as the ride height was reduced. This leading edge suction spike was not observed in the experimental data due to discrete nature of the surface pressure data. Directly downstream of the the leading edge suction peak a decrease in suction was observed at $x/c_s = 0.023$. The curvature of the aerofoil at this location was discontinuous resulting in a region of decelerated flow. Disturbances in the suction surface pressures between $x/c_s = 0.033$ and $x/c_s = 0.180$ were observed, corresponding to yet more discontinuities in the curvature.

The suction surface peak was consistently observed at $x/c_s = 0.190$ increasing in magnitude with decreasing ride height. The suction peak was overpredicted for all ride heights. Downstream of the suction peak existed a region of pressure recovery extending to the trailing edge. The rates at which the pressures recovered along the suction surface were accurately captured for all non-dimensional ride heights with the $k-\omega$ SST model. The Realizable $k-\varepsilon$ model however, overpredicted the pressure recovery rate at $h/c_s = 0.09$ resulting in an inaccurate finite pressure difference at the trailing edge. Overall the $k-\omega$ SST model gives a better prediction at all heights, especially at lower ride heights mainly in the pressure recovery region on the suction surface. The pressures on the pressure surface experience relative small variations over the range of heights.

9.5 Sectional Forces

The sectional forces generated by the aerofoil at various ride heights are presented in Figure 9.4. The predicted sectional downforce (C_{ls}) was compared with the sectional values measured experimentally [42]. The overall trend in downforce variation was captured most accurately with the $k-\omega$ SST model. The Realizable $k-\varepsilon$ model overpredicted the downforce at all ride heights and failed to accurately predict the stall of the aerofoil. There was a marked improvement with the $k-\omega$ SST model, due to better prediction of the pressure recovery process. As mentioned previously the suction surface pressures were overestimated for all ride heights, accordingly the calculated values of downforce were also overestimated. This feature was particularly acute near the maximum downforce ride height. The largest discrepancy occurred at the maximum force height of $h/c_s = 0.112$. At this ride height

the value of downforce predicted by the $k-\omega$ SST model was 2% greater than the measured value and for the Realizable $k-\varepsilon$ model 19% greater. The reduction in downforce at $h/c_s = 0.09$ due to the aerofoil stalling [42] was correctly predicted with the $k-\omega$ SST model whereas the Realizable $k-\varepsilon$ failed to predict the stall.

9.6 Flow between Aerofoil and Ground

Figure 9.5 presents contours of non-dimensional streamwise velocity (u/U_∞) for $h/c_s = 0.448$ and 0.09. The contours for $h/c_s = 0.448$ (Figure 9.5(a)) show a slightly accelerated flow beneath the aerofoil and a thin wake. A small region of recirculation was observed directly downstream of the finite trailing edge. Decreasing the ride height (Figure 9.5(b)) caused the flow beneath the wing to become increasingly accelerated with maximum values of $u/U_\infty = 2.0$ achieved at $h/c_s = 0.09$. The velocity contours indicated that the flow located between the lower boundary of the wake and ground possessed higher than freestream values of velocity. This region of flow was seemingly constrained by the lower boundary of the wake, forming a wall jet. Decreasing the ride height caused the wall jet to become increasingly accelerated, a trend which was observed experimentally [112].

Figure 9.6 presents the streamwise location of separation (x_{sep}/c_s) on the suction surface of the aerofoil. The measured values [42] are also included. The location of separation moved upstream along the suction surface as the ride height was decreased, a trend which was observed in both experiment and computation. This was a direct result of the pressure gradient beneath the aerofoil becoming increasingly adverse as the ride height was reduced. When compared to the experimental separation locations the computed values were overpredicted for all ride heights even though the surface pressures indicated good agreement.

9.7 Wake Flow Field

The turbulent wake downstream of the aerofoil was observed in Figure 9.5. The size of the wake increased as the ride height was reduced. The development of the wake was constrained by the ground plane. As the ride height was reduced the lower boundary of the wake varied. The velocity deficit in the wake increased as the ride height was reduced. Further downstream the velocity deficit slowly recovered which was accompanied by an increase in the thickness of the wake. Figure 9.7 presents the profiles of relative streamwise

velocity, tangential to the ground plane at a streamwise locations of $x/c_s = 1.2$. Only three ride heights are included corresponding to ride heights with available experimental data. A summary of the wake prediction is presented in Table 9.3.

Unlike the surface pressure prediction the Realizable $k - \varepsilon$ model produced the most accurate prediction of the wake profile. Both turbulence models accurately predicted the velocity deficit within the ground boundary layer, associated thickness and the thickening thereof with reducing ride height. The velocity deficit within the wake and top wake boundary were also predicted well by both models, however discrepancies were observed within the prediction of the lower wake boundary. The $k - \omega$ SST model underpredicted the rate of velocity recovery towards the lower wake boundary resulting in an inaccurate prediction of the lower wake boundary, and an overprediction in the wake thickness. The Realizable $k-\varepsilon$ model accurately predicted the lower wake boundary and the corresponding rate of velocity recovery. Accordingly the wake thickness was accurately predicted by the Realizable $k - \varepsilon$ model.

9.8 Discussion

A strong dependence of the surface pressures over the suction surface of the aerofoil on ride height was observed. The channel created between the suction surface of the aerofoil and the ground plane resembled a venturi nozzle. The flow entering between the leading edge and the ground plane was therefore initially accelerated until the throat of the nozzle (the lowest point on the aerofoil suction surface) then decelerated underneath the downstream section of the aerofoil. The rate of acceleration and deceleration was dependent on the shape of the nozzle and hence the ride height, with low ride heights generating greater velocities. The surface pressures illustrated this process with reductions in ride height generating suction surface pressures of greater magnitude, while the pressure surface pressures remain relatively constant. The streamwise location of the suction peak was independent of ride height at $x/c_s = 0.190$, corresponding to the throat of the channel. The surface pressures obtained in the investigation showed improvement over earlier efforts. The $k-\omega$ SST model was found to offer the best prediction of the surface pressures over the entire range of ride heights. At high ride heights the accelerated flow underneath the aerofoil could recover to a freestream value prior to the aerofoil trailing edge. Reducing the ride height created a velocity recovery rate which could not be physically achieved. Therefore a flow which

possessed a greater than freestream value of velocity i.e a wall jet was generated.

The flow beneath the aerofoil exits into a region constrained by the ground plane and the lower wake boundary. Unlike the surface pressures and sectional forces the Realizable $k-\varepsilon$ model was found to produce the best prediction of the wake flow. A jet flow between the lower boundary of the wake and the ground plane was observed, especially at low ride heights ($h/c_s = 0.09$). It is well documented that flows with large mean strain rates, such as jets, are difficult to model using turbulence models. The method adopted by the Realizable $k-\varepsilon$ model was to calculate the eddy viscosity locally therefore allowing the model to remain realizable even in regions of large mean strain rates. Shih *et al* [156] showed that the modification resulted in a much improved simulations of jet flows in particular the spreading rates. It could therefore be hypothesised that improved simulations of the ground jet flow resulted in improved simulations of the lower boundary of the wake and hence the entire wake flow.

It was noted that the thickness of the wake increased as the ride height decreased. However the transverse location of the upper boundary of the wake remained constant at $y/c_s \approx 0.15$, i.e. the transverse location of the lower boundary of the wake decreases with ride height. It has been shown that as the ride height is decreased the magnitude of the wall jet increases. It is felt that the downward translation of the lower wake boundary with decreasing ride height is linked to the strength of the wall jet, however conclusions cannot be drawn without further investigation.

9.9 Chapter Summary

A systematic numerical investigation into an aerofoil in ground effect was undertaken. The effects of turbulence model, grid density and ride height were all investigated. The results indicated that the two-dimensional flow field generated by an inverted aerofoil in ground effect can be accurately modelled by solving the Reynolds Averaged Navier-Stokes equations. In addition the surface pressures and sectional forces were most accurately predicted with the $k-\omega$ SST turbulence model. The most accurate predictions concerning the wake flow field, in particular the lower wake boundary, were obtained with the Realizable $k-\varepsilon$ turbulence model. The formulation of this turbulence model provided improved predictions of the wall jet and hence improved simulations of the lower wake boundary.

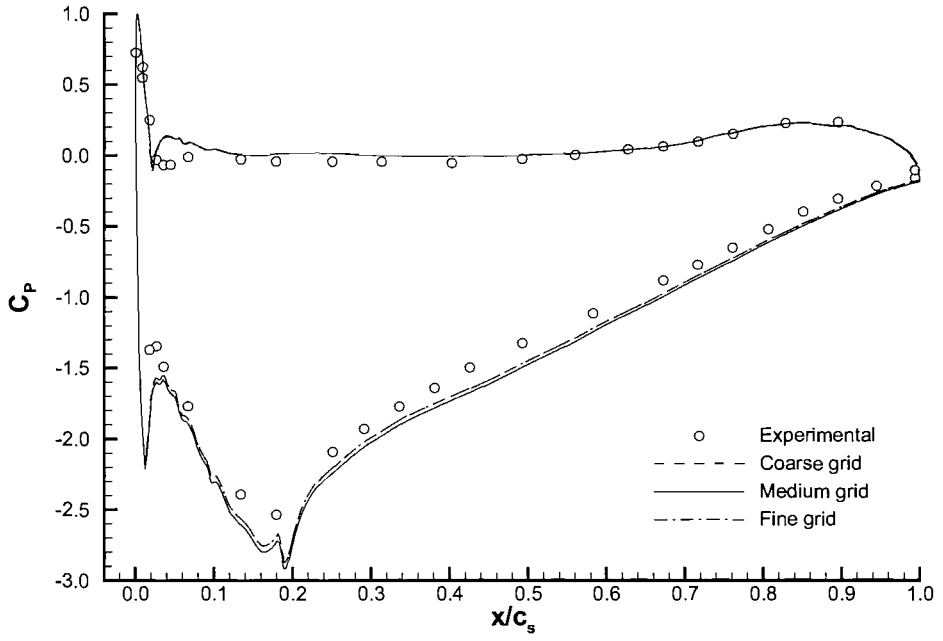

(a)

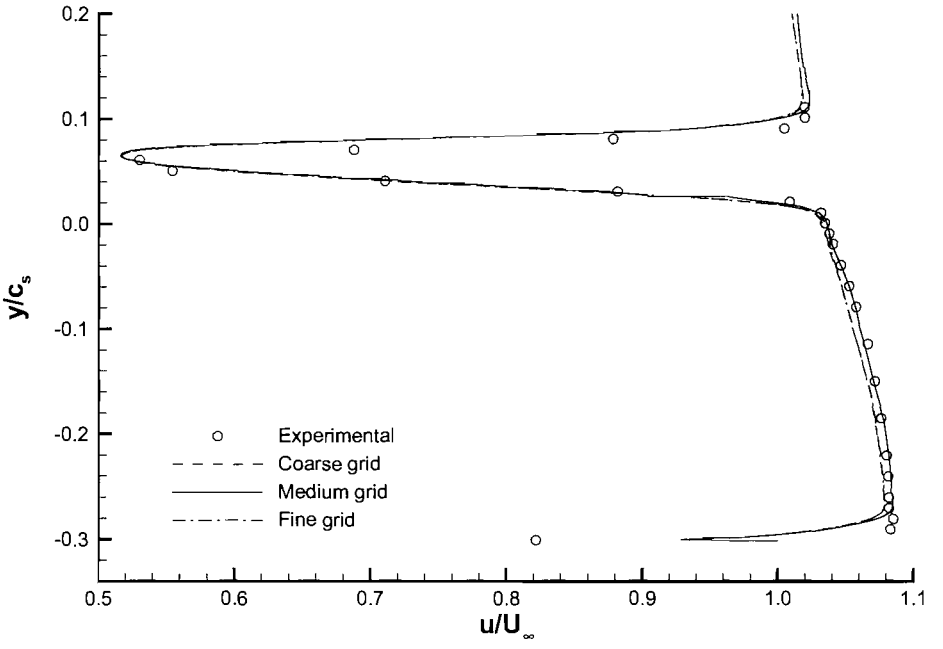

(b)

Figure 9.1: Effects of grid resolution at $h/c_s = 0.224$; (a) surface pressures, (b) wake profiles at $x/c_s = 1.2$.

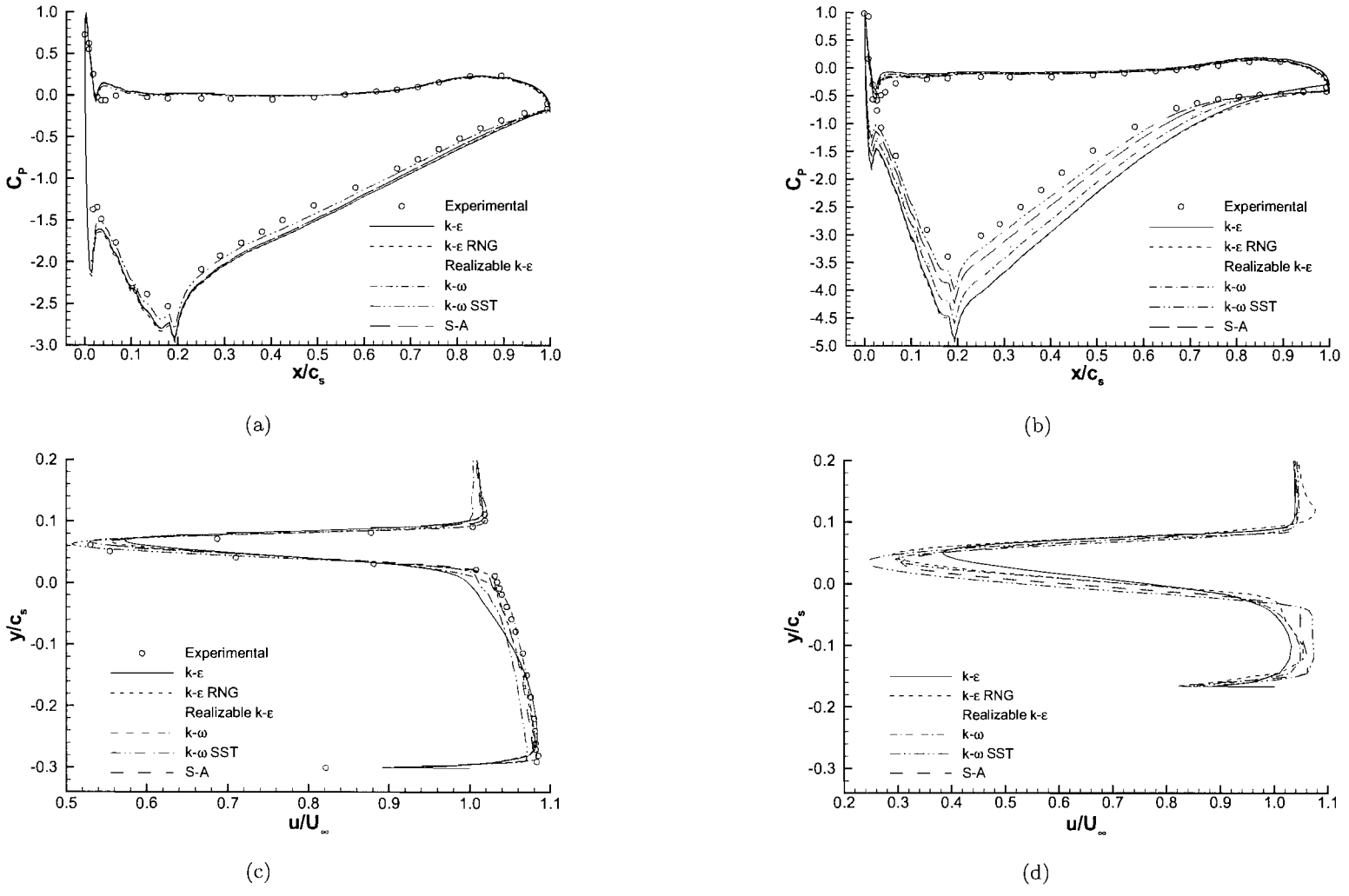

Figure 9.2: Effects of turbulence model; (a) surface pressures at $h/c_s = 0.224$, (b) surface pressures at $h/c_s = 0.09$, (c) wake profiles at x/c_s=1.2 for $h/c_s = 0.224$ and (d) wake profiles at x/c_s=1.2 for $h/c_s = 0.09$.

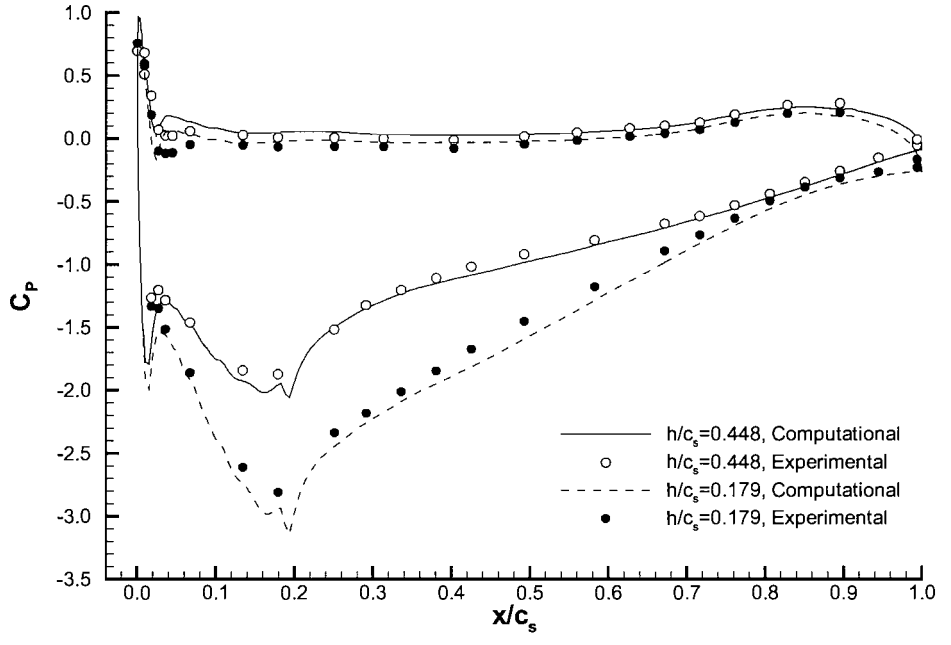

(a)

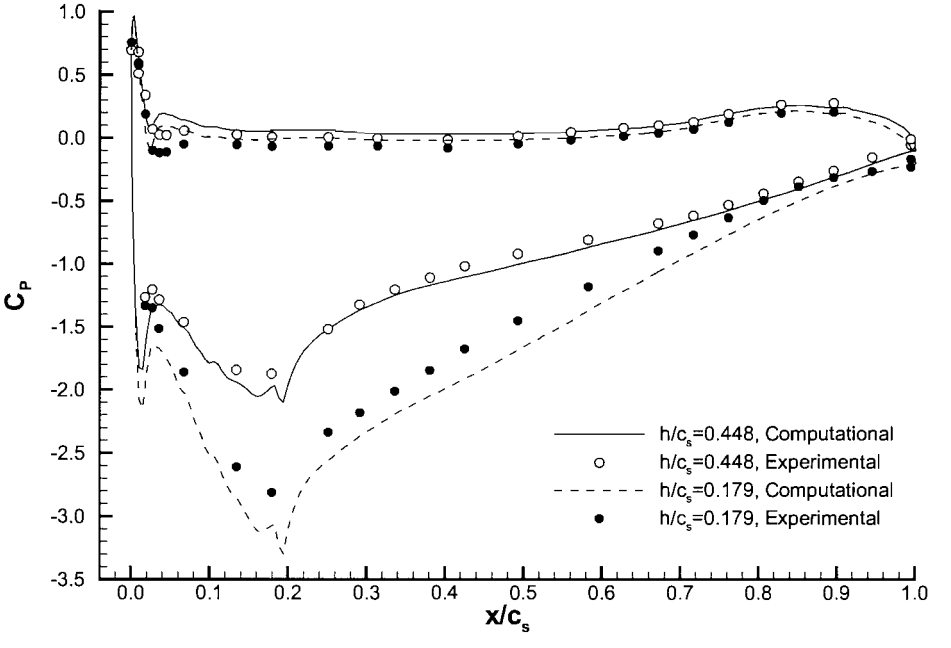

(b)

Figure 9.3: Surface pressures at various ride heights; (a) $k-\omega$ SST model, (b) Realizable $k-\varepsilon$ model.

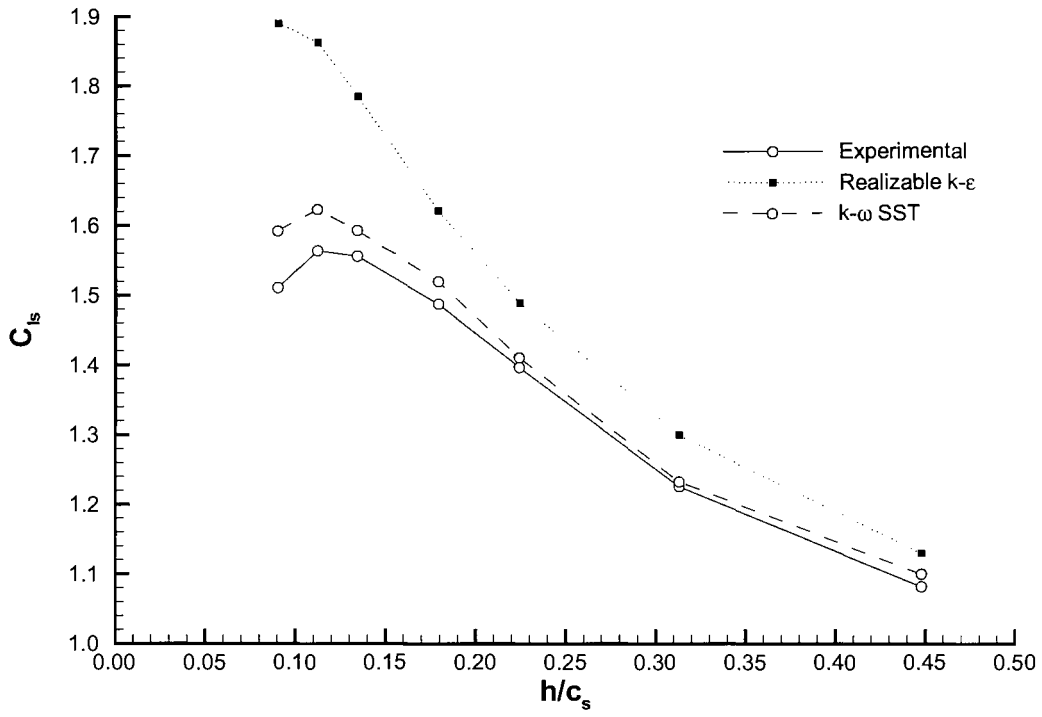

Figure 9.4: Sectional forces at various ride heights.

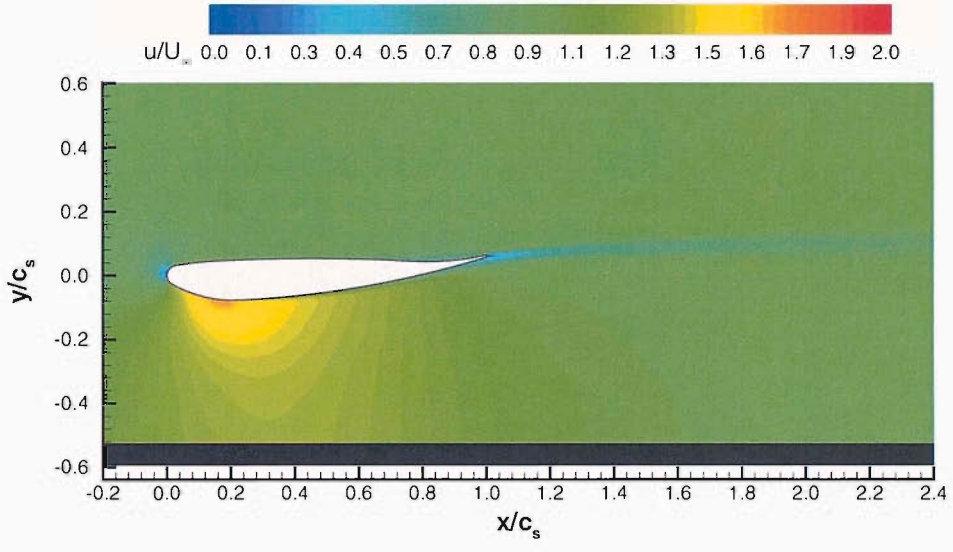

(a)

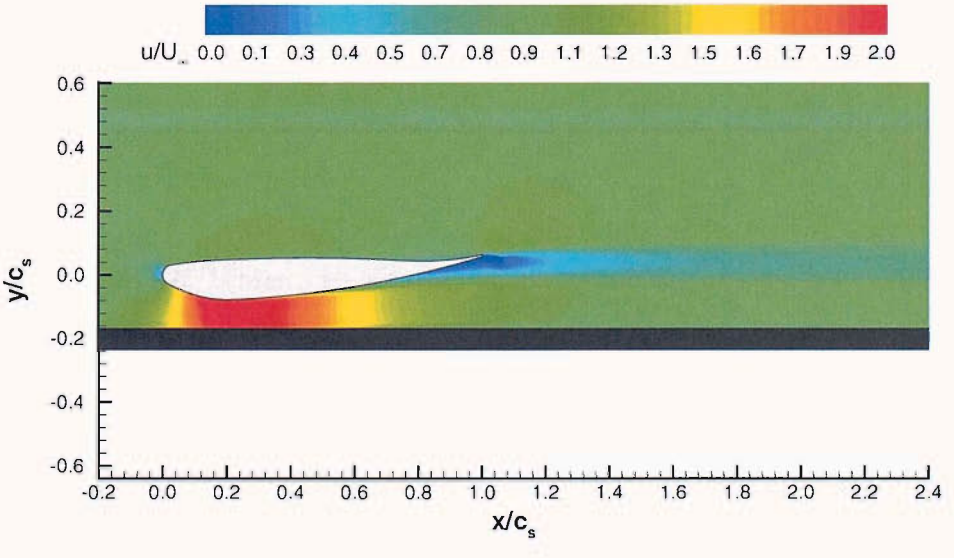

(b)

Figure 9.5: Contours of u/U_∞ with the Realizable $k-\varepsilon$ model: (a) $h/c_s = 0.448$. (b) $h/c_s = 0.09$.

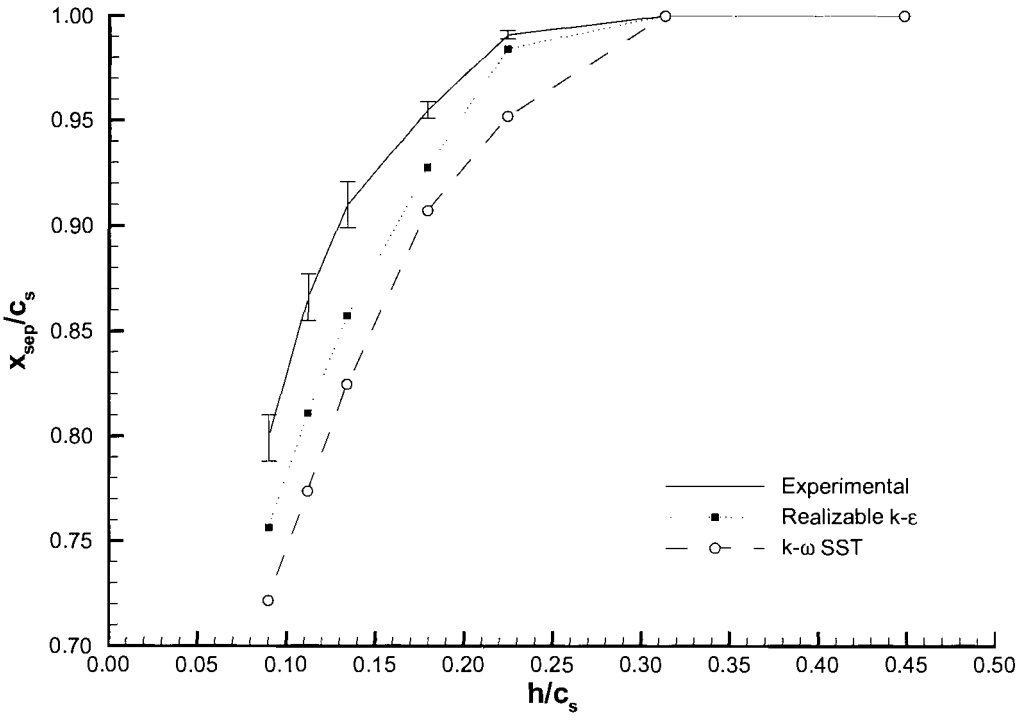

Figure 9.6: Streamwise location of separation for various ride heights.

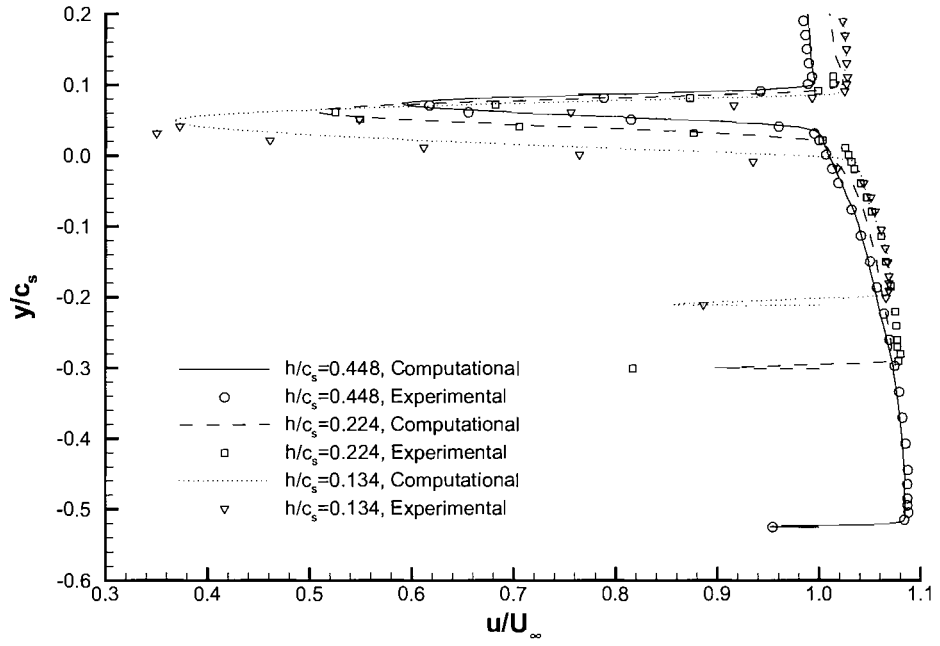

(a)

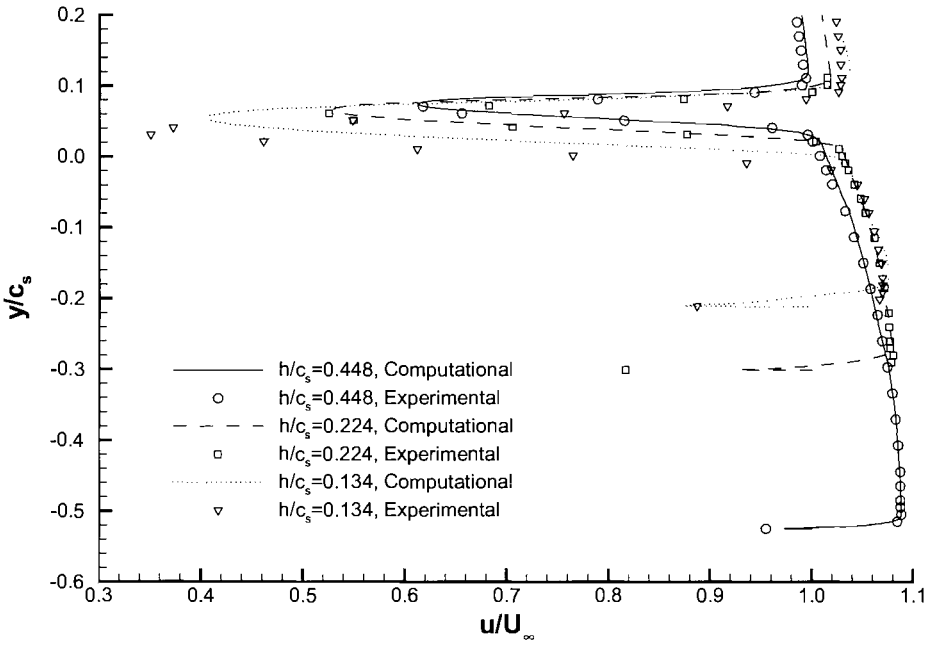

(b)

Figure 9.7: Wake profiles at $x/c_s = 1.2$; (a) $k - \omega$ SST model, (b) Realizable $k - \varepsilon$ model.

Turbulence Model	C_{Psuc}	x/c_s at C_{Psuc}
Experimental	-2.53	0.18
Spalart-Allmaras	-2.92	0.19
Standard $k-\omega$	-2.92	0.19
$k-\omega$ SST	-2.81	0.19
Standard $k-\varepsilon$	-2.94	0.19
$k-\varepsilon$ RNG	-2.97	0.19
Realizable $k-\varepsilon$	-2.92	0.19

Table 9.1: Surface pressure information for various turbulence models; $h/c_s = 0.224$.

Turbulence Model	u_{min}/U_∞	y/c_s at u_{min}	y/c_s at δ_{top}	y/c_s at δ_{bottom}	δ_{99}/c_s
Experimental	0.53	0.06	0.09	0.02	0.07
Spalart-Allmaras	0.55	0.07	0.10	0.02	0.08
Standard $k-\omega$	0.53	0.07	0.10	0.01	0.09
$k-\omega$ SST	0.51	0.06	0.09	0.02	0.07
Standard $k-\varepsilon$	0.57	0.07	0.10	0.01	0.09
$k-\varepsilon$ RNG	0.56	0.07	0.10	0.02	0.08
Realizable $k-\varepsilon$	0.53	0.07	0.09	0.02	0.07

Table 9.2: Wake information for various turbulence models at $x/c_s = 1.2$ and $h/c_s = 0.224$.

h/c_s	Expt/CFD	u_{min}/U_∞	y/c_s at u_{min}	y/c_s at δ_{top}	y/c_s at δ_{bottom}	δ_{99}/c_s
0.448	Experimental	0.617	0.071	0.103	0.032	0.071
	Realizable $k-\varepsilon$	0.613	0.074	0.110	0.004	0.106
	$k-\omega$ SST	0.591	0.073	0.099	0.037	0.062
0.224	Experimental	0.525	0.061	0.090	0.022	0.068
	Realizable $k-\varepsilon$	0.529	0.065	0.098	0.024	0.074
	$k-\omega$ SST	0.507	0.063	0.091	0.022	0.069
0.134	Experimental	0.350	0.031	0.082	-0.016	0.098
	Realizable $k-\varepsilon$	0.405	0.054	0.094	0.004	0.090
	$k-\omega$ SST	0.367	0.049	0.085	-0.001	0.086

Table 9.3: Wake information for various ride heights at $x/c_s = 1.2$.

Chapter 10

RANS Simulations of a Multi-Element Aerofoil in Ground Effect

This chapter presents and discusses computational results for a multi-element aerofoil in ground effect. The applicability of the six turbulence models listed in Section 8.3 will be quantified initially. Results obtained at various ride heights will then presented and quantitatively compared to experimental data.

10.1 Aerofoil Geometry

The aerofoil used in this investigation comprised of two elements in a single slotted flap configuration. The main element was a derivative of the LS(1)-0413 MOD profile and possessed a finite trailing edge of 1.56mm. The flap profile represented a typical profile used within motorsport and possessed a finite trailing edge of 0.95mm. A detailed listing of the both profiles may be found in Zerihan [9]. The chords of the main element and flap were 223.4mm and 165.7mm respectively. For continuity within the results a total chord (c_t) of 380mm was defined. The flap was located with an overlap (δ_o) and gap (δ_g) of $0.024c_t$ and $0.032c_t$ respectively. These values resulted from an experimental optimisation investigation with regards to downforce [111]. The incidences of the main element and flap were $+3.6°$ and $+15.5°$ respectively. All computations were performed at a Reynolds number of 7.86×10^5 based on the total chord of the aerofoil. These conditions corresponded to experimental conditions [111]. The streamwise location of transition was determined from oil flow visualisation results [112]. For ride heights of $h/c_t \geq 0.132$ transition was found to occur at $x/c_t = 0.08$ and 0.02 on the main element suction surface and pressure surface

respectively. For ride heights of $h/c_t \leq 0.105$ transition was found to occur immediately at the main element leading edge hence a laminar zone was not required in these cases.

The design of the support system used within the experiments [9] was such that alterations in aerofoil incidence were observed between the static and wind-on conditions. These alterations in aerofoil incidence due to flexing of the wing were dependent on the forces generated by the wing and ranged between $-0.67°$ and $-1.87°$. For a specific ride height the flexing of the aerofoil and transition locations were taken into account when designing the computational grid.

10.2 Grid Independence Study

Prior to conducting investigations into the influence of ride height, the dependence of the solution on the resolution of the computational grid was quantified. A grid sensitivity study was performed at a ride height of $h/c_t = 0.211$, a ride height typical of the force enhancement region [9]. Three grids were constructed: a coarse grid of 184,335 cells, a medium grid of 380,812 cells and a fine grid of 846,317 cells. The variations in grid density were focused in the wing boundary layer blocks and wake block. The effects of turbulence were modelled using the Realizable $k - \varepsilon$ model. The surface pressures and wake profiles at $x/c_t = 1.066$ are presented in Figure 10.1. For reasons of clarity the surface pressures of the main element and flap are shown separately. Very little variation in the results was observed. Although steady-state simulation were performed it was noted that with the fine grid unsteady features were detected, especially within the wake flow field. These effects were periodic and are illustrated in the wake profile for the fine grid between $y/c_t = -0.06$ and 0.06. In all simulations the coarse grid was used in order to reduce the computational cost.

10.3 Turbulence Model Comparison

A quantitative study of the six turbulence models stated in Section 8.3 was conducted. Two cases were selected ($h/c_t = 0.211$ and 0.079). $h/c_t = 0.211$ represented a flow condition where the ride height of the aerofoil was within the force enhancement region [112] and a thin dual wake flow field was observed. At $h/c_t = 0.079$ the aerofoil was close to maximum downforce and a thick main element wake was observed in addition to the thin flap wake. The suitability of each turbulence model was quantitatively assessed using the surface flow

features and wake characteristics.

At $h/c_t = 0.211$ (Figure 10.2(a)) all the turbulence models accurately captured the surface pressures over both the main element and flap. The leading edge stagnation on both the main element and flap was correctly predicted by all turbulence models at $x/c_t = 0.009$ and $x/c_t = 0.567$ respectively. The streamwise location of the suction peak (C_{Psuc}) was found to be independent of turbulence model, occurring at $x/c_t = 0.11$. The term suction peak referred to the value of maximum downforce downstream of the leading edge suction spike as illustrated in Figure 10.1. The quantitative features of the surface pressures predicted by each turbulence model at $h/c_t = 0.211$ are listed in Table 10.1. Variations were observed in the prediction of the wake profile at $x/c_t = 1.066$ (Figure 10.2(b)). Measurements were obtained using Laser Doppler Anemometry [112]. The agreement between the computational results and the experimental measurements within the core of the wake was poor for all six turbulence models. The agreement between the results obtained with each turbulence model however, was good. All the turbulence models accurately predicted the velocity profile between the ground plane and the lower boundary of the main element wake. It was noted that towards the ground plane the non-dimensional velocity (u/U_∞) decreased to approximately 0.89 then sharply increased to a value of unity. This feature was generated by the ground plane boundary layer. The Spalart-Allmaras and Realizable $k-\varepsilon$ models offered improved predictions concerning the ground boundary layer velocity profile.

The vertical location of the lower boundary of the main element wake was underpredicted by all six turbulence models. Figure 5.25 defines the variables used to describe the wake flow field. The maximum velocity deficit within the main element wake (u_{low}) and corresponding vertical location were underpredicted by five of the six turbulence models. The Realizable $k-\varepsilon$ model overpredicted u_{low}. The vertical location of the confluence point (Figure 10.1) between the flap and main element wakes was underpredicted by all the turbulence models. The associated streamwise velocity (u_{conf}) was captured well with the exception of the standard $k-\varepsilon$ model. The maximum velocity deficit within the flap wake (u_{top}) was overpredicted by all the turbulence models. The vertical location of the upper boundary of the flap wake (δ_{top}) was best predicted by the $k-\varepsilon$ RNG model, all other turbulence models underpredicted the vertical location. Due to the varying predictions of the main element and flap wake boundaries a wide variation was observed within the predictions of the flap wake thickness ($(\delta_{99})_{top}$) and main element wake thickness ($(\delta_{99})_{low}$).

The Realizable $k-\varepsilon$ model and standard $k-\varepsilon$ model provided the best predictions of the main element wake and flap wake thickness respectively. The quantitative features of the wake profiles predicted by each turbulence model at $x/c_t = 1.066$ are listed in Table 10.2.

Figures 10.2(c) and 10.2(d) present the surface pressures and wake profiles at $x/c_t = 1.066$ respectively for a ride height of $0.079c_t$. The variations within the surface pressures due to turbulence model remained consistent with those observed at $h/c_t = 0.211$. However, the variations were more readily observed due to the increased magnitudes of the surface pressures. The surface pressures on both the main element and flap were most accurately predicted with the Realizable $k-\varepsilon$ turbulence model. Experimental data concerning the wake flow field was not available at this lower ride height. However, the variations between the turbulence models remained consistent with those observed at $h/c_t = 0.211$.

10.4 Surface Pressures

With the influence of turbulence models quantified the effects of ride height variation on aerofoil performance could be investigated. Calculations were performed at ride heights of $0.395c_t$, $0.263c_t$, $0.211c_t$, $0.158c_t$, $0.132c_t$, $0.105c_t$ and $0.079c_t$. Data concerning the surface pressures, wake flow field and sectional forces was extracted. Due to the poor agreement concerning the wake profiles the choice of turbulence model was based solely on the performance of each turbulence model with respect to the surface pressures. Accordingly the Realizable $k-\varepsilon$ model was used in the simulations at various ride heights.

The calculated surface pressures are presented with experimental data [9] in Figure 10.3. Figures 10.3(a) and 10.3(b) present the surface pressures for high and low ride heights respectively. At all ride heights the general features of the surface pressures over both elements were accurately predicted. The leading edge stagnation pressures on both the main element and flap were correctly predicted. The streamwise location of stagnation on the main element was found to move upstream with reducing ride height, decreasing from $x/c_t = 0.011$ to 0.006. Stagnation on the flap was found to be independent of ride height consistently occurring at $x/c_t = 0.57$. The pressure surfaces pressures of both elements remained relatively independent of ride height when compared to the suction surface pressures, and were accurately predicted for all ride heights.

The calculated surface pressures on the flap agreed well with the experimental data and captured the increase in suction with decreasing ride height. The main element suction sur-

face pressures were slightly overpredicted at all ride heights. The increase in main element suction with decreasing ride height was accurately predicted. The streamwise location of the suction spike was consistently predicted at $x/c_t = 0.004$ increasing in magnitude with decreasing ride height. Directly downstream of the suction spike a decrease in suction was observed at $x/c_t = 0.02$. The curvature of the main element at this location was discontinuous resulting in a region of decelerated flow. Disturbances in the suction surface pressures between $x/c_t = 0.02$ and 0.11 were observed, corresponding to yet more discontinuities in the curvature. The streamwise location of the suction peak was consistently predicted at $x/c_t = 0.11$. The magnitude of the suction peak increased in magnitude with decreasing ride height. The pressure recovery directly downstream of the suction peak was also accurately simulated at all ride heights.

10.5 Sectional Forces

The calculated sectional forces generated by the aerofoil at various ride heights are presented in Figure 10.4(a). Experimental sectional forces calculated from the measured surface pressures are also shown. The overall trend in downforce (C_{ld}) with ride height was captured. The overprediction of the surface pressures with the Realizable $k-\varepsilon$ model resulted in overpredictions within the sectional downforce. Variations within the downforce trends were observed at $h/c_t = 0.105$ caused by the removal of the laminar zone. The greatest discrepancies between the computational and experimental data was 15% at $h/c_t = 0.132$.

The variation in the downforce generated solely by the main element ($(C_{ld})_m$) and flap ($(C_{ld})_f$) with ride height is shown in Figure 10.4(b). It is clear that the majority of the downforce was generated by the main element which varied similarly to the overall downforce with ride height. The percentage of total downforce due to the main element increased asymptotically as the ride height was reduced. A maximum value of 84% was achieved at $h/c_t = 0.079$. Decreasing the ride height from $h/c_t = 0.395$ to 0.132 caused the downforce generated by the flap to increase linearly. Further decreases in ride height resulted in the flap downforce decreasing until a minimum ride height was achieved. Similar downforce variations with ride height were observed experimentally [111].

10.6 Flow Between Aerofoil And Ground

Figure 10.5 presents contours of non-dimensional streamwise velocity (u/U_∞) for h/c_t = 0.395 and 0.079. The contours for $h/c_t = 0.395$ (Figure 10.5(a)) presented a flow which was slightly accelerated when exiting the channel between the lower boundary of the main element wake and the ground plane. The main element wake was thin and followed the contour of the flap suction surface. A thin ground boundary layer was observed downstream of the aerofoil. The contours for $h/c_t = 0.079$ (Figure 10.5(b)) showed a highly accelerated flow with a maximum streamwise velocity of $u/U_\infty \approx 3.0$. A thick main element wake was observed which was amplified in thickness underneath the flap suction surface. The accelerated flow exiting beneath the main element trailing edge seemed constrained by the ground plane and lower boundary of the lower wake forming a wall jet. The ground boundary layer increased in thickness when compared to the higher ride height.

At ride heights of $h/c_t > 0.079$ no separation was observed on either the main element or flap suction surfaces. A small region of recirculation was observed directly downstream of the main element finite trailing edge at all ride heights. Separation was observed at $x/c_t = 0.539$ on the main element suction surface for $h/c_t = 0.079$. Experimental surface flow field data was not available at this ride height hence it could not be determined which prediction was correct.

10.7 Near Field Main Element Wake Development

The near field development of the main element wake between the flap suction surface and the ground plane is illustrated in Figure 10.5(b). For all ride heights the vertical distance between the top boundary of the main element wake and the flap suction surface remained of the order of the flap gap. It has already been noted that separation was not observed on the main element suction surface for $h/c_t \geq 0.105$. However it must be remembered that the main element suction surface boundary layer was included within the calculation of the lower boundary of the main element wake therefore producing a value of wake thickness greater than would be expected.

The streamwise variation in main element wake thickness ($(\delta_{99})_{low}$) for various ride heights is presented in Figure 10.6. The spreading rate of the main element wake ($\partial\delta_{99}/\partial x$) was found to increase with a third order polynomial trend, for a set ride height. Reductions in ride height resulted in the spreading rate increasing with a maximum value of $\partial\delta_{99}/\partial x =$

0.891 occurring at $h/c_t = 0.079$. For this lowest ride height the main element wake increased in thickness between $x/c_t = 0.624$ and 0.984 by over 430% and at the flap trailing edge was equivalent to 80% of the wake thickness observed at $x/c_t = 1.066$.

10.8 Wake Flow Field

The variation in wake flow field with ride height and streamwise location is presented in Figure 10.7. Figure 10.7(a) presents the variation in wake profiles with ride height at $x/c_t = 1.066$. Three ride heights are shown for reasons of clarity, with the quantitative data listed in Table 10.3. The agreement between the experimental and computational data was good with the exception of the main element wake lower boundary and the velocity deficit within the main element wake. The increase in ground boundary layer thickness with decreases in ride height was captured. However, the velocity deficit within the ground boundary layer was underpredicted for $h/c_t = 0.395$ and overpredicted for $h/c_t = 0.079$. The profile of the wall jet and associated velocities was captured well for all ride heights, however the lower wake boundary was underpredicted.

The velocity deficit within the main element wake was overpredicted for all ride heights. However, the rate of velocity recovery was captured accurately. Reductions in ride height resulted in the velocity deficit increasing and the lower boundary of the main element wake getting closer to the ground plane. The velocity at the confluence point was generally overpredicted and increased, i.e approached freestream, as the ride height decreased. The vertical location of the confluence point was generally underpredicted and decreased with decreasing ride height. The maximum velocity deficit within the flap wake was underpredicted for all ride heights and increased with reductions in ride height. The vertical location of the maximum velocity within the flap wake was also underpredicted and decreased with decreasing ride height. The upper boundary of the flap wake was predicted accurately for all ride heights. However, the recovery to freestream was generally overpredicted resulting in a reduced streamwise velocity value.

The thickness of the main element wake was overpredicted at all ride heights, a result of the underprediction with respect to the main element wake lower boundary. As the ride height was decreased the main element wake increased in thickness primarily due to variations within the vertical location of the lower boundary. The flap wake thickness was overpredicted for all ride heights and decreased as the ride height was reduced. All the

trends within in the computational data were also captured experimentally.

The streamwise variation in wake profile for a ride height of $h/c = 0.105$ with the Realizable $k-\varepsilon$ model is shown in Figure 10.7(b) and listed in Table 10.4. Data concerning the main element wake at $x/c_t = 1.318$ and 1.776 has been omitted from Table 10.4 since the two wakes had merged at these streamwise locations forming a single wake. Although only data at $h/c_t = 0.105$ is presented it was noted that similar trends and features were observed at all the ride heights. The thickness of the ground boundary layer was captured accurately for all streamwise locations. However, the velocity deficit within the boundary layer was overpredicted. With the exception of the main element wake lower boundary being underpredicted, the profile of the wall jet and the corresponding downstream velocity recovery was captured well. The maximum velocity deficit within the main element wake was overpredicted for all streamwise locations. Experimentally the main element wake was found to move upwards a trend which was observed within the computational data albeit at a reduced rate. Accordingly the flap wake upper boundary was underpredicted computationally. The merging of the two wakes into a single wake was overpredicted between $x/c_t = 1.381$ and 1.776 compared to between $x/c_t = 1.184$ and 1.381 within the experimental data.

10.9 Discussion

The circulation around the main element was increased with the addition of the flap (Figure 10.1). The increase in circulation was observed as increased suction on the suction surface and increased pressure on the pressure surface. The pressure recovery over the suction surface of the main element remained constant.

The channel created between the suction surfaces of the aerofoil and the ground plane resembles a venturi nozzle. Reducing the ride height caused the acceleration of the flow beneath the main element to increase. Section 9.8 discusses this flow field variation in more depth for a single element aerofoil. Studying Figure 10.5 it may be noted that presence of the main element wake seemed to divide the flow field beneath the aerofoil into two regions; a region extending downstream from beneath the main element and a region extending downstream from the slot between the two elements. At a ride height of $h/c_t = 0.079$ the flow exiting the slot possessed a greater than freestream velocity with a profile similar to that of a jet. It could be hypothesised that since the slot flow is feeding into a region of

enclosed suction, unlike a freestream case, the velocity must increase through the slot in accordance with continuity. Smith [48] stated that the presence of a second element would not produce a slot flow with high velocity which would seem to be in contradiction with this finding. However in theory this is still correct since the increases in slot flow velocity seemed to be caused by the enclosed suction region beneath the flap and any subsequent variations with ride height. The variations within the velocities corresponding to the slot flow were less than those observed within the wall jet therefore producing smaller variations within the flap suction surface pressures.

The wake generated by the wing consisted predominantly of the main element wake which increased in thickness as the ride height decreased. The thickness of the flap wake and the corresponding velocity deficit was relatively independent of ride height and remained thin for all cases. The majority of the main element wake thickness was generated underneath the flap suction surface where the wake was seemingly amplified by the region of enclosed suction beneath the aerofoil. It may also be noted that within this region of the aerofoil at low ride heights the wall jet, exiting from beneath the main element, started to recover towards a freestream value of velocity. Reducing the ride height resulted in a greater spreading rate of the main element wake (Figure 10.6) and therefore a thicker overall wake. The region of recirculation directly downstream of the main element finite trailing edge contributed greatly to the main element wake. It could therefore be hypothesised that a sharp main element trailing edge would reduce the main element wake significantly. Within a motorsport application the reduced wake could increase the performance of components located downstream of the aerofoil/wing.

The spreading of the main element wake was overpredicted for all cases, in particular the vertical location of the lower boundary was underpredicted. The computations conducted were two-dimensional whereas in reality the flow field generated by a wing in ground effect is intrinsically three-dimensional. Therefore the effects of the wing tip vortices were excluded from the computation. It is hypothesised that the inclusion of upwash effects may influence the wake flow field, deflecting the main element and flap wakes upwards. Improvements may therefore be obtained through the use of three-dimensional simulations of a finite span wing in ground effect.

10.10 Chapter Summary

A systematic numerical investigation into a multi-element aerofoil in ground effect was undertaken. The effects of turbulence model, grid density and ride height were all investigated. The results indicated that the surface pressures generated by an inverted multi-element wing in ground effect can be accurately modelled by solving the Reynolds Averaged Navier-Stokes equations. The wake flow field was predicted less accurately, in particular the vertical location and corresponding boundaries. However the numerical investigation allowed for the initial development of the main element wake to be quantified. The results indicated the thickness of the main element wake was largely a result of the wake dilating underneath the flap.

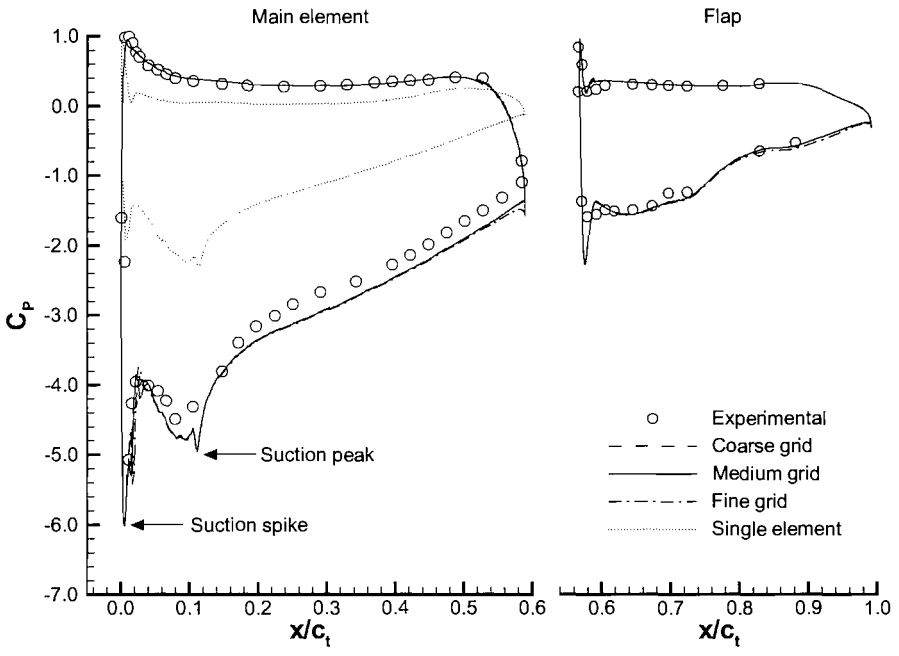

(a)

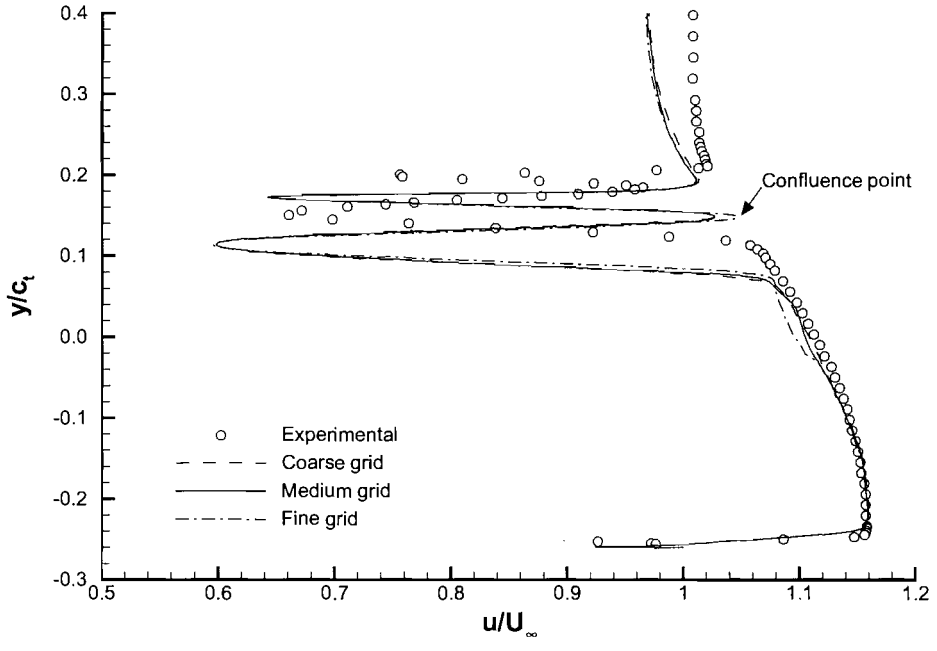

(b)

Figure 10.1: Effects of grid resolution at $h/c_t = 0.211$; (a) surface pressures, (b) wake profiles at $x/c_t = 1.066$.

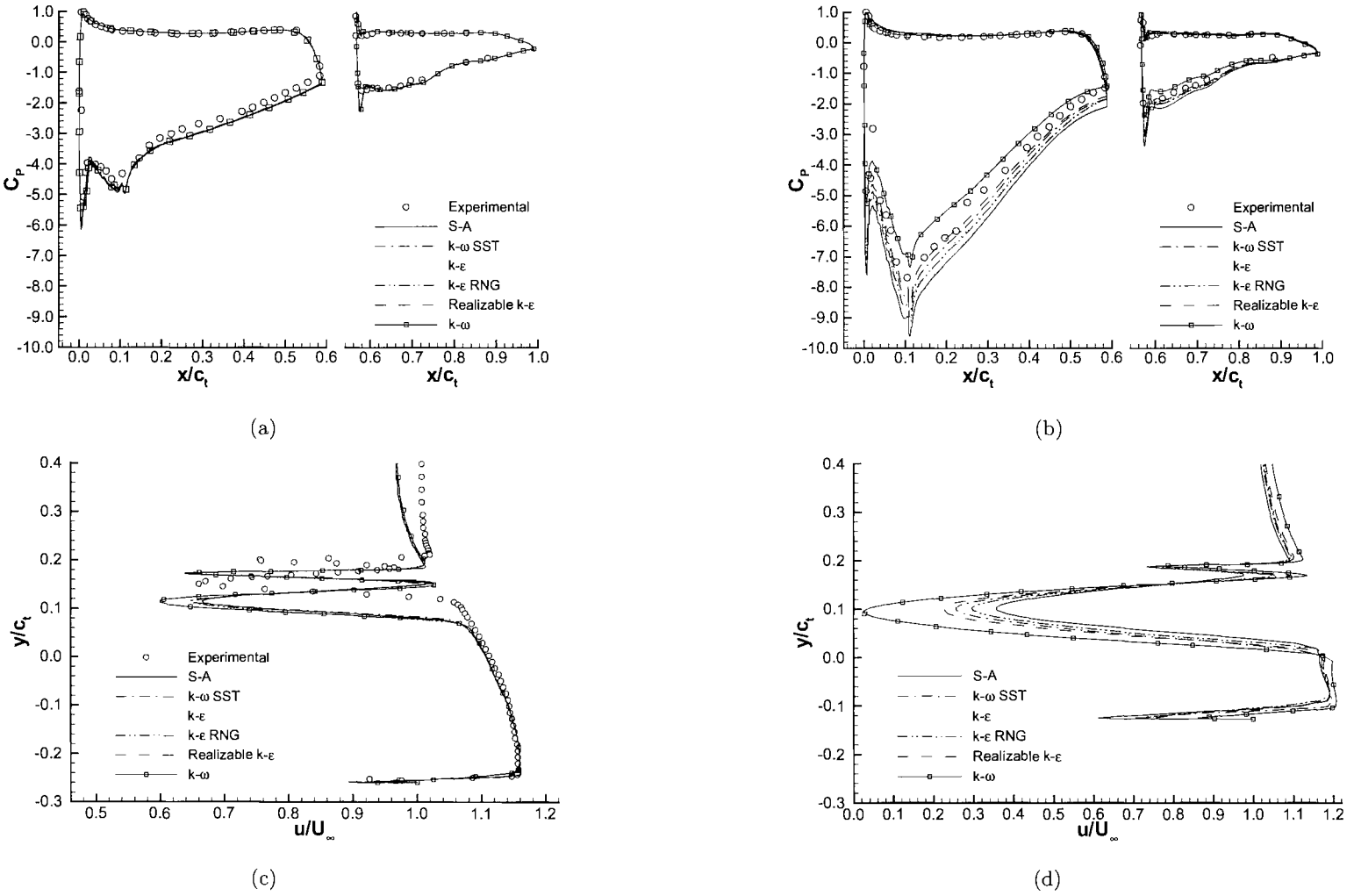

Figure 10.2: Effects of turbulence model; (a) surface pressures at $h/c_t = 0.211$, (b) surface pressures at $h/c_t = 0.079$, (c) wake profiles at x/c_t=1.066 for $h/c_t = 0.211$ and (d) wake profiles at x/c_t=1.066 for $h/c_t = 0.079$.

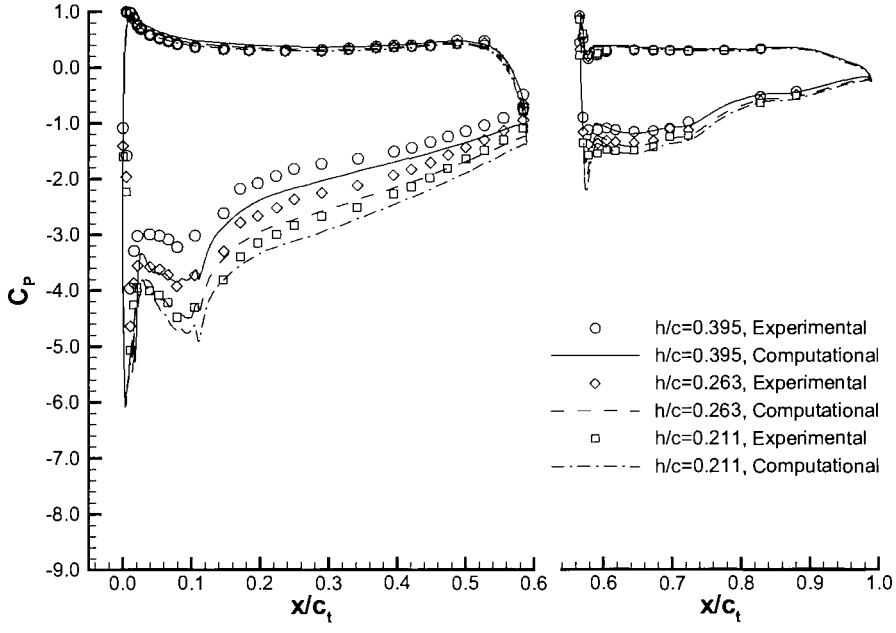

(a)

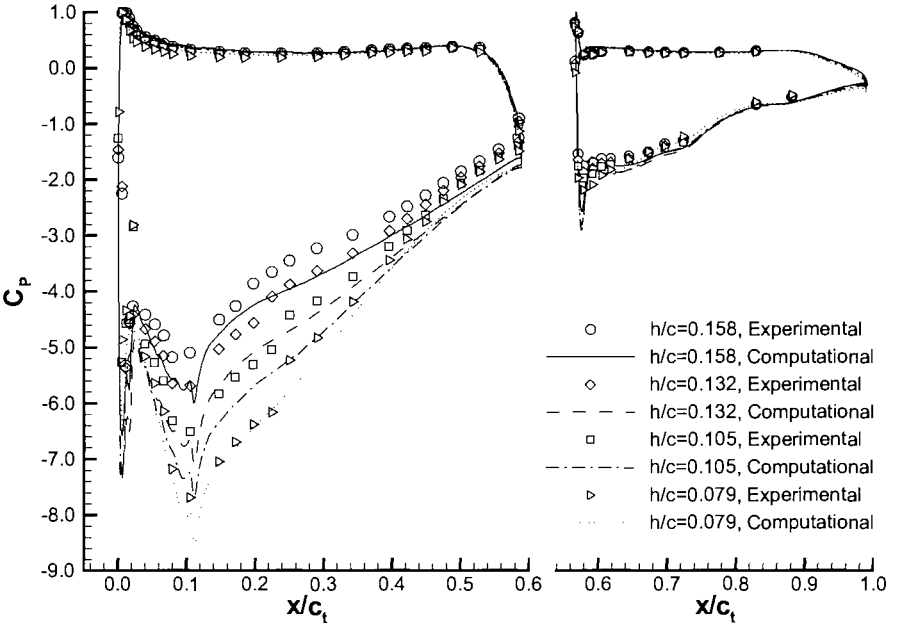

(b)

Figure 10.3: Surface pressures at various ride heights; (a) high ride heights, (b) low ride heights.

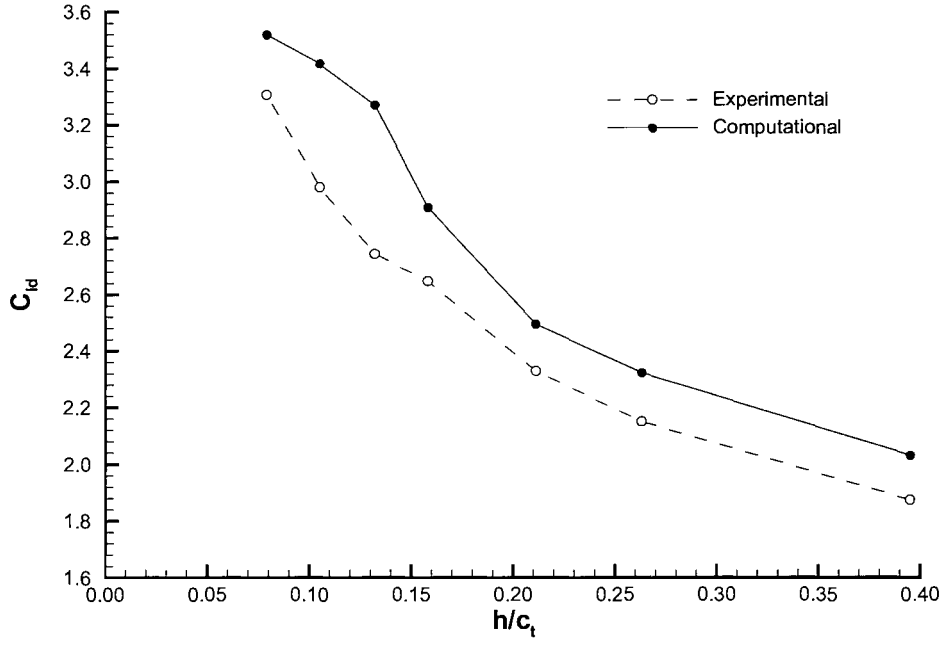

(a)

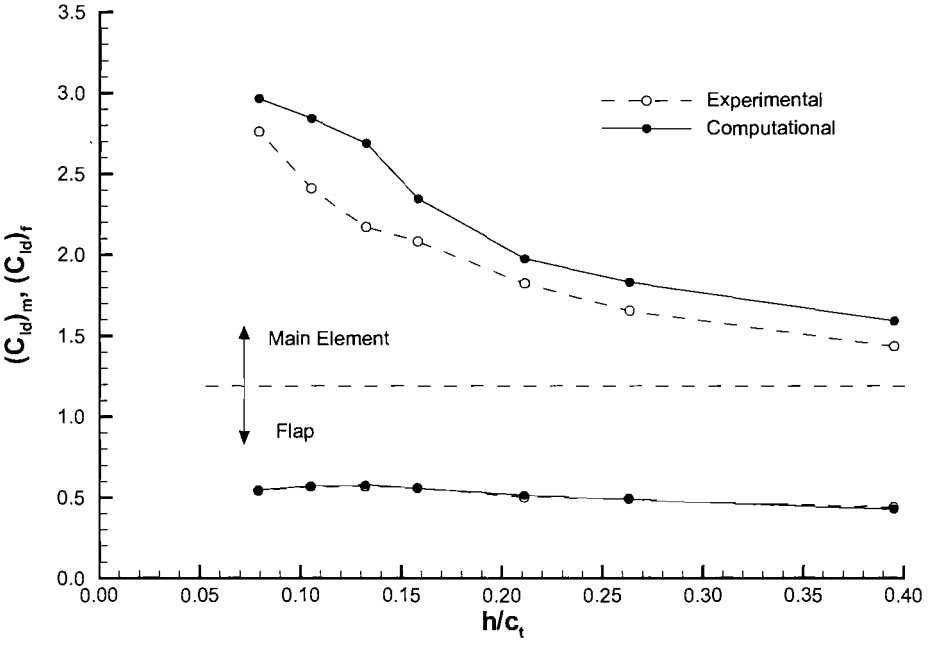

(b)

Figure 10.4: Sectional downforce at various ride heights; (a) total downforce, (b) downforce due to the main element and flap.

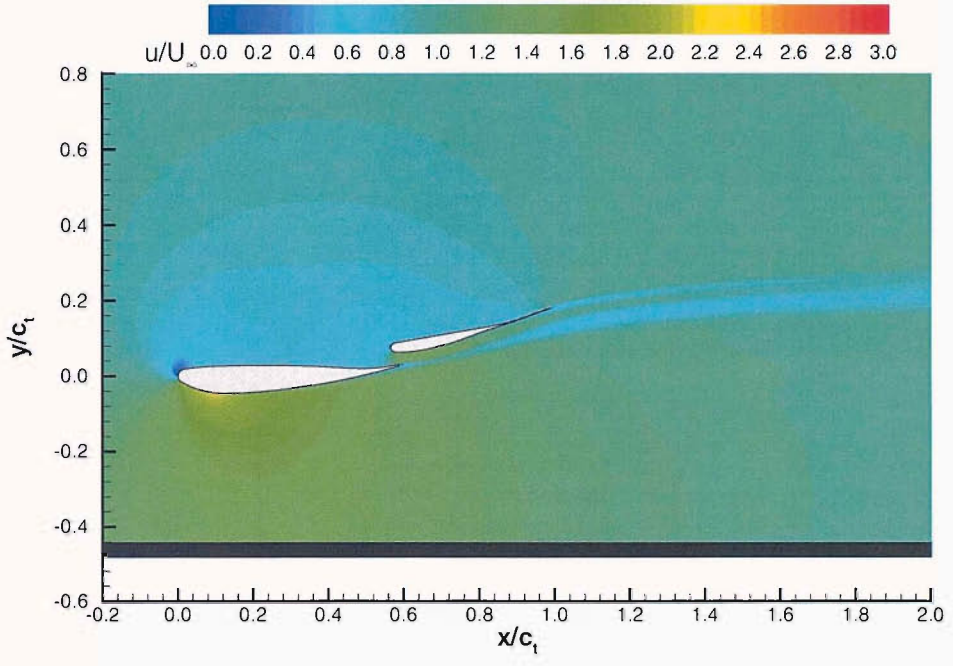

(a)

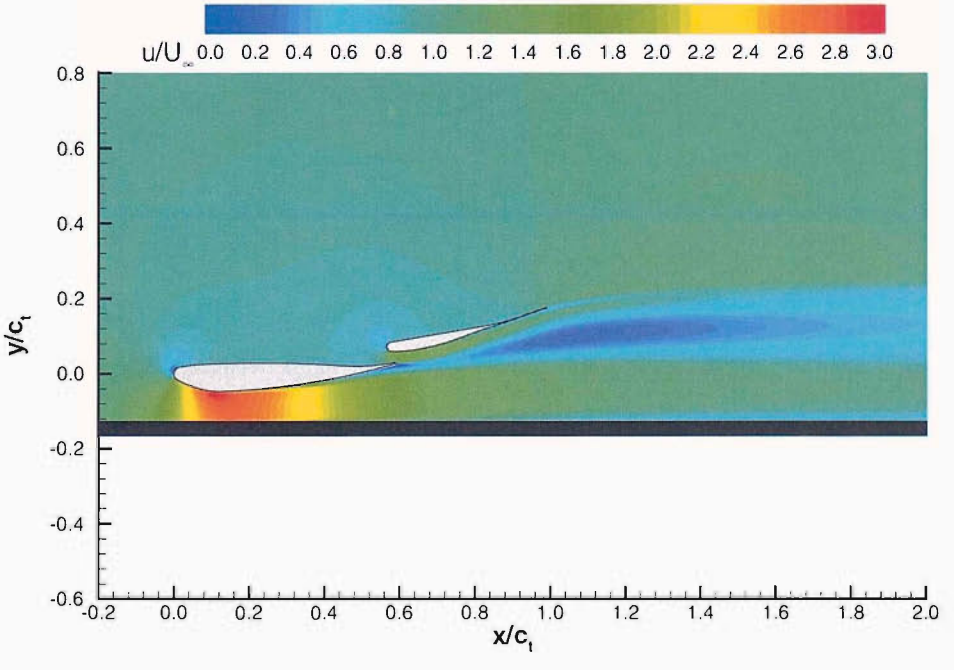

(b)

Figure 10.5: Contours of u/U_∞: (a) $h/c_t = 0.395$, (b) $h/c_t = 0.079$.

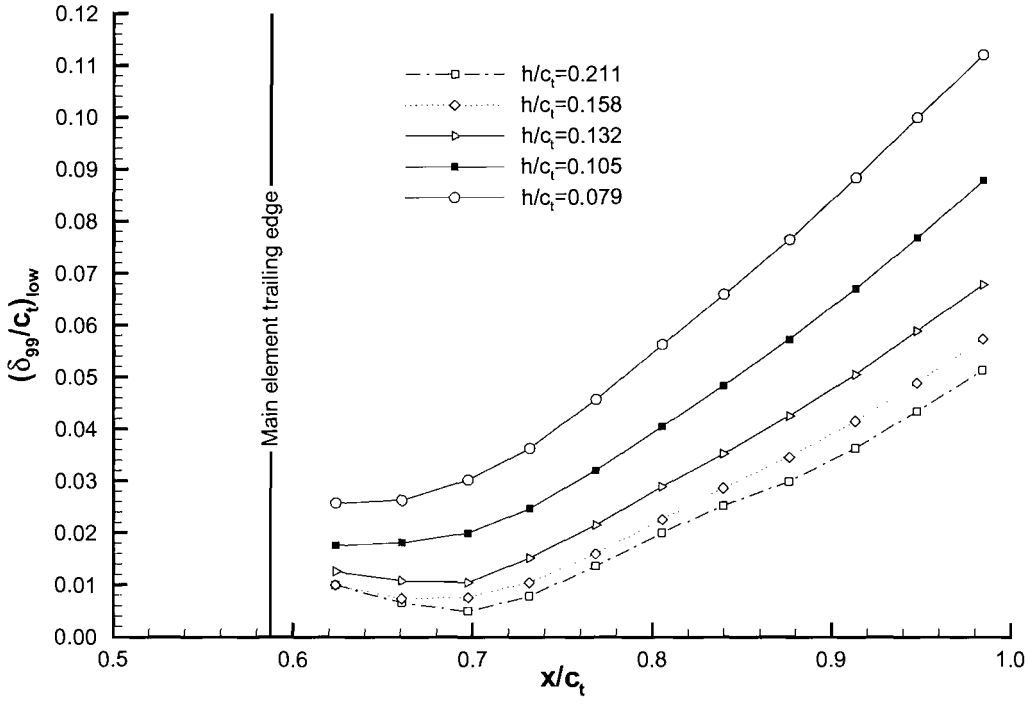

Figure 10.6: Streamwise development of main element wake at various ride heights.

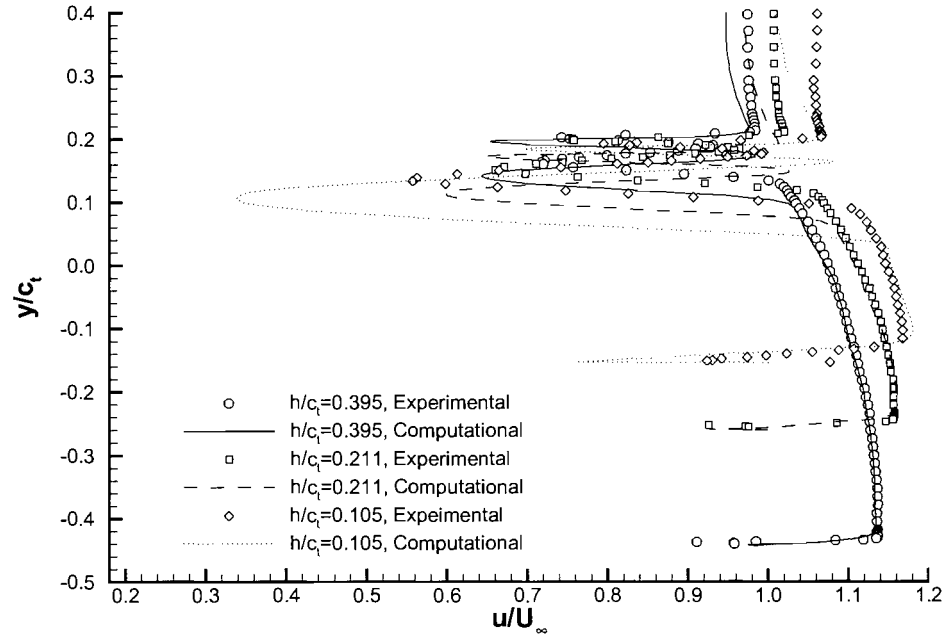

(a)

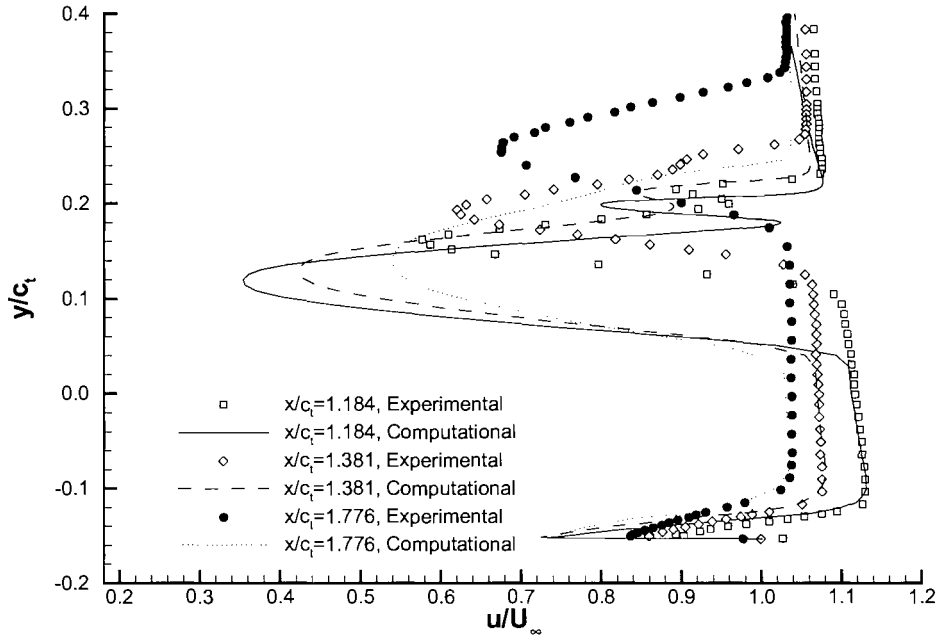

(b)

Figure 10.7: Wake profiles; (a) various ride heights at $x/c_t = 1.066$, (b) various streamwise locations for $h/c_t = 0.105$.

Turbulence Model	C_{Psuc}	x/c_t at C_{Psuc}
Experimental	-4.48	0.08
Spalart-Allmaras	-4.96	0.11
$k-\omega$ SST	-4.95	0.11
Standard $k-\varepsilon$	-4.93	0.11
$k-\varepsilon$ RNG	-4.94	0.11
Realizable $k-\varepsilon$	-4.91	0.11
Standard $k-\omega$	-4.93	0.11

Table 10.1: Surface pressure information for various turbulence models; $h/c_t = 0.221$.

Turbulence	u_{min}/U_∞			y/c_t at u_{min}/U_∞			y/c_t at δ		δ_{99}/c_t	
Model	*low*	*top*	*conf*	*low*	*top*	*conf*	*low*	*top*	*low*	*top*
Experimental	0.69	0.79	0.99	0.150	0.200	0.185	0.126	0.205	0.059	0.020
Spalart-Allmaras	0.67	0.64	1.02	0.113	0.172	0.153	0.082	0.182	0.071	0.029
$k-\omega$ SST	0.65	0.64	1.01	0.113	0.172	0.147	0.084	0.182	0.063	0.035
Standard $k-\varepsilon$	0.65	0.66	0.97	0.111	0.172	0.147	0.078	0.184	0.069	0.037
$k-\varepsilon$ RNG	0.65	0.66	1.02	0.111	0.172	0.151	0.078	0.184	0.073	0.033
Realizable $k-\varepsilon$	0.60	0.65	1.03	0.112	0.172	0.149	0.080	0.184	0.069	0.035
Standard $k-\omega$	0.60	0.65	1.03	0.112	0.172	0.149	0.080	0.184	0.069	0.035

Table 10.2: Wake profile information at $x/c_t = 1.066$ for various turbulence models; $h/c_t = 0.221$.

h/c_t	Expt/CFD	u_{min}/U_∞			y/c_t at u_{min}/U_∞			y/c_t at δ		δ_{99}/c_t	
		low	*top*	*conf*	*low*	*top*	*conf*	*low*	*top*	*low*	*top*
0.395	Expt	0.72	0.74	0.93	0.164	0.203	0.190	0.136	0.217	0.054	0.027
	Real $k-\varepsilon$	0.64	0.65	0.98	0.140	0.195	0.174	0.105	0.215	0.069	0.041
0.211	Expt	0.66	0.76	0.96	0.150	0.200	0.184	0.124	0.207	0.060	0.023
	Real $k-\varepsilon$	0.60	0.65	1.03	0.112	0.172	0.149	0.080	0.184	0.069	0.035
0.105	Expt	0.58	0.80	0.99	0.134	0.192	0.180	0.102	0.198	0.078	0.013
	Real $k-\varepsilon$	0.34	0.70	1.08	0.105	0.184	0.165	0.050	0.192	0.115	0.027

Table 10.3: Wake profile information at $x/c_t = 1.066$ for various ride heights.

x/c_t	Expt/CFD	u_{min}/U_∞			y/c_t at u_{min}/U_∞			y/c_t at δ		δ_{99}/c_t	
		low	*top*	*conf*	*low*	*top*	*conf*	*low*	*top*	*low*	*top*
1.066	Expt	0.58	0.80	1.00	0.134	0.192	0.180	0.102	0.198	0.078	0.013
	Real $k-\varepsilon$	0.34	0.70	1.08	0.105	0.184	0.165	0.050	0.192	0.115	0.027
1.184	Expt	0.58	0.89	0.96	0.162	0.215	0.200	0.120	0.222	0.080	0.022
	Real $k-\varepsilon$	0.35	0.80	1.02	0.120	0.198	0.180	0.055	0.210	0.125	0.030
1.381	Expt	0.62	-	-	0.194	-	-	0.141	0.260	0.119	-
	Real $k-\varepsilon$	0.42	0.85	0.89	0.130	0.210	0.195	0.055	0.225	0.140	0.030
1.776	Expt	0.67	-	-	0.254	-	-	0.180	0.329	0.149	-
	Real $k-\varepsilon$	0.54	-	-	0.140	-	-	0.040	0.240	0.200	-

Table 10.4: Wake profile information at various streamwise locations for $h/c_t = 0.105$.

Chapter 11

RANS Simulations of a Multi-Element Wing in Ground Effect

This chapter presents and discusses computational results for the multi-element wing experimentally investigated in this research. The applicability of the two turbulence models stated in Section 8.3 will be quantified initially. Results obtained at various ride heights will then presented and quantitatively compared to experimental data.

11.1 Wing Geometry

The wing used in this computational investigation was identical to the wing experimentally investigated in this research. The profiles of the main element and flap have been previously stated in Chapter 3. The incidences of the main element and flap were $+4^{\circ}$ and $+24^{\circ}$ respectively. The flap gap and overlap were assigned optimum values of $0.042c$ and $0.035c$ respectively. This wing configuration was identical to that investigated in Chapter 5 allowing for direct comparisons between the experimental measurements and computational data. All computations were performed at a Reynolds number of 5.83×10^5 based on the total chord of the aerofoil (Section 3.5). Transition was included within the computations through the use of laminar zones located at the leading edges of the main element and flap. Due to limitations within the computational grid generator the streamwise locations at which the laminar zones terminated were constant across the span of the wing. The streamwise locations at which the laminar zones terminated corresponded to the transition locations at the centre span of the wing, as determined from oil flow visualisation results (Section 5.4).

11.2 Grid Independence Study

Prior to conducting investigations into the influence of ride height, the dependence of the solution on the resolution of the computational grid was quantified. A grid sensitivity study was performed at a ride height of $h/c = 0.317$, a ride height typical of force region *a* (Chapter 5). Three grids were constructed: a coarse grid of 1.6×10^6 cells, a medium grid of 3.0×10^6 cells and a fine grid of 4.1×10^6 cells. The variations in grid density were focused in the wing boundary layer blocks, vortex blocks and the wake block. The effects of turbulence were modelled using the Spalart-Allmaras turbulence model.

Figure 11.1 presents chordwise surface pressures at the centre span of the wing and near the port wing tip. Minimal variation was observed between the surface pressures predicted with all three grid resolutions. In addition the spanwise surface pressures on both the main element (Figure 11.2) and flap (Figure 11.3) were also largely independent of grid resolution. The surface pressures on the inboard face of the port endplate exhibited a greater dependency on grid resolution (Figure 11.4). The coarse grid resolution predicted significantly reduced values of suction in the vicinity of the lower edge vortex. However, the surface pressures obtained with the medium and fine grids were largely similar indicating the threshold of the grid independence.

Figure 11.5 presents the centre span wake profiles obtained with the three grids at $x/c = 1.127$. The wake profile obtained with a two-dimensional simulation (Chapter 10) is also included and will be discussed later. The increase in grid resolution resulted in a smoother wake profile and reduced values of u_{low} and u_{top} (Figure 5.25). The vertical locations at which the minimum streamwise velocities occurred however, were seemingly independent of grid resolution. Although the most computationally expensive it was decided to use the fine grid resolution within all remaining three-dimensional simulations.

11.3 Turbulence Model Comparison

A quantitative study of the two turbulence models stated in Section 8.3 was conducted. The ride height of the wing was set at $0.317c$, typical of force region *a* with the wing generating a thin dual wake flow field (Chapter 5). The chordwise surface pressures on the wing obtained at the centre span and towards the port wing tip are presented in Figure 11.6. The centre span surface pressures on both the main element and flap were largely independent of turbulence model (Figure 11.6(a)). Both turbulence models underpredicted the centre

span surface pressures with the Spalart-Allmaras model offering improved predictions. The surface pressures near the port tip (Figure 11.6(b)) were more dependent on turbulence model. The $k-\omega$ SST model significantly underpredicted the suction over both the main element and flap. As for the centre span pressures, improved predictions were offered by the Spalart-Allmaras model. Table 11.1 presents quantitative data concerning the centre span surface pressures with both turbulence models.

The spanwise surface pressures on the main element and flap are presented in Figures 11.7 and 11.8 respectively. The pressure surface pressures were accurately predicted with both turbulence models. However a greater variation was observed in the predicted suction surface pressures. Both turbulence models accurately captured the spanwise pressure distribution on the main element, with the Spalart-Allmaras model offering an improved prediction. A similar dependence on turbulence model was observed in the spanwise surface pressures on the flap. However the $k-\omega$ SST model significantly underpredicted the suction towards the port tip, generated by the lower edge vortex. The prediction of the suction generated by the lower edge vortex was more clearly presented in the endplate surface pressures (Figure 11.9). Both turbulence models consistently predicted the suction peak at $y/c = -0.03$, a value close to that observed experimentally. However, the Spalart-Allmaras model offered a more accurate prediction of the suction distribution over the height of the endplate.

The underpredicted suction over the main element and flap by both turbulence models resulted in underpredicted values of downforce. The values of downforce coefficient (C_L) predicted by the Spalart-Allmaras and $k-\omega$ SST models were 1.78 and 1.72 respectively, corresponding to 12% and 15% below experimental. The values of drag coefficient (C_D) were more accurately predicted at 0.247 and 0.245 with the Spalart-Allmaras and $k-\omega$ SST models respectively. These corresponded to overpredictions of 1.8% and 1.0% respectively when compared to an experimental value.

Figure 11.10 presents the centre span wake profiles with both turbulence models at a streamwise location of $1.127c$. The wake profiles were largely independent of turbulence model particularly within the main element and flap wakes. Both turbulence models underpredicted the minimum streamwise velocities within the main element and flap wakes. However the corresponding vertical locations were predicted accurately. The Spalart-Allmaras model offered improved predictions particularly at the confluence between the wakes and towards the lower boundary of the main element wake. Table 11.2 presents quantitative data

concerning the wake profiles obtained with both turbulence models. Due to the improved surface pressure predictions and wake profile predictions the Spalart-Allmaras turbulence model was used within the simulations conducted at various ride heights.

11.4 Surface Pressures

With the influence of the turbulence models quantified the effects of ride height variation on wing performance could be investigated. Calculations were performed at ride heights of $0.634c$, $0.317c$, $0.247c$, $0.211c$, $0.169c$ and $0.141c$. These ride heights were typical of force regions a to c. Ride heights lower than this could not be simulated with the hybrid grid strategy used in this research. For low ride heights the block beneath the wing and the ground boundary layer block merged therefore requiring an alternative design of grid. Turbulence was modelled using the Spalart-Allmaras turbulence model.

11.4.1 Chordwise Pressures at Centre Span

Figure 11.11(a) presents the centre span chordwise surface pressures at various ride heights. For reasons of clarity only experimental data for three ride heights has been included. For all ride heights the pressure surface pressures on both the main element and flap were accurately predicted. Stagnation was consistently predicted at $0.01c$ and $0.46c$ on the main element and flap respectively, in agreement with experimental data. The suction surface pressures were underpredicted for all ride heights on both the main element and flap. The underprediction was relatively independent of ride height with values of approximately 19% and 15% on the main element and flap respectively. Increased values of suction were observed with reductions in ride height, a trend noted experimentally. The rapid flow acceleration, suction peak and downstream pressure recovery on both the main element and flap were accurately captured at all ride heights. The suction peaks on the main element and flap were consistently predicted at $0.02c$ and $0.48c$, in agreement with the experiments. Table 11.3 presents quantitative data concerning the computational centre span surface pressures for various ride heights.

11.4.2 Chordwise Pressures Near Wing Tip

The chordwise surface pressures near the port wing tip for various ride heights are presented in Figure 11.11(b). The pressure surface pressures on both the main element and flap were

accurately predicted for all ride heights. For high hide heights ($h/c \geq 0.211$) the suction surface pressures near the port wing tip were underpredicted computationally on both the main element and flap. However, below a ride height of $0.211c$ the main element suction surface pressures were overpredicted towards the main element trailing edge. Stagnation on the main element and flap was consistently predicted at $0.01c$ and $0.46c$ respectively, as observed experimentally. The variation in surface pressures with ride height experimentally observed was also captured computationally.

11.4.3 Spanwise Pressures

The spanwise distribution of surface pressures on the main element at various ride heights is presented in Figure 11.12. For all ride heights the pressure surface pressures were accurately predicted. The suction however was underpredicted for all ride heights, as observed within the chordwise surface pressures. The underprediction in suction was greatest at the centre span and was relatively independent of variations in ride height. The asymptotic decrease in suction from the centre span to the wing tip observed experimentally, was captured within the computations. Near the port wing tip ($x/c \leq -0.02$) a region of constant suction was observed. This feature was not captured experimentally due to the discrete nature of the pressure tappings.

Figure 11.13 presents the spanwise surface pressures on the flap at various ride heights. For all ride heights the pressure surface pressures were slightly overpredicted. In contrast the suction was underpredicted for all ride heights by approximately 15%. The spanwise variation in suction observed experimentally, was captured computationally. The suction increased from the centre span gradually at first, then rapidly due to the presence of the lower edge vortex. An increase in suction over the span of the flap with reductions in ride height was observed computationally. However, towards the port wing tip for $h/c = 0.141$ a reduction in suction was observed with further reductions in ride height. This reduction in suction at low ride heights was also observed experimentally and attributed to the breakdown of the lower edge vortex.

11.4.4 Endplate Pressures

The surface pressures obtained at various ride heights on the inboard face of the port endplate are presented in Figure 11.14. Due to the small number of experimental pressure tappings the accuracy of the computational results cannot be conclusively stated. For

the highest ride height the suction peak was significantly underpredicted computationally. However for lower ride heights the suction peak was accurately captured, occurring at $y/c \approx -0.03$. Overall the endplate surface pressures were underpredicted for all ride heights.

Reducing the ride height from $0.634c$ resulting an increase in suction at all vertical locations until $0.317c$. Further reductions in ride height resulted in decreased values of suction particularly towards the base of the endplate. This feature was also observed experimentally due to the breakdown of the lower edge vortex, occurring between $0.247c$ and $0.211c$.

11.5 Forces

The experimental and computational variation in downforce coefficient with ride height is presented in Figure 11.15. The underprediction in the surface pressures over both the main element and flap resulted in underpredicted values of downforce coefficient for all ride heights. Overall the predicted downforce was approximately 10% less than the measured values with a maximum variation of 15.8% occurring at $h/c = 0.247$. The asymptotic increase in downforce with ride height observed experimentally was accurately captured computationally albeit offset. The discontinuity in the measured downforce due to the breakdown of the lower edge vortex (force region b), was not captured computationally. However it may be noted that the ride height resolution was coarse when compared to the experiments possibly masking the discontinuity in downforce.

The variation in drag coefficient with ride height is presented in Figure 11.16. Compared to the downforce, the drag was more accurately predicted. For all ride heights the drag was overpredicted with a maximum difference of 5.8% at $h/c = 0.141$. The asymptotic increase in drag with ride height observed experimentally was accurately captured within the computational data.

Figure 11.17 presents the variation in experimental and computational pitching moment with ride height. The underprediction in suction over both the main element and flap resulted in underpredicted values of pitching moment for $h/c \geq 0.169$. However, for the lowest ride height investigated computationally the predicted pitching moment was greater than that observed experimentally. A maximum difference of 10.4% was observed at $h/c = 0.247$, corresponding to the ride height with the worst downforce prediction. Although offset the asymptotic increase in pitching moment observed experimentally, was captured

computationally. However, the peak in pitching moment and subsequent reduction was not captured.

The variation in wing efficiency with ride height is presented in Figure 11.18. The underprediction in downforce coefficient resulted in underpredicted values of wing efficiency for all ride heights. A maximum underprediction of 17.2% occurred at $h/c = 0.247$ corresponding to the ride height with the worst downforce prediction. The gradual increase in wing efficiency within force region a was predicted accurately. The decrease in wing efficiency observed experimentally was not captured computationally. However it was noted that the computational wing efficiency decreased below $h/c = 0.169$ in contrast to the experimental data.

11.6 Wing Tip Flow Field

To investigate the accuracy with which the wing tip flow field was captured, vorticity data was extracted on a spanwise plane at $x/c = 0.995$. This plane corresponded to one where PIV measurements were made. Figure 11.19(a) presents contours of non-dimensional vorticity (Ω_x) resolved in the x-component at a ride height of $0.317c$. The contour levels were set in order to replicate the experimental data (Figure 5.6(a)). For direct comparisons with regards to the locations and sizes of the vortices, experimental velocity vectors obtained using a PIV technique are also included. Both the upper and lower edge vortices were captured within the computational data with the upper edge vortex located at $z/c = 0.08$, $y/c = 0.33$. The spanwise location of the lower edge vortex was accurately predicted at $z/c = -0.08$ however, the vertical location was underpredicted at $y/c = -0.01$. The shear layers originating from the top and base of the endplate observed experimentally, were also predicted accurately. The maximum vorticity within the upper and lower edge vortices was underpredicted computationally at $\Omega_x = -20$ and $\Omega_x = -25$ respectively. A concentrated region of positive vorticity was noted close to the outboard side of the upper edge vortex. This feature was attributed to the boundary connection between the structured upper edge vortex block and the unstructured block. Within the experimental data the vortex identification method of Jeong & Hussain [147] was used. However this method required a regular array of data points and therefore could not be used within the computational data due to the partial unstructured grid design. Accordingly the hydraulic diameters of the edge vortices could not be defined.

Figure 5.6(b) presents vorticity contours at a ride height of $0.247c$. This ride height was close to the boundary between force regions a and b (Figure 5.1). The size and location of the upper edge vortex was largely unchanged by the reduction in ride height. However the strength of the upper edge vortex increased with a maximum vorticity of $\Omega_x = -39$. The lower edge vortex seemingly increased in size and decreased in strength ($\Omega_x = -20$). The lower edge vortex moved inboard to $z/c = -0.10$ whereas the vertical location was unchanged. As for the higher ride heights the agreement between the measured and predicted data was good with respect to the location and size of both the edge vortices.

Reducing the ride height to $0.211c$ resulted in the lower edge vortex significantly increasing in size (Figure 11.20(a)), a feature observed experimentally. This ride height was towards the upper limit of force region c. The strength of the lower edge vortex decreased with a maximum vorticity of $\Omega_x = -11$. At this ride height the lower edge vortex was not present within the experimental data. However as mentioned previously the state of the lower edge vortex within the computational data could not be quantified due to the hybrid nature of the computational grid. The location of the upper edge vortex was unaffected by the ride height reduction. However, the maximum vorticity increased slightly to $\Omega_x = -40$. As for the higher ride heights the agreement between the experimental and computational data was good.

Figure 11.20(b) presents vorticity contours obtained at a ride height of $0.141c$. The location, size and strength of the upper edge vortex was unchanged by the reduction in ride height. However, the lower edge vortex was seemingly replaced by a region of anti-clockwise recirculation, as observed experimentally. Below the lower region of recirculation a concentrated region of negative vorticity was observed. It was noted that the unstructured computational cells within this region were highly skewed. The poor cell quality and corresponding interface between the unstructured block and the structured block beneath the wing resulted in the concentrated region of negative vorticity observed.

Volume ribbons of the wing tip flow field for ride heights of $0.317c$ and $0.141c$ are presented in Figure 11.21. The ribbons are coloured by C_P. For the higher ride height two concentrated vortices were indicated (Figure 11.21(a)). However for the lower of the two ride heights (Figure 11.21(b)) concentrated lower and upper edge vortices were not present. A similar variation in the wing tip flow field was observed experimentally. In addition to the wing tip flow field the surface pressures over the road are also presented. Two main regions of suction were noted, corresponding to the wing and lower edge vortex. Reductions

in ride height resulted in increased suction both beneath the wing and port endplate. To better visualise the lower and upper edge vortices iso-surfaces of $C_P = -0.5$ are presented in Figure 11.22. For the higher ride height (Figure 11.22(a)) the iso-surfaces indicated two concentrated vortices which seemingly interacted resulting in an anti-clockwise rotation. Reducing the ride height to $0.141c$ (Figure 11.22(b)) resulted in the lower edge vortex significantly increasing in diameter, as observed experimentally.

11.7 Surface Flow Field

Figure 11.23 presents the surface pressures over the suction surfaces of the wing and the inboard face of the port endplate at $h/c = 0.317$. In addition computational surface streaklines are presented. The streaklines on the suction surfaces of the wing (Figure 11.23(a)) accurately captured the curvature of the streaklines observed experimentally (Figure 5.10). Transition within the streaklines was not observed computationally since transition within the computational was modelled using a laminar block i.e. instantaneous transition. Figure 11.23(b) presents the surface flow field on the inboard face of the port endplate at $h/c = 0.317$. The strongly curved streaklines observed experimentally due to the lower edge vortex, was captured computationally. A region of suction towards the base of the endplate was observed. This feature was attributed to the suction generated by the lower edge vortex.

The surface flow fields over the wing and port endplate at $h/c = 0.141$ are presented in Figure 11.24. The surface pressure on the suction surfaces of the wing (Figure 11.24(a)) indicated the increased flow acceleration over the main element, particularly at the centre span. The increased curvature of the streaklines with reductions in ride height observed experimentally, was accurately predicted. The surface flow field on the inboard face of the endplate is presented in Figure 11.24(b). The angle between the streaklines towards the base of the endplate and the horizontal was reduced when compared to the higher ride height. This feature was attributed to the fact that the lower edge vortex was seemingly absent within the computational results for $h/c = 0.141$. A similar trend was observed within the experimental results.

11.8 Wake Flow Field

The variation in the wake flow field with ride height at the wing centre span is presented in Figure 11.25. For reasons of clarity experimental data obtained at only three ride heights is included (Section 5.6). For all ride heights the minimum velocities within the main element (u_{low}) and flap (u_{top}) wakes were underpredicted. In addition the streamwise velocity at the confluence point (Figure 5.25) was also underpredicted. In contrast the corresponding vertical locations were accurately predicted at all ride heights. Reductions in ride height resulted in increased thickness of the main element wake and increased flow retardation, as observed experimentally. For all ride heights the upper boundary of the main element wake was captured accurately however, the lower boundary was overpredicted. Accordingly the main element wake thickness was overpredicted for all ride heights. The flap wake and corresponding boundaries were accurately captured computationally.

Close to the ground plane a region of reduced streamwise velocity was observed corresponding to the ground plane boundary layer. Reductions in ride height resulted in a thicker ground boundary layer, a trend previously observed computationally (Section 10.8). The lack of experimental data close to the ground plane prevented validation of the ground plane boundary layer. However, for the lowest ride height ($h/c = 0.141$) the upper boundary was detected experimentally and accurately captured computationally. The regions between the ground plane boundary layer and the lower boundary of the main element wake exhibited velocities greater than freestream. This wall jet has been previously detected computationally (Chapters 9 and 10) and experimentally [9]. Reductions in ride height resulted in the wall jet increasing in magnitude. Experimentally the wall jet was not captured however the existence of the wall jet has been proven previously. The absence of the wall jet within the experimental data was attributed to the measurement technique. Table 11.4 presents quantitative data concerning the wake profiles at various ride heights.

The streamwise development of the wake at the wing centre span for $h/c = 0.247$ is presented in Figure 11.26. The corresponding quantitative data is presented in Table 11.5. The minimum velocities within the main element and flap was underpredicted computationally at all streamwise locations. In addition the velocity at the confluence point was also underpredicted. The corresponding vertical locations were accurately predicted at all streamwise locations. However, the lower boundary of the main element wake was incorrectly predicted. Accordingly the thickness of the main element wake was overpredicted

at all streamwise locations. The merging of the two wakes observed experimentally at $x/c = 1.532$ was captured computationally.

11.9 Discussion

Three-dimensional simulations of any flow field are inherently more computationally expensive to perform than two-dimensional simulations. However it has also been shown for the case of a wing in ground effect, that the choice of turbulence model is also critical to the stability of the solution. Divergent three-dimensional solutions were obtained with the standard $k-\omega$, standard $k-\varepsilon$, Realizable $k-\varepsilon$ and $k-\varepsilon$ RNG turbulence models. Upon investigating the steady-state development of the flow field with each of these four turbulence models a common cause for the divergence was observed. In all cases artificially high values of turbulence were seemingly generated at the boundaries between the structured blocks and the unstructured blocks. It is therefore surmised that the divergent nature of four of the six turbulence models were due to the hybrid design of grid. Due solely to the time limitations within this investigation it was not possible to develop a fully structured three-dimensional grid. This is a topic for future investigation.

Convergent three-dimensional solutions were obtained with the Spalart-Allmaras and $k-\omega$ SST turbulence models. As with the two-dimensional simulations, variations within the prediction of the surface pressures was observed. However, the dependence of the surface pressures on the turbulence model was greatest near the wing tip. The surface pressures on the inboard face of the endplate were particularly dependent. This region represented a highly three-dimensional flow field dominated by a vortex i.e. the most computationally complex region. The dependence of the centre span wake flow field was largely similar to that observed within the two-dimensional investigation (Figure 10.2(c)).

The surface pressures over the suction surfaces of the wing were underpredicted at all ride heights by approximately 18%, in contrast to the two-dimensional simulations. For all ride heights the computed wing tip flow field presented a significantly weaker lower edge vortex than that observed experimentally. In addition the predicted suction over the endplate was reduced. This constant offset within the suction surface pressures was attributed to the inaccurate simulation of the main element leading edge suction peak. It is surmised that underpredicted flow acceleration over the leading edge of the wing resulted in an underpredicted suction peak. Since the suction surface pressure recovery was correctly

predicted the suction over the whole wing was consequently reduced by a constant value. The reduced pressure difference across the endplates resulted in edge vortices of reduced strength when compared to experiments. Accordingly the downforce and pitching moment was underpredicted computationally.

Although the surface pressures were underpredicted it may be noted that the location and size of the lower and upper edge vortices were accurately predicted. In addition realistic qualitative features of the surface flow field were also captured. Within the two-dimensional simulations it was noted that vertical locations of the main element and flap wakes were underpredicted. It was hypothesised that the lack of upwash resulted in reduced wake deflection. Figure 11.5 presents the wake flow field obtained with a two-dimensional simulation of the wing investigated within this chapter. The best practice defined within Chapter 10 was used. It may be noted that the wake profiles obtained within the three-dimensional simulations correctly predicted the vertical locations of the wakes. It is therefore surmised that the lack of upwash within two-dimensional simulations causes underpredicted values of the vertical location of the wake generated by the wing.

11.10 Chapter Summary

A numerical investigation into a multi-element wing in ground effect was performed. The effects of turbulence model, grid density and ride height were all investigated. The stability of the computation was found to be sensitive to the turbulence model implemented. This was primarily attributed to the hybrid design of the computational grid used. The results indicated that the surface pressures over the wing and endplate were underpredicted at all ride heights. The underprediction of the suction peak was found to be the main cause of the inaccuracy. The prediction of the wake flow field offered improvements over the two-dimensional simulations due to the inclusion of three-dimensional effects. In summary it has been shown that the qualitative flow field generated by a multi-element wing in ground effect may be predicted numerically. However the quantitative features are predicted less accurately and clearly warrant future investigation.

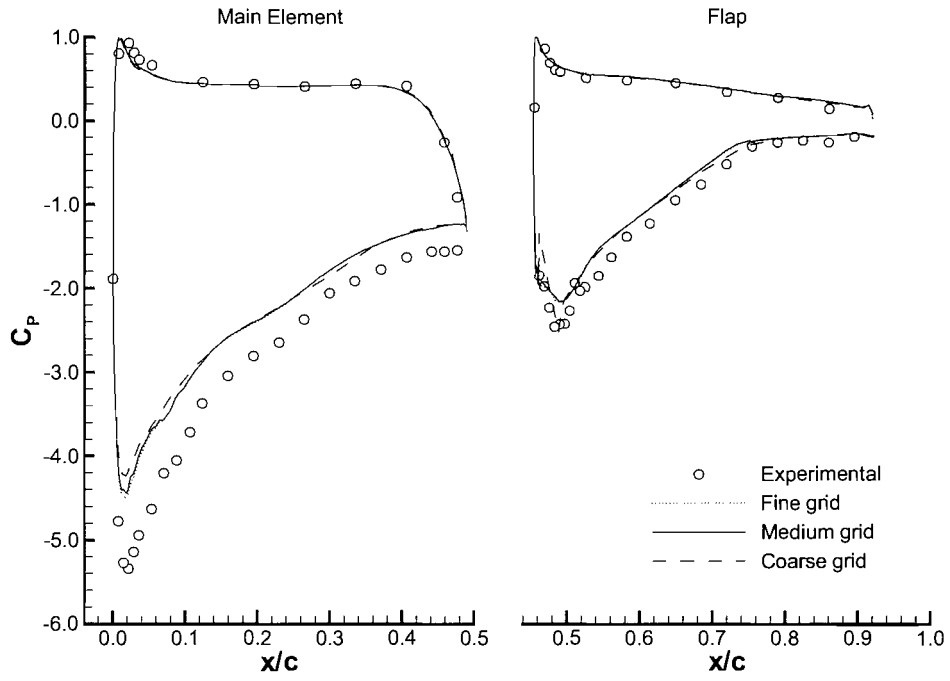

(a)

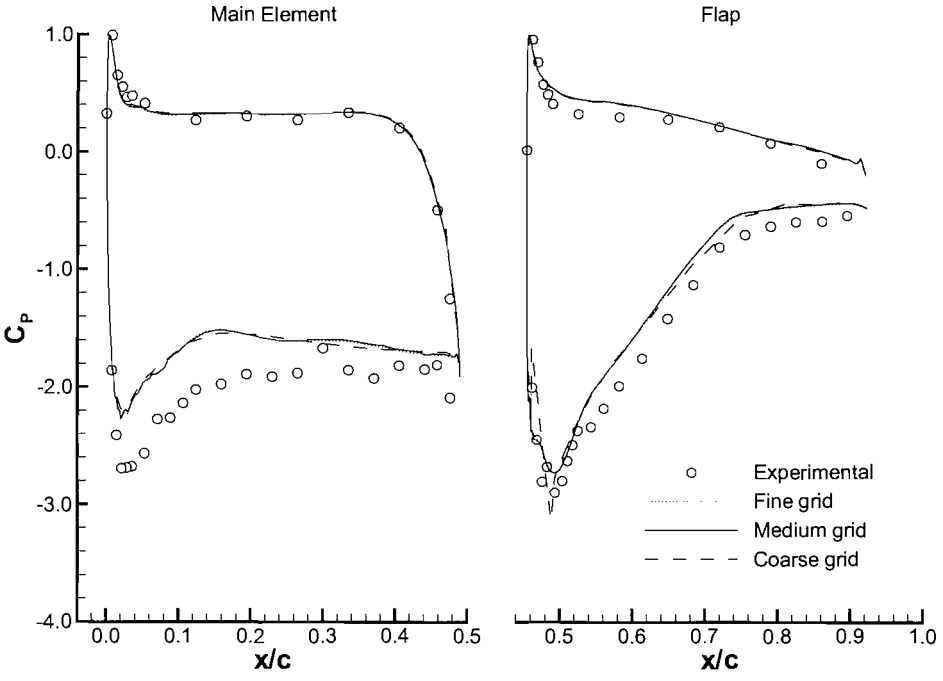

(b)

Figure 11.1: Effects of grid resolution on the chordwise surface pressure distribution; $h/c = 0.317$; (a) centre span, (b) $z/c = -0.088$.

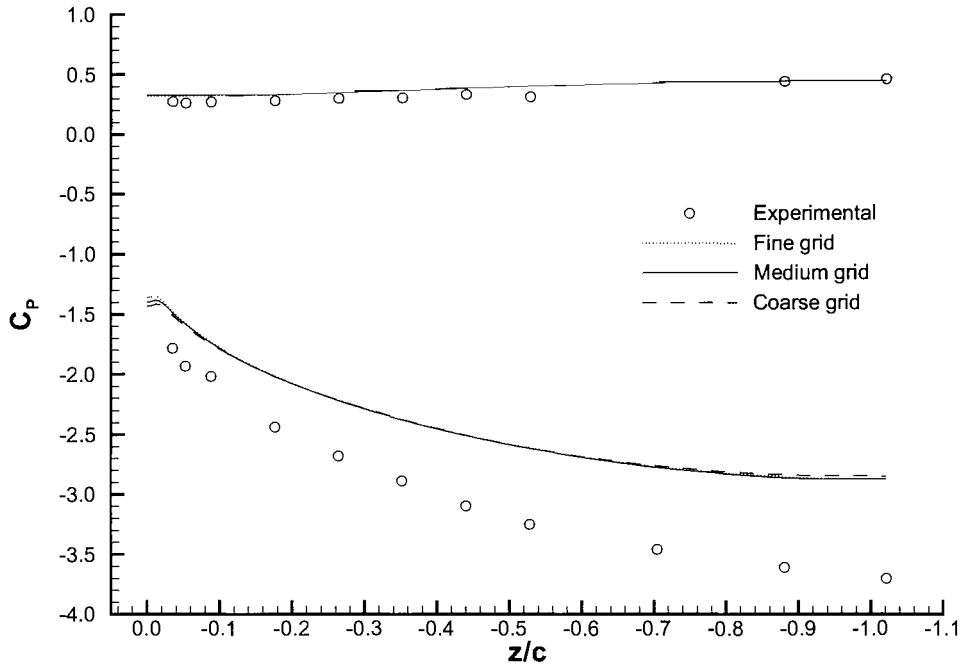

Figure 11.2: Effects of grid resolution on the spanwise surface pressure distribution on the main element; $h/c = 0.317$, $x/c = 0.123$.

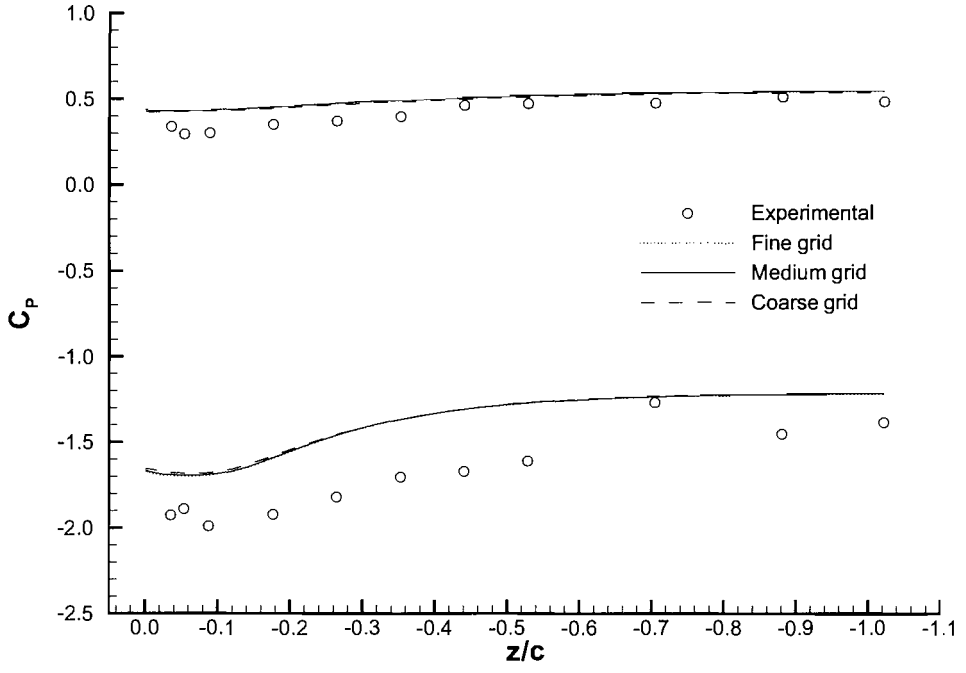

Figure 11.3: Effects of grid resolution on the spanwise surface pressure distribution on the flap; $h/c = 0.317$, $x_f/c = 0.127$.

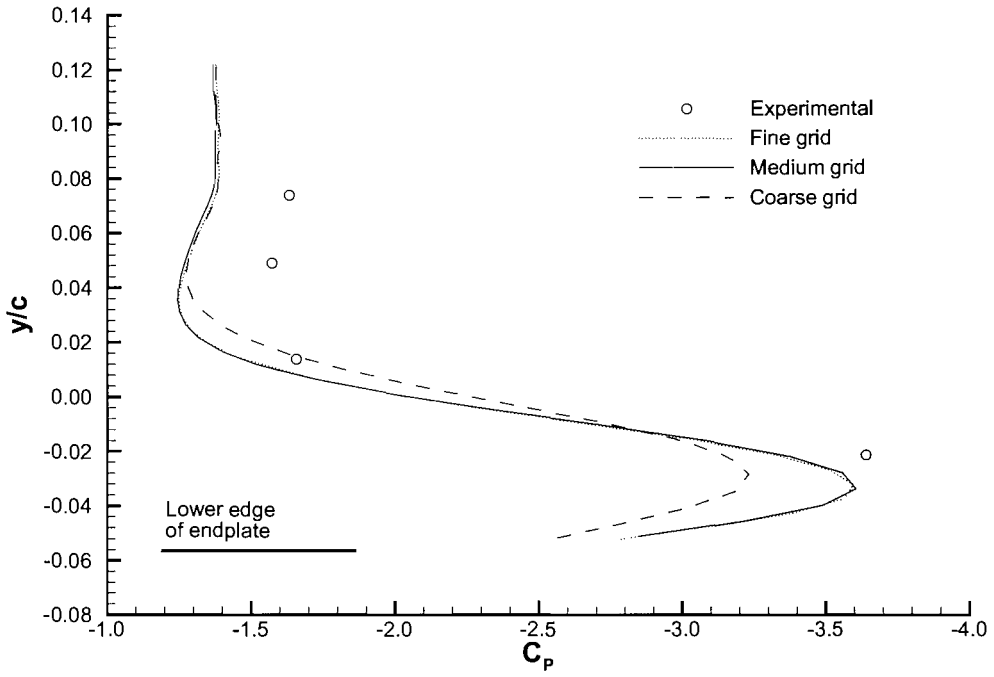

Figure 11.4: Effects of grid resolution on the surface pressure distribution on the inboard face of the port endplate; $h/c = 0.317$, $x/c = 0.614$.

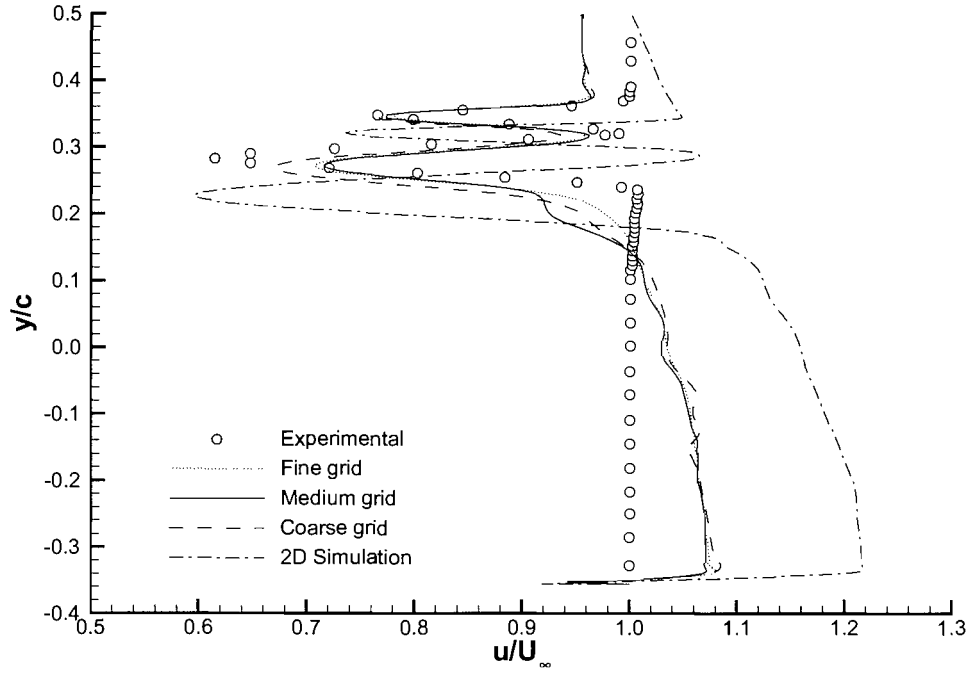

Figure 11.5: Effects of grid resolution on the non-dimensional wake profile at $h/c = 0.317$; $x/c = 1.127$, $z/c = -1.021$.

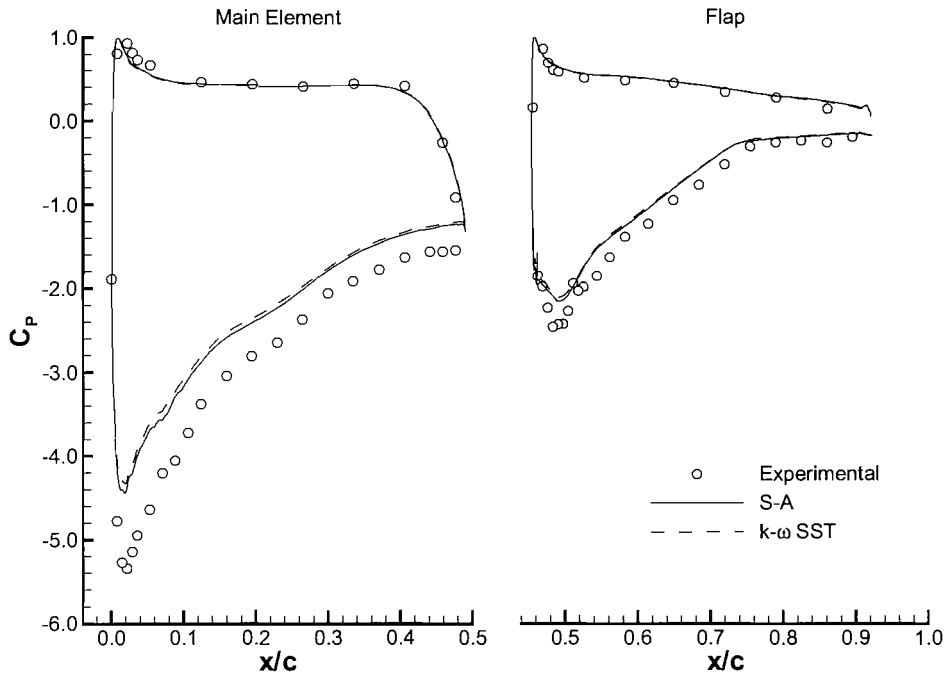

(a)

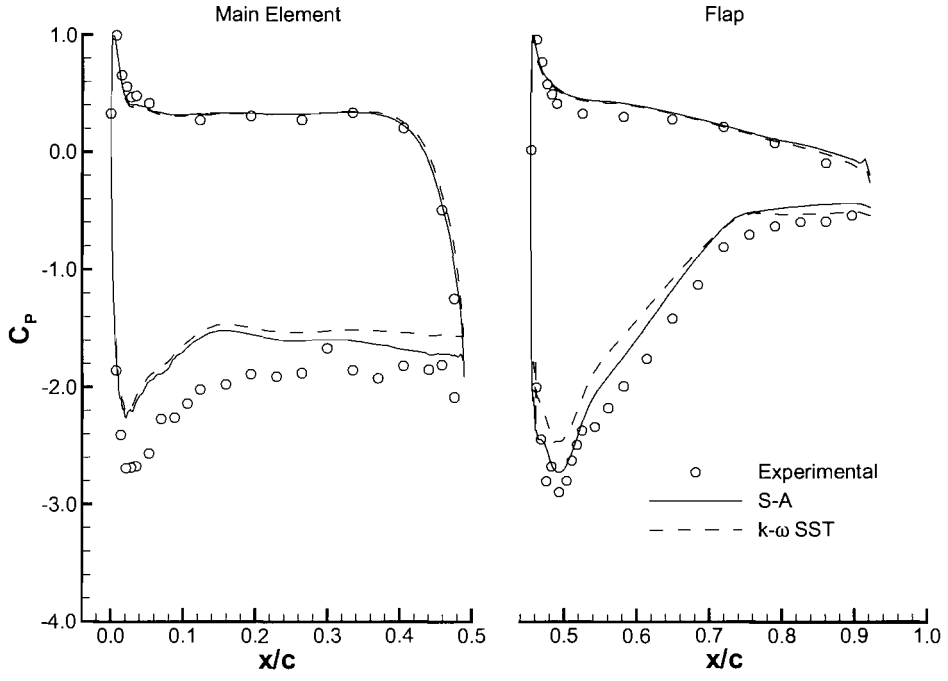

(b)

Figure 11.6: Effects of turbulence model on the chordwise surface pressure distribution; $h/c = 0.317$; (a) centre span, (b) $z/c = -0.088$.

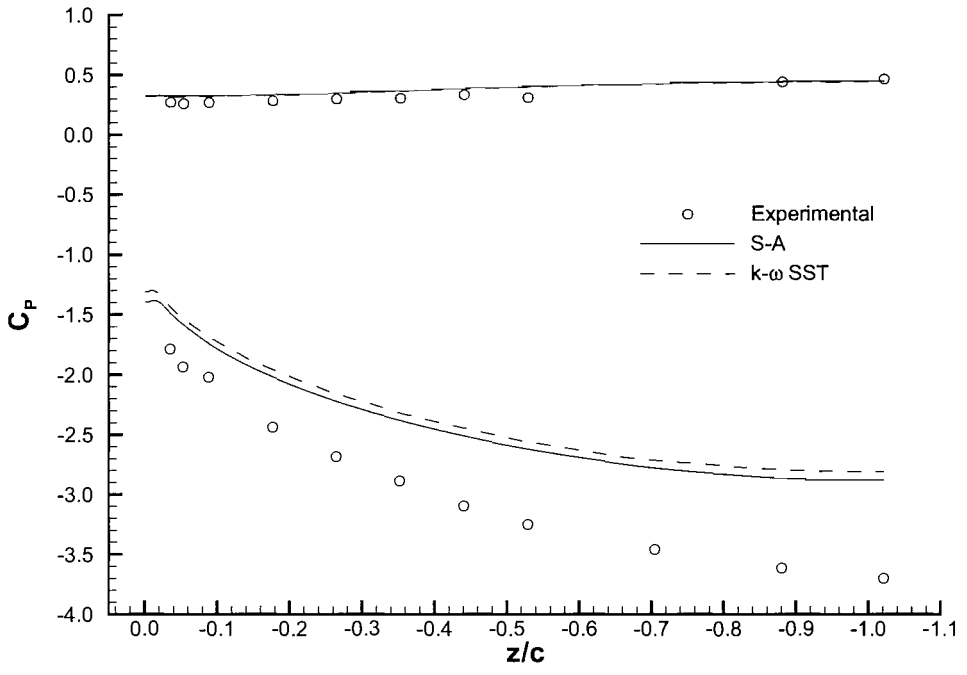

Figure 11.7: Effects of turbulence model on the spanwise surface pressure distribution on the main element; $h/c = 0.317$, $x/c = 0.123$.

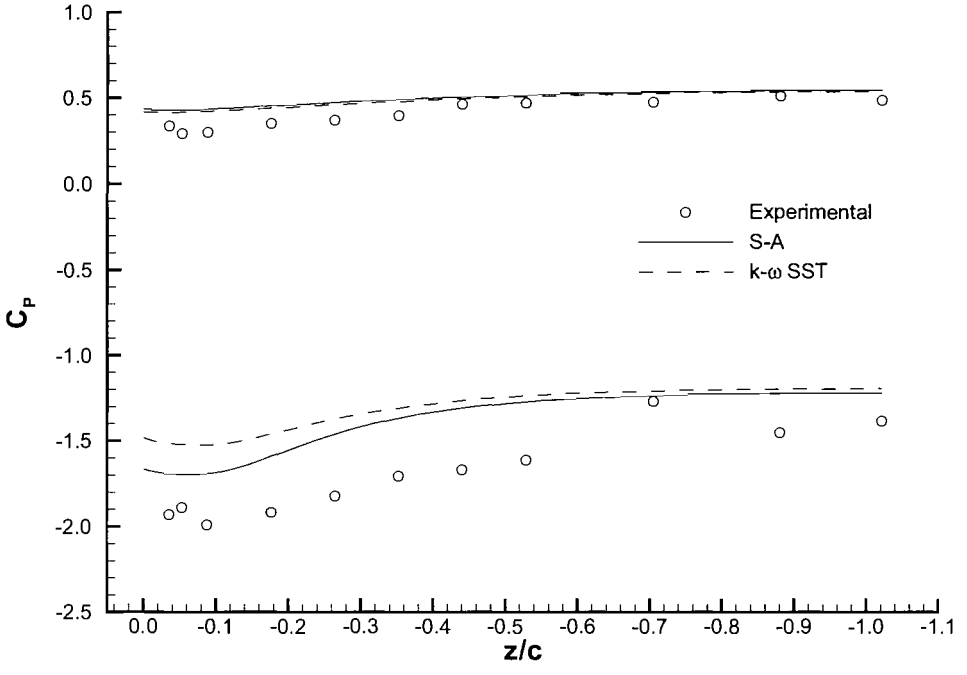

Figure 11.8: Effects of turbulence model on the spanwise surface pressure distribution on the flap; $h/c = 0.317$, $x_f/c = 0.127$.

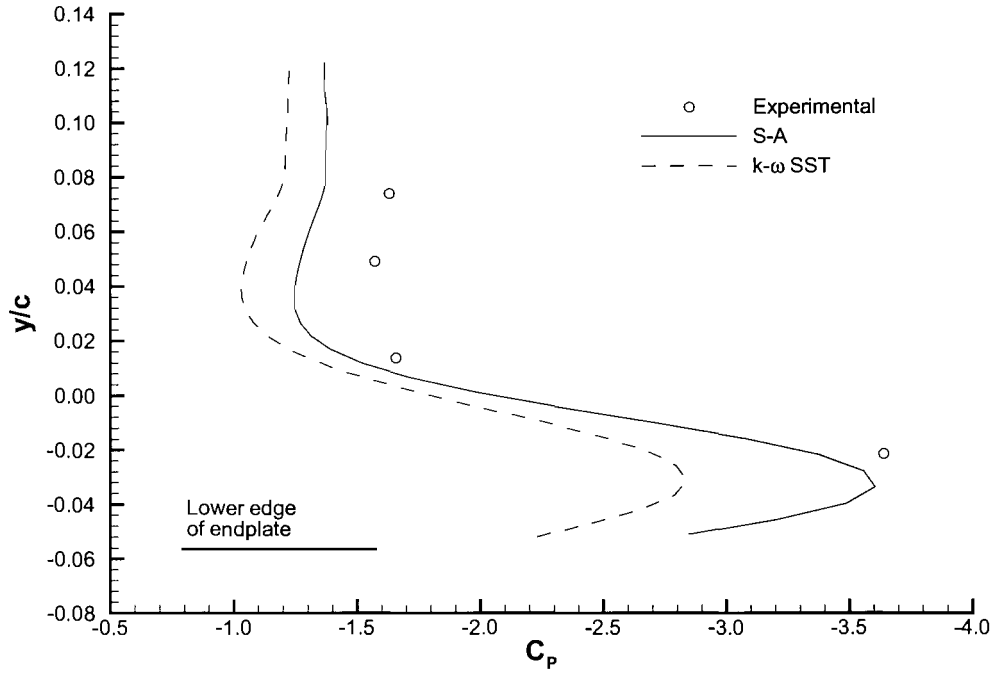

Figure 11.9: Effects of turbulence model on the surface pressure distribution on the inboard face of the port endplate; $h/c = 0.317$, $x/c = 0.614$.

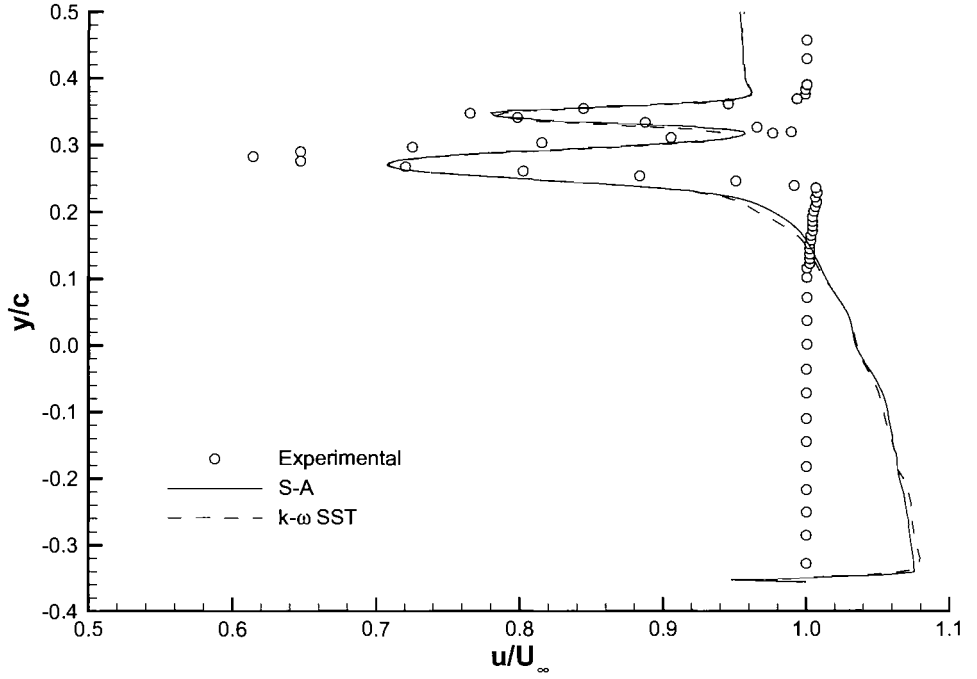

Figure 11.10: Effects of turbulence model on the non-dimensional wake profile at $h/c = 0.317$; $x/c = 1.127$, $z/c = -1.021$.

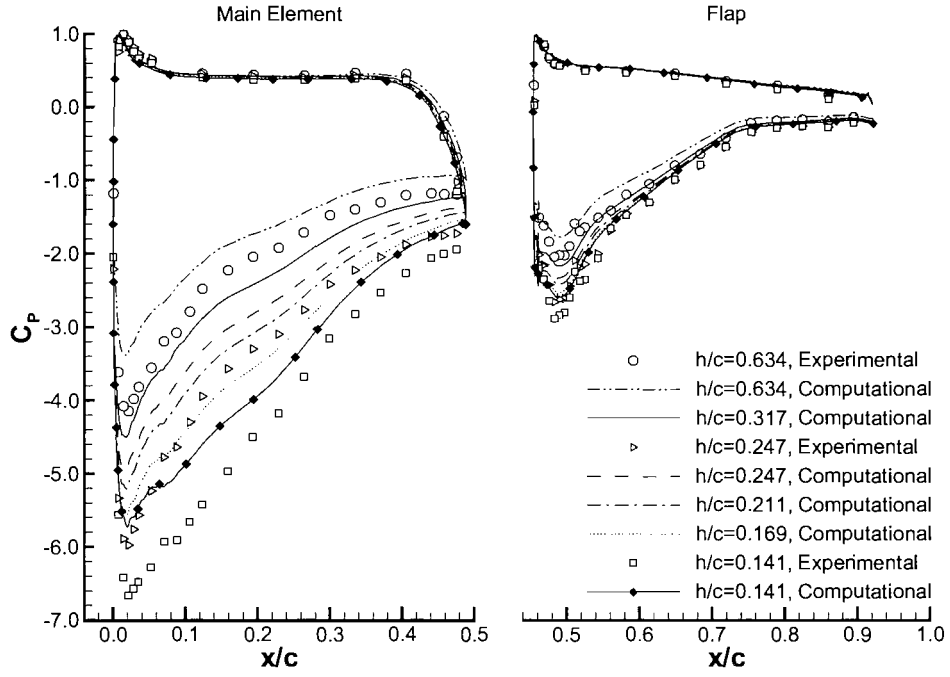

(a)

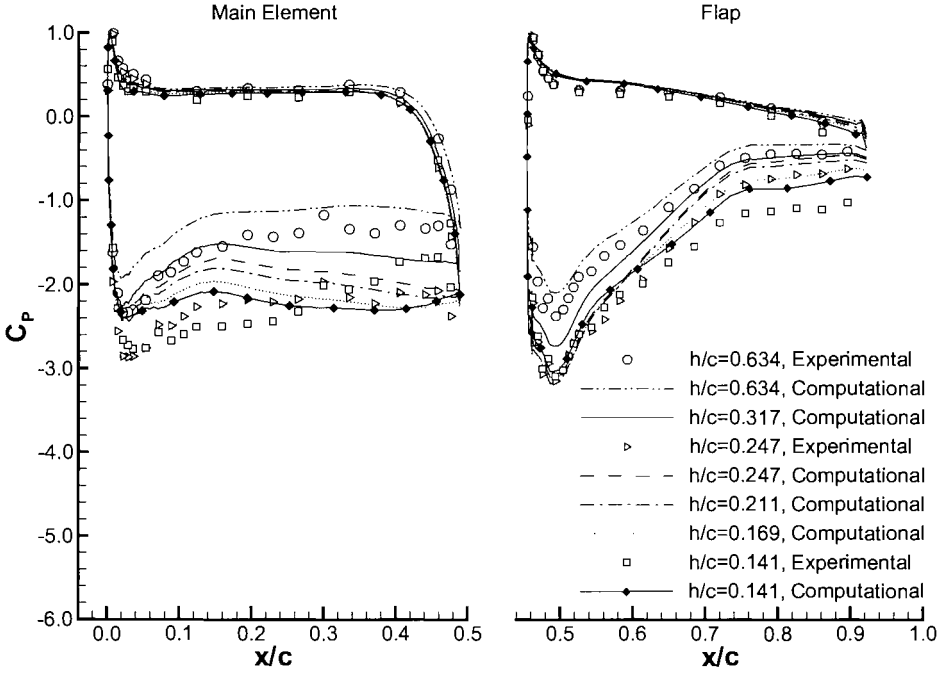

(b)

Figure 11.11: Chordwise surface pressure distributions for various ride heights; (a) centre span, (b) $z/c = -0.088$.

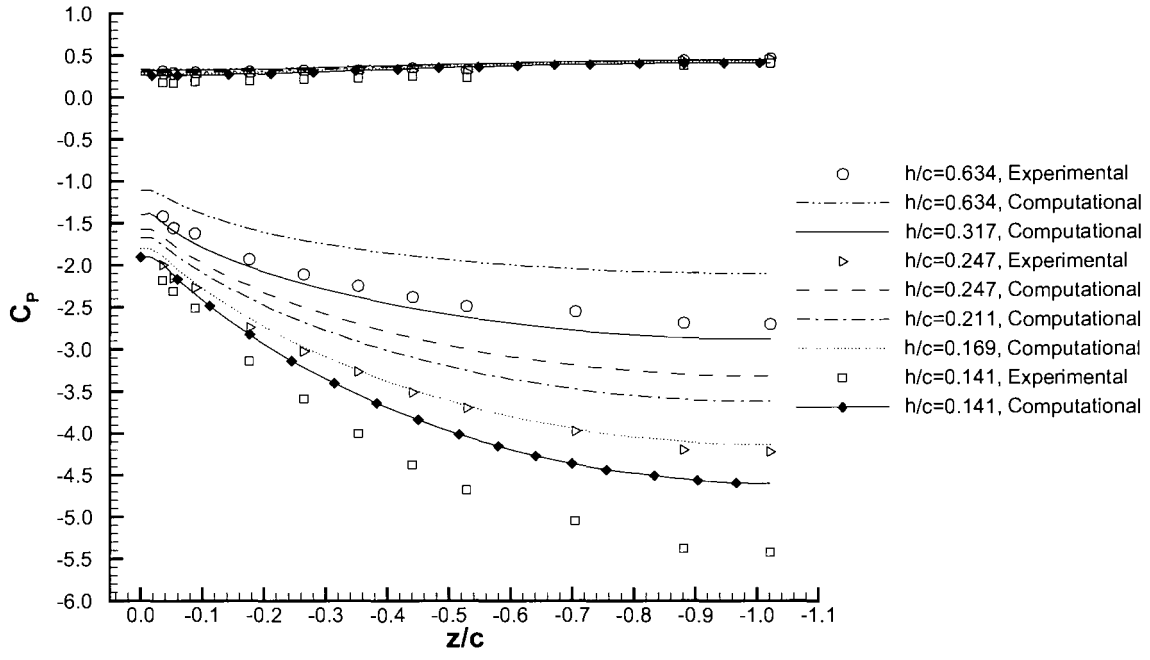

Figure 11.12: Spanwise surface pressure distribution on the main element at various ride heights; $x/c = 0.123$.

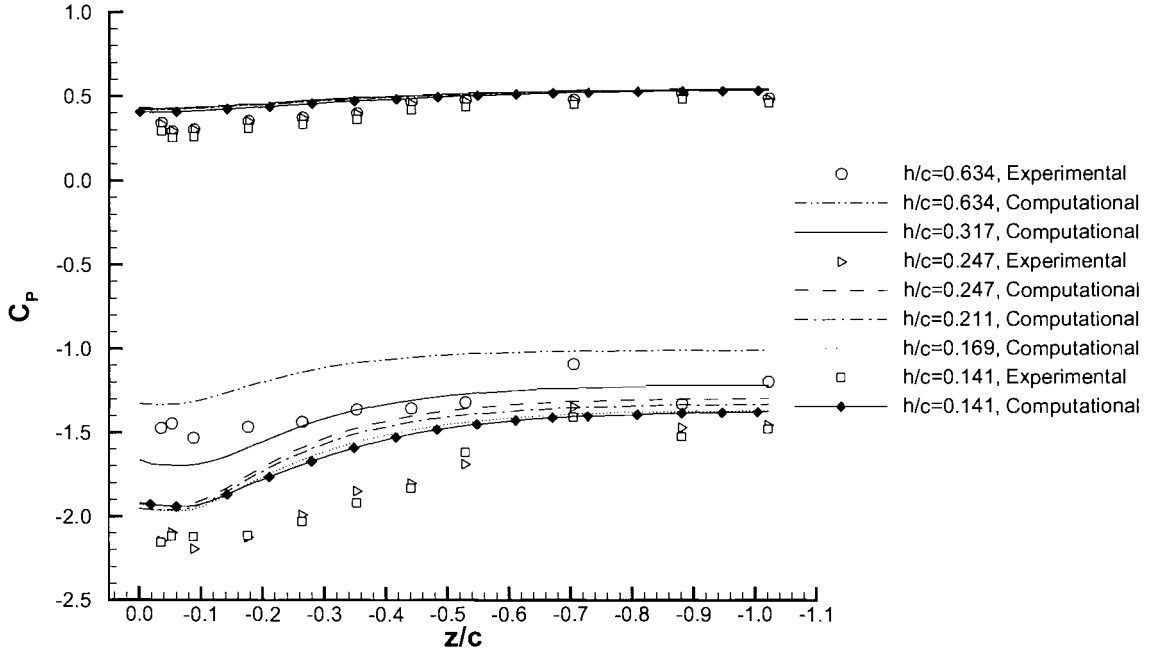

Figure 11.13: Spanwise surface pressure distribution on the flap at various ride heights; $h/c = 0.317$, $x_f/c = 0.127$.

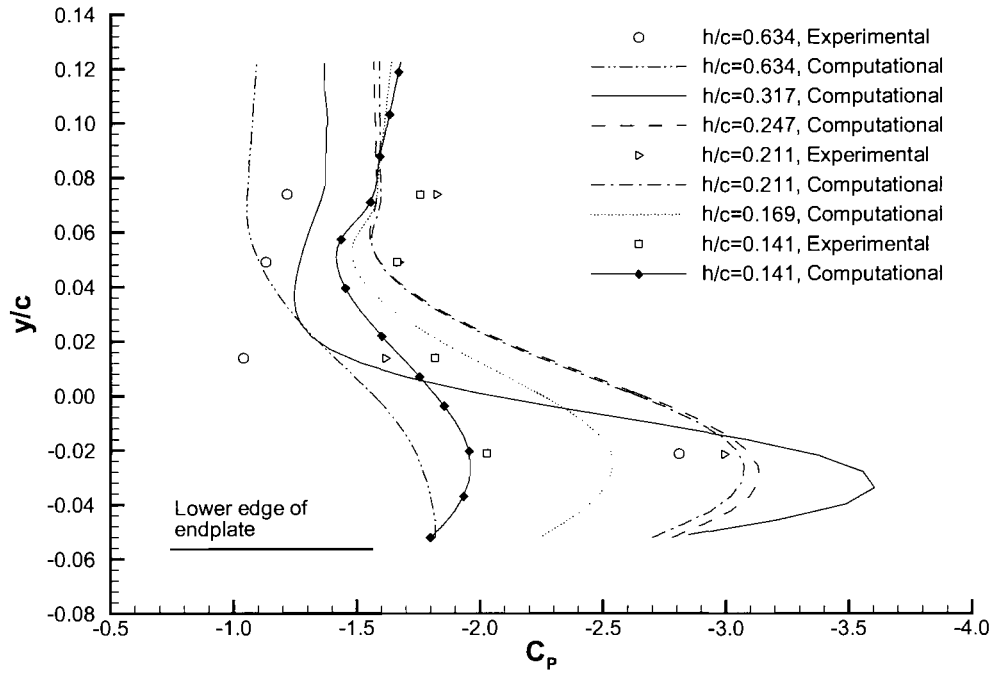

Figure 11.14: Surface pressure distribution on the inboard face of the port endplate at various ride heights; $x/c = 0.614$.

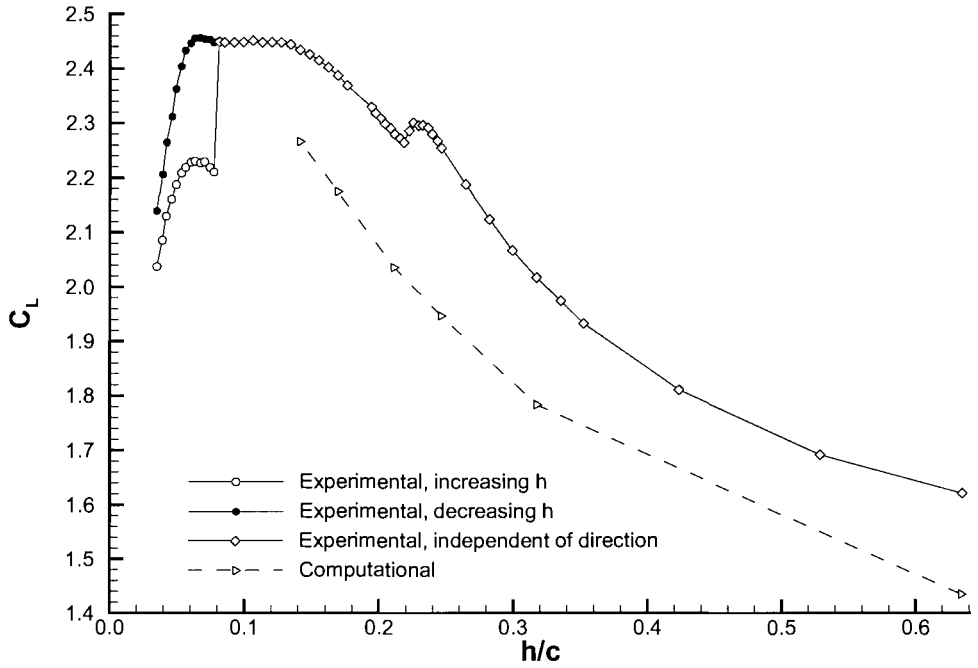

Figure 11.15: Variation of downforce coefficient with ride height; Spalart-Allmaras turbulence model.

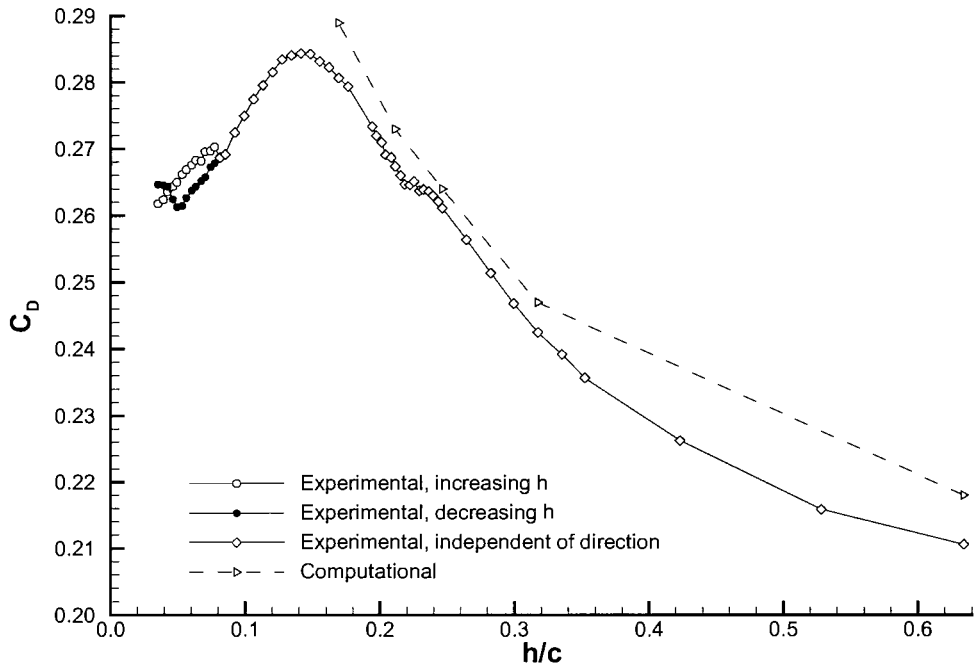

Figure 11.16: Variation of drag coefficient with ride height; Spalart-Allmaras turbulence model.

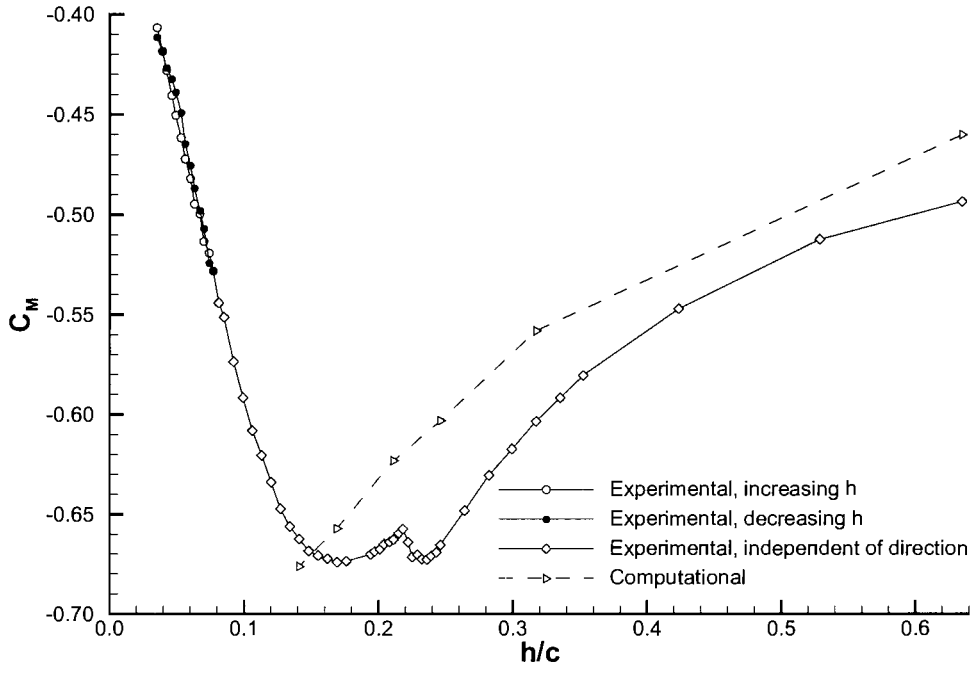

Figure 11.17: Variation of pitching moment coefficient with ride height; Spalart-Allmaras turbulence model.

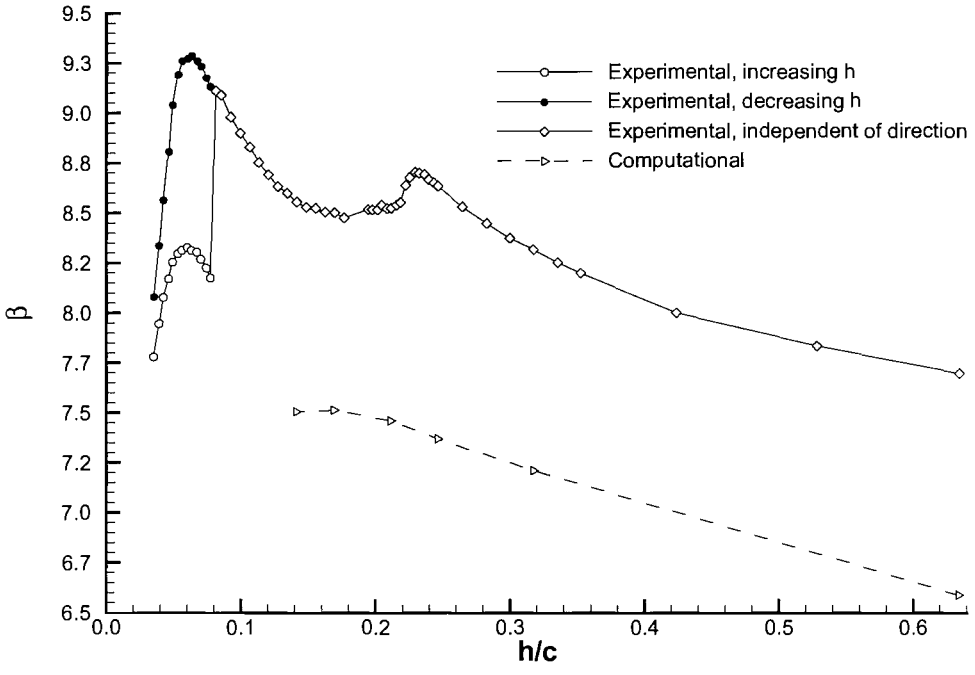

Figure 11.18: Variation of wing efficiency with ride height; Spalart-Allmaras turbulence model.

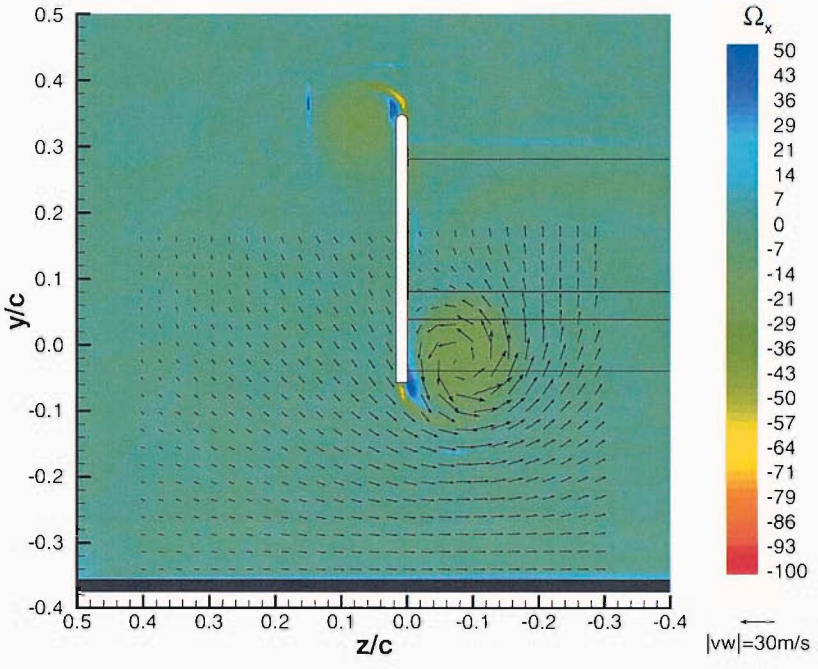

(a)

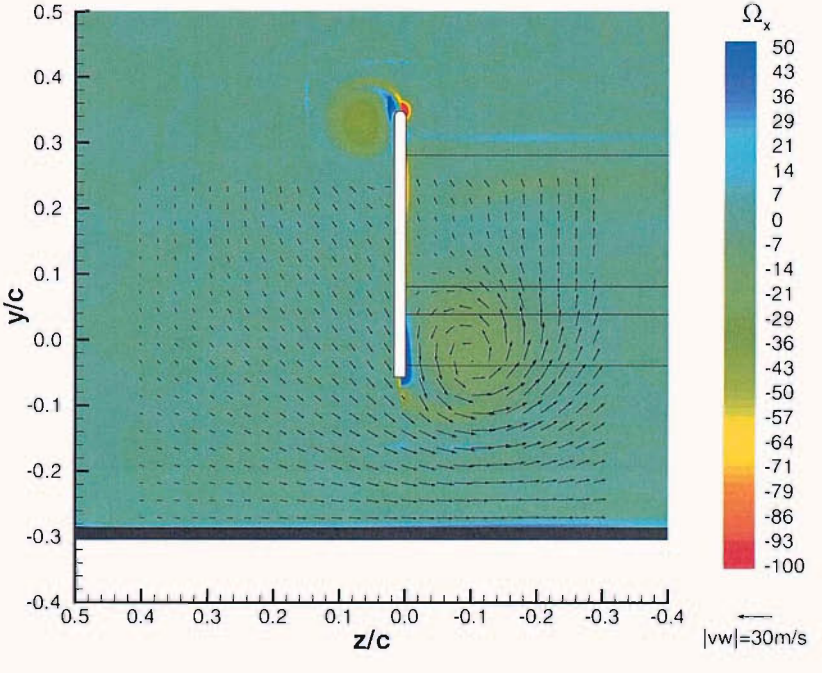

(b)

Figure 11.19: Time-averaged non-dimensional vorticity contours of the port wing tip at $x/c = 0.995$: (a) $h/c = 0.317$ (region a), (b) $h/c = 0.247$ (region a/b boundary).

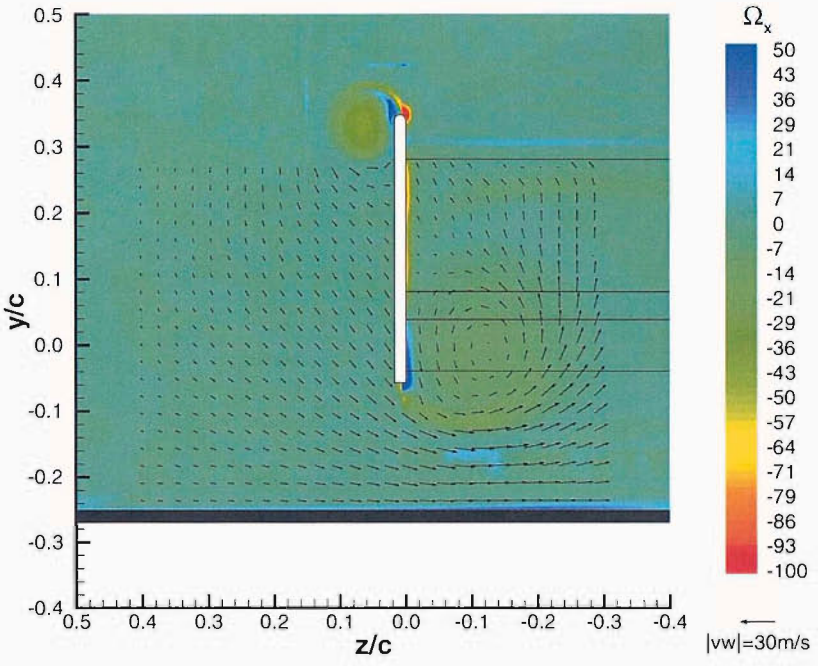

(a)

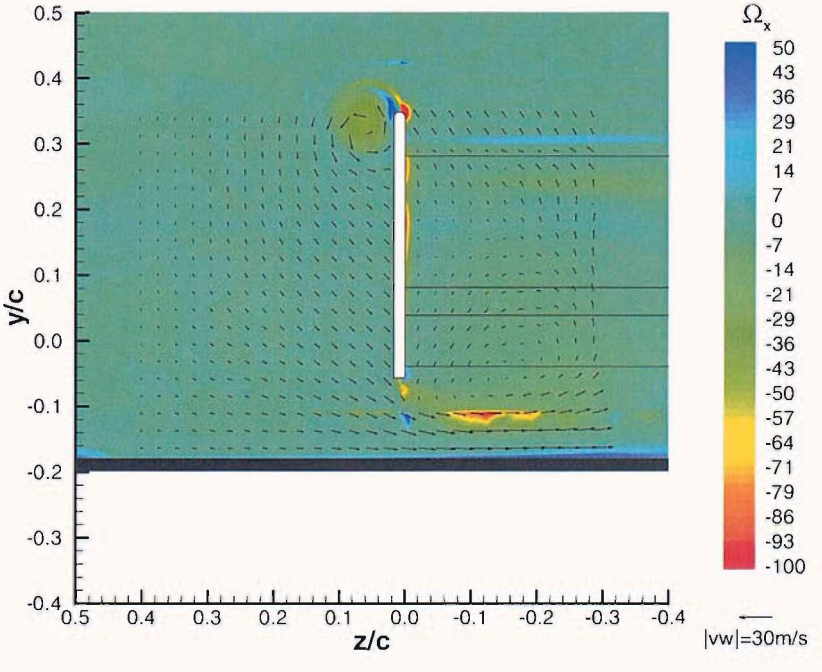

(b)

Figure 11.20: Time-averaged non-dimensional vorticity contours of the port wing tip at $x/c = 0.995$; (a) $h/c = 0.211$ (region b/c boundary), (b) $h/c = 0.141$ (region d).

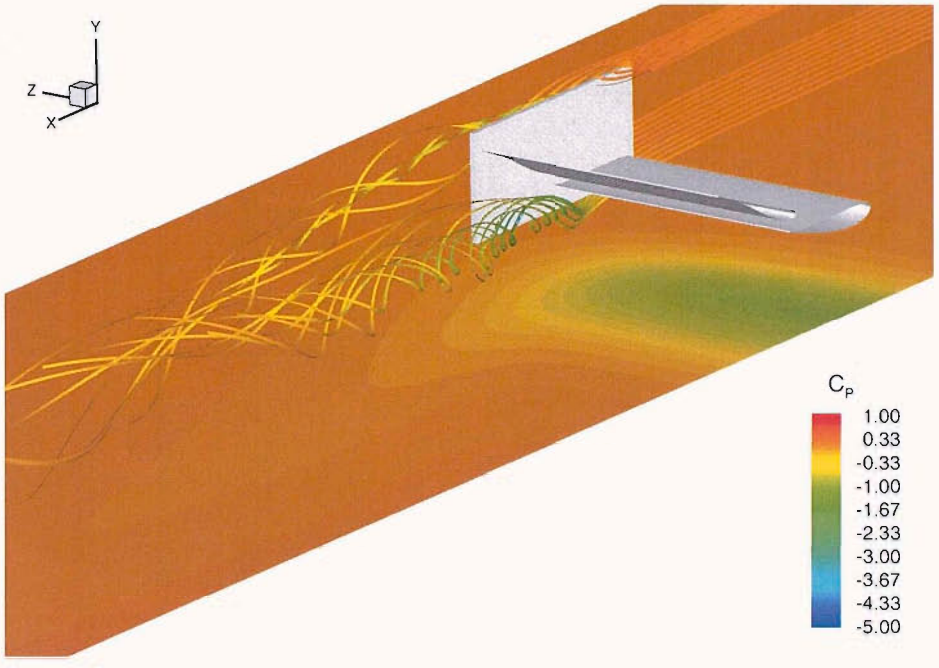

(a)

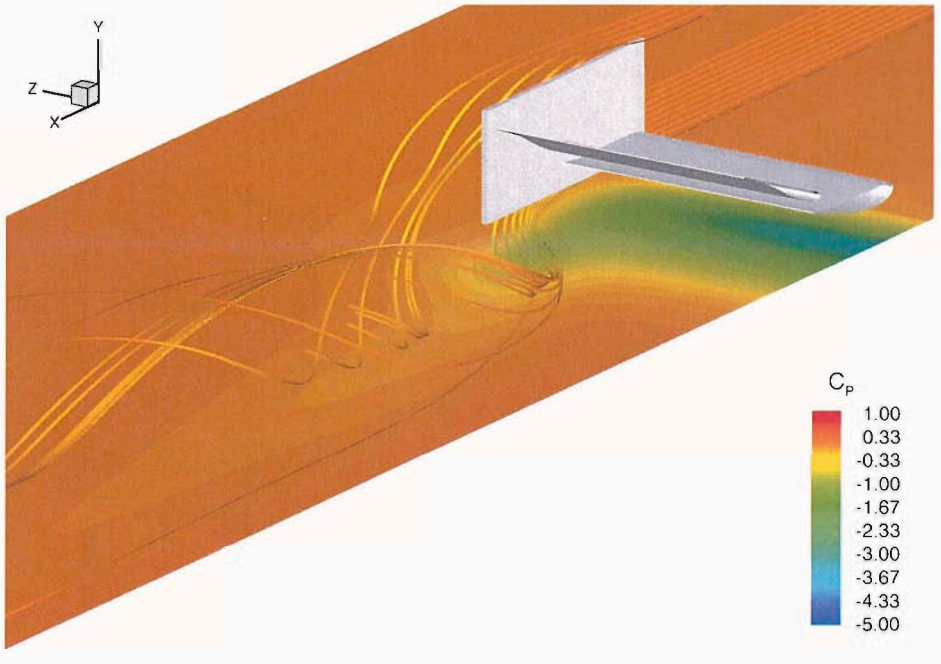

(b)

Figure 11.21: Volume ribbons shaded by C_P for various ride heights: (a) $h/c = 0.317$ (region a), (b) $h/c = 0.141$ (region d).

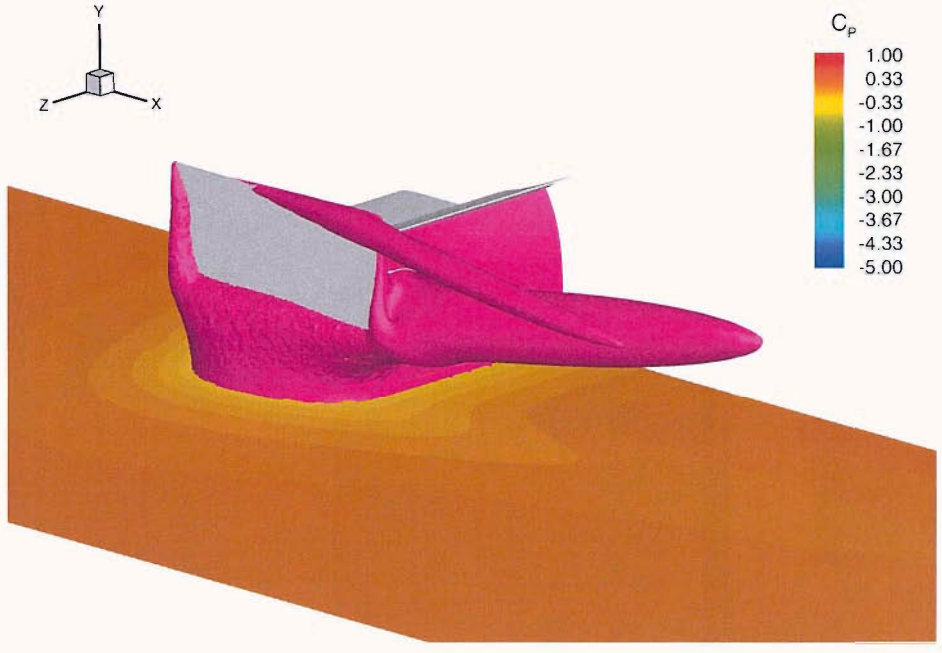

(a)

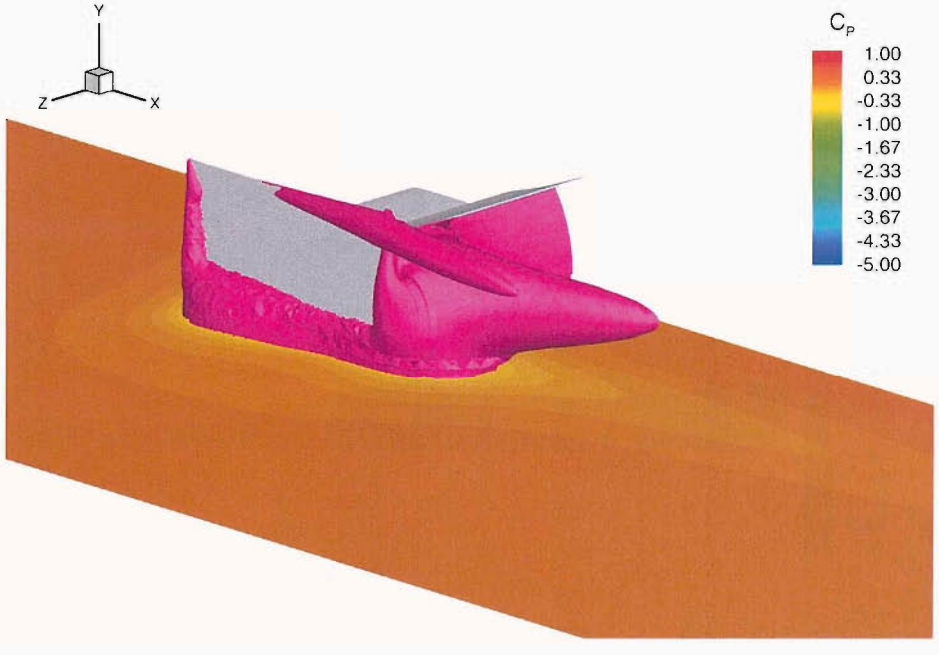

(b)

Figure 11.22: Iso-surfaces of $C_P = -0.5$ for various ride heights: (a) $h/c = 0.317$ (region a), (b) $h/c = 0.141$ (region d).

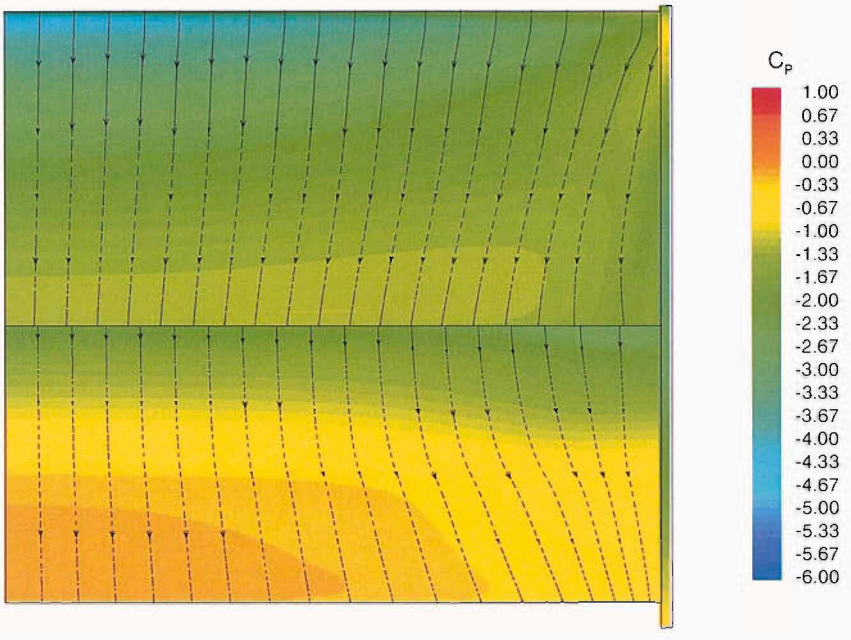

(a) Suction surface of the wing (leading edge upper most).

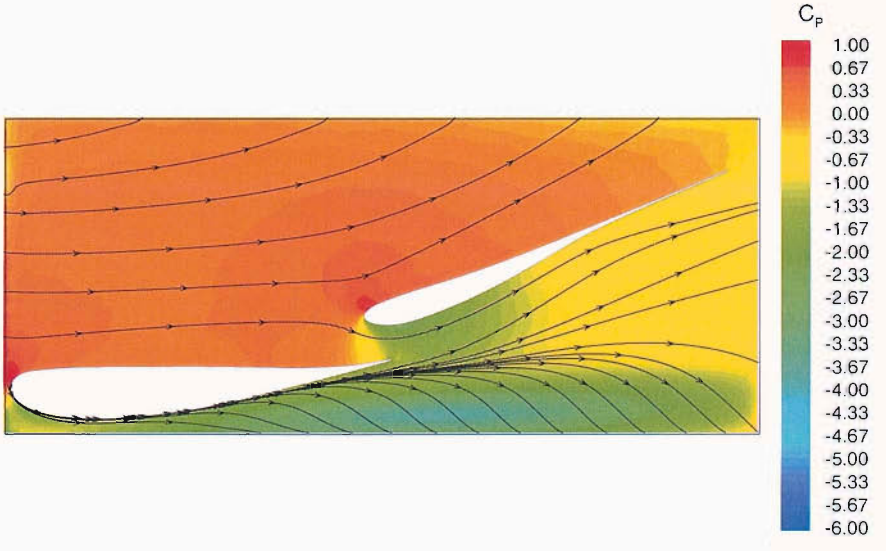

(b) Inboard surface of port endplate (flow from left to right).

Figure 11.23: Contours of pressure coefficient and streaklines at $h/c = 0.317$ (region a): Spalart-Allmaras turbulence model.

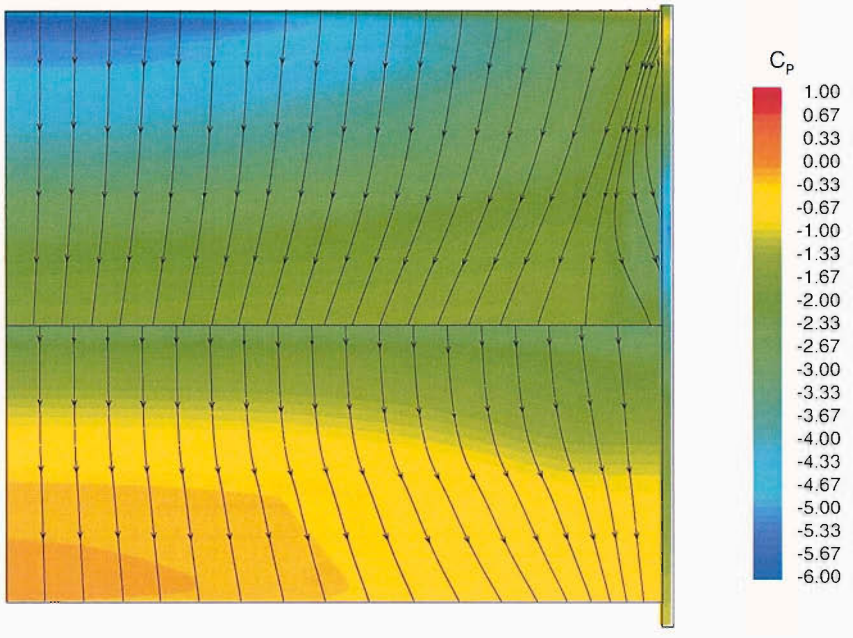

(a) Suction surface of the wing (leading edge upper most).

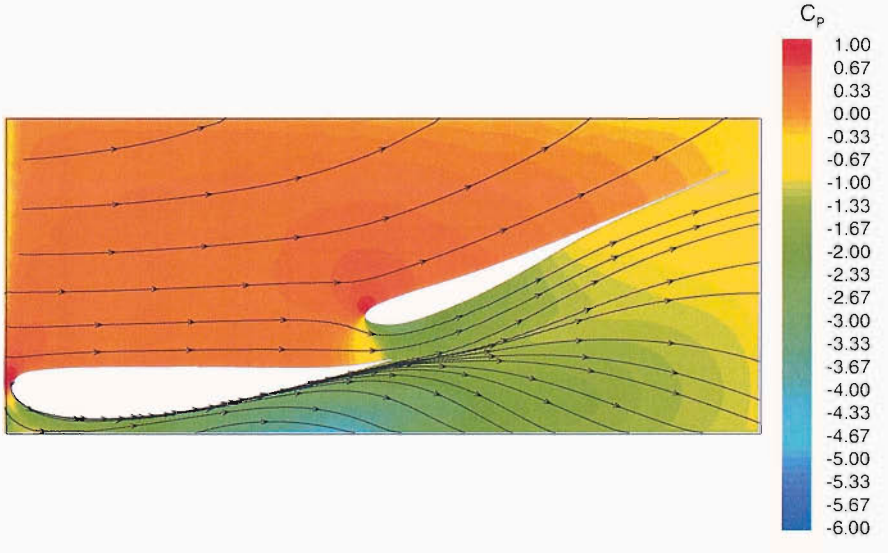

(b) Inboard surface of port endplate (flow from left to right).

Figure 11.24: Contours of pressure coefficient and streaklines at $h/c = 0.141$ (region d): Spalart-Allmaras turbulence model.

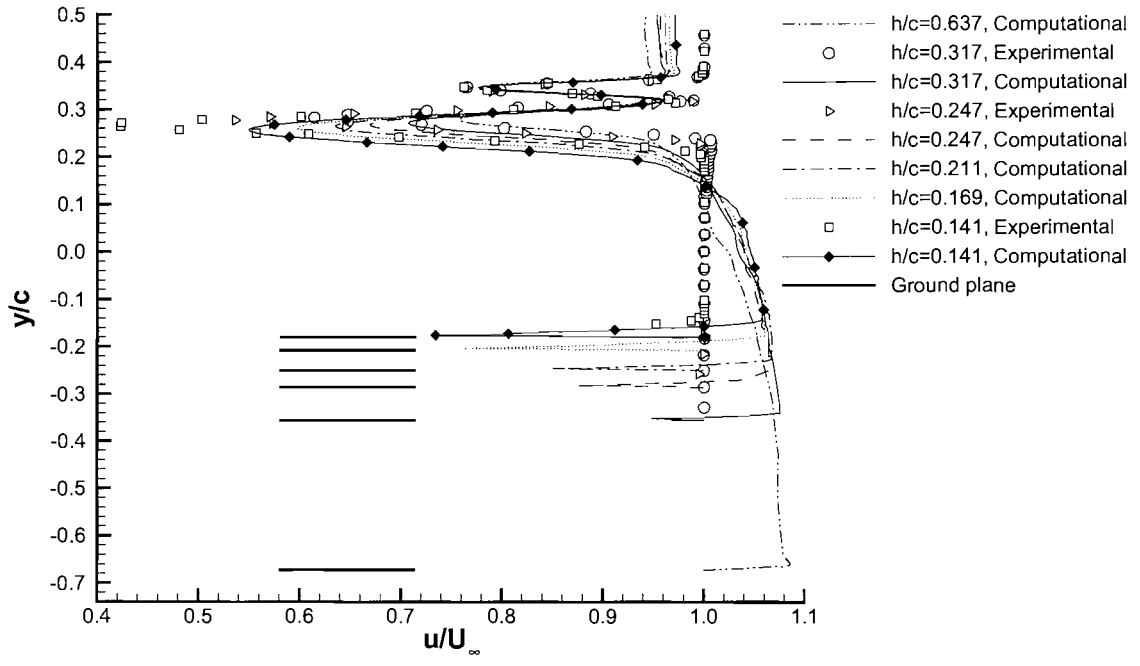

Figure 11.25: Non-dimensional wake profiles for various ride heights at $x/c = 1.127$, $z/c = -1.021$; Spalart-Allmaras turbulence model.

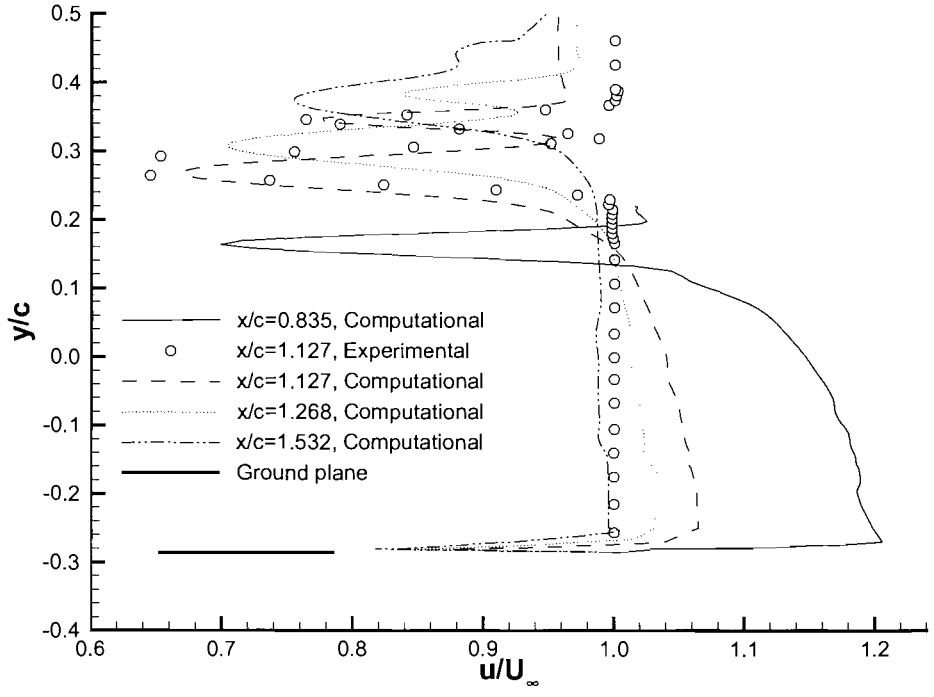

Figure 11.26: Non-dimensional wake profiles at various streamwise locations, $z/c = -1.021$, $h/c = 0.247$; Spalart-Allmaras turbulence model.

Turbulence Model	Main element			Flap		
	C_{Psuc}	x/c at C_{Psuc}	x/c at C_{Pstag}	C_{Psuc}	x/c at C_{Psuc}	x/c at C_{Pstag}
Experimental	-5.35	0.02	0.01	-2.65	0.48	0.46
Spalart-Allmaras	-4.45	0.02	0.01	-2.16	0.49	0.46
$k-\omega$ SST	-4.30	0.02	0.01	-2.10	0.49	0.46

Table 11.1: Centre span surface pressure information for various turbulence models; $h/c = 0.317$, $z/c = -1.021$.

Turbulence Model	u_{min}/U_∞			y/c at u_{min}/U_∞			y/c at δ		δ_{99}/c	
	low	*top*	*conf*	*low*	*top*	*conf*	*low*	*top*	*low*	*top*
Experimental	0.61	0.77	0.99	0.28	0.35	0.32	0.24	0.37	0.08	0.05
Spalart-Allmaras	0.71	0.78	0.96	0.27	0.35	0.32	0.18	0.38	0.14	0.06
$k-\omega$ SST	0.71	0.78	0.95	0.27	0.35	0.31	0.17	0.38	0.14	0.07

Table 11.2: Wake profile information at $x/c = 1.127$ for various turbulence models; $h/c = 0.317$, $z/c = -1.021$.

h/c	Expt/CFD	Main element			Flap		
		C_{Psuc}	x/c at C_{Psuc}	x/c at C_{Pstag}	C_{Psuc}	x/c at C_{Psuc}	x/c at C_{Pstag}
0.617	Expt	-4.15	0.02	0.01	-2.02	0.48	0.46
	S-A	-3.40	0.02	0.01	-1.80	0.48	0.46
0.317	Expt	-5.35	0.02	0.01	-2.65	0.48	0.46
	S-A	-4.50	0.02	0.01	-2.15	0.48	0.46
0.247	Expt	-5.95	0.02	0.01	-2.65	0.48	0.46
	S-A	-4.95	0.02	0.01	-2.35	0.48	0.46
0.211	Expt	-6.25	0.02	0.01	-2.75	0.48	0.46
	S-A	-5.20	0.02	0.01	-2.45	0.48	0.46
0.169	Expt	-6.65	0.02	0.01	-2.88	0.48	0.46
	S-A	-5.55	0.02	0.01	-2.55	0.48	0.46
0.141	Expt	-6.54	0.02	0.01	-2.89	0.48	0.46
	S-A	-5.70	0.02	0.01	-2.60	0.48	0.46

Table 11.3: Centre span surface pressure information for various ride heights; $z/c = -1.021$, Spalart-Allmaras turbulence model.

h/c	Expt/CFD	u_{min}/U_∞			y/c at u_{min}/U_∞			y/c at δ		δ_{99}/c	
		low	*top*	*conf*	*low*	*top*	*conf*	*low*	*top*	*low*	*top*
0.637	S-A	0.76	0.78	0.94	0.28	0.35	0.32	0.15	0.38	0.17	0.06
0.317	Expt	0.61	0.77	0.99	0.28	0.35	0.32	0.24	0.37	0.08	0.05
	S-A	0.71	0.78	0.96	0.27	0.35	0.32	0.18	0.38	0.14	0.06
0.247	Expt	0.54	0.77	0.99	0.28	0.35	0.32	0.23	0.37	0.09	0.05
	S-A	0.67	0.78	0.96	0.27	0.34	0.32	0.17	0.38	0.15	0.06
0.211	Expt	0.50	0.77	0.98	0.28	0.35	0.32	0.22	0.37	0.10	0.05
	S-A	0.64	0.78	0.96	0.26	0.34	0.32	0.17	0.38	0.15	0.06
0.169	S-A	0.60	0.78	0.96	0.26	0.34	0.32	0.16	0.38	0.16	0.06
0.141	Expt	0.42	0.77	0.97	0.26	0.35	0.31	0.21	0.37	0.10	0.06
	S-A	0.55	0.79	0.96	0.26	0.34	0.32	0.15	0.38	0.17	0.06

Table 11.4: Wake profile information at $x/c = 1.127$ for various ride heights; $z/c = -1.021$, Spalart-Allmaras turbulence model.

x/c	Expt/CFD	u_{min}/U_∞			y/c at u_{min}/U_∞			y/c at δ		δ_{99}/c	
		low	*top*	*conf*	*low*	*top*	*conf*	*low*	*top*	*low*	*top*
0.835	Expt	0.37	-	-	0.17	-	-	0.13	0.20	0.07	-
	S-A	0.70	-	-	0.16	-	-	0.13	0.19	0.06	-
1.127	Expt	0.54	0.77	0.99	0.28	0.35	0.32	0.23	0.37	0.09	0.05
	S-A	0.67	0.78	0.96	0.27	0.34	0.32	0.17	0.38	0.15	0.06
1.268	Expt	0.59	0.82	0.95	0.32	0.37	0.35	0.27	0.40	0.08	0.05
	S-A	0.70	0.84	0.93	0.31	0.38	0.36	0.19	0.43	0.17	0.07
1.532	Expt	0.67	0.87	0.90	0.38	0.44	0.43	0.33	0.47	0.10	0.04
	S-A	0.75	0.88	0.89	0.38	0.44	0.43	0.23	0.50	0.20	0.07

Table 11.5: Wake profile information at various streamwise locations for $h/c = 0.247$; $z/c = -1.021$, Spalart-Allmaras turbulence model.

Chapter 12

Conclusions and Recommendations for Future Work

The ultimate goal of this research was to investigate a multi-element wing in ground effect experimentally and computationally in order to further the knowledge concerning ground effect and high-lift flow fields. This goal has been realised within this research. A custom experimental test rig was designed and manufactured utilising the latest technology concerning wind tunnel motion systems and sensors. The experimental data was of high quality and can be used as a foundation for future follow-on research. The computational aspect of this research indicated the current capabilities of numerical techniques and highlighted topics for future investigation.

12.1 Conclusions

The following conclusions were drawn from the experimental section of this research.

- The forces generated by a multi-element wing in ground effect are largely insensitive to variations in flap location. However extreme values of flap gap and flap location resulted in significant reductions in downforce, drag and pitching moment due to the flap stalling.
- For high ride heights, reductions in ride height caused the downforce, drag and pitching moment to increase asymptotically.
- The breakdown of the lower edge vortex resulted in a discontinuous reduction in downforce, drag and pitching moment.

- One of the primary lift limiting mechanisms of a multi-element wing in ground effect is the dilation of the main element wake directly beneath the flap, with the coincidental presence of a region with zero pitot pressure. This finding is novel to this research.
- At low ride heights the forces generated by a multi-element wing in ground effect are dependent on the direction of ride height variation. This force dependency was attributed to the variation in Reynolds number observed during the run-up stage of the wind tunnel. This finding is novel to this research and has implications within industrial wind tunnel testing.
- The force dependency on the direction of ride height variation, observed at low ride heights was attributed to the flap stalling.
- The range of ride heights over which the force dependency was observed was directly dependent on the incidence of the flap. Increased values of flap incidence resulted in an increased range of force dependent ride heights. This finding is novel to this research.
- The addition of horizontal flat plates to the base of the endplates referred to as endplate feet, resulted in significantly increased values of downforce. This research proposed a "*foot pump*" mechanism of the flow beneath the endplate feet resulting in increased suction beneath the wing.
- Through the use of endplate feet the lower edge vortex can be maintained to a lower ride height when compared to the case without endplate feet. The persistence of the lower edge vortex occurred even though the addition of endplate feet generated a more adverse pressure gradient beneath the wing. The maintenance of the lower edge vortex was attributed to an increase in the Rossby number of the lower edge vortex with the addition of endplate feet. This hypothesis is novel to this research.

The computational investigations conducted yielded the following conclusions.

- Accurate predictions of both the on-surface and off-surface flow field generated by a single element aerofoil may be obtained through the solving of the RANS equations.
- Improved predictions of the surface flow field generated by a single element aerofoil in ground effect are obtained through the use of the $k-\omega$ SST turbulence model. This finding is novel to this research.

- Improved predictions of the off-surface flow field generated by a single element aerofoil in ground effect are obtained through the use of the Realizable $k-\varepsilon$ turbulence model. This finding is novel to this research.
- Accurate predictions of the on-surface flow field generated by a multi-element aerofoil may be obtained through the solving of the RANS equations.
- Improved predictions of the surface flow field generated by a multi-element aerofoil in ground effect are obtained through the use of the Realizable $k-\varepsilon$ turbulence model. This finding is novel to this research.
- The vertical location of the main element and flap wakes generated by a multi-element aerofoil in ground effect are underpredicted. This was attributed to the absence of upwash within the two-dimensional computations. Improvements can be obtained through the use of three-dimensional simulations.
- The qualitative flow field generated by a multi-element wing in ground effect may be obtained through solving the RANS equations. This finding is novel to this research.
- The quantitative features of the on-surface and off-surface flow field generated by a multi-element wing in ground effect are underpredicted numerically.
- The numerical inaccuracies observed within simulations of a multi-element wing were largely attributed to the inaccurate prediction of the lower edge vortex.

12.2 Recommendations for Future Work

12.2.1 Experimental

The experimental results obtained within this research have added to the knowledge of multi-element wings in ground effect and high-lift flow fields. However there remain related topics with a lack of understanding which could not be investigated within this research due to time limitations.

The wing profiles and configuration utilised within this research were specifically designed for use within motorsport. The situation of an isolated wing although of interest, is not directly applicable to motorsport due to the lack of surrounding bodywork. A logical progression from this research is to therefore experimentally investigate a multi-element

wing in ground effect in close proximity to wheels. The design of the test rig within this research allows for the addition of wheels directly downstream of the endplates. This future topic is of interest primarily to motorsport.

The wing tested within this research was always set at zero yaw. However in reality front wings of racing cars are frequently placed at a significant yaw angle while cornering. Although beneficial at zero yaw, the impact of yawed endplates and any associated separation on the performance of a multi-element wing in ground effect is unclear. Through minor modifications to supporting system of the test rig it would be possible to test the wing investigated in this research at yaw. The resulting performance variations of the wing would be of particular interest to the motorsport industry.

The computational aspects of this research indicated that the prediction of the lower edge vortex was not of great enough accuracy. For future improvements to be made high quality experimental validation data is required. The investigation of a vortex within a simplified divergent channel located over a moving ground would be of specific interest. In addition such results would be applicable to the topic of flap side edge vortices, in particular the subsequent breakdown at high incidences.

12.2.2 Computational

With the current increase in computational efficiency and progress within the accuracy of RANS solvers, computational investigations of increasing complexity and size are now possible. All the numerical results presented in this research were time-averaged. However inherently time-dependent flow features are present within the flow field generated by a multi-element aerofoil/wing in ground effect (e.g. shear layers, vortex breakdown). A logical progression from this research is therefore to investigate the time-dependent nature of a multi-element aerofoil/wing in ground effect. Experimental validation of the time-dependent flow features would also be required and could be obtained using the experimental rig investigated in this research. This topic would be of fundamental interest to to field of unsteady fluid mechanics.

The ride height of the aerofoil/wing investigated within this research was fixed i.e. a static ride height. However in reality the ride height of a racing car front wing is constantly varying due to breaking, acceleration and track roughness. Obtaining experimental data from an oscillating wing is inherently difficult. However computationally it is relatively simple. Recently a facility for constantly deforming computational grids has been included

within the RANS solver utilised within this research [150]. A logical progression is therefore to computationally investigate wings in ground effect with constantly varying ride height. However prior to this the unsteady nature of the flow field will have to be quantified.

The experimental investigations highlighted a dependency of the forces on the direction of ride height variation. This dependency was attributed to the Reynolds number variation during the run-up stage of the wind tunnel. It would be of interest to investigate whether this force dependency could be captured numerically. Through the use of continuously varying boundary conditions the run-up stage of the wind tunnel could be simulated. This topic would have both industrial and research applications.

12.2.3 Numerical Optimisation

The topic of improving the performance of a multi-element wing in ground effect is one which lends itself to numerical optimisation. Through the combination of an efficient realistic numerical solver and an optimisation code it would in theory be possible to numerically generate an optimal wing design or configuration for a given set of flow conditions. However it has been shown within this research that current numerical solutions are currently not of great enough accuracy. In addition the experimental flow features generated by a multi-element wing in ground effect currently not fully understood. Therefore although numerical optimisation is the next logical step within the design of multi-element wings in ground effect any subsequent results must be validated experimentally.

Bibliography

[1] Wright, P.G. The influence of aerodynamics on the design of formula one racing cars. *International journal of vehicle design*, 3(4):383–397, 1982.

[2] Agathangelou, B. and Gascoyne, M. Aerodynamic deign considerations of a formula 1 racing car, 1998. SAE Technical Paper 98–0399.

[3] Jeffrey, D., Hurst, D.W. and Zhang, X. Aerodynamics of gurney flaps on a single-element high-lift wing. *Journal of Aircraft*, 37(2):295–301, 2000.

[4] Baragona, M., Boermans, L.M.M., van Tooren, M.J.L., Bijl, H. and Beukers, A. Bubble bursting and stall hysterisis on single-slotted flap high-lift configuration. *AIAA Journal*, 41:1230–1237, 2003.

[5] Landman, D. and Britcher, C.P. Experimental investigation of multi-element airfoil lift hysterisis due to flap rigging. *Journal of Aircraft*, 38(4):703–708, 2001.

[6] Biber, K. and Zumwalt, G.W. Hysteresis effects on wind tunnel measurements of a two-element airfoil. *AIAA Journal*, 31(2):326–330, 1993.

[7] Ruhmann, A. and Zhang, X. Influence of diffuser angle on a bluff body in ground effect. *Journal of Fluids Engineering*, 125(2):332–338, 2003.

[8] Khorrami, M.D., Singer, B.A. and Radeztsky Jr. R.H. Reynolds-averaged navier-stokes computations of a flap-side-edge flowfield. *AIAA Journal*, 37:14–22, 1999.

[9] Zerihan, J.D.C. *An investigation into the aerodynamics of wings in ground effect.* PhD thesis, University of Southampton, Southampton, UK, 2001.

[10] Puel, F. and de Saint-Victor, X. Interaction of wake vortices with the ground. *Aerospace and Science Technology*, 4:239–247, 2000.

[11] Spall, R.E. Numerical study of a wing-tip votex using the euler equations. *Journal of Aircraft*, 38:22–27, 2001.

[12] Ragab, S.A. and Youssef, K.S. Computational aspects of trailing vortices. *Journal of Wind Engineering and Industrial Aerodynamics*, 69–71:943–953, 1997.

[13] Devenport, W.J., Rife, M.C., Liapis, S.I. and Follin, G.J. The structure and development of a wing-tip vortex. *Journal of Fluid Mechanics*, 312:67–106, 1996.

[14] Corsiglia, V.R., Schwind, R.G. and Chigier, N.A. Rapid scanning, three-dimensional hot-wire anemometer surveys of wing-tip vortices. *Journal of Aircraft*, 10:752–757, 1973.

[15] McCormick, B.W., Tangler, J.L. and Sherrieb, H.E. Structure of trailing vortices. *Journal of Aircraft*, 5:260–267, 1968.

[16] Mertaugh, L.J., Damania, R.B. and Paillet, F.L. An investigation of the near-field wake behind a full-scale test aircraft. *Journal of Aircraft*, 14:894–902, 1977.

[17] Green, S.I. and Acosta, A.J. Unsteady flow in trailing vortices. *Journal of Fluid Mechanics*, 227:107–134, 1991.

[18] Shekarriz, A., Fu, T.C., Katz, J. and Huang, T.T. Near-field behaviour of a tip vortex. *AIAA Journal*, 31:112–118, 1993.

[19] Katz, J., and Galdo, J.B. Effect of roughness on rollup of tip vortices on a rectangular hydrofoil. *Journal of Aircraft*, 26:247–253, 1989.

[20] Francis, T.B. and Katz, J. Observations on the development of a tip vortex on a rectangular hydrofoil. *Journal of Fluids Engineering*, 110:208–215, 1988.

[21] Gursul, I. and Xie, W. Origin of vortex wandering over delta wings. *Journal of Aircraft*, 37:348–350, 2000.

[22] Menke, M., Yang, H. and Gursul, I. Experiments on the unsteady nature of vortex breakdown over delta wings. *Experiments in Fluids*, 27:262–272, 1999.

[23] Heyes, A.L., Jones, R.F. and Smith, D.A.R. Wandering of wing-tip vortices, 2004. 12th International symposium on applications of laser techniques to fluid mechanics, 12–15 July, Lisbon, Paper number 35.3.

[24] Crow, S.C. Stability theory for a pair of trailing vortices. *AIAA Journal*, 8:2172–2179, 1970.

[25] Türk, L., Coors, D. and Jacob, D. Behaviour of wake vortices near the ground over a large range of Reynolds numbers. *Aerospace Science and Technology*, 3(2):71–81, 1999.

[26] Proctor, F.H., Hamilton, D.W. and Han, J. Wake vortex transport and decay in ground effect: vortex linking with the ground, 2000. AIAA Paper 2000–0757.

[27] Garcia, D.L. and Katz, J. Trapped vortex in ground effect. *AIAA Journal*, 41:674–678, 2003.

[28] Harvey, J.K. and Perry, F.J. Flowfield produced by trailing vortices on the vicinity of the ground plane. *AIAA Journal*, 9:1659–1660, 1971.

[29] Massey, B.S. *Mechanics of Fluids*. Chapman & Hall, 1989. 6^{th} edition.

[30] Cebeci, T., Mosinskis, G.J. and Smith, A.M.O. Calculation of separation points in incompressible turbulent flows. *Journal of Aircraft*, 9(9):618–624, 1972.

[31] Winklemann, A.E. and Barlow, J.B. Flowfield model for a rectangular planform wing beyond stall. *AIAA Journal*, 18(8):1006–1008, 1980.

[32] Leibovich, S. The structure of vortex breakdown. *Annual Review of Fluid Mechanics*, 10:221–246, 1978.

[33] Delery, J.M. Aspects of vortex breakdown. *Progress in Aerospace Sciences*, 30:1–59, 1994.

[34] Sarpkaya, T. On the stationary and travelling vortex breakdowns. *Journal of Fluid Mechanics*, 45:545–559, 1971.

[35] Sarpkaya, T. Vortex breakdown in swirling conical flows. *AIAA Journal*, 9:1792–1799, 1971.

[36] Wentz Jr, W.H., Kohlman, D.L. Vortex breakdown on slender sharp-edged wings. *Journal of Aircraft*, 8:156–161, 1971.

[37] Menke, M. and Gursul, I. Unsteady nature of leading edge vortices. *Physics of Fluids*, 9:2960–2966, 1997.

[38] Lucca-Negro, O. and O'Doherty, T. Vortex Breakdown: a review. *Progress in Energy and Combustion Science*, 27:431–481, 2001.

[39] Chanaud, R.C. Observations of oscillatory motion in certain swirling flows. *Journal of Fluid Mechanics*, 21:111–127, 1965.

[40] Gursul, I. and Xie, W. Buffeting flows over delta wings. *AIAA Journal*, 37:58–65, 1999.

[41] Khorrami, M.R., Berkman, M.E., Li, F. and Singer, B.A. Computational simulations of a three-dimensional high-lift wing, 2002. AIAA Paper 2002–2804.

[42] Zerihan, J.D.C. and Zhang, X. Aerodynamics of a single element wing in ground effect. *Journal of Aircraft*, 37(6):1058–1064, 2000.

[43] Senior, A. and Zhang, X. The force and pressure of a diffuser-equipped bluff body in ground effect. *Journal of Fluids Engineering*, 123:105–111, 2001.

[44] Kapadia, S., Roy, S. and Wurtzler, K. Detached eddy simulation over a reference ahmed car model, 2003. AIAA Paper 2003-0857.

[45] Verzicco, R., Fatica, M., Iaccarino, G., Moin, P. and Khalighi, B. Large eddy simulation of a road vehicle with drag-reduction devices. *AIAA Journal*, 40(12):2447–2455, 2002.

[46] Experiments on models of aeroplane wings at the national physical laboratory, 1914. Aeronautical Research Council Technical Report, R&M No. 110.

[47] Page, F.H. The Handley Page slotted wing. *The Aeronautical Journal*, page 263, 1921.

[48] Smith, A.M.O. High-Lift aerodynamics. *Journal of Aircraft*, 12(6):501–530, 1975.

[49] Maddah, S.R. and Bruun, H.H. An investigation of flow fields over multi-element aerofoils. *Journal of Fluids Engineering*, 124:154–165, 2002.

[50] Bario, F., Charnay, G. and Papailiou, K.D. An experiment concerning the confluence of a wake and a boundary layer. *Journal of Fluids Engineering*, 104:18–24, 1982.

[51] Squire, L.C. Interactions between wakes and boundary-layers. *Progress in Aerospace Sciences*, 26:261–288, 1989.

[52] Zhou, M.D. and Squire, L.C. The interaction of a wake with a turbulent boundary layer. *Aeronautical Journal*, 1985. Paper No. 1256.

[53] Olson, L.E. and Orloff, K.L. On the structure of turbulent wakes and merging shear layers of multi-element airfoils, 1981. AIAA Paper 81–1238.

[54] Thomas, F.O., Nelson, R.C. and Liu, X. Experimental investigation of the confluent boundary layer of a high-lift system. *AIAA Journal*, 38:978–988, 2000.

[55] Ying, S.X. and Spaid, F.W. Investigation of confluent boundary layers in high lift flows, 1998. AIAA Paper 98–2622.

[56] Ying, S.X., Spaid, F.W., McGinley, C.B. and Rumsey, C.L. Investigation of confluent boundary layers in high-lift flows. *Journal of Aircraft*, 36(3):550–562, 1999.

[57] McGinley, C.B., Anders, J.B. and Spaid, F.W. Measurements of Reynolds stress profiles on a high lift airfoil, 1998. AIAA Paper 98–2620.

[58] Liou, W.W. and Lui, F. Spatial linear instability of confluent wake/boundary layer. *AIAA Journal*, 39(11):2076–2081, 2001.

[59] Chin, V.D., Peters, D.W., Spaid, F.W. and McGhee, R.J. Flowfield measurements about a multi-element airfoil at high Reynolds numbers, 1993. AIAA Paper 93–3137.

[60] Rumsey, C.L. and Ying, S.X. Prediction of high lift: review of present CFD capability. *Progress in Aerospace Sciences*, 38:145–180, 2002.

[61] Petrov, A.V. Certain types of separated flow over slotted wings. *Fluid Mechanics - Soviet Research*, 7:80–88, 1978.

[62] Petrov, A.V. Separated flow about high-lift wings and active control, 1995. High lift and separation control, Proceedings of the conference, University of Bath, UK, 1995.

[63] Drela, M. Design and optimization method for multi-element airfoils, 1993. AIAA Paper 93–0969.

[64] Valarenzo, W.O. Topics in high-lift aerodynamics, 1993. AIAA Paper 93–3136.

[65] Valarenzo, W.O., Dominik, C.J. and McGhee, R.J. Multi-Element airfoil performance due to Reynolds and Mach number variations. *Journal of Aircraft*, 30(5):689–694, 1993.

[66] Spaid, F.W. High Reynolds number multi-element airfoil flowfield measurements. *Journal of Aircraft*, 37(3):499–507, 2000.

[67] Schell, I., Özger, E. and Jacob, D. Influence of different flap settings on the wake-vortex structure of a rectangular wing with flaps and means of alleviation with wing fins. *Aerospace Science and Technology*, 4(2):79–90, 2000.

[68] Lin, J.C. and Dominik, C.J. Parametric investigation of a high-lift airfoil at high Reynolds numbers. *Journal of Aircraft*, 34(4):485–491, 1997.

[69] Valarezo, W.O., Dominik, C.J., McGhee, R.J., Goodman, W.L. and Paschal, K.B. Multi-Element airfoil optimization for maximum lift at high Reynolds numbers, 1991. AIAA Paper 91–3332–CP.

[70] Landman, D. and Britcher, C.P. Experimental geometry optimization techniques for multi-element airfoils. *Journal of Aircraft*, 37(4):707–713, 2000.

[71] Mueller, T.J. and Batill, S.M. Experimental studies of separation on a two-dimensional airfoil at low Reynolds number. *AIAA Journal*, 20(4):457–463, 1982.

[72] Mason, W.H. Leading edge - trailing edge airfoil interactions, 1995. AIAA Paper 95–0436.

[73] Rogers, S.E., Roth, K.R, and Nash, S.M. CFD validation of high lift flows with significant wind tunnel effects, 2000. AIAA Paper 2000–4218.

[74] Rogers, S.E. Progress in high-lit aerodynamic calculations. *Journal of Aircraft*, 31(6):1244–1251, 1994.

[75] Mathias, D.L., Roth, K.R., Ross, J.C., Rogers, S.E. and Cummings, R.M. Navier-Stokes analysis of the flow about a flap edge. *Journal of Aircraft*, 35(6):833–838, 1998.

[76] Kim, C.S., Kim, C. and Rho, O.H. Parallel computations of high-lift airfoil flows using two-equation turbulence models. *AIAA Journal*, 38:1360–1368, 2000.

[77] Anderson, W.K., Bonhaus, D.L., McGhee, R.J. and Walker, B.S. Navier-Stokes computations and experimental comparisons for multi-element airfoil configurations, 1993. AIAA Paper 93–0645.

[78] Valarezo, W.O. and Mavriplis, D.J. Navier-Stokes applications to high-lift airfoil analysis. *Journal of Aircraft*, 32(3):618–624, 1995.

[79] Anderson, W.K., Bonhaus, D.L., McGhee, R.J. and Walker, B.S. Navier-Stokes computations and experimental comparisons for multi-element airfoil configurations. *Journal of Aircraft*, 32(6):1246–1253, 1995.

[80] Moitra, A. Automated CFD analysis of two-dimensional high-lift flows. *Journal of Aircraft*, 39(4):662–667, 2002.

[81] Rumsey, C.L. and Gatski, T.B. Recent turbulence model advances applied to multi element airfoil computations, 2000. AIAA Paper 2000-4323.

[82] Zahm, A.F. and Bear, R.M. Ground-plane influnece on airplane wings. *Journal of the Franklin Institute*, 191:687–693, 1921.

[83] Recant, I.G. Wind-tunnel investigation of ground effect on wings with flaps, 1939.

[84] Hsiun, C.-M. and Chen, C.-K. Aerodynamic characteristics of a two-dimensional airfoil with ground effect. *Journal of Aircraft*, 33(2):386–392, 1996.

[85] Nuhait, A.O. and Mook, D.T. Numerical simulation of wings in steady and unsteady ground effects. *Journal of Aircraft*, 26(12):1081–1089, 1989.

[86] Kwag, S-H. Lift/drag prediction of 3-dimensional WIG moving above free surface. *KSME International Journal*, 15:384–391, 2001.

[87] Wang, Q-X. Flow around an unsteady thin wing close to curved ground. *Journal of Fluid Mechanics*, 226:175–187, 1991.

[88] Tuck, E.O. Nonlinear extreme ground effect on thin wings of arbitrary aspect ratio. *Journal of Fluid Mechanics*, 136:73–84, 1983.

[89] Tuck, E.O. A nonlinear unsteady one-dimensional theory for wings in extreme ground effect. *Journal of Fluid Mechanics*, 98:33–47, 1980.

[90] Newman, J.N. Analysis of small-aspect-ratio lifting surfaces in ground effect. *Journal of Fluid Mechanics*, 117:305–314, 1982.

[91] Widnall, S.E. and Barrows, T.M. An analytic solution for two- and three-dimensional wings in ground effect. *Journal of Fluid Mechanics*, 41:769–792, 1970.

[92] Im, Y-H. and Chang, K-S. Unsteady aerodynamics of a wing-in-ground-effect airfoil flying over a wavy wall. *Journal of Aircraft*, 37(4):690–696, 2000.

[93] Plotkin, A. and Dodbele, S.S. Slender wing in ground effect. *Journal of Aircraft*, 26(4):493 494, 1998.

[94] Recant, I.G. Wind-tunnel investigation of ground effect on wings with flaps, 1939. NACA Report No.705.

[95] Ranzenbach, R. and Barlow, J.B. Two-Dimensional airfoil in ground effect, an experimental and computational study, 1994. SAE Technical Paper 942509.

[96] Ranzenbach, R., Barlow, J.B. and Diaz, R.H. Multi-Element airfoil in ground effect - an experimental and computational study, 1997. AIAA Paper 97-2238.

[97] Jasinski, W.J. and Selig, M.S. Experimental study of open-wheel race car front wings, 1998. SAE Technical Paper 983042.

[98] Stalker, E.A. A reflection plate representing the ground. *Journal of the Aeronautical Sciences*, 1:151–152, 1934.

[99] Mercker, E. and Wiedemann, J. Comparison of different ground simulation techniques for use in automotive wind tunnels, 1990. SAE Technical Paper 900321.

[100] Werlé, H. Simulation de l'effet de sol au tunnel hydrodynamique. *La Recherche Aérospatiale*, 95:7–15, 1963.

[101] Klemin, A. A belt method of representing the ground. *Journal of the Aeronautical Sciences*, 1:198–199, 1934.

[102] Garry, K.P. Some effects of ground clearence and ground plane boundary layer thickness on the mean base pressure of a bluff vehicle type body. *Journal of Wing Engineering and Industrial Aerodynamics*, 62(1):1–10, 1996.

[103] Burgin, K., Adey, P.C. and Beatham, J.P. Wind tunnel tests on road vehicle models using a moving belt simulation of ground effect. *Journal of Wind Engineering and Industrial Aerodynamics*, 22:227–236, 1986.

[104] Kim, M.S. and Geropp, D. Experimental investigation of the ground effect on the flow around some two-dimensional bluff bodies with moving-belt technique. *Journal of Wind Engineering and Industrial Aerodynamics*, 74-76:511–519, 1998.

[105] Katz, J. Investigation of negative lifting surfaces attached to an open-wheel racing car configuration, 1985. SAE Technical Paper 85–0283.

[106] Dominy, R.G. Aerodynamics of grand prix cars. *Journal of Automobile Engineering, Part D*, 206:267–274, 1992.

[107] Knowles, K., Donoghue, D.T. and Finnis, M.V. A study of wings in ground effect, 1994. Vehicle Aerodynamics, Proceedings of the conference, University of Loughborough, UK.

[108] Ranzenbach, R. and Barlow, J. Cambered airfoil in ground effect - an experimental and computational study, 1996. SAE Technical Paper 960909.

[109] Zhang, X. and Zerihan, J.D.C. Turbulent wake behind a single element wing in ground effect, 2000. 10^{th} International Symposium on Applications of Laser Techniques to Fluid Mechanics, 10-13 July, Lisbon, Portugal.

[110] Zhang, X., Zerihan, J.D.C., Ruhrmann, A. and Deviese, M. Tip vortices generated by a wing in ground effect, 2002. 11^{th} International Symposium on Applications of Laser Techniques to Fluid Mechanics, 8-11 July, Lisbon, Portugal.

[111] Zhang, X. and Zerihan, J. Aerodynamics of a double element wing in ground effect. Technical Report 2002–0834, AIAA, 2002.

[112] Zhang, X. and Zerihan, J. Aerodynamics of a double-element wing in ground effect. *AIAA Journal*, 41:1007–1016, 2003.

[113] Lawson, N.J., Knowles, K., Hart, R.J.E., Wray, J.N. and Eyles, J.M. An experimental investigation using PIV of the underflow of a GA(W)-1 aerofoil section in ground effect. 2002. MIRA, 4^{th} International Vehicle Aerodynamics Conference, 16-17 October, Rugby, UK.

[114] Katz, J. Calculation of the aerodynamic forces on automotive lifting surfaces. *Journal of Fluids Engineering*, 107:438–443, 1985.

[115] Launder, B.E. and Spalding, D.B. The numerical computation of turbulent flows. *Computer Methods in Applied Mechanics and Engineering*, 3:269–289, 1974.

[116] Zerihan, J. and Zhang, X. A single element wing in ground effect: comparisons of experiments and computation, 2001. AIAA Paper 2001-0423.

[117] Spalart, P.R. and Allmaras, S.R. A one-equation turbulence model for aerodynamic flows, 1992. AIAA Paper 92–0439.

[118] Menter, F.R. Two-Equation eddy-viscosity turbulence models for engineering applications. *AIAA Journal*, 32(8):1598–1605, 1994.

[119] Piegl, L. and Tiller, W. *Boundary layer and flow control.* Pergamon Press, 1961. 1^{st} edition.

[120] Hoerner, S.F. and Borst, H.V. Fluid-dynamic lift, 1975. 1^{st} edition, ISBN 76-111572.

[121] Gopalarathnam, A. and Selig, M.S. Design of high-lift airfoils for low aspect ratio wings with endplates, 1997. AIAA Paper 97–2232.

[122] Jeffrey, D. and Zhang, X. Some aspects of the aerodynamics of gurney flaps on a double-element wing. *Journal of Fluids Engineering*, 123:99–104, 2001.

[123] Zerihan, J.D.C. and Zhang, X. Aerodynamics of gurney flaps on a wing in ground effect. *AIAA Journal*, 39(5):772–780, 2001.

[124] Gai, S.L. and Palfrey, R. Influence of trailing-edge flow control on airfoil performance. *Journal of Aircraft*, 40(2):332–337, 2003.

[125] Liebeck, R.H. Design of subsonic airfoils for high-lift. *Journal of Aircraft*, 15(9):547 561, 1978.

[126] Myose, R., Papadakis, M. and Heron, I. Gurney flap experiments on airfoils, wings and reflection plane model. *Journal of Aircraft*, 35(2):206–211, 1998.

[127] Ross, J.C., Storms, B.L. and Carranmanto, P.G. Lift-Enhancing tabs on multi-element airfoils. *Journal of Aircraft*, 32(3):649–655, 1995.

[128] Papadakis, M., Myose, R.Y. and Matallana, S. Experimental investigation of gurney flaps on a two element general aviation airfoil, 1997. AIAA Paper 97-0728.

[129] Carrannanto, P.G., Storms, B.L., Ross, J.C. and Cummings, R.M. Navier-Stokes analysis of lift-enhancing tabs on multi-element airfoils. *Aircraft Design*, 1(3):145–158, 1998.

[130] Storms, B.L. and Jang, C.S. Lift enhancement of an airfoil using a gurney flap and vortex generators. *Journal of Aircraft*, 31(3):542–547, 1994.

[131] Lin, J.C., Robinson, S.K. and McGhee, R.J. Separation control on high Reynolds number multi-element airfoils, 1992. AIAA Paper 92-2636.

[132] Kerho, M. and Kramer, B. Enhanced airfoil design incorporating boundary layer mixing devices, 2003. AIAA Paper 2003-0211.

[133] Thompson, B.E. and Whitelaw, J.H. Flow around airfoils with blunt, round and sharp trailing edges. *Journal of Aircraft*, 25(4):334–342, 1988.

[134] Thompson, B.E. and Whitelaw, J.H. Trailing edge region of airfoils. *Journal of Aircraft*, 26(3):225–234, 1989.

[135] Thompson, B.E. and Lotz, R.D. Divergent trailing edge airfoil flows. *Journal of Aircraft*, 33(5):950–955, 1996.

[136] Brune, G.W. and Sikavi, D.A. Experimental investigation of the confluent boundary layer of a multielement low speed airfoil, 1983. AIAA Paper 83-0566.

[137] King, D.A. and Williams, B.R. Developments in computational methods for high-lift aerodynamics. *Aeronautical Journal*, pages 265–288, 1988.

[138] Rogers, S.E., Wiltberger, N.L. and Kwak, D. Efficient simulation of incompressible viscous flow over single and multi-element airfoils. *Journal of Aircraft*, 30(5):736–743, 1993.

[139] Johnston, G.W., Nelson, T.E. and Zingg, D.W. Compressible Navier-Stokes computations of multi-element airfoil flows using multiblock grids. *AIAA Journal*, 32(3):506–511, 1994.

[140] Rogers, S.E., Menter, F., Durbin, P.A. and Mansour, N.N. A comparison of turbulence models in computing multi-element airfoil flows, 1994. AIAA Paper 94-0291.

[141] Godin, P., Zingg, D.W. and Nelson, T.E. High-lift aerodynamic computations with one- and two-equation turbulence models. *AIAA Journal*, 35:237–243, 1997.

[142] Rumsey, C.L., Gatski, T.B., Ying, S.X. and Bertelrud, A. Prediction of high-lift flows using turbulent closure models. *AIAA Journal*, 36(5):765–774, 1998.

[143] Czerwiec, R., Edwards, J.R., Rumsey, C.L. and Hassan H.A. Theory and experiment of multielement airfoils - a comparison, 2000.

[144] Khorrami, M.R., Berkman, M.E. and Choudhari, M. Unsteady flow computations of a slat with a blunt trailing edge. *AIAA Journal*, 38(11):2050–2058, 2000.

[145] Rumsey, C.L., Lee-Rausch, E. and Watson, R.D. Three-dimensional effects in multi-element high lift computations. *Computers & Fluids*, 32:631–657, 2003.

[146] Federation Internationale de L'Automobile. *Formula One Technical Regulations*, 2002.

[147] Jeong, J. and Hussain, F. On the identification of a vortex. *Journal of Fluid Mechanics*, 285:69–94, 1995.

[148] Lambourne, N.C. and Bryer, D.W. The bursting of leading-edge vortices - Some observations and discussion of phenomenon, 1962. Aeronautical Research Council, R & M No. 3282.

[149] Spall, R.E., Gatski, T.B. and Grosch, C.E. A criterion for vortex breakdown. *Physics of Fluids*, 30:3434–3440, 1987.

[150] Fluent Incorporated. *Fluent version 6.0 manual*, 2001.

[151] Spalart, P.R. and Allmaras, S.R. A one-equation turbulence model for aerodynamic flows, 1992. AIAA Paper 92–0439.

[152] Launder, B.E. and Spalding, D.B. The numerical computation of turbulent flows. *Computer Methods in Applied Mechanics and Engineering*, 3:269–289, 1974.

[153] Wilcox, D.C. Multiscale models for turbulent flows. *AIAA Journal*, 26(11):1311 - 1320, 1988.

[154] Menter, F.R. Two-Equation eddy-viscosity turbulence models for engineering applications. *AIAA Journal*, 32(8):1598–1605, 1994.

[155] Yakhot, A. and Orszag, S. Renormalisation group analysis of turbulence: I basic theory. *Journal of Scientific Computing*, 1(1):1–51, 1986.

[156] Shih, T-H, Liou, W.W, Shabbir, A., Yang, Z. and Zhu, J. A new k-ϵ eddy viscosity model for high reynolds number turbulent flows. *Computers & Fluids*, 24:227–238, 1995.

[157] Pointwise Incorporated. *Gridgen version 14.06 manual*, 2001.

[158] Aerotech ATE Ltd. 3-component front wing balance calibration report, 2002. Report No. RP2246-1.

[159] Engineering Sciences Data Unit. *Blockage corrections for bluff bodies in confined flows*, 1998. ESDU Data Unit 80024.

[160] Moffat, R.J. Contibutions to the theory of single-sample uncertainty analysis. *Journal of Fluids Engineering*, 104:250–260, 1982.

[161] Moffat, R.J. Describing the uncertainties in experimental results. *Experimental Thermal and Fluid Science*, 1:3 -17, 1998.

[162] Parsad, A.K. Stereoscopic particle image velocimetry. *Experiments in Fluids*, 29:103–116, 2000.

[163] Krishnan, V., Sundaram, S. and Viswanath, P.R. Transition-related studies on two low-drag airfoils. *Current Science*, 79:829–833, 2000.

[164] Lee, H. and Kang, S.-H. Flow characteristics of transitional boundary layers on an airfoil in wakes. *Journal of Fluids Engineering*, 122:522–532, 2000.

[165] Bertelrud, A. Transition on a three element high lift configuration at high Reynolds number, 1998. AIAA Paper 98–0703.

[166] Drela, M. Xfoil 6.9 user guide, 2001.

[167] Drela, M. and Giles, M.B. Viscous-inviscid analysis of transonic and low reynolds number airfoils. *AIAA Journal*, 25:1347–1355, 1987.

Appendix A

Primary Effects of Slots Within Wings

The five primary effects of slots between individual elements of a multi-element wing, as stated by Smith [48] are listed and illustrated below.

- Slat Effect: In the vicinity of the leading edge of a downstream element, the velocities due to circulation on a forward element run counter to the velocities on the downstream element and so reduce pressure peaks on the downstream element. Figure A.1 presents an illustration of slat effects using a simplified approximation of a slat through the use of a point vortex.

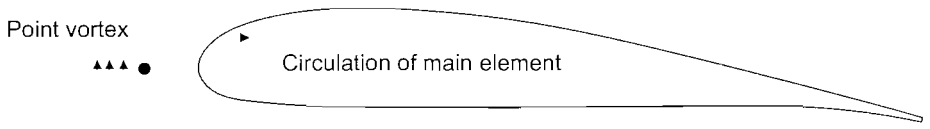

Figure A.1: Simplified representation of slat effects on a multi-element wing.

- Dumping Effect: Because the trailing edge of a forward element is in a region of velocity appreciably higher than freestream, the boundary layer "dumps" at a high velocity. The higher discharge velocity relieves the pressure rise impressed on the boundary layer, thus alleviating separation problems or permitting increased lift.
- Off-the-surface Pressure Recovery: The boundary layer from forward elements is dumped at velocities appreciably higher than freestream. The final deceleration to freestream of the wake occurs out of contact with a wall. Such a method is more effective than the best possible deceleration in contact with a wall.
- Circulation Effect: A downstream element causes the trailing edge of the adjacent upstream element to be in a region of high velocity that is inclined to the mean line at the rear of the

forward element. Figure A.2 presents an illustration of circulation effects using a simplified approximation of a single slotted flap using of a point vortex. The flow inclination at the trailing edge induces greater circulation on the forward element due to the enforcement of the Kutta condition.

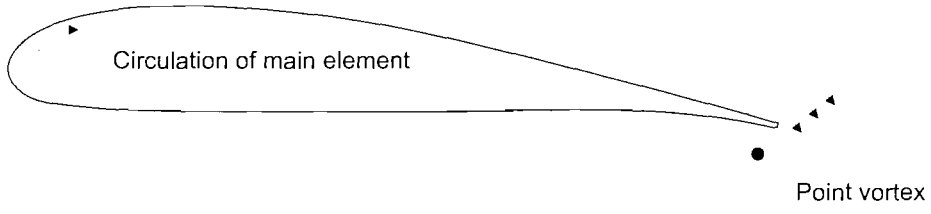

Figure A.2: Simplified representation of circulation effects on a multi-element wing.

- Fresh-boundary-layer Effect: Each new element starts out with a fresh boundary-layer at its leading edge. Thin boundary layers can withstand stronger adverse gradients than thick ones.

Appendix B

Three Component Load Cell Calibration

This chapter discusses the calibration of the Aerotech three component load cell (serial number 0487) used within this research. The load cell was originally calibrated by the manufacturers [158] however the unorthodox integration with the data acquisition system in the 2.1m×1.7m wind tunnel meant that re-calibration was required.

B.1 Calibration Setup

The calibration of the load cell was conducted within the 2.1m×1.7m wind tunnel test section with the model support system installed. The wing was replaced with a solid aluminium bar rectangular in cross section, attached to the pillar feet. The design of the load cell was such that the three force components were coupled with each component contributing to the final measurement. Each component was calibrated individually with simultaneous measurements obtained for all three components.

Calibration of the downforce component was achieved though the use of weights placed on the aluminium bar symmetric about the centre span location and mid chord location. The weights were varied providing a pure downforce ranging between 2kg and 60kg. The drag component was calibrated using a cable and pulley system which was attached to the centre span of the bar and extended downstream, over the pulley and through the floor of the wind tunnel (Figure B.1). The cable was kept horizontal at all times therefore producing a pure drag force on the load cell. The drag force imposed was varied between 1kg and 15kg. The pitching moment component was calibrated through the use of a bar 1m in length attached to the rectangular aluminium bar. The ends of the pitching bar were equidistant about the mid chord location of the rectangular aluminium bar. In order to produce a pure pitching moment the pitching bar was subjected to a simultaneous upwards

force at the upstream end through the use of a pulley, and a downwards force at the downstream end through the use of weights. Figure B.2 illustrates the setup for calibrating the pitching moment component. The pitching moment imposed on the load cell was varied between 1kgm and 6kgm.

Combining the force measurements obtained during the calibration of each of the three components it was possible to quantify the coupling between each component and therefore produce a calibration matrix.

B.2 Force Conversion

The first stage of obtaining forces from the three component load cell is to convert the raw voltages from each channel of the load cell into forces. The gains for each channel within the data acquisition system were setup to maximise the sensitivity of the load cell since the voltage variations were relatively small. Equations B.1 to B.3 present the conversions between the raw voltages and the coupled forces for a constant dynamic head (h_d) for the downforce, drag and pitching moment respectively.

$$L_{coup} = \left(\frac{(((V_L - V_{Lzero}) \times 2.3533001) \times 60000) \times (56.19/h_d)}{100}\right) \times \left(\frac{h_d}{56.19}\right) \tag{B.1}$$

$$D_{coup} = \left(\frac{(((V_D - V_{Dzero}) \times 14457) \times 2) \times (56.19/h_d)}{100}\right) \times \left(\frac{h_d}{56.19}\right) \tag{B.2}$$

$$M_{coup} = \left(\frac{(((V_M - V_{Mzero}) \times -18102) \times 2) \times (56.19/h_d)}{100}\right) \times \left(\frac{h_d}{56.19}\right) \tag{B.3}$$

where V_L, V_D, V_M are the raw voltages and V_{Lzero}, V_{Dzero}, V_{Mzero} are the zero voltages for the downforce, drag and pitching moment respectively. L_{coup}, D_{coup} and M_{coup} represent the coupled downforce, drag and pitching moment respectively with units of Netwons for downforce and drag and Newton-meters for pitching moment. Once converted from raw voltages the uncoupled forces (L, D, M) may then be calculated using the following equations.

$$L = \left(\frac{L_{coup} + 0.2214}{1.0027}\right) - \left(\frac{-0.0443 \times D_{coup}}{2}\right) - ((-0.0614 \times M_{coup}) + 0.1291) \tag{B.4}$$

$$D = ((-0.0039 \times L_{coup}) - 0.0707) + \left(\frac{D_{coup} - 0.0355}{1.005}\right) - ((-0.0156 \times M_{coup}) - 0.1993) \tag{B.5}$$

$$M = -(0.0153 \times L_{coup}) - (0.9135 \times D_{coup}) + \left(\frac{M_{coup} + 0.0042}{0.9922}\right) \tag{B.6}$$

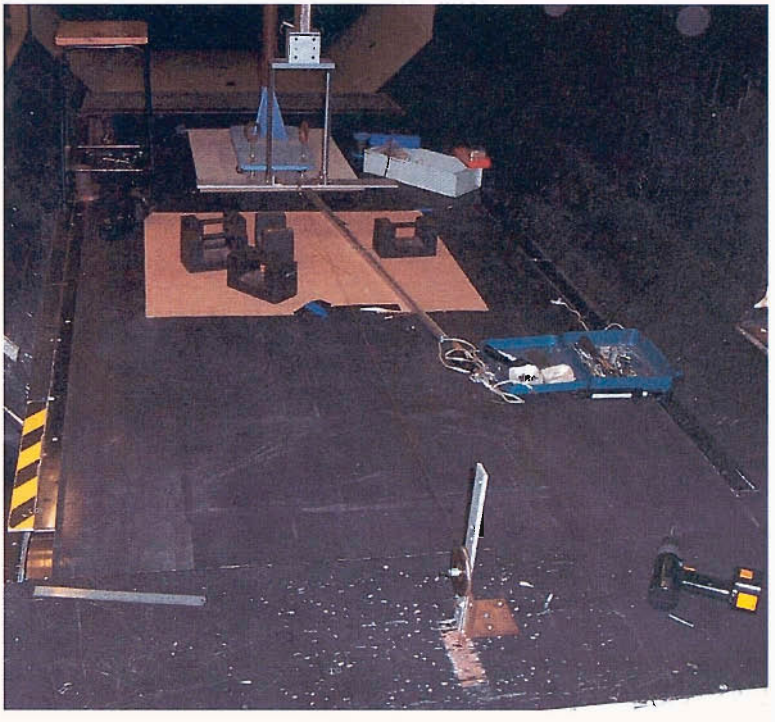

Figure B.1: Setup for calibration of the drag component.

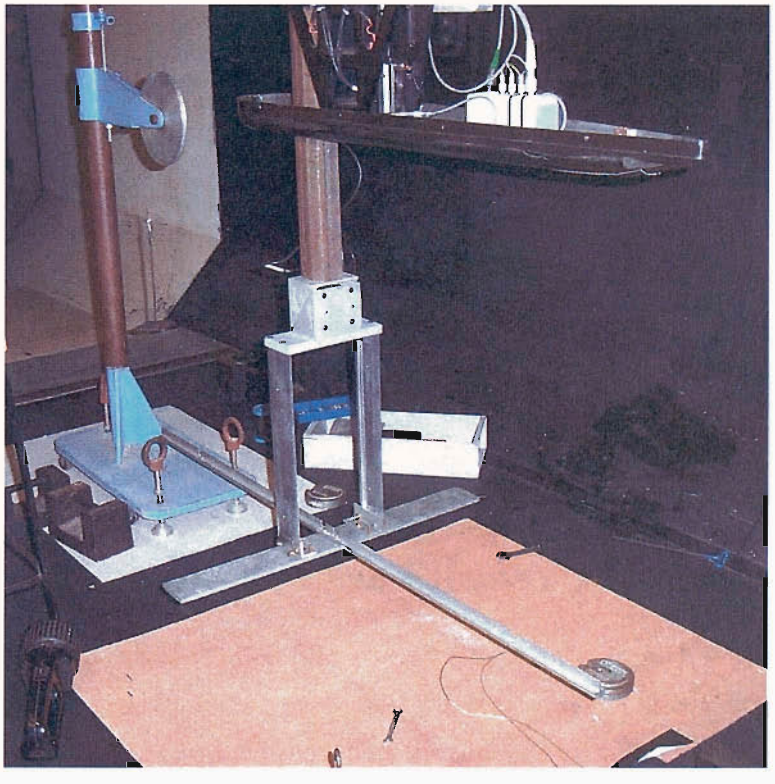

Figure B.2: Setup for calibration of the pitching moment component.

Appendix C

Blockage Effects, Uncertainty and Repeatability

This chapter discusses the quality of the experimental data in particular the uncertainties contained within the data, the repeatability of the data and the blockage effects. For each classification of measured data e.g. forces, surface pressures and PIV, the uncertainties will be quantified. In addition the short, medium and long term repeatability of the data will be discussed. Short term repeatability refers to data obtained within a single wind tunnel run with the wind in a continuous wind-on condition. This data typically highlights variations within the flow conditions due to variations in atmospheric conditions and temperature. Medium repeatability measurements refer to data obtained after a configuration change has been made to the model with the model in situ in a wind-off situation e.g. a variation in flap incidence. These measurements indicate the ability of the model to be accurately configured and were obtained within the same testing session. The long term repeatability of the model was investigated by using a datum wing configuration which was tested at the start and end of each testing session over a period of 13 months. The datum wing configuration consisted of a main element incidence of $+4^{\circ}$ and flap incidence of $+24^{\circ}$ with an optimum flap gap and overlap. This type of repeatability highlights any long term degradation of the model.

C.1 Correction for Blockage Effects

Blockage effects are a result of the flow field generated by a body within a wind tunnel test section, being constrained by the walls of the test section. These interactions have a direct impact upon the flow field generated by the body and hence effect the surface flow field, forces and surface pressures. The magnitude by which the wind tunnel measurements are effected and therefore the integrity of the recorded data, is dependent upon the size of the test rig relative to the wind tunnel test section.

Various theories exist concerning the evaluation blockage effects depending on the shape of the body, freestream conditions and design of wind tunnel.

The design of the wind tunnel test rig was such that the frontal area of the test rig was dependent on the specified ride height, main element incidence and flap incidence. Considering the wing in a datum configuration the combined frontal area of the model and support system (A_r) ranged between 0.21m^2 and 0.22m^2 for a ride heights of 180mm and 5mm respectively. The cross-sectional area of the 2.1m×1.7m wind tunnel (A_{wt}) remained constant at 3.40m^2 resulting in a blockage ratio ranging between 6.2% and 6.5%.

The model investigated by definition was a three-dimensional streamlined lifting body with asymmetric separation, when present. Accordingly the method used to quantify the blockage correction factors for the forces was a scheme specifically for lifting bodies [159]. The method considered the design of the wind tunnel test section (λ_1) and wind tunnel model (λ_2, λ_3) through the use of three configuration variables. The force correction factor (C_{Ff}/C_F) for a three-dimensional streamlined lifting body within a solid wall closed jet wind tunnel is stated in equation C.1.

$$\frac{C_{Ff}}{C_F} = 1 - \lambda_1\lambda_3\left(1 + \frac{1}{\lambda_2}\frac{b}{c}\right)\frac{c\,A_{wt}}{A_r^{1.5}} - 0.5\,(C_D - C_{Di})\frac{A_{wt}}{A_r} \tag{C.1}$$

where:

$$\lambda_1 = 0.72 \times \left(\frac{b_d}{H_w} + \frac{H_w}{b_d}\right)$$

$$\lambda_2 = \frac{4}{\pi}\frac{Maximum\ body\ cross\ sectional\ area}{b\ c}$$

$$\lambda_3 = \frac{Body\ volume}{c\ A_{wt}}$$

The values of drag coefficient and induced drag coefficient (C_{Di}) were dependent on the ride height of the wing resulting in a variable blockage correction coefficient defined by the ride height. The force correction factor ranged between 0.990 and 0.991 indicating that the experimental forces were overpredicted when compared to the true situation by a value between 1.0% and 0.9%. The effect of correcting for the blockage effects on the downforce generated by the wing is presented in Figure C.1.

C.2 Uncertainty of Force Measurements

Force measurements were obtained using a three component load cell capable of simultaneously recording values of downforce, drag and pitching moment. The sampling rate of the forces was set

within and limited by the motion and data acquisition system utilised within the 2.1m×1.7m wind tunnel. The sampling frequency of the forces was fixed at a value of 100Hz. Steady-state values of downforce, drag and pitching moment were obtained by sampling for 30 seconds then averaging using a moving-average scheme. The design of the data acquisition system was such that the raw data could recorded during a single 30 second sample could not be obtained. Statistic analysis of the force data was therefore not possible.

In addition to the uncertainty introduced by the data acquisition system, the forces measurements were subject to uncertainties generated by the accuracy with which the model was configured and the flow conditions set. These uncertainties were quantified using the accuracy with which each configuration variable was set in conjunction with the sensitivity of each force component to each configuration variable. The ride height of the wing was set using metal shims which were slid between the suction surface of the wing and the ground plane. The position of the moving belt while setting the ride height was kept constant using two markers, one on the belt and the other on the ground platern. The ride height was set to within an accuracy of ±0.05mm corresponding to maximum uncertainty values of $\pm 0.01017 C_L$, $\pm 0.00083 C_D$ and $\pm 0.00372 C_M$ at ride heights of $0.352c$, $0.423c$ and $0.423c$ respectively.

The main element incidence was set to within an accuracy of ±0.005° using a digital inclinometer. Maximum uncertainty values of $\pm 0.00056 C_L$, $\pm 0.00017 C_D$ and $\pm 0.00013 C_M$ were obtained at ride heights of $0.211c$, $0.211c$ and $0.070c$ respectively. The incidence of the flap was also set using a digital inclinometer also to within an accuracy of ±0.005°. The maximum uncertainties values within the forces due to the flap incidence were $\pm 0.00115 C_L$, $\pm 0.00018 C_D$ and $\pm 0.00039 C_M$ at ride heights of $0.148c$, $0.634c$ and $0.634c$ respectively.

The freestream velocity within the wind tunnel test section was set through a value of dynamic head with units of mm of water. The dynamic head was set to within an accuracy of ±0.05mm of water resulting in maximum uncertainty values of $\pm 0.00705 C_L$, $\pm 0.00132 C_D$ and $\pm 0.00755 C_M$ at ride heights of $0.042c$, $0.317c$ and $0.078c$ respectively.

The overall values of uncertainty within the force measurements were calculated using the root-sum-square method described by Moffet [160, 161]. The overall values of uncertainty with a 95% confidence were $\pm 0.0103 C_L$, $\pm 0.0014 C_D$ and $\pm 0.0079 C_M$ at ride heights of $0.352c$, $0.423c$ and $0.423c$ respectively. Figure C.2 presents the uncertainties within the downforce measurements at all ride heights during both the upstroke and downstroke stages.

C.3 Repeatability of Force Measurements

The repeatability of the force measurements obtained was separated into three categories; short term, medium term and long term. In all cases the wing was configured in the datum configuration. The short term repeatability of the forces was observed as variations in the forces, for identical

wing configurations within a single wind tunnel test run. Comparing the force data obtained during the upstroke and downstroke stages of a single test run ($h/c \geq 0.081$) allowed the short term repeatability to be quantified. The maximum variation in forces due to short term repeatability was quantified at $\pm 0.0043 C_L$, $\pm 0.0007 C_D$ and $\pm 0.0026 C_M$.

The medium term repeatability of the forces was quantified by comparing the data obtained during two separate test runs, the second after an alteration in model configuration. The maximum variation in the forces due to medium term repeatability was quantified at $\pm 0.0057 C_L$, $\pm 0.0010 C_D$ and $\pm 0.0045 C_M$.

The long term repeatability of the test rig was investigated by comparing the force data obtained during the earliest wind tunnel tests with that obtained during the last tests. Figure C.3 presents the force data obtained during both the original tests and the last tests, 13 months later. The resolution of the most recent force data between $h/c = 0.211$ and 0.247 was reduced when compared to the original data, due to time restrictions. The long term repeatability was found to be excellent for downforce, drag and pitching moment with maximum variations of $\pm 0.0037 C_L$, $\pm 0.0042 C_D$ and $\pm 0.0088 C_M$.

C.4 Uncertainty of Surface Pressure Measurements

Surface pressures measurements over the wing and port endplate were obtained using a zero, operate and calibrate (ZOC22B) pressure transducer manufactured by Scanivalve. The ZOC22B pressure transducer is capable of simultaneously measuring 32 channels however through the use of a dual switching system present on each channel a total of 64 channels may be measured in two groups of 32. The surface pressure data was recorded using the data acquisition system previously mentioned. The sampling frequency of the surface pressures, as for the forces was fixed at 100Hz within the data acquisition system. Initial tests were performed to investigate the effect of sampling time on the surface pressures in order to obtain time-averaged surface pressures independent of sampling period. A sampling period of 60 seconds per channel was set as a result since above this value no variation in the surface pressures was observed.

The main cause of uncertainty within the surface pressure measurements was temperature variation and the resulting temperature drift on each channel of the pressure transducer. In an attempt to minimise sensor drift the wind tunnel was run for typically an hour prior to any pressure measurements. This run-in period allowed the temperature of the pressure transducer and the air temperature within the test section to stabilise. In addition the pressure transducer was calibrated at the start of each run. In order to check for any variations within the surface pressures due to sensor drift during a single run a repeat of the first data point was conducted at the end of the run.

In addition to the uncertainty introduced by the sensor drift the surface pressure measurements were subject to uncertainties generated by the accuracy with which the model was configured and

the flow conditions set. These uncertainties were quantified using the accuracy with which each configuration variable was set in conjunction with the sensitivity of the surface pressures to each configuration variable. A linear variation in surface pressure with the variation of each configuration variable was assumed. The uncertainty of the surface pressure measurements obtained at each tap location was quantified.

The ride height of the wing was set using metal shims to within an accuracy of ± 0.05mm. The position of the moving belt while setting the ride height was kept constant using two markers, one on the belt and the other on the ground platern. The accuracy of the ride height produced a maximum uncertainty value of $\pm 0.03699 C_P$ at a ride height of $0.039c$ for the increasing ride height case, on the main element suction surface at $x/c = 0.014$, $z/c = -1.021$. The incidence of the flap was set using a digital inclinometer to within an accuracy of $\pm 0.005°$. The corresponding value of maximum uncertainty was $\pm 0.00277 C_P$ at a ride height of $0.141c$ on the flap suction surface at $x/c = 0.525$, $z/c = -1.021$. The freestream velocity within the test section was set using a value of dynamic head to within an accuracy of ± 0.05mm of water. The maximum uncertainty value due to this level of accuracy was $\pm 0.0008 C_P$ on the flap suction surface at a location of $x/c = 0.489$, $z/c = -1.021$.

The overall values of uncertainty within the surface pressure measurements were calculated using the root-sum-square method described by Moffet [160, 161]. The overall maximum value of uncertainty with a 95% confidence was $\pm 0.03699 C_P$ at a ride height of $0.039c$ for the increasing ride height case, on the main element suction surface at a location of $x/c = 0.014$, $z/c = -1.021$. The mean uncertainty within the surface pressure measurements was $\pm 0.00868 C_P$. Figure C.4 illustrates the uncertainties within the centre span surface pressures for the worst case ride height.

C.5 Repeatability of Surface Pressure Measurements

The repeatability of the surface pressure measurements was separated into three categories: short term, medium term and long term. The medium term and long term repeatability could not be quantified due to the short period of time over which all the surface pressures measurements were obtained.

The short term repeatability was quantified by comparing the surface pressures obtained during the upstroke and downstroke stages of a single test run ($h/c \geq 0.081$). The maximum variation in surface pressures due to short term repeatability was quantified at $\pm 0.082 C_P$ at a ride height of $h/c = 0.211$, on the flap suction surface at the pressure tapping located at $x/c = 0.511$, $z/c = -0.088$. This location corresponded to the region in which transition occurred on the flap suction surface. In addition the pressure tapping was located directly above the lower edge vortex in a ride height region where vortex breakdown was found to occur. Figure C.5 illustrates the short term repeatability for the chordwise surface pressures at the port tip for the worst case ride height.

C.6 Perspective Errors within PIV Measurements

Two-dimensional PIV is a technique which measures two components of velocity through the tracking of seeding particles within a medium, in this case air. Within the majority of flow fields the instantaneous velocity of a seeding particle is a combination of three velocity components u, v and w. The laser sheet used to illuminate the seeding particles is of finite thickness. Therefore in situations where the out-of-plane velocity component is large an error is introduced by the motion of the particle through the laser sheet. Figure C.6 illustrates the cause for this error known as perspective error using the coordinate system defined in section 3.3. The distance from the lens plane to the object plane is defined as d_i while the focal length of the camera lens is represented by d_o. The perspective error (γ) is defined as the difference between the true and measured in-plane displacement and is defined in Equation C.2 [162].

$$\gamma = (\gamma_y, \gamma_z) = \left(\frac{\triangle x}{\triangle y} tan\xi_y, \frac{\triangle x}{\triangle z} tan\xi_z \right) \tag{C.2}$$

where $\triangle x$ is the laser sheet thickness and $\triangle y$ and $\triangle z$ are the measured particle displacements in the y-direction and z-direction respectively. ξ_y and ξ_z are the angles of azimuth and inclination relative to the x-axis projected onto the $x-z$ and $y-z$ planes respectively.

Within this research PIV techniques were used to obtain spanwise and vertical flow field data at the port wing tip. It was observed that the out-of-plane velocity component (u) was much greater than the in-plane velocity components measured (v, w). Therefore the perspective errors within the PIV images needed to be quantified. A time averaged velocity vector map obtained at a ride height of $0.141c$ was investigated. The flap was positioned with an optimal location and the incidences of the main element and flap were $+4°$ and $+24°$ respectively. Within this case the camera was equipped with a 105mm focal length lens and located 2.3m downstream of the object plane. The thickness of the laser sheet was approximately 3mm within the measurement region fired with a time interval of $20\mu s$. The calculated vertical (γ_y) and spanwise (γ_z) perspective errors were of relatively uniform value across the image with a maximum value of 1%.

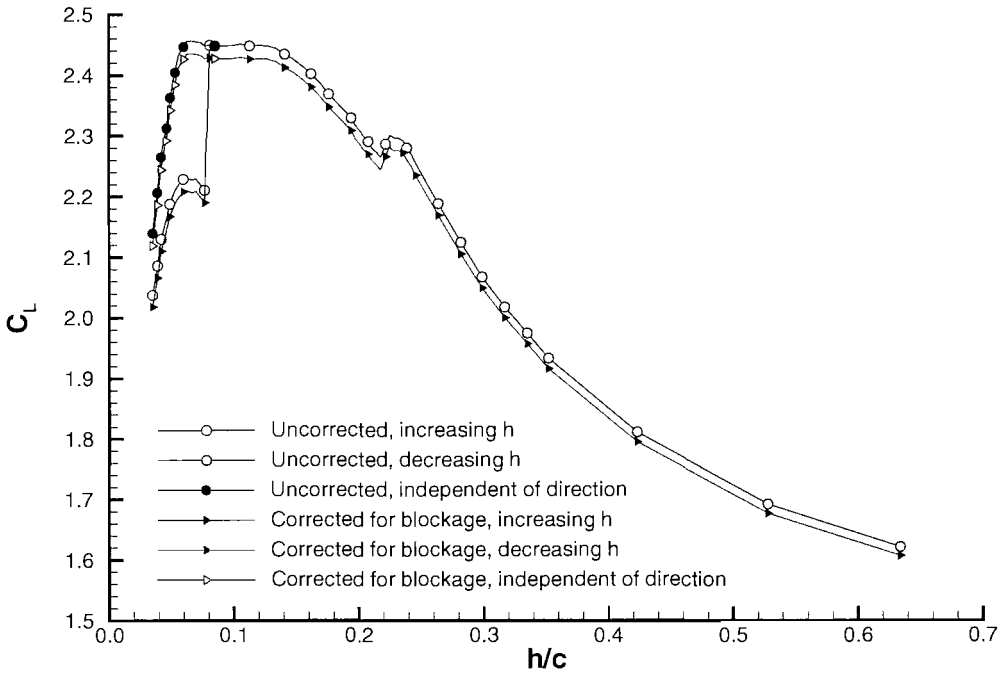

Figure C.1: Effect of blockage correction on downforce coefficient for various ride heights.

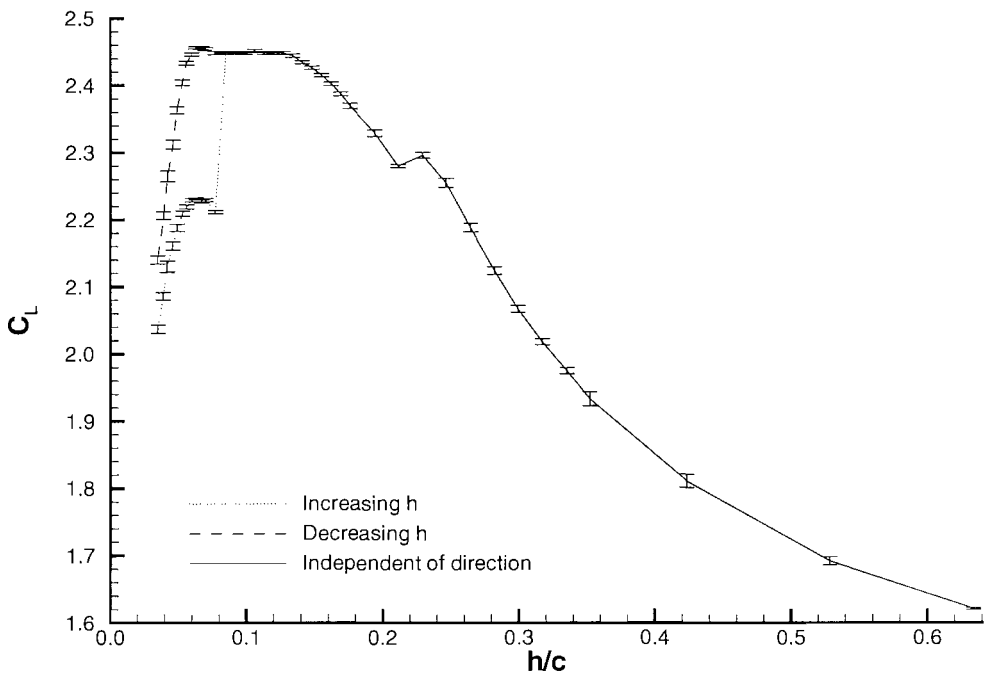

Figure C.2: Uncertainty within the downforce coefficient measurements for various ride heights.

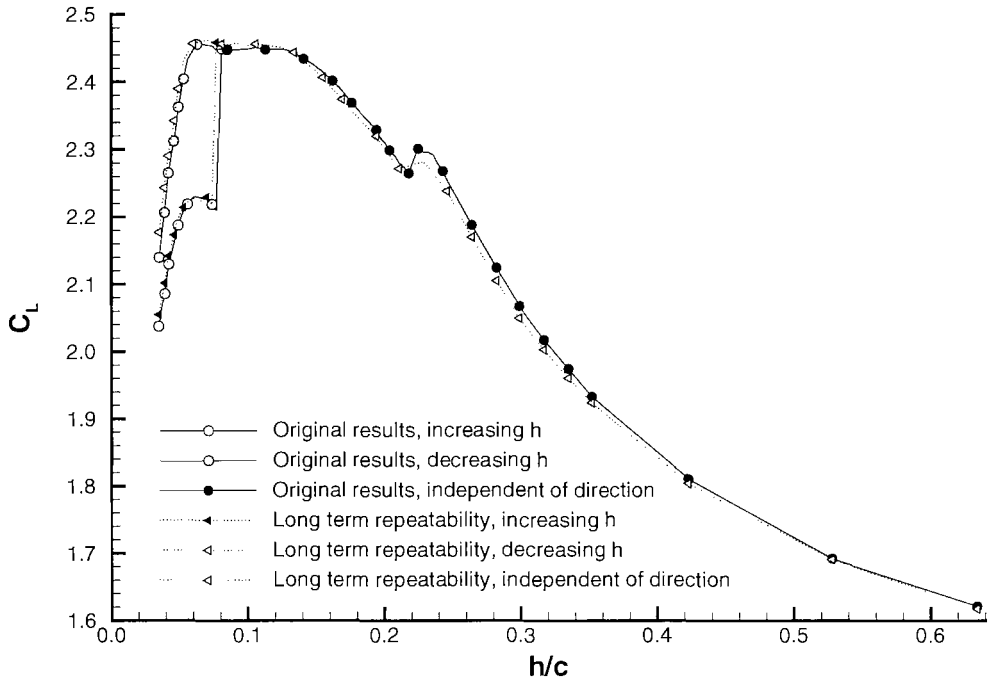

Figure C.3: Long term repeatability for the downforce coefficient.

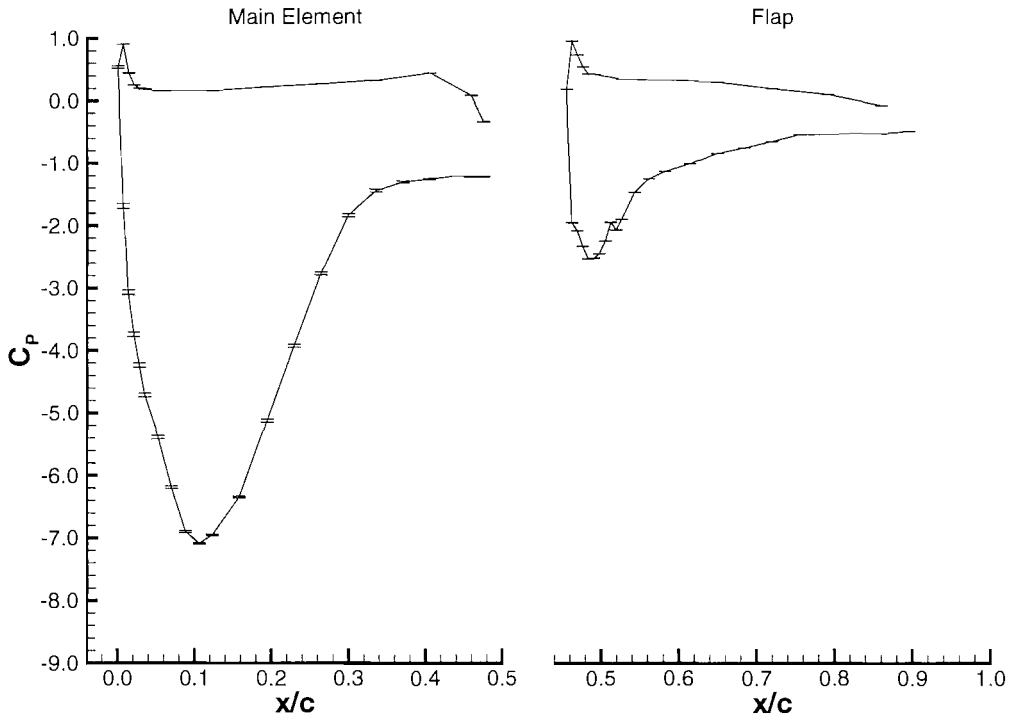

Figure C.4: Uncertainty within the centre span surface pressures; $h/c = 0.039$ increasing h.

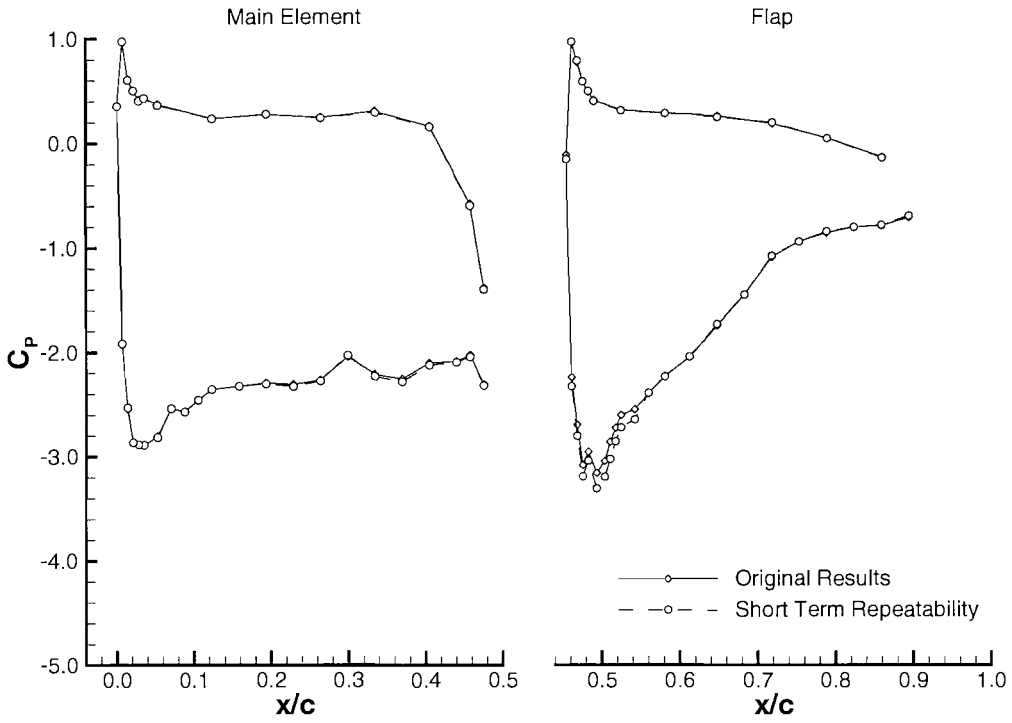

Figure C.5: Short term repeatability for the port tip surface pressures; $h/c = 0.211$.

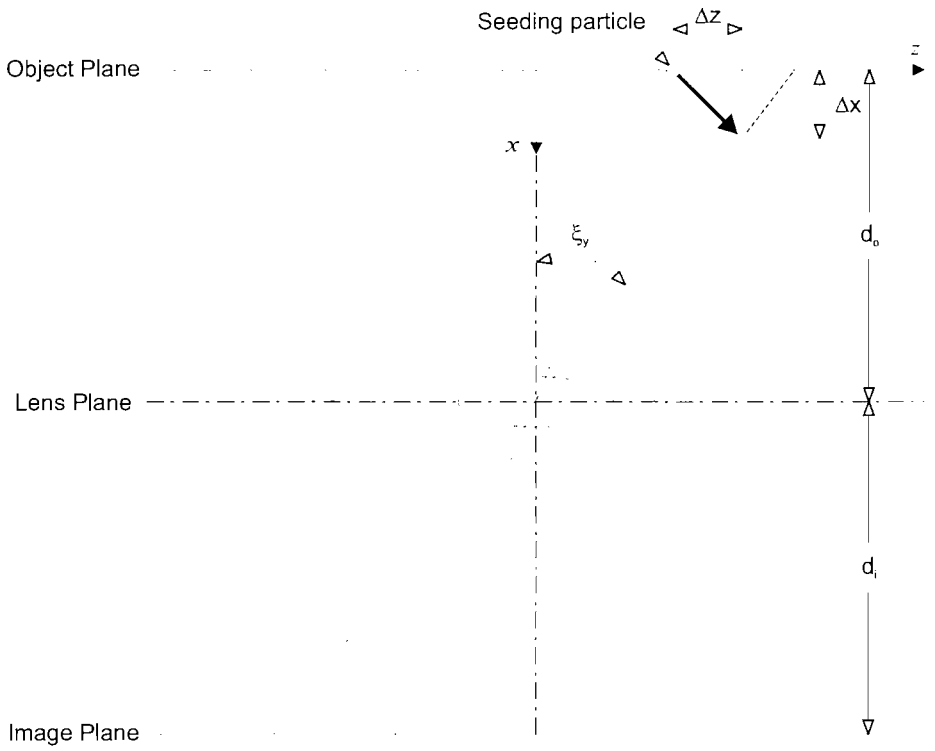

Figure C.6: Error in the measurement of in-plane displacements due to out-of-plane motion within a two-dimensional PIV image.

Appendix D

Boundary Layer Transition Identification

Boundary layer transition on a surface may be detected through the use of staggered hot-films positioned at various chordwise locations [163–165]. Hot-film methods were not available during this research therefore an alterative detection method was required. Within this research the surface flow field over the wing was visualised using oil flow techniques generating surface streaklines. The detection of transition using such a method is unclear due to the qualitative nature of the data obtained. This chapter discusses the identification and validation of boundary layer transition to turbulent through the use of oil flow visualisation techniques and numerical methods.

D.1 Experimental Method

Transition to turbulent of a boundary layer on a multi-element wing in ground effect is complex and highly three-dimensional. A simplified case was therefore investigated consisting solely of the main element at an incidence of $+4^\circ$ and a ride height of $1.295c_m$. The single element wing was equipped with endplates described in Section 3.2.3 in order to minimise the three-dimensionality of flow field. The test was conducted at a constant dynamic head of 56.19mm of water. The suction surface flow field was visualised using an oil flow technique.

Figure D.1 presents the streaklines over the suction surface of the wing. The streaklines indicated an abrupt change in surface flow field at $x/c_m \approx 0.26$. At the centre span of the main element the abrupt change in streakline structure is absent. It was noted that large particles of flow visualisation were located directly upstream of this spanwise location which disturbed the downstream flow field producing the non-uniform region observed. To verify that the abrupt variation in surface flow field was boundary layer transition numerical validation was required.

D.2 Numerical Method

The transition of a boundary layer to turbulent may be numerically predicted using a model based on instability theory. The e^n method is one such model which uses spatial-amplification theory based on the Orr-Sommerfeld equation. The e^n transition prediction method is used within XFOIL [166], a two-dimensional high-order panel method with a fully coupled viscous-inviscid interaction method deigned specifically for aerofoils. A detailed description of the boundary layer formulation used within XFOIL is stated by Drela & Giles [167].

The experimental conditions experienced while obtaining the oil flow visualisation were replicated within XFOIL v6.9. The incidence of the main element was set at $+4^\circ$ with the aerofoil in freestream. The aerofoil was modelled using 280 panels with the panels refined towards the leading edge and on the suction surface. The formulation of the Reynolds number within the panel method was not standard (Equation D.1) therefore the experimental conditions were used to calculate a modified Reynolds number (Re_{mod}). Simulations were performed accordingly with $Re_{mod} = 2.0 \times 10^6$.

$$Re_{mod} = \frac{U_\infty \rho}{\mu} \tag{D.1}$$

The vertical velocity profiles within a laminar and turbulent boundary layer are inherently different with the turbulent boundary layer possessing a more asymptotic profile. Therefore an alteration in the shape of the velocity profile within the boundary layer is a reliable indication of transition. The shape parameter (H_s) at a given streamwise location is defined in Equation D.2 where δ^* and θ are the displacement thickness and momentum thickness of the boundary layer respectively.

$$H_s = \frac{\delta^*}{\theta} \tag{D.2}$$

Figure D.2(b) presents the variation in shape parameter over the suction surface of the main element. A sudden decrease in the shape parameter was observed at $x/c_m = 0.23$ from a value typical for a laminar boundary layer ($H_s \approx 3$) to a value typical for a turbulent boundary layer ($H_s \approx 1.5$) indicating transition. Figure D.2(a) presents the oil flow visualisation of the suction surface scaled to allow for direct comparison with the shape parameter variation. It was noted that the numerical results indicated a short transition region. The experimental streaklines however indicated a long region of transition. This discrepancy was a attributed to the assumption of immediate transition to turbulent within the numerical method.

D.3 Chapter Summary

It has been shown that boundary layer transition to turbulent may be identified using oil flow visualisation techniques. Numerical validation has verified the surface streakline patterns which represent boundary layer transition.

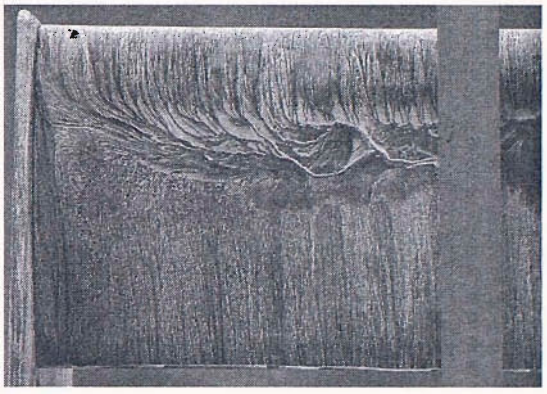

Figure D.1: Suction surface streaklines on the starboard tip of the main element; $h/c_m = 1.295$.

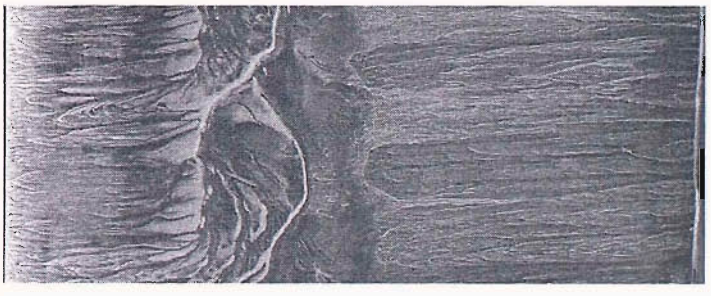

(a)

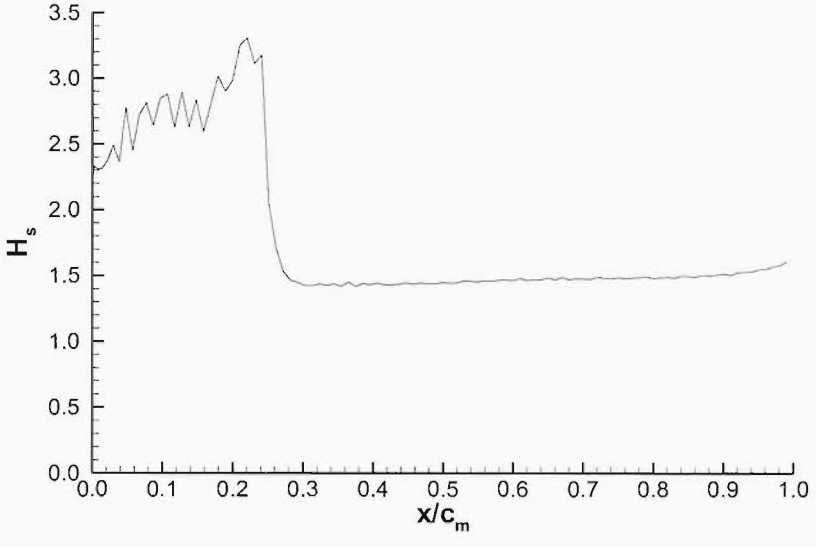

(b)

Figure D.2: Comparison of experimental and numerical results; (a) experimental oil flow visualisation of the suction surface (flow from left to right), (b) shape parameter variation along the suction surface of the main element.